SHOCK TUBE STUDY OF CYANIDE SPECIES KINETICS AND SPECTROSCOPY

By

MICHEL YVES LOUGE

Report #10-243

HIGH TEMPERATURE GASDYNAMICS LABORATORY
Mechanical Engineering Department
Stanford University

SHOCK TUBE STUDY OF CYANIDE SPECIES KINETICS AND SPECTROSCOPY

By

Michel Yves LOUGE

Report # 10-243

High Temperature Gasdynamics Laboratory
Department of Mechanical Engineering
Stanford University
Stanford, California

October 1984

I certify that I have read this thesis and that in my opinion it is fully adequate, in scope and quality, as a dissertation for the degree of Doctor of Philosophy.

_____

(Principal Adviser)

I certify that I have read this thesis and that in my opinion it is fully adequate, in scope and quality, as a dissertation for the degree of Doctor of Philosophy.

_____

I certify that I have read this thesis and that in my opinion it is fully adequate, in scope and quality, as a dissertation for the degree of Doctor of Philosophy.

_____

Approved for the University Committee on Graduate Studies:

_____

Dean of Graduate Studies & Research

Acknowledgments

This work was supported by the Environmental Protection Agency under Grant R-810019.

I wish to express my gratitude to the faculty and students of the High Temperature Gasdynamics Laboratory, and to my research advisor Prof. Ronald K. Hanson, for their support and continuous advice throughout this research project.

Je dédie cette thèse à mon épouse Nadine, ma fille Nathalie, et à Georges, Arlette et Alain.

Abstract

The high-temperature kinetics of various elementary reactions of C_2N_2, HCN, CN and NCO have been investigated using a shock tube and in situ spectroscopic measurement techniques.

The primary diagnostic techniques included broad-band absorption of CN at 388 nm $[B^2\Sigma^+(v=0) \leftarrow X^2\Sigma^+(v=0)]$ and narrow-line absorption of NCO at 440 nm using a remotely-located cw ring dye laser source. Spectroscopic models were developed to interpret the absorption levels of CN at 388 nm and NCO at 440 nm. A spectral survey of NCO absorption near the $P_2+{}^PQ_{12}$ head of the $[A^2\Sigma^+(00^00) \leftarrow X^2\Pi_i(00^10)]$ band was obtained at 1450°K and an oscillator strength of 0.0026 was inferred for the $(00^00) \leftarrow (00^10)$ band.

Mixtures of cyanogen, oxygen and nitrous oxide diluted in argon were shock-heated to measure the rate constants of

$$C_2N_2 + O \rightarrow CN + NCO, \quad (2)$$

$$CN + O \rightarrow CO(v) + N, \quad (3)$$

$$CN + O_2 \rightarrow NCO + O, \quad (4)$$

$$NCO + O \rightarrow CO + NO, \quad (5)$$

and

$$NCO + M \rightarrow N + CO + M, \quad (6)$$

with the results $k_2=10^{11.70(+0.25,-0.19)}$ $cm^3/mole/sec$
and $k_3=10^{13.26(\pm 0.26)}$ $cm^3/mole/sec$ near 2000°K,
$k_4=10^{12.68(+0.27,-0.19)}$ $cm^3/mole/sec$ near 2400°K,
$k_5=10^{13.75(+0.20,-0.26)}$ $cm^3/mole/sec$ near 1450°K,
and $k_6=10^{16.8(\pm 0.4)}T^{-0.5}\exp[-24000/T]$ $cm^3/mole/sec$
in the temperature range $2150<T<2400$°K and at the average pressure $p=0.65$ atm.

Other experiments in mixtures of hydrogen cyanide, oxygen and nitrous oxide diluted in argon enabled a determination of the ratio k_8/k_2

$$HCN + O \rightarrow NCO + H. \quad (8)$$

At 1440°K, $k_8/k_2=2.4(+2.4,-0.9)$.

Utilizing a value extrapolated to 1440°K from the present measurement of k_2 at 2000°K, $k_8=10^{11.70(+0.40,-0.35)}$ cm^3/mole/sec at 1440°K.

An additional mixture of cyanogen, oxygen, hydrogen and nitrous oxide diluted in argon was shock-heated and NCO was monitored to infer the rate constants for

$$NCO + H \rightarrow CO + NH, \tag{9}$$

$$NCO + H_2 \rightarrow HNCO + H, \tag{10}$$

and the ratio k_{11}/k_{12}

$$C_2N_2 + H \rightarrow CN + HCN, \tag{11}$$

$$CN + H_2 \rightarrow HCN + H. \tag{12}$$

At 1490°K, $k_9=10^{13.73(+0.42,-0.27)}$ cm^3/mole/sec,

$k_{10}=10^{12.1(+0.4,-0.7)}$ cm^3/mole/sec,

and $k_{11}/k_{12}=0.81(+0.89,-0.47)$.

Table of Contents

List of Tables

List of Figures

List of Symbols

a	Voigt parameter.
a	Shock attenuation (μsec^{-1}) (see Fig. A1.4).
A	Rate constant pre-exponential factor.
$\mathbf{A}$	Vector of profile features.
A_c	Pre-exponential factor of k_c in Arrhenius form (cm^3/mole/sec).
$A_{u\to\ell}$	Einstein A-coefficient (sec^{-1}).
A_v	Spin-orbit coupling constant of vibrational level v (cm^{-1}).
$A(\chi)$	"Accuracy" of an absorption diagnostic.
B_v	Rotational constant of vibrational level v (cm^{-1}).
c	Speed of light ($2.998\ 10^{10}$ cm/sec).
C, D	Herman-Wallis constants for vibration-rotation interaction.
d	Vectorial separation of normal coordinates (cm $g^{1/2}$).
d	Experimental dilution (see appendix 7).
D_v	Rotational (centrifugal distortion) constant of vibrational level v (cm^{-1}).
e	Charge of the electron ($1.602\ 10^{-19}$ C).
E_i	Activation energy of reaction (i) (kcal/mole).
$E_0^{\ddagger}$	Barrier height (kcal/mole).
$E(v,J)$	Energy of the (v,J) level (cm^{-1}).
$F(T)$	Calibration constant (see appendix 7).
$F(J)$	Rotational energy (cm^{-1}).
$f_{v'v''}$	Oscillator strength of the band ($v'\leftarrow v''$).
f_{el}	"Electronic" oscillator strength.
f_i	Lower uncertainty factor on k_i.
F_i	Upper uncertainty factor on k_i (see appendix 6).
g	Level degeneracy.
$\mathbf{G}$	Kinetic energy matrix (g^{-1}).
$G(v)$	Vibrational energy (cm^{-1}).
h	Planck's constant ($6.63\ 10^{-27}$ erg sec).
H_v	Hermite polynomial of degree v.
i	Transmitted power (mW).
i_0	Reference power (mW).

J	Rotational quantum number.
$\mathbf{J}$	Jacobian matrix.
K	Quantum number of vibronic angular momentum (polyatomic molecules).
K	Quantum number of the total angular momentum apart from spin (diatomic molecules).
$\mathbf{K}$	Vector of kinetics parameters.
k_c	Line-of-center collision rate constant (cm^3/mole/sec).
k_i	Rate constant of reaction (i) (cm^3/mole/sec).
k_{de}	Rate of vibrational de-excitation (cm^3/mole/sec).
k_e	Rate of vibrational excitation (cm^3/mole/sec).
k_f	Forward rate (cm^3/mole/sec).
k_b	Backward rate (cm^3/mole/sec or cm^6/$mole^2$/sec for termolecular reactions).
K_p	Equilibrium constant ($atm^{\Delta n}$); Δn=number of molecules created by the reaction.
ℓ	Quantum number of vibrational angular momentum.
L	Absorption path length (cm).
m	Rate constant temperature exponent.
m	Rotational line index ($m=-J$ for $\Delta J=-1$, $m=J+1$ for $\Delta J=+1$).
M	Third-body (usually argon).
M	Mach number.
m_e	Mass of the electron ($9.11\ 10^{-28}$ g).
$M(\nu)$	Monochromator slit function.
MW	Molecular weight (amu, g/mole).
n	Electronic level index.
N	Avogadro's number ($6.023\ 10^{23}$).
N	Quantum number of total angular momentum apart from spin.
N	Number of wavemeter fringes.
N_i	Number density of species i (cm^{-3}).
$n(\lambda)$	Index of refraction of air at wavelength λ.
p	Splitting constant for Λ- or K-doubling (cm^{-1}).
p_i	Partial pressure of species i (atm).
p_2	Total post-shock pressure (atm).
$P(\nu)$	Lamp relative spectral intensity.

$P_j^{i\to k}$	Fraction of fuel-nitrogen participating in reaction (j).
Q_e	Electronic partition function.
Q_r, Q_{rot}	Rotational partition function.
Q_{tot}	Total partition function.
Q_{tr}	Translational partition function (cm^{-3}).
Q_v, Q_{vib}	Vibrational partition function.
$Q_{\ddagger}$	Activated complex partition function (excluding the vibrational mode along the reaction coordinate).
Q_{v_i}	Partial vibrational partition function of normal mode v_i.
$q_{v'v''}$	Franck-Condon factor of the band ($v' \leftarrow v''$).
r	Inter-atomic distance (Å).
R	Universal gas constant ($8.31\ 10^7$ erg $°K^{-1}$ $mole^{-1}$ or 82.1 atm cm^3/mole/°K).
R(v',v")	Overlap integral.
R	Vectorial change of equilibrium positions (cm).
$RR_j^{i\to k}$	Rate of reaction (j) (sec^{-1}).
S	Absorption line strength ($cm^{-2}atm^{-1}$).
S	Vector of internal displacement coordinates (cm).
S_0	Band strength ($cm^{-2}atm^{-1}$).
S_{CO}	Equilibrium CO line strength ($cm^{-2}atm^{-1}$).
$S_{CO(v=1)}$	CO(v=1) line strength ($cm^{-2}atm^{-1}$).
$S_{J''J}$, S	Rotational line strength.
S/N	Signal-to-noise ratio.
$S(\chi)$	"Sensitivity" of an absorption diagnostic.
$\mathbf{s}_{t\alpha}$	"Effectiveness" vector.
t	time (μsec).
$t_{1/2}$	Time-to-reach half a final concentration (μsec).
$t_{1/e}$	1/e time (time-to-reach 63% of final concentration).
T	Temperature (°K).
T_2	Total post-shock temperature (°K).
$T_e(n)$	Electronic energy (cm^{-1}); reference, bottom of potential well.
v	Vibrational quantum number.
V	Voltage (mV).
V(a,x)	Voigt function.

v_s	Shock speed (mm/μsec).
x	Normalized Voigt frequency.
x	Gas cylinder dilution (% in argon).
x_e	Degree of advancement of a reaction.
x_e	Anharmonicity correction of the vibrational matrix elements.
X, A, B	Indices of successive electronic levels of a linear molecule.
Y_{ik}	Dunham coefficient (cm^{-1}).
Z	Collision frequency (sec^{-1}).

Note: (") indicates a ground state and (') an excited state.
[i] refers to the concentration of species i ($mole/cm^3$).
For branch notation (e.g. P_1, $^0P_{12}$, etc...), see ref. [51].
(‡) refers to an activated complex.
Asterisks (*) refer to equilibrium conditions.

Greek

α	Parameter see eq. (A2.28).
α	Parameter see eq. (A4.19).
α	Linear temperature coefficient of n(λ).
α, β	Spin splitting indices.
β	Parameter see eq. (A4.19).
β(λ or ν)	Absorption coefficient ($cm^{-1}atm^{-1}$).
β^*	Approximate absorption coefficient using ϕ^* ($cm^{-1}atm^{-1}$).
γ	Ratio of specific heats.
γ	Parameter see eq. (A4.19).
2γ(T)	Collision width per unit pressure ($cm^{-1}atm^{-1}$).
2γ°	Collision width at 300°K ($cm^{-1}atm^{-1}$).
δ	Non-resonance frequency (cm^{-1}).
δ	Uncertainty in $\Delta Hf_0°$ (kcal/mole).
ΔH	Heat of reaction (kcal/mole).
$\Delta Hf_0°(i)$	Heat of formation of species (i) at 0°K (kcal/mole).
$\Delta\nu_C$	Collision width (cm^{-1}).
$\Delta\nu_D$	Doppler width (cm^{-1}).
$\Delta S_f°$	Total entropy change for a reaction (kcal/mole/°K).

ε_0	Permittivity of free space ($8.85\ 10^{-12}$ F/m).
$\varepsilon(\lambda)$	Wavemeter correction at wavelength λ.
θ	Activation temperature (=E/R, °K).
θ_{vib}	Vibrational temperature (°K).
λ	Wavelength (nm or Å).
λ	Proportionality constant (see eq. 5.4).
Λ	Quantum number of the total electronic orbital angular momentum about linear axis; Λ=0, Σ-state; Λ=1, Π-state.
μ	Reduced mass (amu, g/mole).
ν	Frequency (cm^{-1}).
$\bar{\nu}_0$	Average band frequency (cm^{-1}).
ν_{00}, ν_{10}	Band origin frequencies (cm^{-1}).
ν_i	Vibrational mode.
ρ_{21}	Density ratio across the shock wave.
σ	Collision cross-section diameter (Å).
σ	Variance.
τ	Characteristic time (μsec).
ϕ	Equivalence ratio.
ϕ	Inter-atomic angular displacement.
$\phi(\lambda$ or $\nu)$	Broadening function (cm).
ϕ^*	Approximate broadening function (cm); see eq. (A3.38).
χ_i	Mole fraction of species i.
Ω	Quantum number of total electronic angular momentum about internuclear axis.
ω_e, ω_i	Normal vibration frequencies (cm^{-1}); reference, bottom of potential well.
$\omega_i{}^\circ$	Normal vibration frequency (cm^{-1}); reference, zero-point energy.

Chapter 1

Introduction

Nitric oxide is a major source of pollution in large urban areas [1]. Through its partial oxidation to NO_2, it usually contributes to the familiar photochemical smog. As a source of nitric acid (HNO_3), it is also partially responsible for acid rain.

A major source of nitric oxide results from the direct oxidation of atmospheric nitrogen. A successful model for this formation of "thermal NO" has been attributed to Zeldovich [2] and consists of a three reaction sequence

$$N_2 + O \rightarrow NO + N, \qquad (15)$$
$$N + O_2 \rightarrow NO + O, \qquad (-16)$$
$$N + OH \rightarrow NO + H. \qquad (-22)$$

Thermal-NO emission can often be successfully controlled by reducing temperature and available oxygen.

Another important source of nitric oxide results from the combustion of nitrogen compounds imbedded in the structure of most fossil fuels [3], which are commonly burned in large stationary combustors. The mechanism for this transformation (commonly referred to as the "fuel-nitrogen mechanism") is more complex and involves a multi-reaction process, which is sketched in Fig. 1.1. Unlike the Zeldovich mechanism, this process results in emissions of NO at lower temperatures and richer stoichiometries. Despite its apparent complexity, it can be regarded as a sequence of four global steps.

The first step in premixed flames consists of a rapid conversion of fuel-nitrogen to hydrogen cyanide (HCN) in the reaction zone. Experiments under rich stoichiometries have suggested that such production of HCN is fast and nearly complete, regardless of the original nitrogen compound [3]. Various mechanism which depend on the nature of the fuel-nitrogen coumpound have been proposed to explain the chemistry of HCN

production in the reaction zone [4,5]. Because of its apparent speed, this initial step has not been considered rate-limiting, and many studies of the fuel-nitrogen mechanism have focused on the subsequent transformation of HCN to NO or N_2. In particular, we note the recent experiments of Miller and co-workers [6], who directly added HCN into the premixed reactants of an H_2/O_2/argon low-pressure flame.

The second step occurs in the post flame gases. Hydrogen cyanide reacts with active radicals and atoms to form cyano species such as CN, NCO, and possibly HNCO. In the next phase, the strong C-N bond is broken and the cyano intermediates give rise to amine species (NH_i) such as N, NH, and NH_2. Finally, the amine species react to form either NO or N_2.

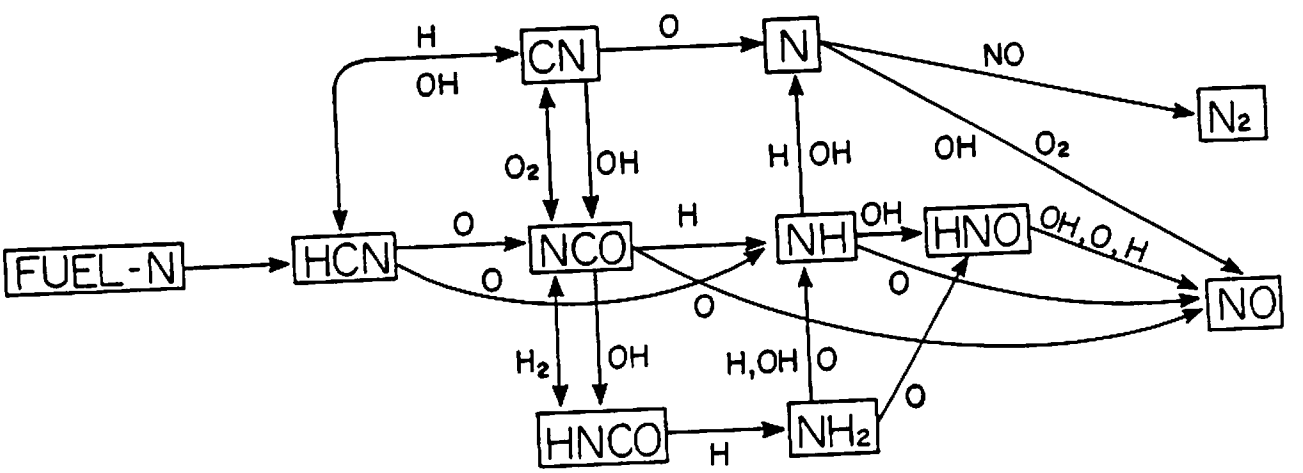

FUEL-NITROGEN MECHANISM

Fig. 1.1 The fuel-nitrogen mechanism in the post-flame zone of a typical premixed flame.

Nitric oxide can also appear in the reaction zone of rich hydrocarbon/air flames without fuel-nitrogen [7]. Fenimore discovered this phenomenon and called it the "prompt-NO" mechanism [8]. Despite some controversy on the actual chemistry of prompt-NO, it is generally believed that reactions of molecular nitrogen with hydrocarbon radicals can result in the production of HCN [7,9]. As before, HCN is eventually converted to NO or N_2 by the mechanism in Fig. 1.1. Thus, molecular nitrogen reacts like other fuel-nitrogen coumpounds, despite a slower rate of conversion to HCN [10].

Hydrogen cyanide is therefore an important precursor of nitric oxide in hydrocarbon/air flames. To achieve a better understanding of NO formation in such flames, it is essential to measure the rates of key reactions in the mechanism of Fig. 1.1.

In this study, a shock tube was used to measure the rates of several reactions important in the HCN to NH_i conversion

$$HCN + O \rightarrow NCO + H, \tag{8}$$

$$CN + O \rightarrow CO + N, \tag{3}$$

$$CN + O_2 \rightarrow NCO + O, \tag{4}$$

$$NCO + O \rightarrow CO + NO, \tag{5}$$

$$NCO + M \rightarrow N + CO + M, \tag{6}$$

$$NCO + H \rightarrow NH + CO, \tag{9}$$

$$NCO + H_2 \rightarrow HNCO + H. \tag{10}$$

As indicated in Fig. 1.1, CN and NCO play a key role in the conversion of HCN to NH_i. Therefore, the development of quantitative CN and NCO diagnostic techniques has constituted another essential aspect of this study.

In order to simplify the reaction mechanism and minimize interfering reactions, mixtures of gases containing only three atoms (C, N and O) were first shock-heated. Using measurements of CN, CO and NO, the rates of

$$C_2N_2 + O \rightarrow CN + NCO, \tag{2}$$

$$CN + O \rightarrow CO + N, \quad (3)$$

$$CN + O_2 \rightarrow NCO + O, \quad (4)$$

were inferred behind incident shock waves in mixtures of cyanogen (C_2N_2), nitrous oxide (N_2O), oxygen and argon, and the formation of NCO from C_2N_2 and CN was characterized. Two novel laser techniques were subsequently developed to monitor NCO in absorption at 305 and 440 nm. Then, additional mixtures of C_2N_2, N_2O and O_2 diluted in argon were shock-heated and NCO was monitored to measure the rates of

$$NCO + O \rightarrow CO + NO, \quad (5)$$

$$NCO + M \rightarrow N + CO + M, \quad (6)$$

and to characterize the new NCO diagnostic techniques. Fundamental spectroscopic parameters were extracted using reproducible levels of NCO generated in the shock tube, thus making the NCO absorption diagnostic quantitative. Finally, other NCO reactions were studied using the new NCO diagnostic

$$HCN + O \rightarrow NCO + H, \quad (8)$$

$$NCO + H \rightarrow CO + NH, \quad (9)$$

$$NCO + H_2 \rightarrow HNCO + H. \quad (10)$$

Direct determinations of the above rate constants at flame temperatures are limited. Shaub [11] determined k_3 using a single-pulse shock tube with analysis by gas chromatography. Mulvihill and Phillips [12] conducted a flame study using $H_2/O_2/N_2/C_2N_2$ mixtures and followed the reaction with a mass spectrometer to infer k_4. Many authors, however, have studied k_2, k_3 and k_4 at lower temperatures. Their techniques and results have been extensively reviewed by Baulch, et al. [13]. There are no previous data for k_5 and k_6, and data for k_8 are limited. Roth, Lohr, and Hermanns [14] measured k_8 by shock-heating HCN/N_2O/argon mixtures in the range $1800<T<2500°K$ and monitoring the H- and O-atom concentrations using an ARAS technique. Davies and Thrush [15] conducted a discharge flow study to find k_8 in the range $469<T<574°K$. Recently, Perry and

Melius [16] inferred the rate of the global reaction

$$HCN + O \rightarrow \text{products} \tag{1.1}$$

from measurements of NO_2 chemiluminescence using a laser photolysis technique ($575<T<840°K$), and observed NCO in laser-induced fluorescence to infer k_8 ($540<T<900°K$). There are no previous data for k_9 and k_{10}.

Measurements of NCO are limited. Anderson, et al. [17] observed the NCO spectrum in a flame by intracavity laser excitation and reported relative NCO concentration profiles. Bullock and Cooper [18] monitored relative NCO absorption at 438.48 nm in a kinetic study of the gas phase reactions of CN at low temperatures. Perry and Melius [16] observed NCO in laser-induced fluorescence and used HNCO for calibration.

The shock tube facility will be described in chapter 2 of this thesis. In chapter 3, we will examine the kinetics of cyanogen oxidation, and study the rates of CN formation and removal. In chapter 4, we will discuss the generation of reproducible NCO levels and the design of the NCO diagnostic. In chapter 5, additional measurements of NCO reaction rates will be reported. Concluding remarks and recommendations for future work will be given in chapter 6.

Chapter 2

The Shock Tube

Shock tubes have been a major source of experimental data for elementary reaction rates at high temperatures. Precise control of temperature and pressure can be achieved behind shock waves, and low experimental scatter has commonly been reported for the measurements of reaction rates [19]. In large diameter shock tubes (d>5 cm), small shock attenuations and limited boundary layer effects result in substantial reductions of the overall uncertainties in temperature, pressure and particle time. Dilution of the test mixtures with an inert gas such as argon can further reduce the effect of interfering reactions in the chemical mechanism, thereby making the species histories dependent on a small number of elementary reactions of interest. Recent advances in the species diagnostics such as the introduction of dye lasers have reduced experimental uncertainties associated with spectroscopic interferences and have promoted specific measurements of intermediate radicals such as NCO. Digital data recording of experimental traces has also enabled better computer data reduction procedures. The concerted use of a shock tube of large diameter, advanced laser diagnostics and good data acquisition capabilities has been an effective way to determine elementary reaction rates at temperatures greater than 1000°K.

Our experiments were conducted in the shock tube facility of the High Temperature Gasdynamics Laboratory at Stanford University. A picture of the shock tube taken from the driver section is shown in Fig. 2.1. The shock tube consists of two sections, which are shown schematically in Fig. 2.2. The driver section (id, 6"; length, 2.3m) and the test section (id, 6"; length, 10.4 m) were made of stainless steel of circular cross section. The inner surface of the test section has been honed to a smooth finish.

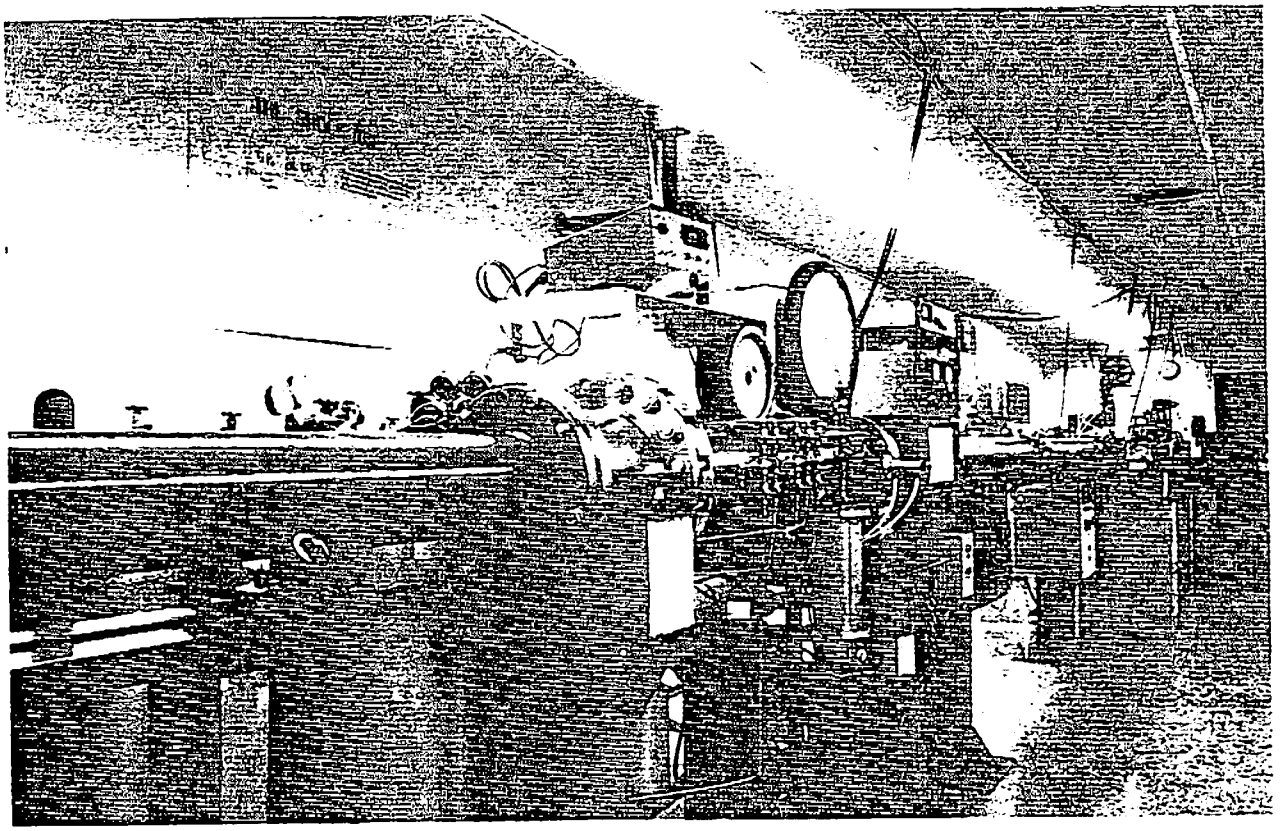

Fig. 2.1 A photograph of the shock tube, taken from the driver section.

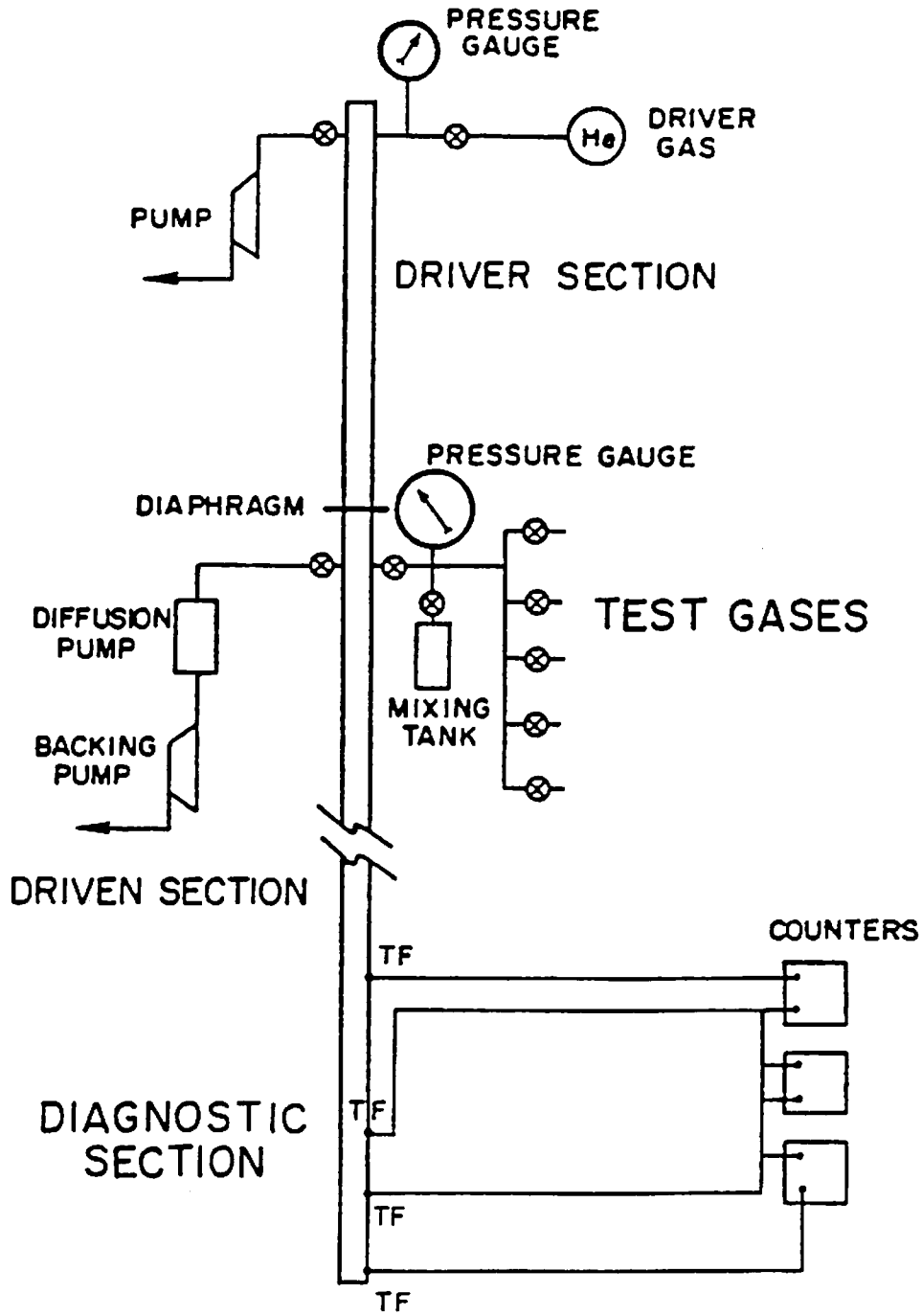

Fig. 2.2 A schematic of the shock tube apparatus.

Near the beginning of the test section, a mixing manifold connects the test gas bottles to a stainless steel mixing tank (id, 9.73cm; height, 30.48cm) provided with a magnetically driven mixing rod. Three pressure gauges connected to the manifold were used to monitor the mixture preparation. A MKS Baratron gauge with digital readout (0 to 1000 torr, 0.1% resolution) was used to monitor low gas pressures, and a Wallace and Tiernan gauge (-30 to 170 "Hg) was used to monitor larger pressures of argon diluent. Additional pressure information was obtained from a Heise gauge (0 to 15 psia). Commercially available test gases were used in all experiments, with purities indicated in Table 2.1.

Before each experiment, the shock tube was evacuated with a 15 cm oil diffusion pump backed by a Welch model 197 rotary pump to a pressure of 2×10^{-5} torr or lower. Pneumatically actuated valves were used to control the flow of gases in the entire shock tube, mixing manifold and vacuum system. Leak plus outgassing rates in the test section were monitored with a Veeco RG 31A ionization gauge controlled by a Varian 843 unit. Typical rates were small enough (1 to 5×10^{-5} torr/min) to prevent any significant air impurities from contaminating the test gas before each experiment.

Pressure-driven incident shock waves were generated in all experiments. A Lexan diaphragm was sealed with O-rings between flanges at the junction of the two shock tube sections. After evacuation of the driver section, commercial helium (see Table 2.1) was gradually introduced to build up pressure and slowly distort the diaphragm. A crossed knife-edge located a short distance downstream was used to puncture the diaphragm in four uniform petals, thereby initiating a shock wave in the test gas. Test gas pressure and diaphragm thickness were chosen to control the temperature and pressure behind the shock wave, using a semi-empirical correlation outlined in Appendix 1. Commercially available Lexan was used in four different thicknesses (0.01", 0.02", 0.04" and 0.06"). Experimental temperatures and pressures behind the shock were computed from the measured incident shock speeds. Four platinum thin film gauges mounted flush with the inner shock tube surface provided pulse signals to trigger three time interval counters (Eldorado 255-1). The counters

Table 2.1 - Analysis of the Test Gases

Species	Manufacturer	Impurities
N_2O >99.9%	Liquid Carbonic	<0.1% air
O_2 >99.95%	Matheson	
H_2 >99.999%	Liquid Carbonic	<1 ppm O_2 <5 ppm N_2 <1 ppm H_2O
C_2N_2 [a]	Matheson	<50 ppm HCN <50 ppm CNCl <50 ppm CO_2 <20 ppm O_2
HCN 7.4% [b]	Airco	<1 ppm H_2O <0.2 ppm SO_2 <1 ppm O_2 <1 ppm CO_2
Argon	Matheson	1.19 ppm O_2 0.91 ppm H_2O <0.05 ppm Total HC ≈ CH_4
He [c] >99.995%	Liquid Carbonic	

[a] Three cylinders: C_2N_2, 0.95%, 1.03% and 1.01% dilute in argon.
[b] Measured dilution in argon, see Appendix 7.
[c] Driver gas.

were calibrated with a time mark generator (Tektronix model 180A) to check the specified ±0.1 μsec accuracy. Shock attenuation attributed to non-ideal effects [20,21] was observed in all experiments. Shock speeds were found to decrease linearly with distance. The attenuation was typically 1.2%/m (maximum 2.5%/m) for the weakest shocks (T=1500°K) and 0.9%/m for the strongest (T=2400°K). The effects of attenuation on typical experimental conditions are further discussed in Appendix 1.

Chapter 3

Cyanogen Oxidation Kinetics

This chapter focuses on the study of important CN reactions in the fuel-nitrogen mechanism. In order to simplify the reaction mechanism and minimize interfering reactions, mixtures of gases containing only three atoms (C,N and O) were shock-heated. One mixture was composed of N_2O and C_2N_2 diluted in argon. Measurements of the CN and CO time histories were performed to determine the rate constants of reactions (2) and (3), the rate constant for (1) already being well established [22]

$$N_2O + M \rightarrow N_2 + O + M, \quad (1)$$

$$C_2N_2 + O \rightarrow CN + NCO, \quad (2)$$

$$CN + O \rightarrow CO(v=1) + N. \quad (3)$$

Another mixture containing O_2 and C_2N_2 diluted in argon was shock heated and CN was monitored to infer k_4 and the ratio k_5/k_6

$$CN + O_2 \rightarrow NCO + O, \quad (4)$$

$$NCO + O \rightarrow CO + NO, \quad (5)$$

$$NCO + M \rightarrow N + CO + M. \quad (6)$$

In this chapter, the optical diagnostics for CN, CO(v=1) and NO will be described, then the data reduction and results for each of the mixtures will be presented.

3.1 Experimental Considerations

The shock tube test section and optical diagnostic systems for CO and CN are shown schematically in Fig. 3.1. The signals obtained from all spectroscopic diagnostics were acquired by a digital oscilloscope (Nicolet Explorer III, dc-coupled through a 100 kHz upper frequency cut-off filter) and stored on tape using a computer interface for further data reduction.

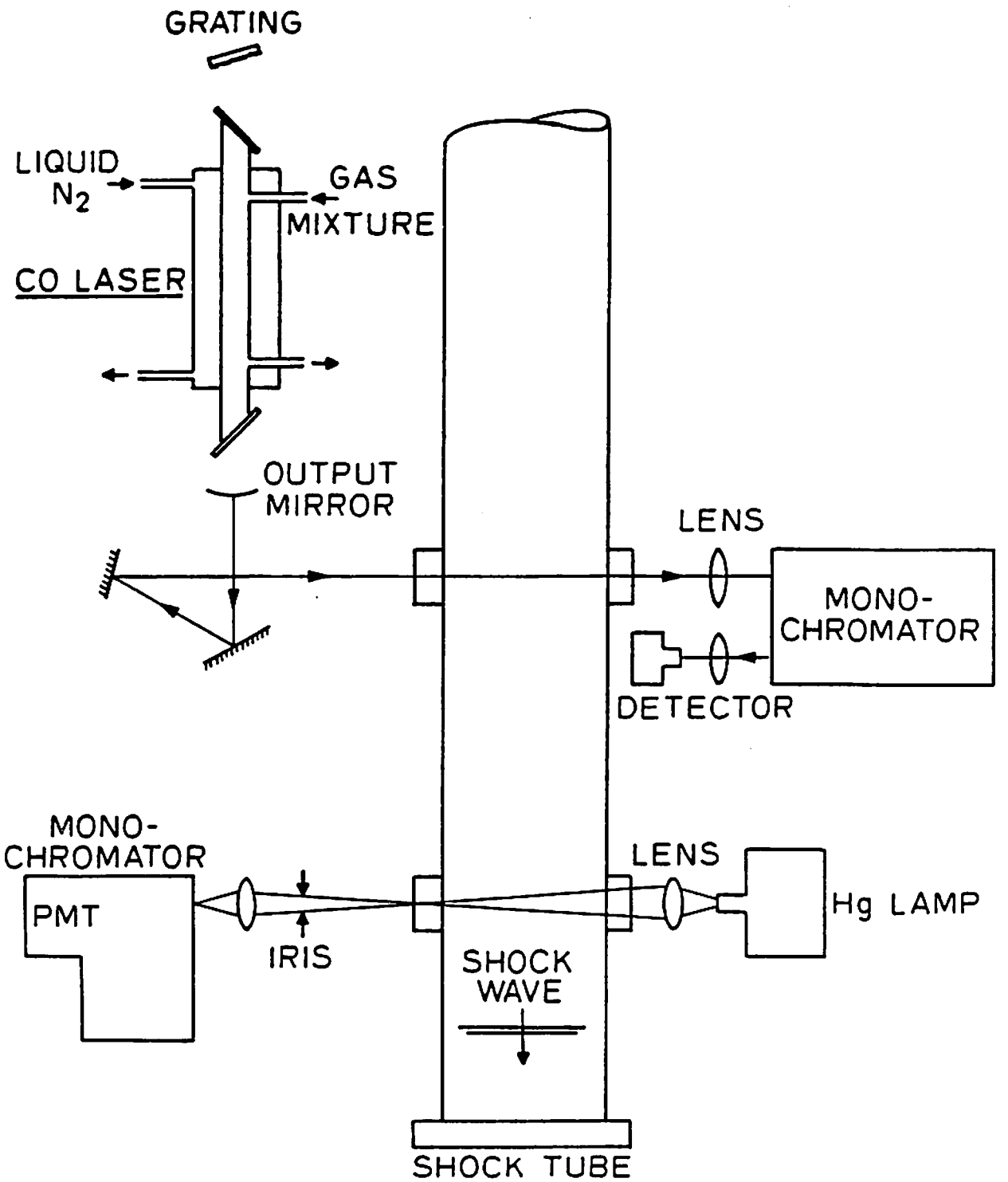

Fig. 3.1 A schematic of the CN and CO(v=1) absorption diagnostics.

3.1.1 CN absorption system

The absorption from the $[B^2\Sigma^+(v=0) \leftarrow X^2\Sigma^+(v=0)]$ band of CN at 388 nm was used as a CN diagnostic. The system consisted of a high-pressure broad-band Hg lamp (Oriel, 200 Watts), focusing optics, a 0.3 meter monochromator and a photomultiplier tube (RCA 1P28A) with a 6kΩ load resistor.

The monochromator (Instruments S.A., holographic grating blazed at 250 nm, linear dispersion 12.5 Å/mm) was calibrated using a Hg spectral lamp (Oriel) and an Ar^+ laser. The entrance and exit slit widths were measured to be 190 and 103 μm by recording a scan of the slit function under illumination from a He-Ne laser. An iris was used to block extraneous CN emission (see Fig. 3.1). Although the lamp blackbody temperature was always higher than the experimental heat bath, it was discovered from separate measurements that CN emission exceeded that expected for electronic equilibrium. This confirmed, under our experimental conditions, the findings of Setser and Thrush [23], who attributed the non-equilibrium emission to the reaction

$$O + O + CN \rightarrow CN^* + O_2. \tag{3.1}$$

In fact, the detected signal may be as much as 1000 times higher than the equilibrium CN emission for the $N_2O/C_2N_2/Ar$ mixtures and 50 times for the $O_2/C_2N_2/Ar$ mixtures, which is consistent with a strong dependence of the non-equilibrium emission with O-atom concentration. In order to find the upper temperature for emission-free experiments, a few tests were conducted with the Hg lamp blocked. It was found that the non-equilibrium emission could be neglected below 2100°K for the $N_2O/C_2N_2/Ar$ mixtures and below 2450°K for the $O_2/C_2N_2/Ar$ mixtures.

A computer program to predict the CN transmission under specified conditions was written in a manner similar to that reported by Colket [24]. Spectroscopic constants for CN were taken from various sources [24-27]. The position, strength and shape of each line seen by the photomultiplier were computed to generate an absorption coefficient profile $\beta(\nu)$ as a function of frequency,

$$\beta(\nu)=\sum_{\text{lines}}\left(\frac{\pi e^2}{m_e c^2}\right)\frac{(2J''+1)\exp\left[-\frac{hc}{kT}\left(T_e(n'')+G(v'')+F(J'')\right)\right]}{Q_e\ Q_v\ Q_r}\times$$

$$\frac{N}{RT}\ f_{el}\ q_{v'v''}\ \frac{S_{J'J''}}{(2J''+1)}\ \phi(\nu-\nu_0)\quad (\mathrm{cm}^{-1}\mathrm{atm}^{-1}), \tag{3.2}$$

where $T_e(n'')$, $G(v'')$ and $F(J'')$ are the electronic, vibrational and rotational energies of the lower state (cm^{-1}); R is the universal gas constant (atm cc/mole/°K); N is Avogadro's number; f_{el}, $q_{v''v'}$ and $S_{J''J'}$ are the oscillator strength, the Franck-Condon factor and the rotational line strength, respectively; Q_e, Q_v and Q_r are the electronic, vibrational and rotational partition functions; $\phi(\nu-\nu_0)$ is the lineshape factor (cm). (The quantity $\pi e^2/m_e c^2 = 8.826\ 10^{-13}$ cm.) A more complete description of CN quantitative spectroscopy is given in Appendix 2. The monochromator slit function $M(\nu)$ and the lamp spectral intensity $P(\nu)$ were integrated to obtain the predicted transmission,

$$\frac{i}{i_0}=\frac{\int P(\nu)\ M(\nu)\ \exp[-\beta(\nu)\ p_{CN}\ L]\ d\nu}{\int P(\nu)\ M(\nu)\ d\nu}\ . \tag{3.3}$$

The computer program was used to relate the experimental transmission traces to the actual CN time-history. This procedure is necessary since CN is a strong absorber and in most experiments the gas is not optically thin. Further considerations on experimental sensitivity of the CN diagnostic are discussed in Appendix 2. A listing of the computer model is given in Appendix 5.

Calibration experiments were performed by shock-heating C_2N_2 and Ar. Partial equilibrium of reaction (7) was assumed and the CN plateau was used as a reference,

$$C_2N_2 + M \rightarrow CN + CN + M. \tag{7}$$

A significant uncertainty in the heat of formation of CN prompted us to run these experiments at a relatively high temperature, where conversion of C_2N_2 to CN was virtually complete. A discussion of the sensitivity of

the calibration procedure to the heat of formation of CN is given in Appendix 2. Typical conditions were: $0.31<p_2<0.36$ atm , $2890<T_2<3150$°K , $150<\chi_{CN}<197$ ppmv. The monochromator wavelength setting was fine-tuned by running experiments with slightly different settings; the position that produced the maximum absorption was retained (the theory predicts this setting to be 3884 Å for our spectral bandpass, about 2.4Å).

Since we used known CN spectroscopic parameters, a calibration was in principle superfluous. However, small errors in the monochromator dial position and slit function could have a significant effect on the actual transmission. The calibration runs were thus aimed at establishing an "effective" value for the oscillator strength f_{el}, which could later be used to extrapolate transmission calculations to other conditions. The quantity was found to be 0.024, which is within the range of the literature values [28]. The experimental scatter was less than 6%, which implies an equal uncertainty in the inferred CN concentration.

Additional uncertainties in [CN] are due to the lamp noise ($\Delta\chi_{CN}/\chi_{CN} = (\Delta i/i_0)/A(\chi) = 7\%$, see Appendix 2) and to the error introduced by extrapolating the calibration to conditions outside the range of calibration (<15%). The three uncorrelated [CN] uncertainties mentioned above may be combined to give a global calibration uncertainty of $[\Sigma(\text{uncertainty})^2]^{1/2} = \pm 18\%$.

3.1.2 CO Laser Absorption System

The CO laser system is sketched in Fig. 3.1. It is composed of a liquid nitrogen cooled CW electric discharge CO laser, aligning and focusing optics, a monochromator (Jarrell-Ash, 0.5 meter, 4μm grating) and a fast (1μsec) InSb infrared detector (Judson J-10, with Perry 720 preamplifier). The laser has been described by Hanson, et al. [29]. The grating (blazed at 5.2 μm) enables tuning of the output beam to the desired CO line. The monochromator is used to remove adjacent interfering laser lines. This diagnostic takes advantage of certain spectral coincidences between high-lying CO laser lines and lower-lying CO absorption lines (see Fig. 3.2). Only two such coincidences were found in the spectral range of our laser (Table 3.1). The quantity δ is the

frequency spacing between the laser line and the CO absorption line center (cm^{-1}). Both choices provide an absorption diagnostic sensitive to the CO population in the first vibrational state v"=1.

Table 3.1 - CO-CO coincidences

CO laser line [30]		CO absorption line [a]		non-resonance δ	line strength $S_{CO(v=1)}$ at 2000°K [b]
transition	$\nu(cm^{-1})$	transition	$\nu(cm^{-1})$	cm^{-1}	$cm^{-2}\ atm^{-1}$
v(6→5) J(15→16)	1948.7274	v(2←1) J(37←38)	1948.7429	0.0155	0.374
v(9→8) J(6→7)	1907.6872	v(2←1) J(45←46)	1907.6765	0.0107	0.175

[a] Extrapolated to J=38 from Todd, et al. [30], using their Dunham coefficients.
[b] Using the experimental band strength at 273.2°K of 282 $cm^{-2}\ atm^{-1}$ (Varghese and Hanson [31]).

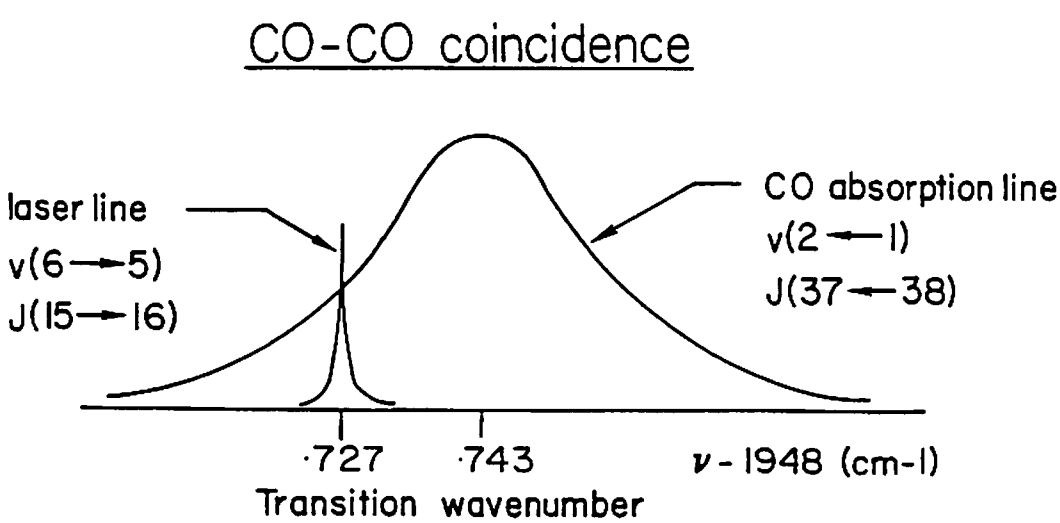

Fig. 3.2 A schematic of the CO-CO spectral coincidence. The abscissa shows frequencies in vacuo (cm^{-1}) minus 1948 cm^{-1}.

The first coincidence (1948 cm^{-1}) was used, because it provided better detection limits and more reliable lasing conditions. Calibration runs were performed to measure $2\gamma(300°K)$, the collision width per unit pressure, which is needed to calculate the Voigt absorption lineshape factor for the high temperature experiments. Knowledge of $2\gamma(300°K)$ and the CO(v=1) line strength is sufficient to calculate the concentration of CO(v=1) from a transmission measurement at known pressure and temperature [29,31]. Using Beer's law,

$$i/i_0=\exp[-\beta p_{CO(v=1)}L] \tag{3.4}$$

and

$$\beta=S_{CO(v=1)}(T)\phi(2\gamma p,T;\delta), \tag{3.5}$$

where $S_{CO(v=1)}$ is the line strength of the CO transition and ϕ the line shape factor. A plot of $S_{CO(v=1)}$ for the transition CO[v(2←1), J(37←38)] is shown in Fig. 3.3. Additional considerations for the CO(v=1) system are discussed in Appendix 3.

In the calibration runs, mixtures of CO and Ar were shock-heated under the following conditions: $2040°K<T_2<2430°K$, $0.58<p_2<0.70$ atm, CO:Ar=2:98. The temperature dependence that Hanson [32] had determined for the P(11) line was assumed here,

$$2\gamma(300°K)=2\gamma(T)(T/300)^{0.73}, \tag{3.6}$$

yielding the result $2\gamma(300°K)=0.10\pm0.03$ $cm^{-1}atm^{-1}$. This value is in good agreement with the recent findings of Varghese and Hanson [31,32].

To interpret the CO absorption records, the vibrational relaxation (about 500 μsec particle time for $p_2=0.7$atm and $T_2=2000°K$) was modeled using the following excitation/de-excitation process:

$$CO(v=1) + M \underset{k_e}{\overset{k_{de}}{\rightleftharpoons}} CO(v\neq1) + M , \tag{3.7}$$

where CO(v≠1) represents all vibrational states but v=1. In Appendix 3, it is shown that

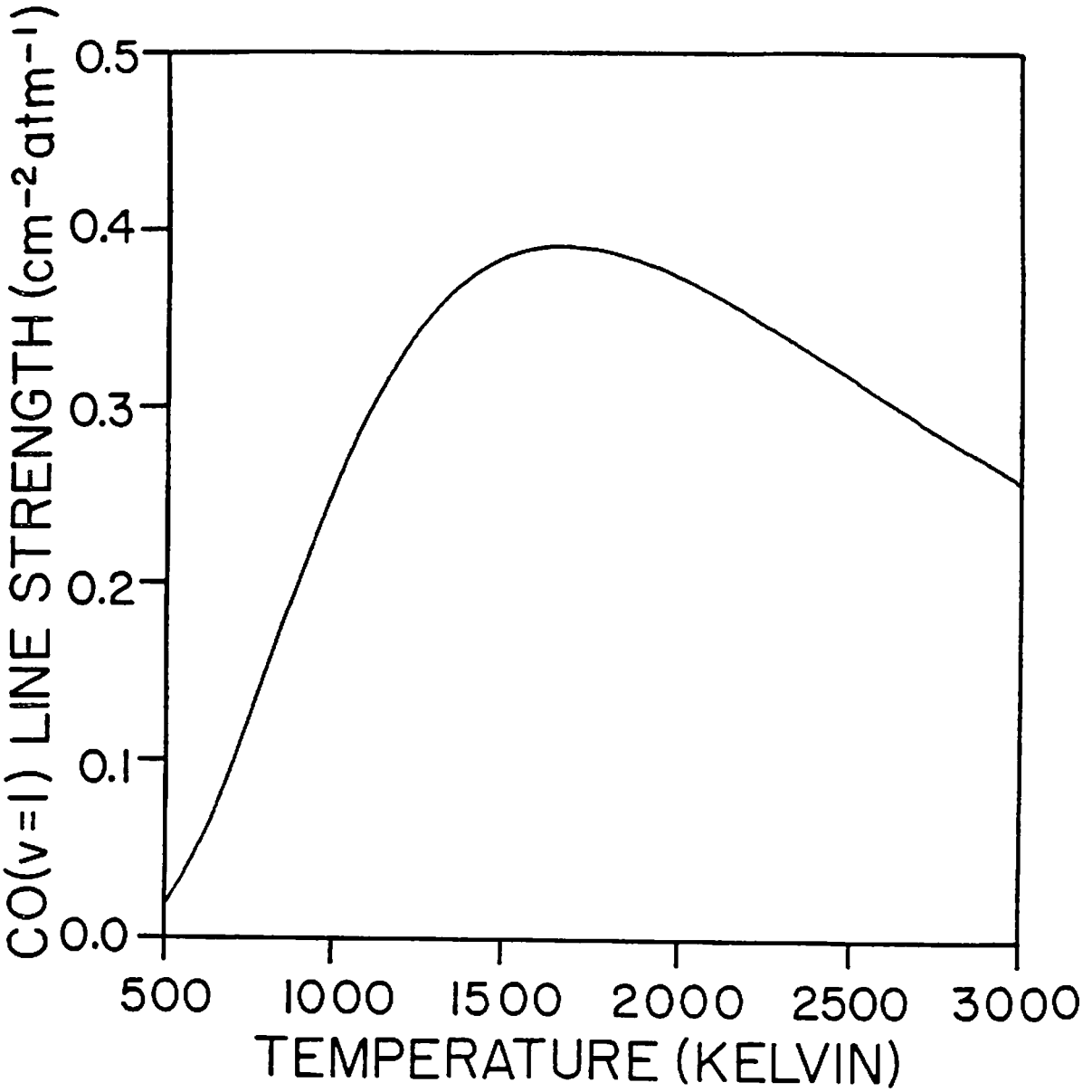

Fig. 3.3 Temperature dependence of the CO(v=1) line strength for the transition CO[v(2←1), J(37←38)].

$$\frac{k_e}{k_{de}} \equiv \frac{[CO(v\neq 1)]^*}{[CO(v=1)]^*} = \frac{\exp[-\theta_{vib}/T]}{Q_{vib} - \exp[-\theta_{vib}/T]} , \tag{3.8}$$

and

$$p\tau(v=1) = \frac{RT}{k_e + k_{de}} , \tag{3.9}$$

where τ is the vibrational relaxation time from v=1; θ_{vib} is the vibrational temperature = $hc\omega_e/k$; Q_{vib} is the vibrational partition function; the asterisk (*) refers to equilibrium conditions. Millikan and White's [33] results for $p\tau$ were used. These results agreed within 16% with our own measurements conducted in CO/Ar mixtures with $1800 < T_2 < 2900$°K. From the above expressions, k_e and k_{de} were extracted and fit to Arrhenius expressions for use in the kinetics modeling. Vibrational relaxation of CO is discussed in more detail in Appendix 3.

In all kinetics experiments a background absorption of the CO laser was observed that we attributed to N_2O. Accordingly, the absorption spectrum of N_2O in the vicinity of the CO laser lines [34-38] was calculated for a temperature of 2000°K. At this temperature N_2O has a large number of high-level υ_3 sub-bands which might produce the observed background interference. Many lines of strengths up to 0.001 cm^{-2} atm^{-1} likely are present in this spectral region. Assuming reasonable broadening parameters, the initial background absorption is consistent with the experimental observations. The CO(v=1) theoretical profiles were numerically converted to fractional transmission and corrected for the N_2O absorption background prior to comparison with the actual experimental traces,

$$\frac{i}{i_0} = \left(\frac{i}{i_0}\right)_{CO=1} \times \left(\frac{i}{i_0}\right)_{t=0}^{\frac{\chi_{N_2O}}{(\chi_{N_2O})_{t=0}}} , \tag{3.10}$$

where $(i/i_0)_{CO=1}$ is the transmission corresponding to the first vibrational level of CO, $(i/i_0)_{t=0}$ is the observed transmission at t=0, χ_{N_2O} the computed mole fraction of N_2O and (i/i_0) the corrected transmission.

In a few experiments, the CO laser diagnostic was tuned to coincidence with an NO(v=0) absorption line [Λ-doublet, Ω(3/2←3/2), v(1←0), J(39/2←37/2)] using the CO laser line at 1935.48165 cm^{-1} [v(7→6), J(12→13)], see Hanson, et al. [29]. Interference from the N_2O background was observed again in these experiments. Computed NO profiles were converted to fractional transmission using the line strength and broadening parameter reported by Hanson, et al. [29], and corrected for N_2O interference prior to comparison with the experimental traces.

3.2 C_2N_2/N_2O/argon Mixtures

3.2.1 Kinetics Experiments

Seven runs were conducted with mixtures of $N_2O:C_2N_2:Ar \approx 12:3:985$ and conditions in the range: $0.67 < p_2 < 0.75$ atm, $1920 < T_2 < 2110$°K, $3.51 < \rho_{21} < 3.61$. (ρ_{21} is the density ratio across the shock and also the ratio of particle time to laboratory time.) Shock speeds varied between 1.37 and 1.45 mm/μsec, with attenuation of 1%/m or less. Typical leak plus outgassing rates were $1\text{-}3\times10^{-5}$ torr/min. Gases were taken directly from commercial cylinders (Table 2.1), with C_2N_2 (0.95%) dilute in argon.

In these $N_2O/C_2N_2/Ar$ mixtures, spontaneous emission considerations in the CN absorption system placed an upper bound on the temperature. The lower bound on temperature was set by reaction rate and detection limit considerations. Excess N_2O was used to minimize interferences from reactions other than (2) and (3); however, the initial $[N_2O]/[C_2N_2]$ ratio was kept below 4.5 to avoid excessive N_2O background absorption and possible production of undesirable radicals such as NCN [39] by the postulated reaction sequence

$$N_2O + CN \rightarrow NCN + NO, \tag{32}$$

$$NCN + O \rightarrow CN + NO, \tag{33}$$

$$NCN + N \rightarrow CN + N_2. \tag{34}$$

The C_2N_2 level was adjusted to ensure an optimum sensitivity of the absorption system in measuring the peak value of [CN] (see Appendix 2).

3.2.2 Reaction Mechanism

The complete reaction mechanism utilized is shown in Table 3.2, but a simplified description can be given as follows. At early times, N_2O rapidly decomposes to provide O-atoms; C_2N_2 then reacts to form CN, which in turn is removed by O-atoms to give CO,

$$N_2O + M \rightarrow N_2 + O + M, \tag{1}$$

$$C_2N_2 + O \rightarrow CN + NCO, \tag{2}$$

$$CN + O \rightarrow CO(v) + N. \tag{3}$$

The rate of change of CN concentration is given by

$$\frac{d[CN]}{dt} = k_2[C_2N_2][O] - k_3[CN][O] \ . \tag{3.11}$$

At the peak of the CN trace

$$\frac{d[CN]}{dt} = 0 \ , \quad \text{and hence} \quad \frac{[CN]}{[C_2N_2]} = \frac{k_2}{k_3} \ . \tag{3.12}$$

It follows that the relative CN profile (using the peak as a reference) depends primarily on the rate of reaction (3) since, for this simplified model

$$\frac{d}{dt}\left(\frac{[CN]}{[CN]^{peak}}\right) = k_3[O]\left(1 - \frac{[CN]}{[CN]^{peak}}\right) \ . \tag{3.13}$$

The [CN] peak value thus depends primarily on the ratio k_2/k_3, and the relative time behavior depends on k_3. A record of [CN] is therefore sufficient to infer k_2 and k_3.

3.2.3 Experimental Fit

A numerical routine derived from the NASA-Lewis general chemical kinetics program [40] incorporating the mechanism in Table 3.2 was used for the kinetics calculations. The calculated CN concentrations were numerically converted into transmission profiles for comparison with the experimental traces (see Appendix 2).

Table 3.2 - Reaction Mechanism - C/N/O System

	Reactions	ΔH [a]	equil. const [b]	rate constants [c]			Source (Ref #)
				$\log_{10}A$	m	θ(°K)	
1	$N_2O+M \rightarrow N_2+O+M$	+40	-2.1	23.89	-2.5	32710	[22]
2	$C_2N_2+O \rightarrow CN+NCO$	+3	0.5	12.66	0	4440	This study
3	$CN+O \rightarrow CO(v=1)+N$	-75	6.7	13.31	0	210	This study
4	$CN+O_2 \rightarrow NCO+O$	-1	0.1	12.75	0	0	This study
5	$NCO+O \rightarrow CO+NO$	-106	10.5	13.75	0	0	This study
6	$NCO+M \rightarrow N+CO+M$	+48	-3.7	16.80	-0.5	24000	This study
7	$C_2N_2+M \rightarrow CN+CN+M$	+126	-10.0	34.46	-4.5	63150	[82]
13	$N_2O+O \rightarrow NO+NO$	-39	5.3	13.84	0	13400	[22]
14	$N_2O+O \rightarrow N_2+O_2$	-83	8.3	14.00	0	14100	[22]
15	$N_2+O \rightarrow N+NO$	+75	-6.8	14.26	0	38370	[22]
16	$NO+O \rightarrow N+O_2$	+32	-3.8	9.58	1.0	20820	[22]
17	$NCO+N \rightarrow N_2+CO$	-182	17.3	13.30	0	0	[44]
18	$NCO+N \rightarrow CN+NO$	-31	3.7	14.66	0	5530	[45][d]
19	$CN+N \rightarrow C+N_2$	-44	4.0	14.64	0	4530	[92]
32	$N_2O+CN \rightarrow NCN+NO$	+4	0.8	4.60	2.5	6080	[93]
33	$NCN+O \rightarrow CN+NO$	-43	4.5	10.20	1.1	1160	[93]
34	$NCN+N \rightarrow CN+N_2$	-119	11.3	10.50	0.9	0	[93]
35	$NCO+C \rightarrow CN+CO$	-137	13.3	14.00	0	0	estimate
	$CO_{v=1}+M \rightarrow CO+M$ [e]	-6	0.7	-5.81	4.6	3610	[33][f]

[a] Heat of reaction at 2200°K (kcal/mole) [63]. Thermochemical data was taken from the JANAF tables for all species [63], except for CN, where we used $\Delta Hf_0^0(CN)=101.2$ kcal/mole , an average of the values of Colket [24] and JANAF [63].

[b] $\log_{10}(k_{forward}/k_{backward})$ at 2200°K [63].

[c] Using the notation $k=A\ T^m \exp[-\theta/T]$ (cm^3/mole/sec).

[d] Colket measured $k_{backward}=10^{14}\exp[-21190/T]$ (cm^3/mole/sec); the expression $k_f/k_b=4.54\ \exp[15660/T]$ was assumed.

[e] Single step vibrational relaxation model for CO(v=1); see eq. (3.7).

[f] See Appendix 3, ¶ A3.3.

Figure 3.4 shows a best computer fit (solid lines) to the CN and CO traces simultaneously recorded in one experimental run. The error bars correspond to the calibration uncertainties, namely $\Delta[CN]/[CN]=\pm 18\%$ for CN and $\Delta[2\gamma(300°K)]=0.03\ cm^{-1}atm^{-1}$ for CO. The dotted line that appears on the CO record is a computer prediction which assumes that reaction (3) produces CO in the ground vibrational state. In this case, according to the model, CO(v=1) would barely absorb any incoming laser radiation at the early stages of the experiment, since its relaxation is very slow. We conclude therefore that reaction (3) produces CO in excited vibrational states; the quality of the fit further suggests that CO(v=1) is the principal product of this reaction. For a more detailed discussion of the products of reaction (3) at room temperature, the reader is directed to the paper by Schmatjko and Wolfrum [41].

3.2.4 Discussion and Results

For the $N_2O/C_2N_2/Ar$ mixtures, the peak [CN] value is nearly proportional to the ratio k_2/k_3. The uncertainty in the fit to the peak is therefore also the uncertainty in k_2/k_3. Figure 3.5 shows the influence of varying k_2/k_3 in the kinetic calculation by ±18% (the overall calibration uncertainty for [CN]; see Table 3.3).

For a fixed k_2/k_3 ratio, the shape of the CN trace is dependent on the specific values of k_2 and k_3. The uncertainty in k_2 and k_3 (associated with the fitting process) is thus determined by the range of values that produce an acceptable fit. Figure 3.6 shows the sensitivity of the fit to excursions of both k_2 and k_3, with the ratio k_2/k_3 fixed. The +50% excursion particularly affects the time-to-peak and the fit after 40μsec. Larger excursions clearly would not provide an acceptable fit. The -30% excursion fails to reproduce the initial slope. Note that these excursions produce equally unacceptable fits of the CO(v=1) trace. Conservative minimum uncertainties in k_2 and k_3 are therefore +50%, -30% (see "uncertainty in the fit" in Table 3.3). The reader is directed to Appendix 6 for a determination of uncertainty factors.

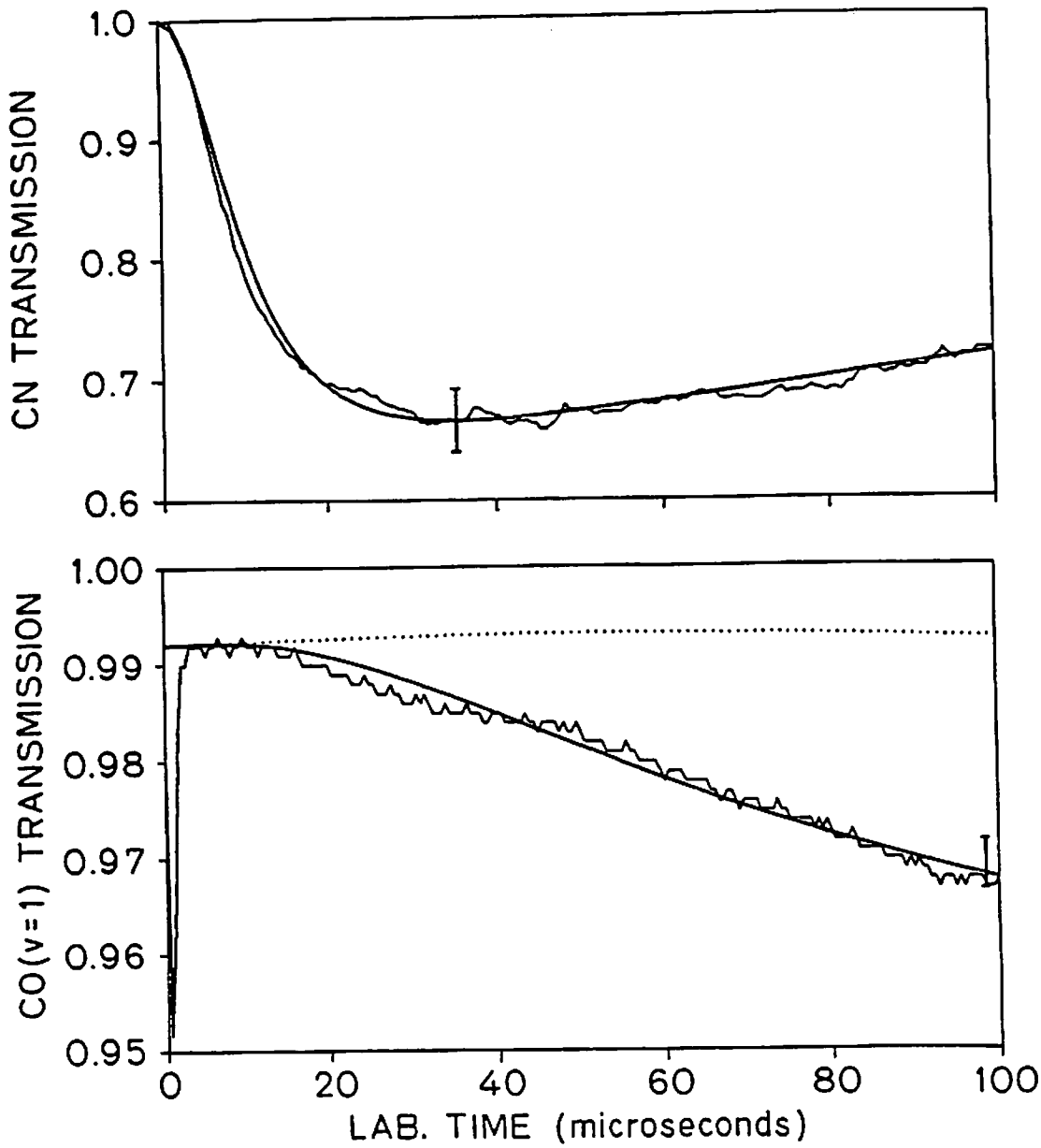

Fig. 3.4 Best fit of simultaneous CN and CO(v=1) transmission records. The conditions are: T_2=1943°K, p_2=0.67 atm, $N_2O:C_2N_2:Ar$= 12:3:985. The solid line is a best computer fit using $k_2=10^{11.67}$, $k_3=10^{13.26}$ (cm^3/mole/sec), and other rates shown in Table 3.2. The dotted line is a computer-generated profile assuming CN+O→CO(v=0)+N. The initial absorption corresponds to the N_2O background interference (see appendix 3).

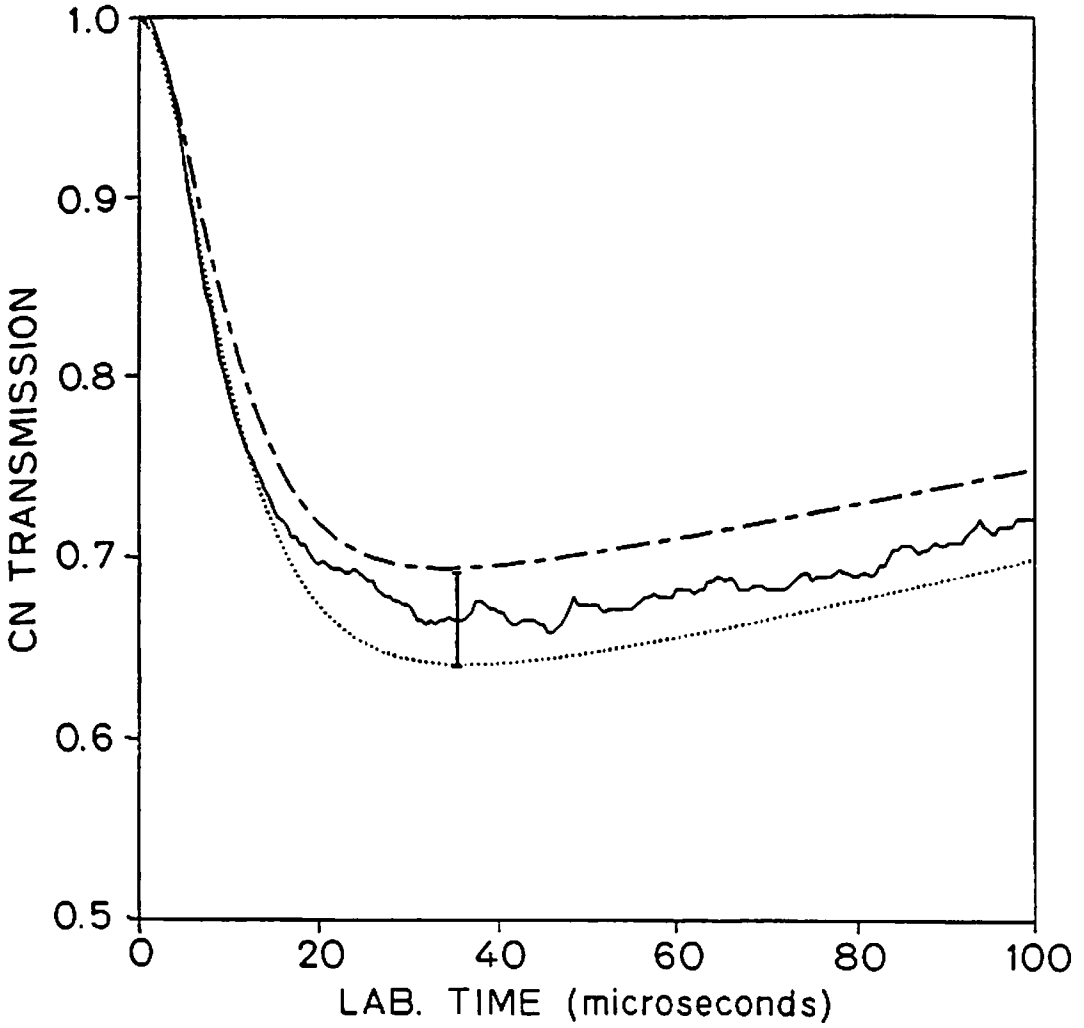

Fig. 3.5 Sensitivity of the CN fit to excursions in k_2/k_3. The conditions are identical to Fig. 3.4. The dotted lines are computer-generated profiles using the best rates in Fig. 3.4 except (•••) k_2/k_3 (+20%); (- • -), k_2/k_3 (-20%).

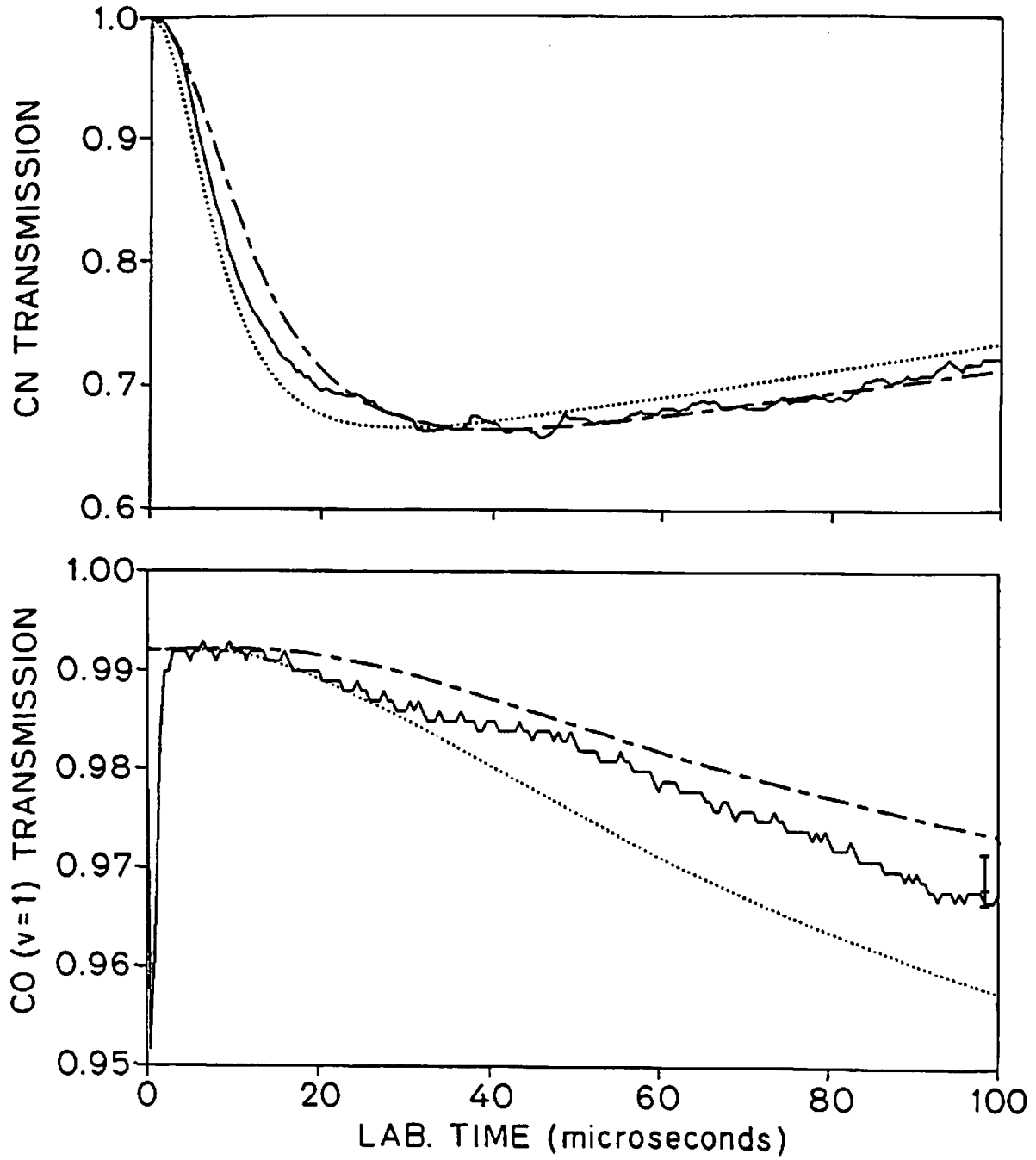

Fig. 3.6 Sensitivity of the CN and CO(v=1) fits to excursions in k_2 and k_3. The conditions are identical to Fig. 3.4. The dotted lines are computer-generated profiles using the best rates in Fig. 3.4 except (- · -), k_2 and k_3 (-30%); (···), k_2 and k_3 (+50%).

Table 3.3 - Uncertainty Analysis for k_2 and k_3

Reactions	Uncertainty factors	effect on:					
		k_2		k_3		k_2/k_3	
1 $N_2O+M \rightarrow N_2+O+M$	1.22	-18%		-18%		0%	
	0.82		+18%		+18%	0%	
5 $NCO+O \rightarrow CO+NO$	10.0	0%		-4%			+4%
	0.1	0%			+4%	-4%	
6 $NCO+M \rightarrow N+CO+M$	10.0	0%		-8%			+8%
	0.1	0%			+8%	-8%	
19 $CN+N \rightarrow C+N_2$ [a]	1.45	-12%		-40%			+18%
calibration	+18%	-9%			+9%	-18%	
uncertainty	-18%		+9%	-9%			+18%
uncertainty			+50%		+50%	0%	
in the fit		-30%		-30%		0%	
exp. scatter		-20%	+20%	-20%	+20%	-20%	+20%
total uncertainty [b] $=[\Sigma(\text{uncert.})^2]^{1/2}$		-43%	+57%	-58%	+58%	-28%	+34%

[a] This reaction was introduced in the mechanism with $k=(4.4\pm2)\ 10^{14}\ \exp(-4530/T)\ cm^3/mole/sec$ (Slack [92]).

[b] The individual uncertainties are statistically independent.

Additional uncertainties in k_2 and k_3 may result from uncertain knowledge of other rates of reactions present in the mechanism. In order to estimate these uncertainties, individual rates (Table 3.3) were adjusted by reasonable factors (based on current literature or our judgment); k_2 and k_3 were subsequently modified to ensure the return to an optimum fit. Table 3.3 summarizes the uncertainty analysis. The reaction $CN+N \rightarrow C+N_2$ was introduced as a possible interference to the proposed mechanism, although there is considerable question regarding its rate constant (see Baulch, et al. [13]). Note that, according to our fitting method, k_2 and k_3 are dependent quantities (e.g., the uncertainty in k_1 produces equal uncertainties in k_2 and k_3; see Table 3.3). As a consequence, the relative uncertainty in the ratio k_2/k_3 is less than the sum of the respective uncertainties in k_2 and k_3.

On the basis of this analysis, at temperatures near 2000°K:

$$k_2 = 10^{11.70(+0.25,-0.19)} \quad cm^3/mole/sec$$

$$k_3 = 10^{13.26 \pm 0.26} \quad cm^3/mole/sec$$

and

$$k_2/k_3 = 10^{-1.56(+0.15,-0.12)}.$$

No noticeable temperature dependence was observed in the limited range of these experiments ($1920 < T < 2110$°K).

This measurement of k_2 is plotted in Fig. 3.7 along with the result of Boden and Thrush [42] (shown with error bars recommended by Baulch, et al. [13]). An activation energy of 8.8±2.0 kcal/mole can be deduced assuming a straight-line fit (labelled "this evaluation") to the high and low temperature data.

Figure 3.8 shows the present result for k_3 plotted on the compilation of Baulch, et al. [13]. As expected for this exothermic reaction, the activation energy of k_3 is low. An accurate determination of this activation energy is prohibited by the size of our error bars and the scatter of low temperature data. A simple straight-line fit (labelled "this evaluation") to the present data at 2000°K and the room temperature recommendation of Baulch, et al. [13] was used for the detailed kinetics modeling.

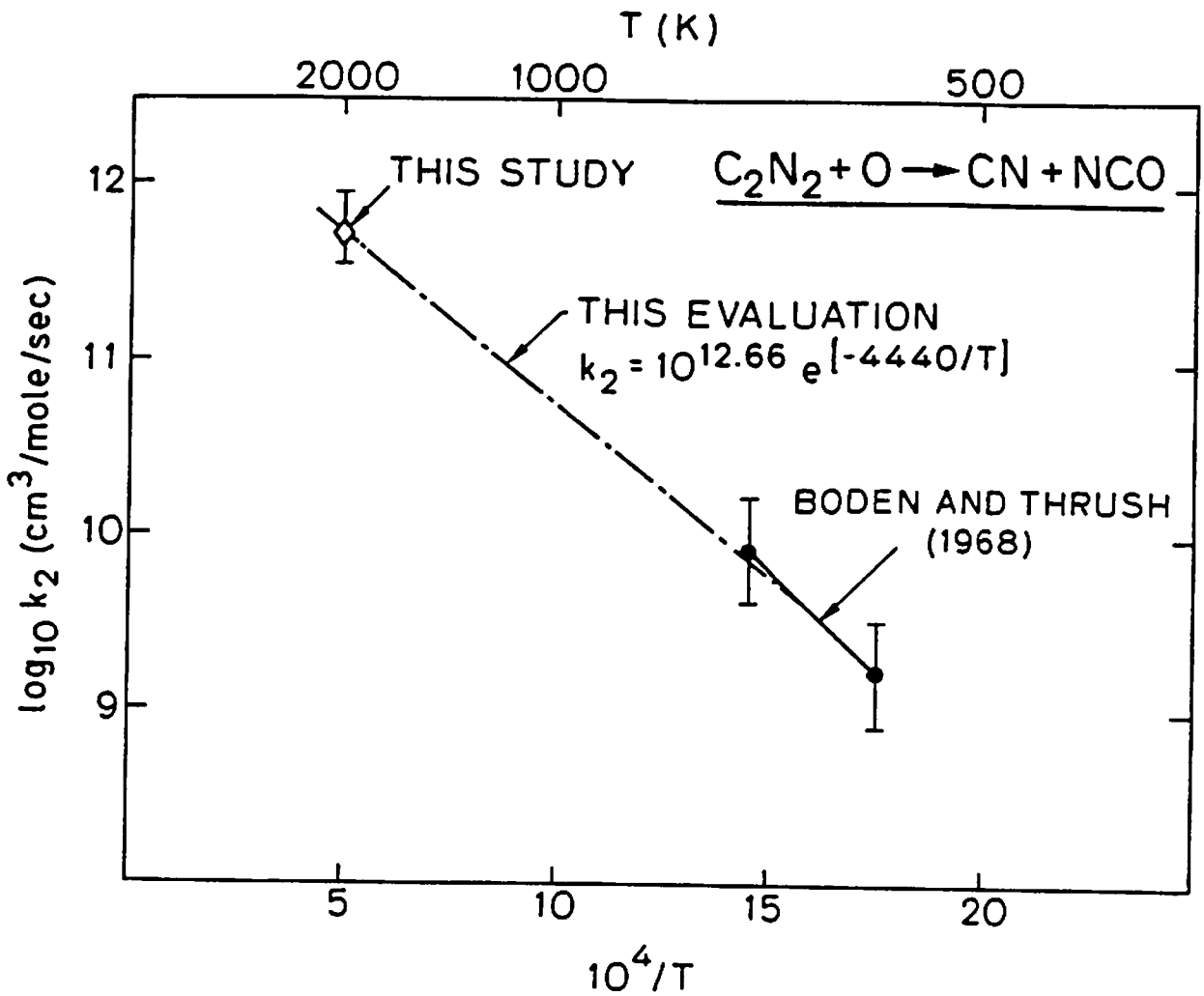

Fig. 3.7 Arrhenius plot for k_2. Note that (– · –) is an Arrhenius fit to the high- and low-temperature data. The abscissa shows reciprocal temperatures $10^4/T$ (K^{-1}).

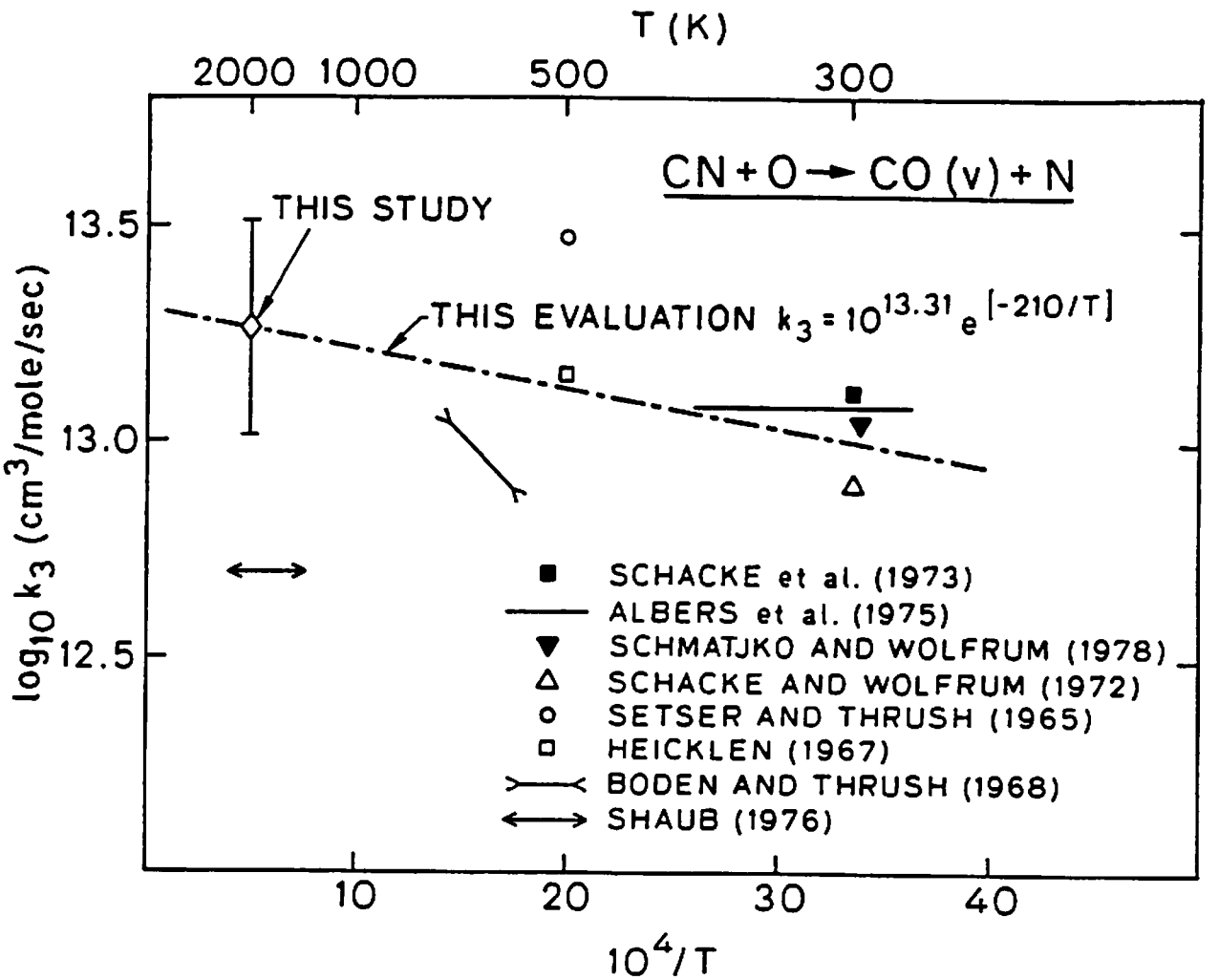

Fig. 3.8 Arrhenius plot for k_3.

In a few experiments, the CO laser diagnostic was tuned to coincidence with an NO(v=0) absorption line. Vibrational equilibrium of NO was assumed, even though there is some evidence for NO production in excited vibrational states (see Basco [43]). A NO transmission record, corrected for N_2O absorption, was calculated using the computer-generated NO profile and compared with the experimental trace. Modeling shows that the NO profile is reasonably sensitive to the ratio k_5/k_6 with larger values of k_5 producing more NO; on the contrary, larger values of k_6 lead to increased levels of N-atoms, which in turn remove NO by reaction (-15):

$$N + NO \rightarrow N_2 + O \qquad (-15)$$

Figure 3.9 shows the computer fit (solid line) using $k_2=10^{11.56}$ cm^3/mole/sec , $k_3=10^{13.08}$ cm^3/mole/sec, and $k_5/k_6=10^{3.36\pm0.27}$ for $T_2=2150°K$. The dashed line is the computer fit obtained by assuming previous literature values for k_5 and k_6 ($k_5=10^{13}$ cm^3/mole/sec [44] and $k_6=10^{13}T^{0.5}$ exp(-20630/T) [45]), and the set of rate constants which would, within reasonable bounds, predict the largest production of NO. It is clear that the literature-based value for k_5/k_6 [44,45] cannot fit the experimental NO trace and is too low. This observation is confirmed at higher temperatures in the discussion of $O_2/C_2N_2/Ar$ mixtures and in chapter 4.

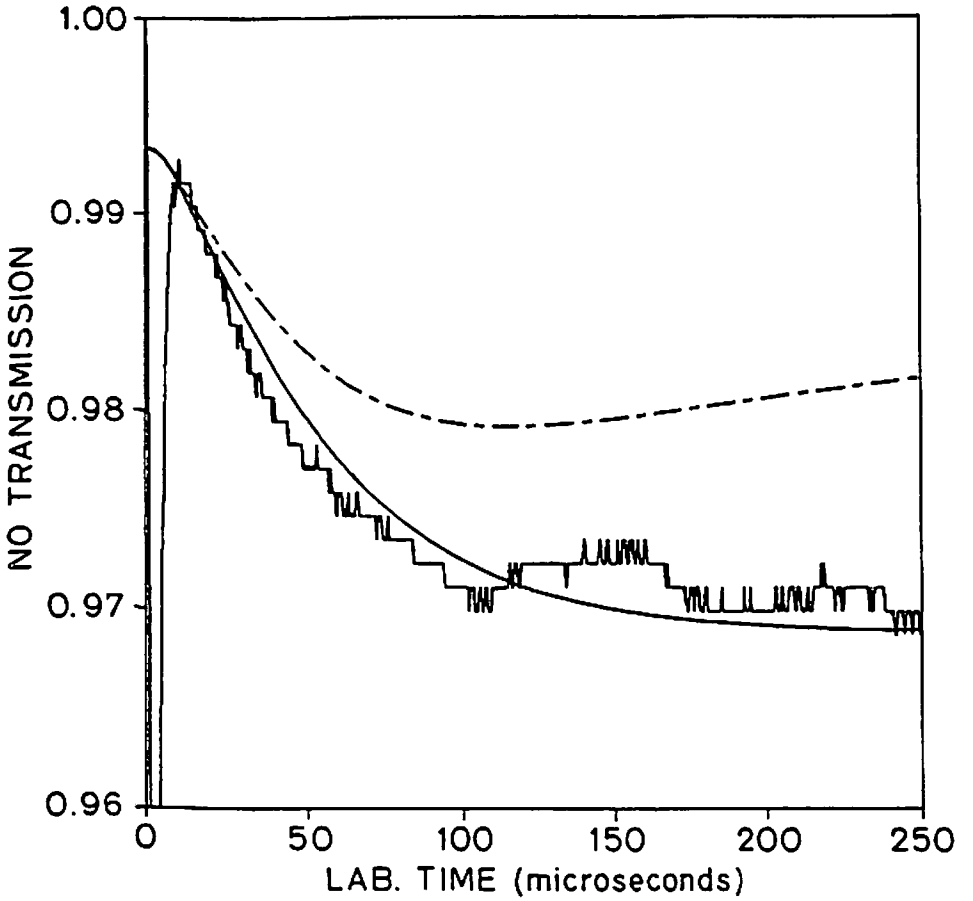

Fig. 3.9 Best fit of a typical NO transmission profile. The conditions are T_2=2150°K, p_2=0.65 atm, $N_2O:C_2N_2:Ar$=12:3:985. The solid line is a best computer fit to the trace using $k_2=10^{11.56}$, $k_3=10^{13.08}$ cm^3/mole/sec, $k_5/k_6=10^{3.36}$, and other rates shown in Table 3.2. The dotted line is a computer-generated profile assuming $k_5/k_6=10^{2.50}$ (previous literature values for k_5 [44] and k_6[45]) and the set of rate constants that would, within reasonable bounds, predict the largest production of NO. The initial absorption corresponds to the N_2O background interference.

3.3 $O_2/C_2N_2/Ar$ Mixtures-Analysis and Results

Four runs were conducted with mixtures of $O_2:C_2N_2:Ar=6:6:988$ and $0.56<p_2<0.61$ atm, $2320<T_2<2450°K$, $3.62<\rho_{21}<3.65$. Shock speeds varied between 1.52 and 1.58 mm/μsec, with attenuation of 0.9%/m or less. The temperature of the experiments was set by considerations of growing interferences from spontaneous emission at higher temperatures and by insufficient rates of CN production by reaction (7) at lower temperatures,

$$C_2N_2 + M \rightarrow CN + CN + M. \qquad (7)$$

Despite the apparent simplification of this mixture (no N_2O is present), the reaction paths prove to be more complicated. Figure 3.10 shows a sketch of the global mechanism.

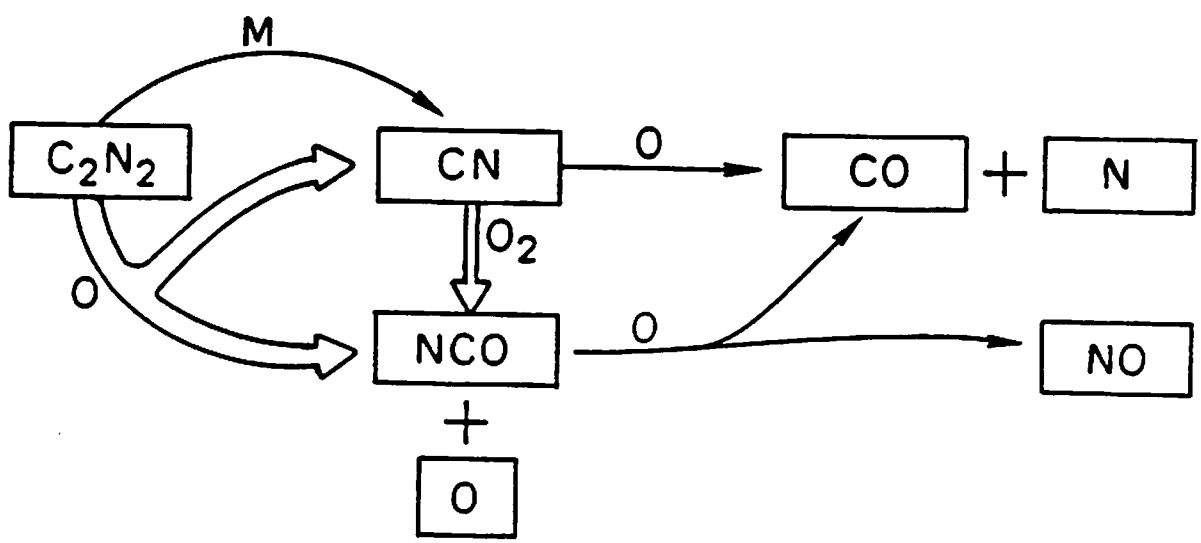

Fig. 3.10 Reaction paths for the C_2N_2/O_2/argon mixtures. Note the critical role of O-atoms in this mechanism.

As a first step, C_2N_2 decomposes slowly via reaction (7) to give CN. The latter then reacts immediately with oxygen to form O-atoms,

$$CN + O_2 \rightarrow NCO + O. \tag{4}$$

As soon as they are produced, the O-atoms provide a sink for C_2N_2 via reaction (2). As the chemistry proceeds, more O-atoms are available to attack CN (reaction 3) or NCO (reaction 5). O-atoms obviously play a critical role in this system and any reaction involving them can affect the history of all species, including CN. With an overall mechanism that allows little simplification, a computer fitting technique proves necessary.

Figure 3.11 shows a best computer fit (solid line) to an experimental trace. The dotted lines illustrate the dependence of the fit on k_4. It appears that increasing or decreasing k_4 generates a parallel fit which retains a similar overall shape.

Using the computer model, it was showed that an increase in k_5 or a decrease in k_6 (and conversely) produced equivalent variations in the predicted CN profile. The fit therefore depends on the ratio k_5/k_6. Furthermore, it was found that this ratio, unlike k_4, controls not only the peak CN value, but also the shape of the fit, especially at late times. This effect is due to the critical role of O-atoms mentioned above. If k_5 is large, reaction (5) consumes O-atoms to a greater extent, thus preventing a faster decay of CN by reaction (3). An equivalent situation arises from a small k_6. In this case, NCO levels are increased, reaction (5) becomes the preferential NCO removal path and O-atoms consumption via reaction (5) is again increased. Note that the opposite effect (acceleration of the CN decay) would be obtained through a smaller k_5 or a larger k_6.

It therefore appears possible to determine k_4 and k_5/k_6 by fitting the CN trace alone: a unique set of values for k_4 and k_5/k_6 can fit both the slope of the CN decay (influenced by k_5/k_6) and the peak CN concentration (influenced by k_5/k_6 and k_4). Figure 3.12 illustates the effect of k_5/k_6 on the slope of the CN decay.

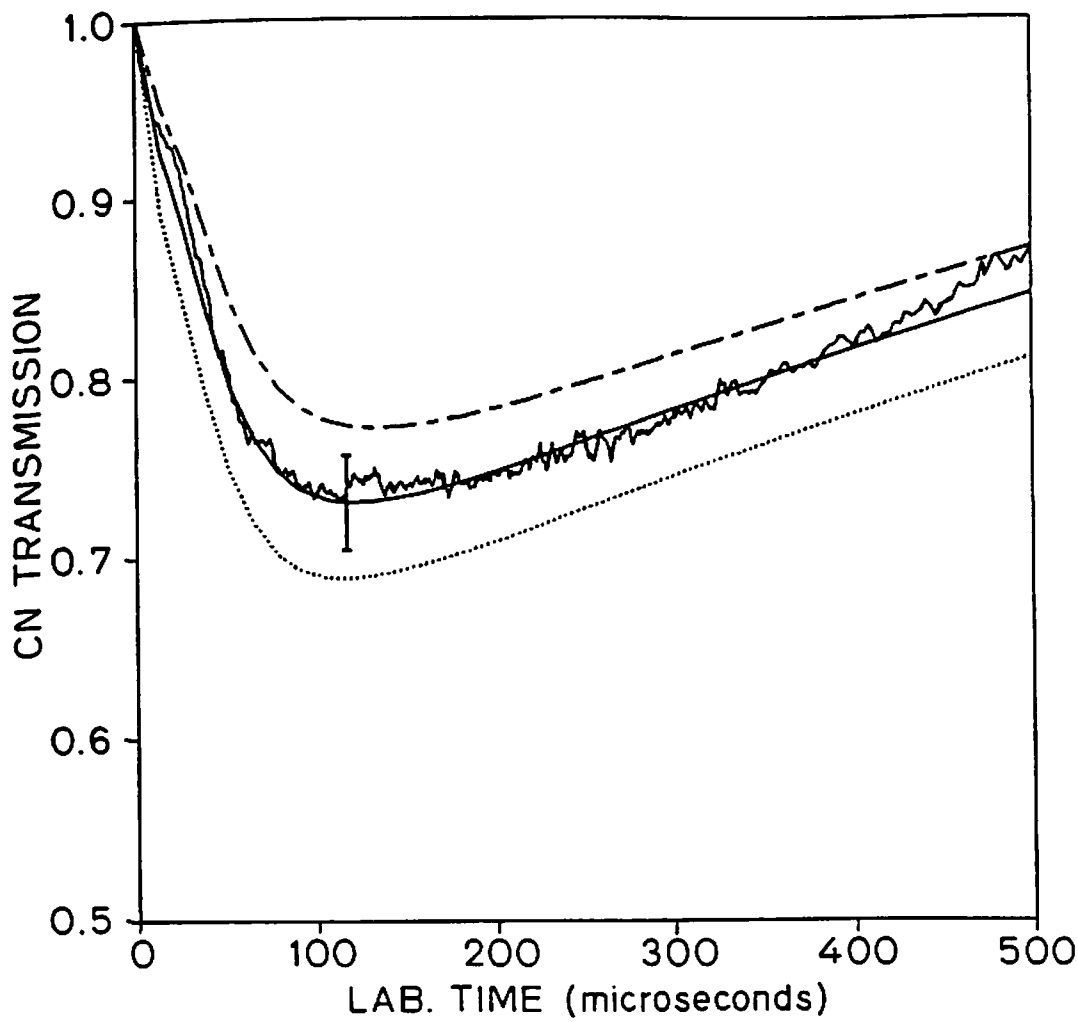

Fig. 3.11 Best fit of a typical CN transmission profile in a C_2N_2/O_2/argon experiment. The conditions are T_2=2315°K, p_2=0.61 atm, $O_2:C_2N_2:Ar$=6:6:988. The solid line is a best computer fit using $k_4=10^{12.70}$ cm^3/mole/sec, $k_5/k_6=10^{2.93}$ and other rates shown in Table 3.2. The dotted lines are computer-generated profiles using the best rates except (- · -), k_4 (+60%); (···), k_4 (-60%)

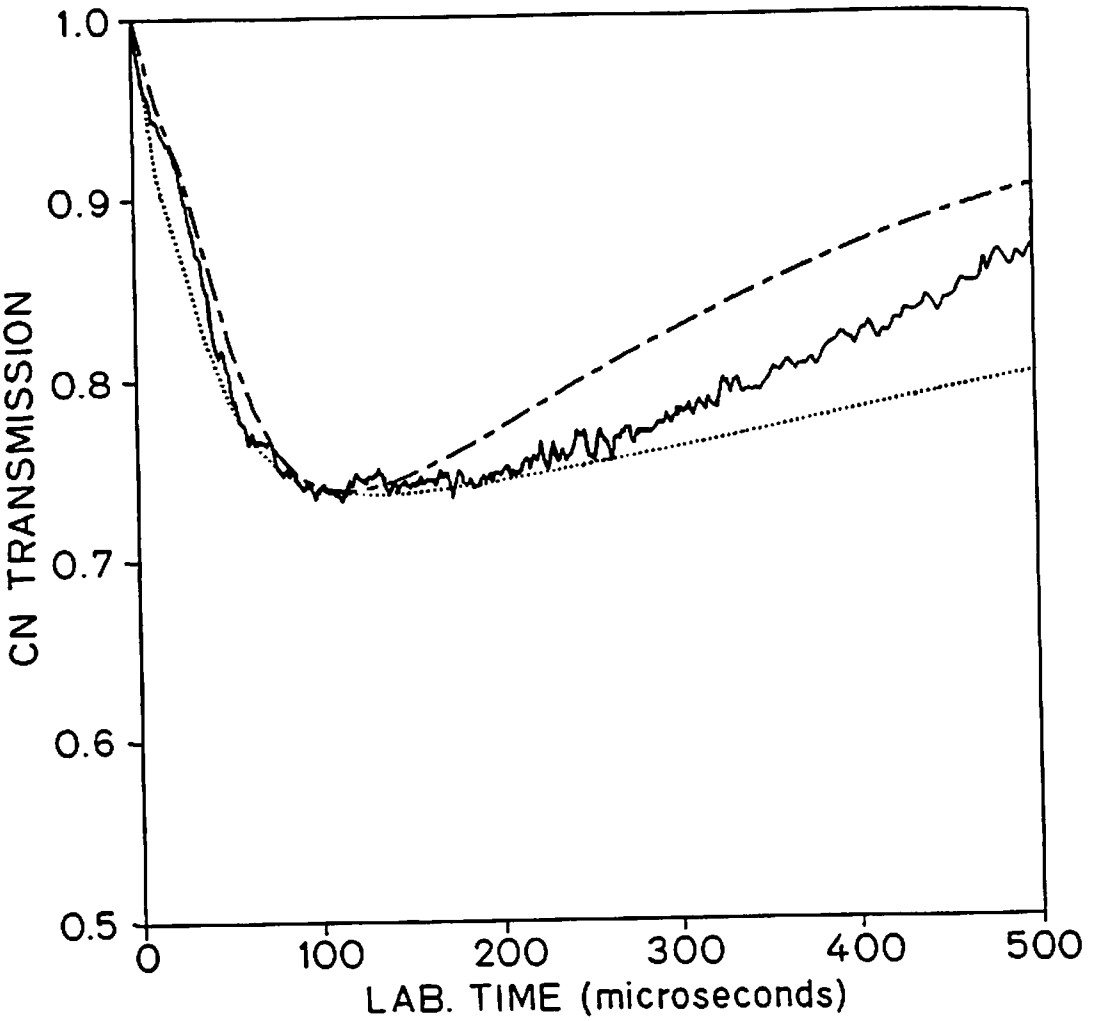

Fig. 3.12 Sensitivity of the CN fit to excursions in k_5/k_6. The conditions are identical to Fig. 3.11. The dotted lines are computer-generated profiles using the best rates, except (···), k_5/k_6 (+60%) and k_4 (-34%); (- · -), k_5/k_6 (-60%) and k_4 (+56%).

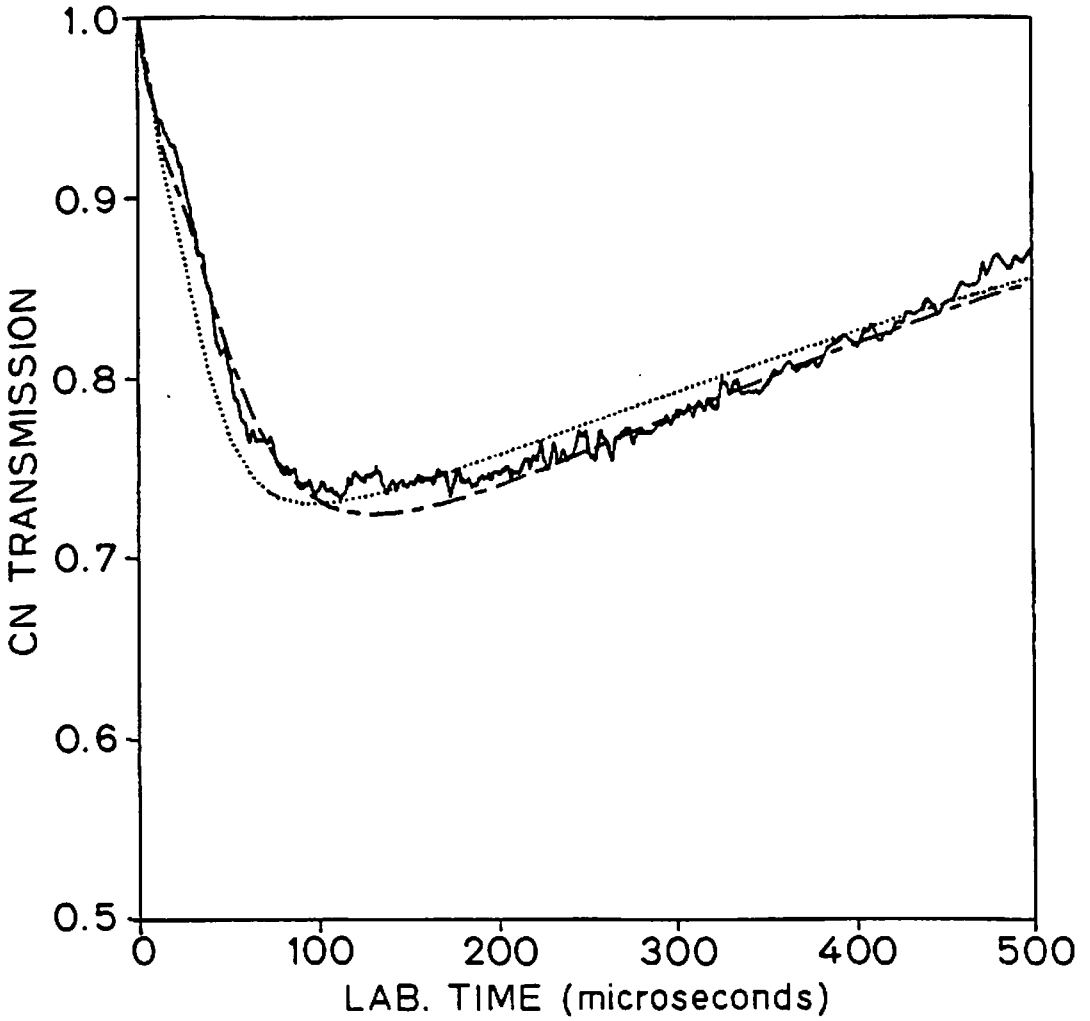

Fig. 3.13 Insensitivity of the CN fit to simultaneous excursions in k_2, k_3 and k_5/k_6. The conditions are identical to Fig. 3.11. The dotted lines are computer-generated profiles using the best rates except (•••), k_2 and k_3 (+40%); k_5/k_6 (+40%); (- • -), k_2 and k_3 (-40%); k_5/k_6 (-40%).

Table 3.4 - Uncertainty Analysis for k_4 and k_5/k_6

Reactions	Uncertainty factors	effect on:			
		k_4		k_5/k_6	
2 $C_2N_2+O \rightarrow CN+NCO$ [a]	1.79		+13%		+58%
and					
3 $CN+O \rightarrow CO+N$ [a]	0.56		+24%	-58%	
7 $C_2N_2+M \rightarrow 2CN+M$ [b]	1.67		+18%		+8%
	0.60	-11%			0%
17 $NCO+N \rightarrow N_2+CO$	10.0	-11%		-26%	
18 $NCO+N \rightarrow CN+NO$	10.0		+30%		0%
calibration	+18%		+37%		0%
uncertainty	-18%	-37%			0%
exp. scatter		-18%	+18%	-15%	+15%
total uncertainty = $[\Sigma(\text{uncert.})^2]^{1/2}$		-44%	+61%	-65%	+60%

[a] Both k_2 and k_3 were equally modified.

[b] This rate controls the early CN slope and could be adjusted accordingly.

In order to estimate the uncertainties in these determinations, Table 3.4 was constructed in a fashion similar to that used in our analysis of $N_2O/C_2N_2/Ar$ mixtures. An important feature of this table is the influence of the previous uncertainties in k_2 and k_3. If a known ratio k_2/k_3 is assumed, then most of the uncertainty in k_2 and k_3 is translated into a similar uncertainty in k_5/k_6. This effect is illustrated in Fig. 3.13. Here, k_2, k_3 and k_5/k_6 are simultaneously varied by ±40%. The result of these excursions still appears as a reasonable fit; thus, any variation in (k_2,k_3) can approximately be offset by the same variation in k_5/k_6.

The inferred values for k_4 and k_5/k_6 at temperatures near 2400°K are

$$k_4=10^{12.68(+0.27,-0.19)}\ cm^3/mole/sec$$

and

$$k_5/k_6=10^{2.69\pm0.28}.$$

This value of k_5/k_6 at 2400°K is higher than the literature estimate by at least a factor of two. A more detailed discussion of k_5/k_6 will be given in chapter 4.

Figure 3.14 is an Arrhenius plot adding the present value for k_4 to the review of Baulch, et al. [13]. Measurements of E_4, the activation energy of reaction (4), are limited. Boden and Thrush [42] conducted experiments in the range $570<T<687$°K and concluded that $E_4=0$ by comparison with the work of Basco at lower temperatures [43]. Bullock and Cooper [18] claimed a slightly negative activation energy for k_4 in the range $303<T<375$°K. On the other hand, Albers, et al. [70] inferred $E_4=1.0\pm0.3$ kcal/mole in the range $298<T<391$°K, despite their reported individual error bars suggesting $0<E_4<3$ kcal/mole. The present measurement agrees well with previous work, except for the flame study of Mulvihill & Phillips [12]. Within the scatter of the low and high temperature results, the reaction shows no significant temperature dependence. This observation is consistent with the recommendation of Baulch, et al. [13] for the activation energy $E_4=0.9\pm0.9$ kcal/mole. This low activation energy is otherwise plausible for a mildly exothermic reaction ($\Delta H_R=-4$ kcal/mole at 298°K). The value $k_4=10^{12.75(+0.20,-0.15)}$ cm^3/mole/sec is recommended over the temperature range $300<T<2400$°K.

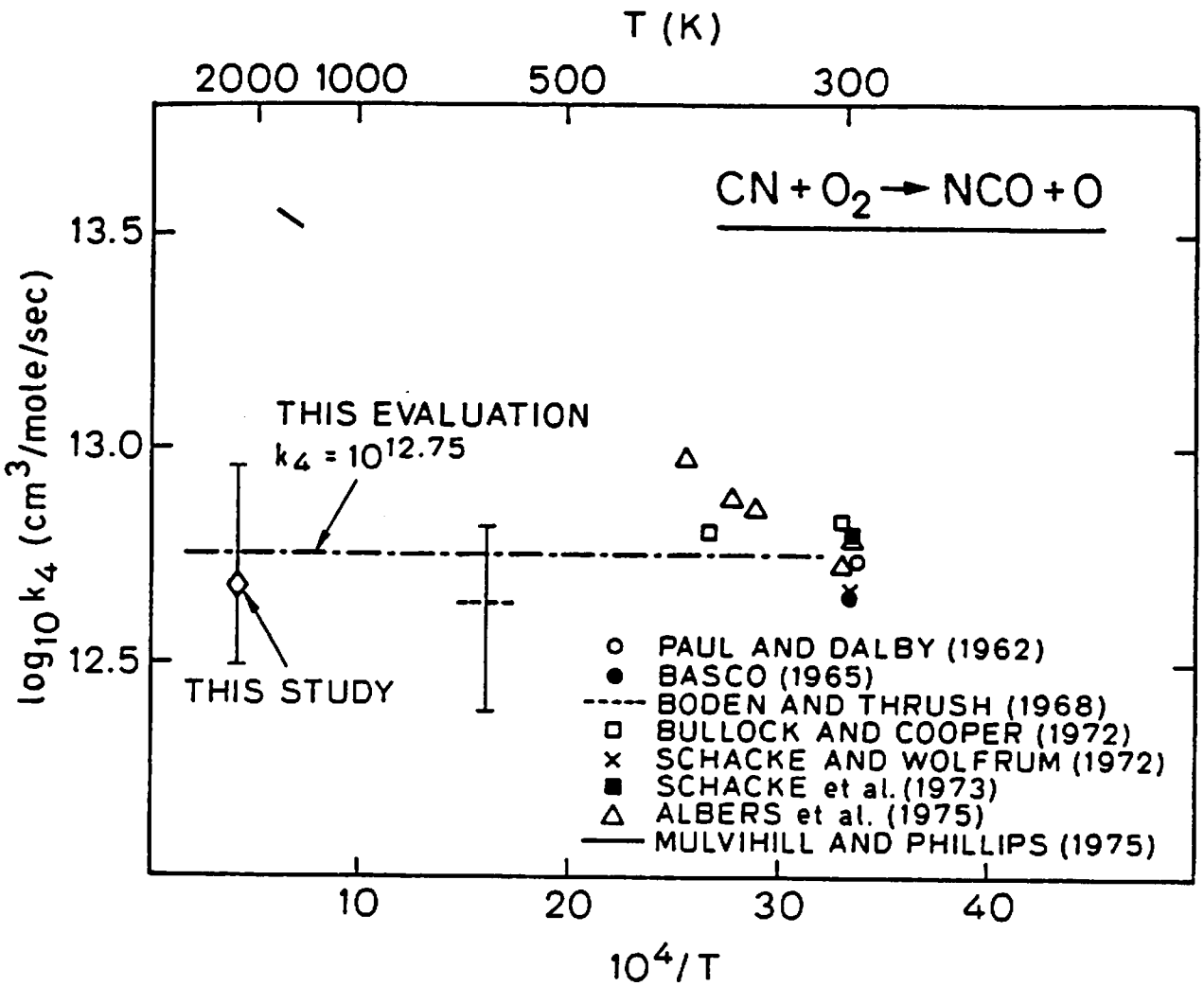

Fig. 3.14 Arrhenius plot for k_4. The abscissa shows reciprocal temperatures $10^4/T$ (K^{-1}).

3.4 Conclusions

Using mixtures of C_2N_2, N_2O and O_2 dilute in argon, the rates of reactions (2), (3) and (4) were inferred at high temperatures

$$C_2N_2 + O \rightarrow CN + NCO, \quad (2)$$

$$CN + O \rightarrow CO(v=1) + N, \quad (3)$$

$$CN + O_2 \rightarrow NCO + O, \quad (4)$$

and the ratio k_5/k_6 was measured at 2150°K and 2400°K,

$$NCO + O \rightarrow CO + NO, \quad (5)$$

$$NCO + M \rightarrow N + CO + M. \quad (6)$$

Reactions (3) and (4) are important in the fuel-nitrogen mechanism. Furthermore, our recommendation for k_2, k_3 and k_4 can be used to predict levels of NCO produced in $C_2N_2/N_2O/O_2$/argon mixtures. This information will be used in the next chapter to characterize the NCO laser absorption diagnostic at 305 and 440 nm, and to perform additional measurements of k_5 and k_6 at high temperatures.

Chapter 4

NCO Generation and Quantitative Spectroscopy

The radical NCO is of interest in combustion; as mentioned in chapter 1, it serves as a critical intermediate in the formation of NO during combustion of nitrogen-containing fuels. The spectral characteristics of NCO have been studied extensively, but few attempts have been made to perform quantitative measurements of NCO in a combustion environment.

In this study, two novel laser absorption diagnostics of NCO were demonstrated in the shock tube. Mixtures of C_2N_2, N_2O and O_2 dilute in argon and mixtures of HCN, N_2O and O_2 dilute in argon were shock heated to generate reproducible levels of NCO under specified conditions of pressure (0.6 atm) and temperature (1450°K). Narrow-linewidth absorption spectra around 440.5 and 304.7 nm were mapped out by conducting a series of nearly identical experiments, each at a different laser wavelength. Using the relative NCO time-histories from the C_2N_2 mixtures, the rate of reaction (5)

$$NCO + O \rightarrow CO + NO, \tag{5}$$

was inferred, thus providing a measurement of NCO concentrations. Absolute peak absorption coefficients near 440.5 and 304.7 nm were subsequently inferred and compared with theoretical models to extract band oscillator strengths and Franck-Condon factors at both wavelengths.

In this chapter, the experimental facility and optical techniques will first be described. The method for generating NCO in the shock tube will then be discussed, and the spectroscopic models and results for the two techniques will be presented. Finally, a determination of the rate of NCO decomposition (reaction 6) will be reported to illustrate the use of the diagnostic at 440 nm,

$$NCO + M \rightarrow N + CO + M. \tag{6}$$

4.1 Experimental Considerations

The experiments were conducted behind incident shock waves in our 15.24 cm internal diameter pressure-driven shock tube. Typical leak plus outgassing rates were $3\text{-}5\times10^{-5}$ torr/min.

4.1.1 Experiments at 305 nm

The absorption from the R_1 band head of the $[B^2\Pi_1(10^10)\leftarrow X^2\Pi_1(00^10)]$ band of NCO at 304.68 nm (vac) was observed using the optical set-up shown in Fig. 4.1. The laser system consisted of an Ar^+ laser (Spectra-Physics model 164) and a ring dye laser (Spectra-Physics model 380C), frequency-doubled using an intracavity crystal (AD^*A) placed in a temperature-controlled oven [46]. The available power from the Ar^+ laser (4 W all lines) provided a typical UV dye laser output of 5 mW. Single-mode operation of the visible dye laser beam was verified using a confocal interferometer (Spectra-Physics model 470, free spectral range 2 GHz). A wavemeter (Burleigh model WA-10) was used to set the visible laser wavelength. The UV output was single-passed through the shock tube test section using UV-coated fused silica windows (Fig. 4.1). An iris was used to block extraneous spontaneous emission from the test gas, without reducing the incident power on detector D_2. A small fraction of the beam was split off before and after passing through the shock tube to enable measurement of the fractional transmission. Prior to each experiment, the laser light was chopped and the reference signal (i_0) and transmitted signal (i) were balanced (i.e., equalized) by adjusting the angle of the beam splitters to vary the surface reflectance, hence the reflected intensity. The detectors (EG&G UV 100B photodiodes) were mounted in an amplifier/filter package with a 240kHz (-3dB) cut-off frequency and shielded from the room lights by Corning broadband-pass filters (80% transmission from 300 to 400 nm). The difference signal (i_0-i) and the reference signal (i_0) were recorded on two separate channels of a digital storage oscilloscope (Nicolet Explorer III, dc-coupled through a 100 kHz upper frequency cut-off filter). The data were subsequently transferred to the computer for analysis.

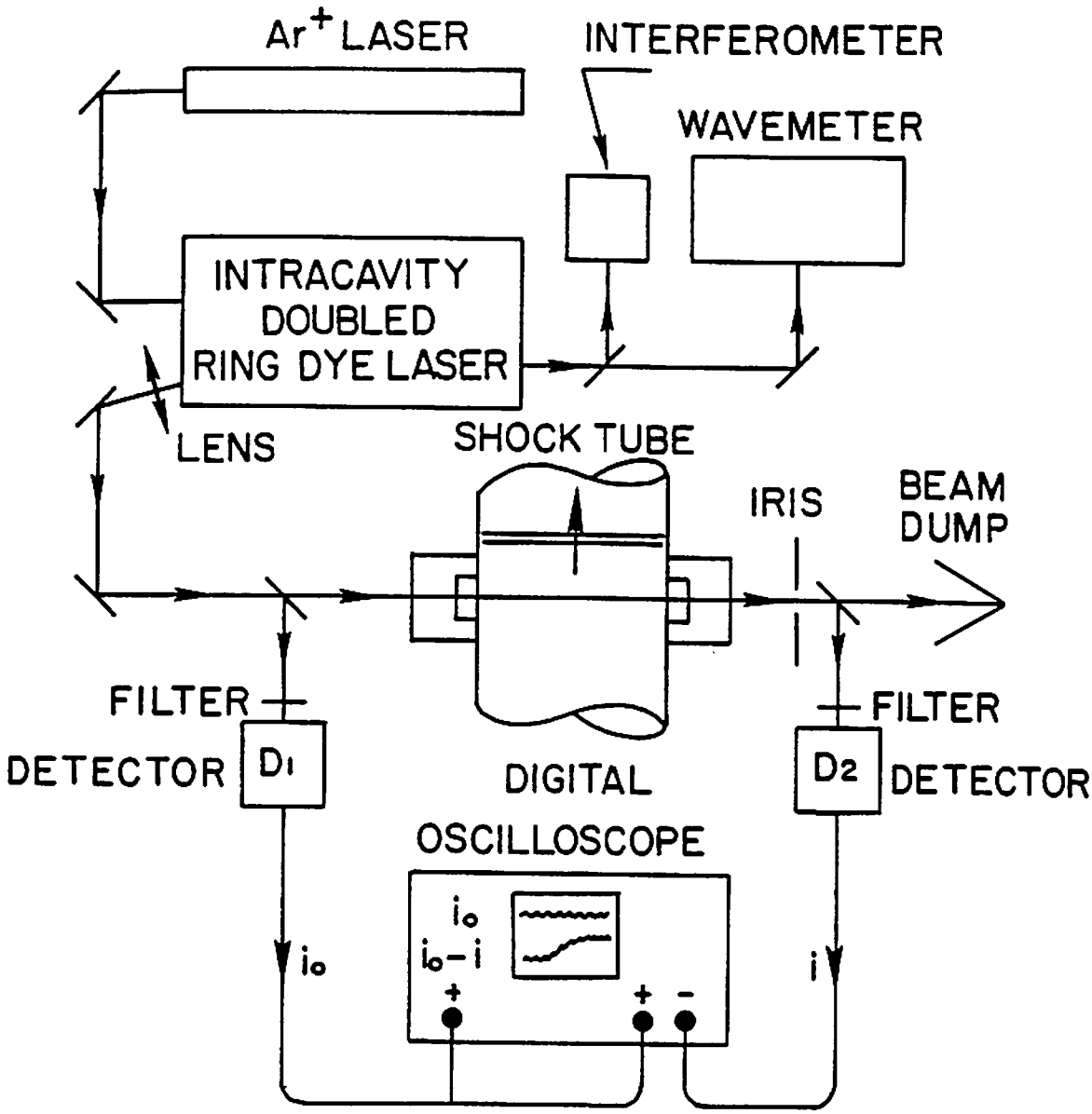

Fig. 4.1 A schematic of the NCO laser absorption system at 305 nm.

Fourteen runs were conducted with the following C_2N_2 mixtures and conditions: $N_2O:O_2:C_2N_2:Ar=4:1:8:987$, $T_2=1470\pm15°K$, $p_2=0.63$ atm and $\rho_{21}=3.36$ (ρ_{21} is the density ratio across the shock and also the ratio of particle time to laboratory time.) Shock speeds varied between 1.16 and 1.18 mm/μsec, with attenuation of 1.3%/m or less. Gases were taken directly from commercial cylinders, with C_2N_2 (1.03%) dilute in argon (Table 2.1). For these experiments, the laser was set at nine different wavelengths in the range $304.638<\lambda<304.752$ nm (vac).

4.1.2 Experiments at 440 nm

The absorption from the $P_2+{}^PQ_{12}$ band head of the $[A^2\Sigma^+(00^00)\leftarrow X^2\Pi_i(00^10)]$ band of NCO at 440.479 nm (vac.) was used to monitor NCO. The laser system consisted of a UV-enhanced Ar^+ laser (Spectra-Physics model 171-18) and a standard Spectra-Physics 380A ring dye laser. The available Ar^+ UV power (1.9 W all lines) was sufficient to excite the stilbene S3 dye above threshold, providing a typical dye laser output power of 60 mW. The nominal laser wavelength was varied using a standard 3-plate birefringent filter; fine tuning was achieved with an uncoated 5 mm-thick fused silica etalon in a temperature-controlled oven. Single mode output of the laser was verified using a confocal interferometer (Spectra-Physics model 470, free spectral range 2 GHz). An amplitude stabilizer (Coherent Associates model 307) was employed to improve the signal quality. The component of the laser power rejected by the amplitude stabilizer was sufficient to drive the wavemeter (Burleigh model WA-10) used for setting the laser wavelength. It was necessary to correct the displayed wavelength for the change in the index of refraction of air between the He-Ne reference wavelength at 632.991 nm and the blue wavelength at 440.479 nm (correction= actual - displayed wavelength= +0.002 nm, see Appendix 4).

The laser light was coupled into a 200μm fused silica optical fiber for transport to the shock tube facility (length, 65 m). The output from the optical fiber was double-passed through the shock tube test section using UV-coated fused silica windows (see Fig. 4.2). The incident and return beams were monitored on two separate detectors D_1 and D_2 (EG&G UV

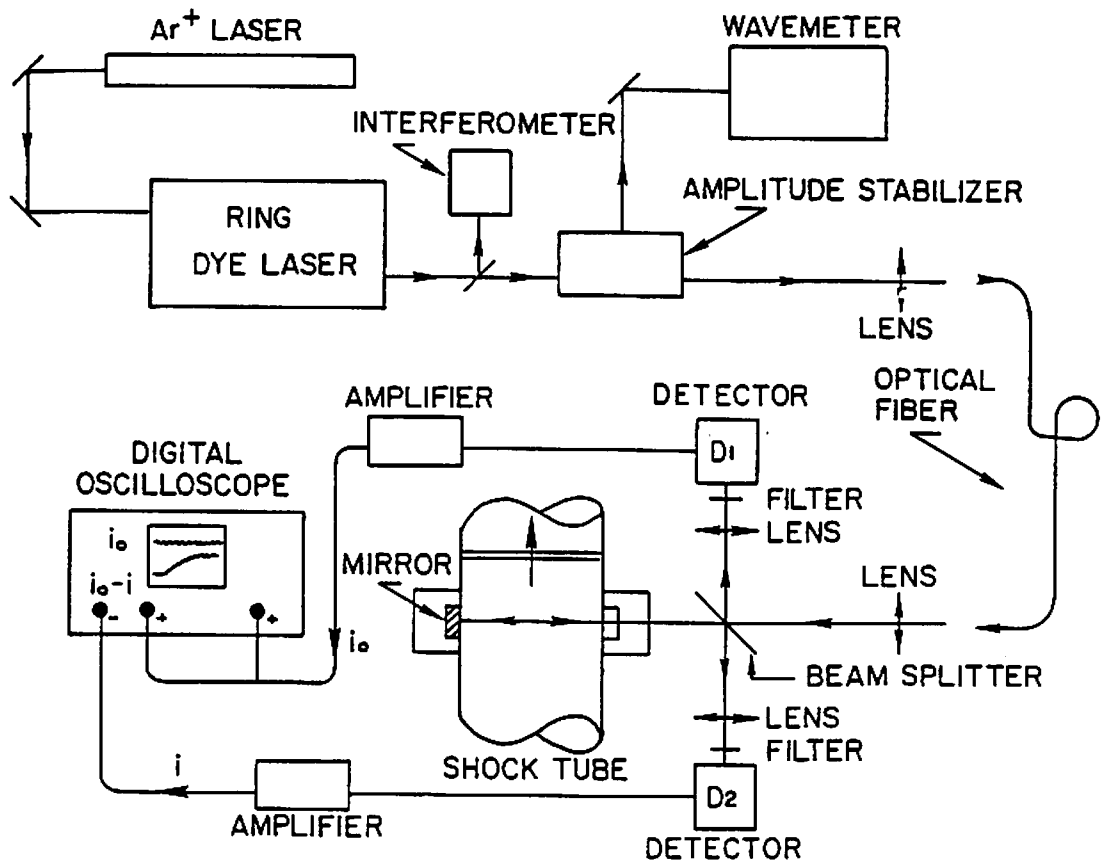

Fig. 4.2 A schematic of the NCO laser absorption system at 440 nm.

100B silicon photodiodes mounted in an amplifier/filter package with a 240kHz (-3dB) cutoff frequency). Neutral density filters (transmission, 10^{-1}) were used to reduce the incident power of 1 mW below the saturation limit of the detectors while proportionally reducing the spontaneous emission from the test gas. Narrow bandpass filters (FWHM, 40 nm; centered at 450 nm) were used to discriminate against other sources (primarily room lights). Detectors and filters were tilted slightly to prevent extraneous reflections from striking the photodiodes. The shock tube window was also tilted to prevent multiple reflections inside the tube. The signal from each detector was passed through a differential amplifier (Tektronix model AM 502, dc-1MHz bandwidth). Prior to each experiment, the laser light was chopped to balance (i.e., equalize) the reference signal (i_0) and the return signal (i) using small dc offset and gain adjustments on one of the differential amplifiers. The difference (i_0-i) and the reference signal (i_0) were recorded on two separate channels of the digital oscilloscopes, thereby providing a direct measurement of the fractional absorption through the system. The transport via optical fiber was made necessary by the absence of an adequate power outlet for the Ar^+ laser in the shock tube laboratory. To prevent excessive laser power attenuations, a relatively large fiber optic (200μm) was used, but the fiber diameter prevented good spatial confinement of the collimated output beam. Consequently, no iris could be used to further limit the interference of spontaneous emission from the test gas without reducing the laser power on detector D_2. This restriction placed an upper bound on temperature for experiments free of emission interference.

Nine runs were conducted with the following HCN mixtures and conditions: N_2O:O_2:HCN:Ar≈8:1:8:983, T_2=1430±20°K, p_2≈0.60 atm, ρ_{21}≈3.32, and wavelengths in the range: 440.474<λ<440.482 nm (vac). Shock speeds varied between 1.14 and 1.17 mm/μsec, with a typical attenuation of 2.5%/m. Three additional runs were conducted with C_2N_2 mixtures at 440.479 nm, the peak absorption wavelength, and N_2O:O_2:C_2N_2:Ar≈4:1:4:991, T_2=1450±10°K, p_2≈0.60 atm, ρ_{21}≈3.31. Shock speeds varied between 1.15 and 1.16 mm/μsec, with a typical attenuation of 1.2%/m. Gases were

taken directly from commercial cylinders, with C_2N_2 (1.01%) dilute in argon (Table 2.1).

The temperature of the experiments was set by considerations of growing interference on NCO removal by reaction (6) at higher temperatures,

$$NCO + M \rightarrow N + CO + M, \tag{6}$$

and increasing uncertainty in the rate of reaction (1) at lower temperatures. In addition, a few tests were conducted with the laser blocked to monitor possible spontaneous emission interferences from the test gas. These emission levels were found to be insignificant.

4.2 Generation and Oxidation of NCO in Cyanogen Mixtures

The fractional transmission of both laser systems is related to the level of NCO through the Lambert-Beer law

$$i/i_0 = \exp[\ -\beta(\lambda)\ p_{NCO}\ L\ ]\ , \tag{4.1}$$

where i/i_0 is the fractional transmission, $\beta(\lambda)$ is the absorption coefficient at wavelength λ, p_{NCO} is the partial pressure of NCO and L is the optical path length (15.24 cm for the system at 305 nm and 30.5 cm for the system at 440 nm). Under our experimental conditions, both HCN and C_2N_2 mixtures provided reproducible NCO plateau levels. By running nearly identical experiments and recording the plateau absorption levels, we were able to measure relative absorption coefficients of NCO as a function of wavelength.

In addition, information from the relative NCO time-histories in the C_2N_2 mixtures was used to measure the rate of reaction (5)

$$NCO + O \rightarrow CO + NO, \tag{5}$$

thereby putting the absorption coefficients on an absolute basis.

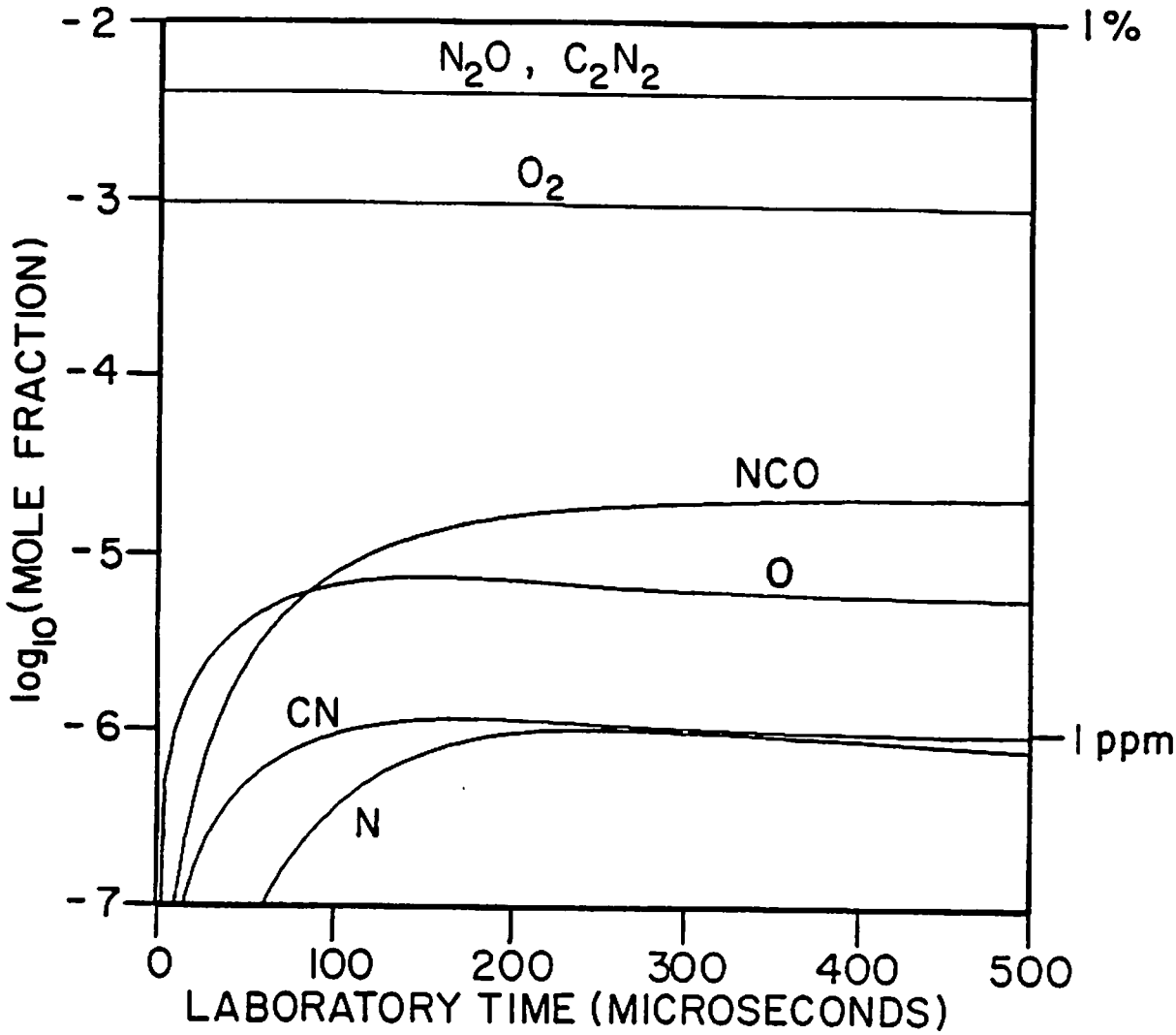

Fig. 4.3 Computer-generated profiles of N_2O, C_2N_2, O_2, NCO, O, CN and N mole fractions using the rates shown in Table 3.2. The conditions are T_2=1440°K, p_2=0.60 atm, $N_2O:O_2:C_2N_2:Ar$= 4:1:4:991 and ρ_{21}=3.31.

4.2.1 Reaction Mechanism

A complete reaction mechanism was utilized in the data reduction (see Table 3.2), but the following simplified description is helpful in understanding how k_5 and β were inferred from NCO absorption profiles. At early times, N_2O rapidly decomposes to provide O-atoms; C_2N_2 then reacts to form NCO, which in turn is removed by O-atoms,

$$N_2O + M \rightarrow N_2 + O + M, \tag{1}$$

$$C_2N_2 + O \rightarrow CN + NCO, \tag{2}$$

$$NCO + O \rightarrow CO + NO. \tag{5}$$

The presence of molecular oxygen converts the CN into additional NCO and replenishes the O-atom pool via reaction (6),

$$CN + O_2 \rightarrow NCO + O. \tag{4}$$

Assuming a steady-state of [CN] between reaction (2) and (4), the rate of change of NCO concentration is given by

$$\frac{d[NCO]}{dt} = 2\ k_2[C_2N_2][O] - k_5[NCO][O]\ . \tag{4.2}$$

Since O and C_2N_2 are nearly constant throughout the process (see Fig. 4.3), the NCO profile eventually reaches a plateau ($d[NCO]/dt=0$) where

$$\frac{[NCO]^{plateau}}{[C_2N_2]} \simeq 2\ \frac{k_2}{k_5}\ . \tag{4.3}$$

It follows that the relative NCO profile (using the plateau as a reference) depends primarily on the rate of reaction (5), since, for this simplified model,

$$\frac{d[NCO]/[NCO]^{plateau}}{dt} \simeq k_5[O]\ \left(1 - [NCO]/[NCO]^{plateau}\right)\ . \tag{4.4}$$

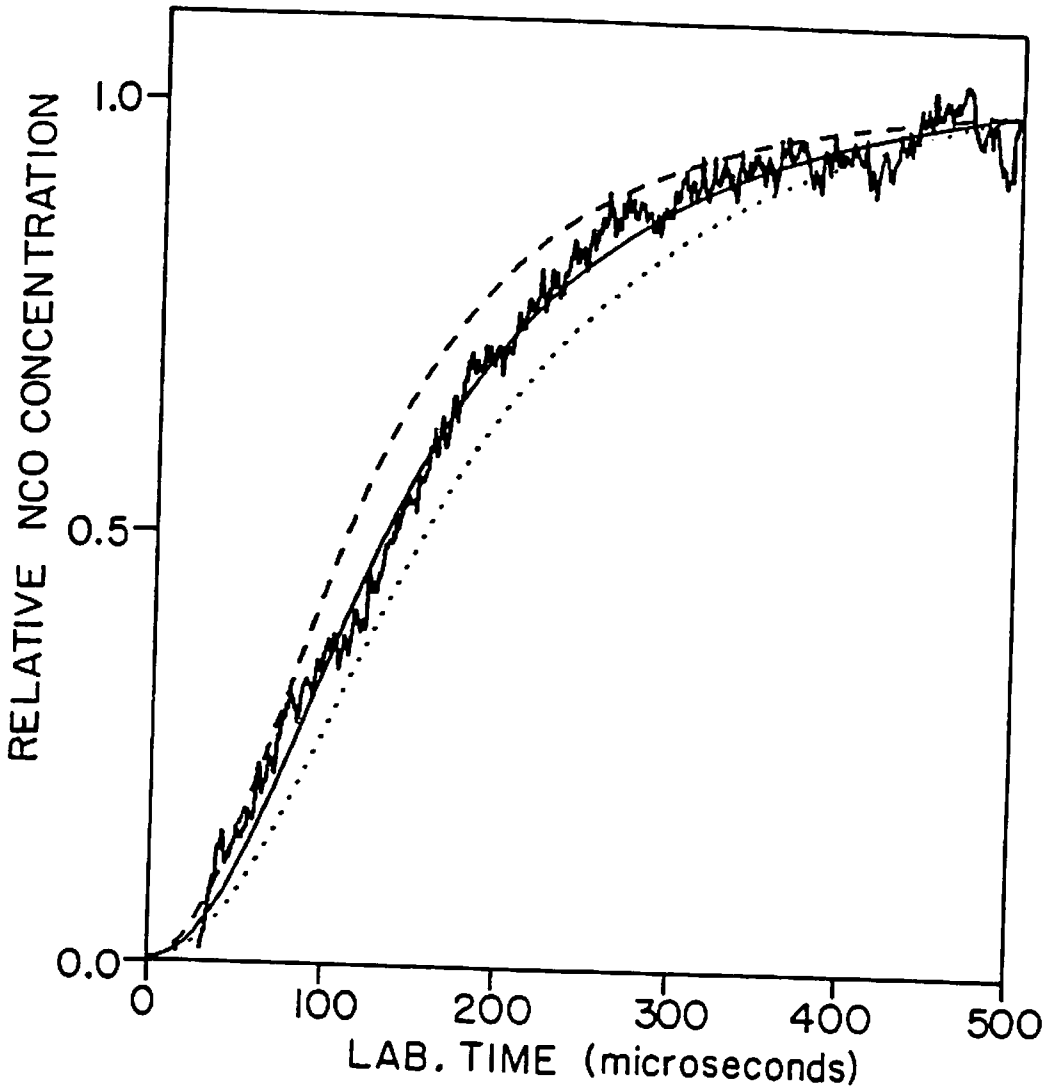

Fig. 4.4 Best fit of a typical NCO profile in a $C_2N_2/O_2/N_2O$/argon experiment using the absorption diagnostic at 440 nm. The conditions are T_2=1440°K, p_2=0.60 atm and $N_2O:O_2:C_2N_2:Ar$= 4:1:4:991. The absorption at 500μsec is 4.6%. The solid line is a best computer fit using $k_5=10^{13.75}$ cm^3/mole/sec and other rates shown in Table 3.2. The dotted lines are computer-generated profiles using the best rates except (- -), k_5 × 1.50; (•••), k_5 × 0.67.

The NCO plateau concentration thus depends primarily on the ratio k_2/k_5 and the relative time behavior depends on k_5. A record of NCO is therefore sufficient to infer k_5 and, using the recommended value of k_2, the plateau value for the NCO concentration and the absorption coefficient β. This approach for the establishment of a known level of NCO forms the basis of the present study of NCO spectroscopy.

Vibrational equilibrium of NCO was assumed, even though there is some evidence for NCO production in excited vibrational states from reaction (4) at lower temperatures [47].

4.2.2 Results and Discussion

A numerical routine incorporating the mechanism in Table 3.2 was used for the kinetics calculations. Values for k_5 were inferred from best fits to the measured relative NCO concentration profiles. Figure 4.4 shows such a best fit (solid line) to the relative NCO trace and the influence of varying k_5 by factors of 0.67 and 1.50 (dashed lines). The modified curves clearly fail to fit the data. The range of possible values for an acceptable fit is conservatively [×0.74, ×1.35] around the reported rate. Additional uncertainties in k_5 may result from uncertain knowledge of other rates of reactions present in the mechanism. In order to estimate these uncertainties, individual rates (Table 4.1) were adjusted by reasonable factors (based on current literature or our judgment); k_5 was subsequently modified to ensure the return to an optimum fit. The resulting uncertainty in k_5 were approximately [×0.60, ×1.42]. The two uncorrelated uncertainties mentioned above may be combined to give a global uncertainty of $[\Sigma(\text{uncertainty})^2]^{1/2}$ = [×0.55, ×1.60]. On the basis of this analysis, at temperatures near 1450°K,

$$k_5=10^{13.75(-0.26,+0.20)}\ \text{cm}^3/\text{mole/sec.}$$

There are no previous data available for comparison.

From the computer-predicted NCO plateau and the corresponding experimental absorption, a value for the absorption coefficient can be inferred at the peak wavelength.

Table 4.1 - Uncertainty Analysis for k_5

Reactions	Uncertainty factors	effect on k_5	
1 $N_2O+M \rightarrow N_2+O+M$	1.2	-16%	
	0.6		+21%
2 $C_2N_2+O \rightarrow CN+NCO$	1.85		+14%
	0.54	-5%	
4 $CN+O_2 \rightarrow NCO+O$	1.60	-16%	
	0.63		+18%
6 $NCO+M \rightarrow N+CO+M$	5.0	-42%	
	0.2		+12%
17 $NCO+N \rightarrow N_2+CO$	10.	-11%	
	0.1		+5%
Uncertainty in	2.0		+5%
$K_f°(CN)$	0.5	-5%	
Uncertainty in the fit		-30%	+30%
Total uncertainty=$[\Sigma(\text{uncert.})^2]^{1/2}$		-58%	+45%

4.3 NCO Absorption at 440 nm - Analysis and Results

4.3.1 Spectroscopic Model

Under typical experimental conditions, the $P_2+{}^PQ_{12}$ band head of the $[A^2\Sigma^+(00^00)\leftarrow X^2\Pi_i(00^10)]$ band of NCO at 440.48 nm is the strongest absorption feature of this electronic system and, apart from a weak ${}^OP_{12}$ branch, it does not overlap with neighboring branches or other vibrational bands [48]. These features are important in establishing a sensitive and quantitative diagnostic for NCO.

A computer program was written to predict the absorption spectrum of the $(00^00)\leftarrow(00^10)$ band under specified conditions. Spectroscopic constants were taken from Dixon [48]. The position, strength and shape of each line were computed to generate a relative absorption coefficient profile $\beta(\lambda)/f_{00}$ as a function of wavelength

$$\frac{\beta(\lambda)}{f_{00}} = \left(\frac{\pi e^2}{m_e c^2}\right) \sum_{\text{lines}} \frac{(2J''+1)\exp[-\frac{hc}{kT}F(J'')]}{Q_{total}} \times$$

$$\frac{N}{RT}\frac{S_{J'J''}}{(2J''+1)}\phi(\lambda-\lambda_0) \quad (\text{cm}^{-1}\text{atm}^{-1}), \tag{4.5}$$

where $F(J'')$ is the rotation energy of the lower state (cm^{-1}); R is the universal gas constant (atm cm^3/mole/°K); N is Avogadro's number; f_{00} is the oscillator strength of the $(00^00)\leftarrow(00^10)$ band; Q_{total} is the total partition function (see below); $S_{J'J''}$ is the rotational line strength; $\phi(\lambda-\lambda_0)$ is the line shape factor (cm) computed using a Voigt profile. (A uniform value of the Voigt parameter is assumed for all lines in the band.) The quantity $\pi e^2/m_e c^2$ is equal to 8.826 10^{-13} cm. Figure 4.5 shows a computed spectrum of NCO around 440 nm for the conditions T= 1500°K, a=0.1 (Voigt parameter).

To calculate rotational term energies and line positions, we adopted for simplicity the Hill and Van Vleck formulae which Dixon used to fit rotational constants in the $A^2\Sigma^+$ and $X^2\Pi_i$ states of NCO [48]. For the $X^2\Pi_i$ state, a more complete description that accounts for rovibronic

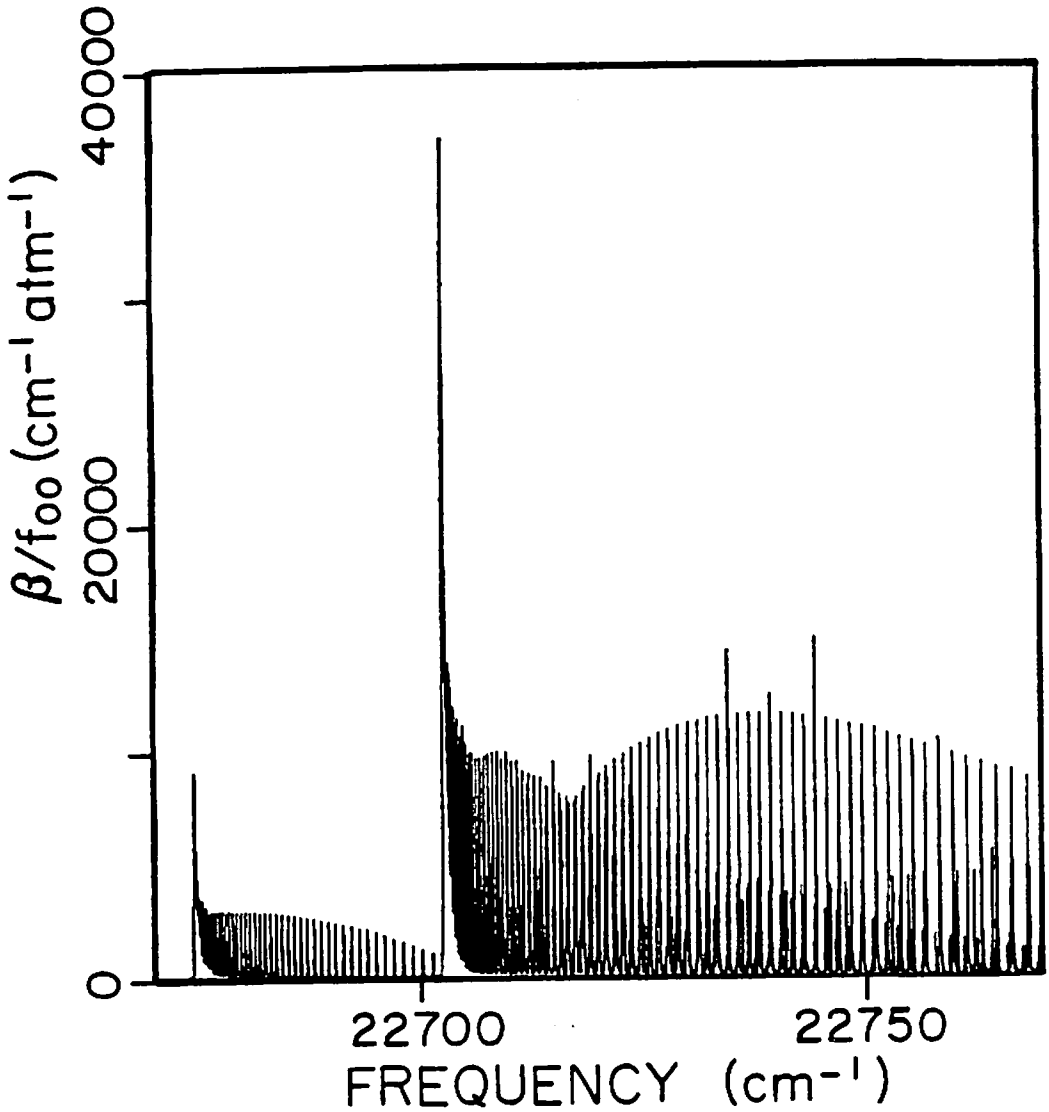

Fig. 4.5 Theoretical absorption spectrum of NCO around 440 nm, computed for T=1500°K using an average Voigt parameter a=0.1. The abscissa shows frequencies in vacuo. The ordinate shows the relative absorption coefficient β/f_{00} (cm^{-1} atm^{-1}), where f_{00} is the oscillator strength for the $[A^2\Sigma^+(00^00) \leftarrow X^2\Pi_i(00^10)]$ band. Note the $^0P_{12}$ band head at 22676 cm^{-1} and the $P_2+^PQ_{12}$ band head at 22703 cm^{-1}.

interactions was later derived by Hougen (see below) [49], but the simpler Hill and Van Vleck formulae (eq. 4.6) provide an excellent description of the rotational structure of low-lying vibrational states with no Renner-Teller interaction. Thus, for the $X^2\Pi_i$ state

$$F_\beta''(J) = B_v''\left((J+1/2)^2-K^2\right)\pm\left(B_v''(J+1/2)^2+1/4\ A_v''(A_v''-4B_v'')\Lambda^2\right)^{1/2} \\ -D_v''\left((J-1/2)(J+1/2)^2(J+3/2)+1\right) , \tag{4.6}$$

where, in this this case, $\Lambda=1$ (Π-state) and $K=|\Lambda\pm\ell|=1$. The + sign gives the level $F_2(J)$ ($\beta=2$, $J=N-1/2$) and the - sign $F_1(J)$ ($\beta=1$, $J=N+1/2$), where N is the quantum number of the total angular momentum apart from spin. Note that eq. (4.6) holds for the present inverted doublet ($^2\Pi_i$, $A<0$), and that F_1 and F_2 form $^2\Pi_{3/2}$ and $^2\Pi_{1/2}$, respectively [50]. A small K-doubling of the lower $X^2\Pi_{1/2}$ state ($\beta=2$) was also considered to calculate rotational term energies. Using the selection rule for rotational symmetry ($+ \leftrightarrow -$), it can be shown that R_2, $^PQ_{12}$ and P_2 branches originate from levels of energy $F_2''(J)+0.5p(J+1/2)$, as $^QR_{12}$, Q_2 and $^OP_{12}$ branches originate from levels of energy $F_2''(J)-0.5p(J+1/2)$.

For the $^2\Sigma^+$ upper electronic state,

$$F_\alpha'(N) = B_v'\left(N(N+1)-\ell^2\right)-D_v'\left(N(N+1)-\ell^2\right)^2 , \tag{4.7}$$

where, in this case, $\ell=0$ (Σ level, no excited ν_2 bending). N is again the quantum number of the total angular momentum apart from spin and $J=N+1/2$ for $\alpha=1$ and $J=N-1/2$ for $\alpha=2$. Spin splitting was neglected in $F'_\alpha(N)$, which Dixon did not observe for the $A^2\Sigma^+(00^00)$ level [48]. The line positions for the $A^2\Sigma^+(00^00)\leftarrow X^2\Pi_i(00^10)$ band were calculated using

$$\nu=\nu_{00}+F_\alpha(J')-F_\beta(J''), \tag{4.8}$$

where ν_{00} is the measured band origin [48]. A summary of spectroscopic constants is given in Table 4.2 [48].

Table 4.2 - Summary of NCO Spectroscopic Constants

Vibronic State	$B^2\Pi_i(10^10)$	$A^2\Sigma^+(00^00)$	$X^2\Pi_i(00^10)$
B_v	0.3765	0.40211	0.38940
D_v	$0.15.10^{-6}$	$0.177.10^{-6}$	$0.149.10^{-6}$
A_v	-30.8	-	-95.59
p	-	-	0.002
	$\nu_{10}[B\leftarrow X]=32781.13$		
		$\nu_{00}[A\leftarrow X]=22753.98$	

All quantities in cm^{-1}.

Since the NCO molecule maintains a linear configuration throughout its transition (the bending vibration ν_2 is not excited), the electronic, vibrational and rotational energies can be considered separately, according to the Born-Oppenheimer approximation. Consequently, the rotational line strengths $S_{J'J''}$ are identical to those calculated for diatomic molecules in the appropriate electronic configuration.

By convention, the lower energy level of a given rotational transition was defined such that its degeneracy is equal to (2J"+1). For the Π-ground state of NCO, this assumption implies that each term of a K-doubled component is regarded as a separate initial level, despite the small energy difference. As a consequence, the normalization rule for the rotational line strength $S_{J'J''}$ must read for a given J"

$$\begin{aligned} S({}^SR_{21})+S(Q_1)+S({}^QP_{21}) &= \\ S(R_1)+S({}^RQ_{21})+S(P_1) &= \\ S(R_2)+S({}^PQ_{12})+S(P_2) &= \\ S({}^QR_{12})+S(Q_2)+S({}^OP_{12}) &= 2J''+1, \end{aligned} \tag{4.9}$$

where, for example, $S({}^SR_{21})$ is the rotational line strength of the transition

$$[A^2\Sigma^+(J'=J''+1,\alpha=2)\leftarrow X^2\Pi_{3/2}(J'',\beta=1)];$$

the present notation follows Mavrodineanu and Boiteaux [51]. The rotational line strengths were taken from Kovacs [26] and multiplied by a factor of two to be consistent with the above normalization rule. A listing of the computer model for the transition at 440 nm is given in Appendix 5.

In the calculation of the total partition function, the contribution of excited electronic states of NCO were neglected. For a linear XYZ molecule in a Π-configuration such as NCO in its ground state, Renner [52], Pople [53] and Hougen [49] have shown that it is generally not a good approximation to consider separately the electronic and vibrational energies, when the ν_2 bending vibration of the molecule is excited. Consequently, the total partition function should not obey the factorization rule, and hence was computed as follows:

$$Q_{tot} = \left(\sum_{v_2'',K'',J'',\pm 1/2} g \exp[-\frac{hc}{kT} F_{\pm 1/2}(v_2'',K'',J'')] \right) Q_{\nu_1} Q_{\nu_3}, \quad (4.10)$$

where v_2'' and J'' are, respectively, the vibration and rotation quantum numbers, and

$$K'' = |\Lambda \pm \ell| = v_2''+1,\ v_2''+1-2,\ \ldots, v_2''+1-2j,\ \ldots,\ 0 \text{ or } 1. \quad (4.11)$$

$F_{\pm 1/2}(v_2'',K'',J'')$ is the rovibronic energy of the $X^2\Pi_i(v_2'',K'',J'',\pm 1/2)$ level of NCO with $v_1''=v_3''=0$ (cm^{-1}). The appropriate formulae were derived by Hougen [49]; the zero-point energy follows Dixon's convention [48]. g is the K-doubling degeneracy and is equal to 1 for K=0 and 2 for K≠0. Q_{ν_1} and Q_{ν_3} are the contributions of the ν_1 and ν_3 stretching modes to the partition function, where

$$Q_{\nu_j} = [1-\exp(-\frac{hc}{kT}\omega_j^0)]^{-1} \quad (4.12)$$

for j=1,3; the values of Milligan and Jacox [54] for $\omega_1°$ and $\omega_3°$ were used in the present model.

Despite this complicated rovibronic structure of NCO, it was found that the total partition function can be adequately approximated by assuming no interaction between the rotation and electronic energies, and by considering all vibronic states with a given v_2'' as a single level of degeneracy $2\times2(v_2''+1)$. (There are two levels arising from the possible orientations of the electronic orbital angular momentum, two levels arising from electronic spin, and $(v_2''+1)$ levels associated with the degenerate bending.) This simplified approach leads to the approximate expression

$$Q_{total} \approx 4\, Q_{rot}\, Q_{v_1}\, Q_{v_2}^{\,2}\, Q_{v_3}\,, \tag{4.13}$$

where $Q_{rot}=(kT/hcB''_v)$ is the rotational partition function. A computer program incorporating Hougen's formulae was written to compare the complete summation with this approximate expression. The agreement between this approximation and the complete summation is better than 3% in the range $500<T<4000°K$. A listing of the partition function program is given in Appendix 5.

4.3.2 Results

The reproducible NCO plateau absorption generated by the HCN mixtures (see chapter 5) was used for mapping the relative absorption coefficient as a function of wavelength. The measured absorption coefficient (corrected for slight variations in the initial conditions) was plotted along with the computer-predicted profile (Fig. 4.6). The Voigt a parameters were extracted by comparing the theoretical and measured relative absorption spectra (using the peak absorption coefficient as a reference). Reasonable agreement was found for Voigt a parameters in the range $0<a<0.4$. This range corresponds to an uncertainty of [×0.80, ×1.06] in the peak absorption coefficient, which was found near 440.479 nm (in good agreement with Dixon [48].) This low value of the Voigt a parameter is expected at high temperatures, where UV absorption lines are typically dominated by Doppler broadening [55].

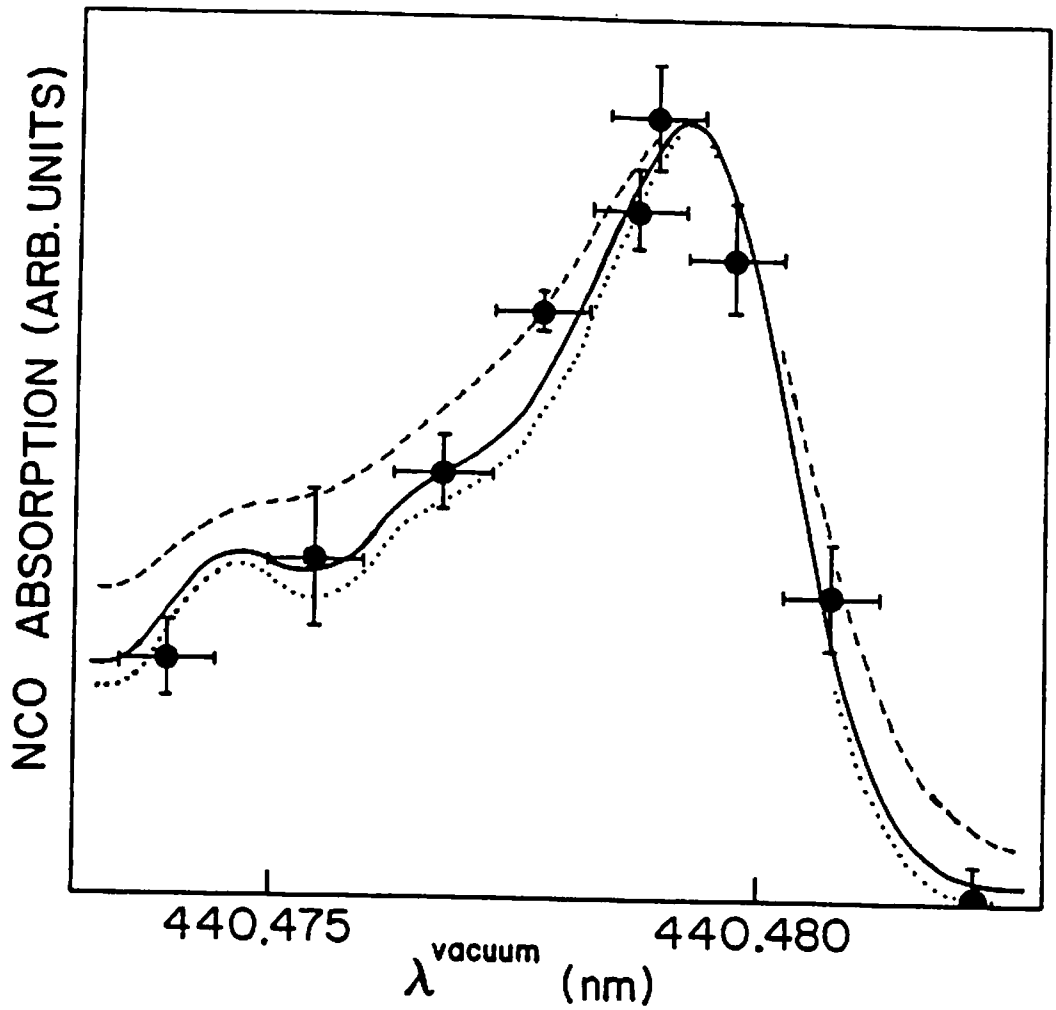

Fig. 4.6 NCO absorption spectrum at 440.479 nm. The abscissa shows wavelengths in vacuo, and the ordinate relative absorption coefficients β/β^{peak}. The horizontal error bars on the experimental data (•) corresponds to the wavemeter resolution; the vertical error bars correspond to uncertainties in the measured absorption. The solid line is a best fit to the spectrum using our spectroscopic model and an Voigt parameter a=0.1. The dashed lines are computer-generated spectra using a=0.4 (- -) and a=0 (•••) (Doppler limit). The average conditions of these experiments were T=1430°K, p=0.60 atm and $N_2O:O_2$: HCN:Ar ≈ 8:1:8:983.

Table 4.3 - Uncertainty Analysis for β

Reactions	Uncertainty factors	effect on β	
1 $N_2O+M \rightarrow N_2+O+M$	1.2	-5%	
	0.6		+17%
2 $C_2N_2+O \rightarrow CN+NCO$	1.85	-41%	
	0.54		+46%
3 $CN+O \rightarrow CO+N$	1.85	-1%	
	0.54		+1%
4 $CN+O_2 \rightarrow NCO+O$	1.60	-3%	
	0.63		+5%
5 $NCO+O \rightarrow CO+NO$	1.60		+35%
	0.55	-36%	
6 $NCO+M \rightarrow N+CO+M$	5.0		+30%
	0.2	-5%	
17 $NCO+N \rightarrow N_2+CO$	10.		+4%
	0.1	-2%	
32 $N_2O+CN \rightarrow NCN+NO$	10.		+26%
	0.1	-4%	
Uncertainty in $K_f°(CN)$	2.0	0%	
	0.5		+20%
Voigt parameter	4.0	-22%	
	0.0		+6%
Experimental scatter		-6%	+6%
Total uncertainty=$[\Sigma(\text{uncert.})^2]^{1/2}$		-60%	+76%

The three additional runs with C_2N_2 mixtures provided an absolute value for the absorption coefficient β at the peak wavelength. From the computer-predicted NCO plateau (p_{NCO}=0.012 torr) and the corresponding experimental absorption (5%), it was inferred

$$\beta(1450°K,\ 0.60\ atm) = 110(-50,+130)\ cm^{-1}atm^{-1},$$

at 440.479 nm with a≈0.1. Uncertainties in β include experimental scatter [×0.94, ×1.06], uncertainty in the Voigt a parameter [×0.80, ×1.06], and the uncertain knowledge of some reaction rates [×0.57, ×2.15] including k_2 and k_5 (see Table 4.3). These three uncorrelated uncertainties combine to give the upper and lower bounds reported above, $60<\beta<240$. A significant reduction in the overall uncertainty could thus be achieved if a better technique for generating known levels of NCO were available.

Using the computer-predicted value of $\beta/f_{00} = 43000\ cm^{-1}atm^{-1}$, $f_{00}=0.0026$ is extracted. This value is in good agreement with Reisler, et al. [47] and Charlton et al. [56], who respectively reported $f_{el}=0.0033\pm 0.0001$ and $f_{el}=0.0040\pm0.0005$ (see Appendix 4). Using the average value of $f_{el}=0.0037$ and the present value for f_{00}, we find for q_{00}, the Franck-Condon factor of the $(00^00)\leftarrow(00^10)$ transition,

$$q_{00}=0.0026/0.0037=0.70.$$

This result is in agreement with a theoretical calculation based on the simplified approach of Smith and Warsop [57] and Sharp and Rosenstock [58]. Using this approach, $q_{00}=0.81$ was obtained (see Appendix 4).

The indicated experimental value of β(1450°K) can be extrapolated to other temperatures using the spectroscopic model. Figure 4.7 is a theoretical plot of β/f_{00} as a function of temperature. Owing mostly to the strong temperature dependence of the total partition function, the peak absorption coefficient decreases substantially as temperature increases. This effect translates into increased NCO detection limits at higher temperatures. At the temperature of our experiments (1450°K), a signal-to-noise ratio (S/N) of 30 was achieved for an absorption of 5%. (The signal-to-noise ratio was limited by laser power fluctuations). Hence, the detection limit (S/N=1) was about 0.8 ppmv of NCO at 0.60 atm. The equivalent detection limits calculated at other temperatures and the same pressure are 11 ppmv at 2500°K and 0.2 ppmv at 1000°K.

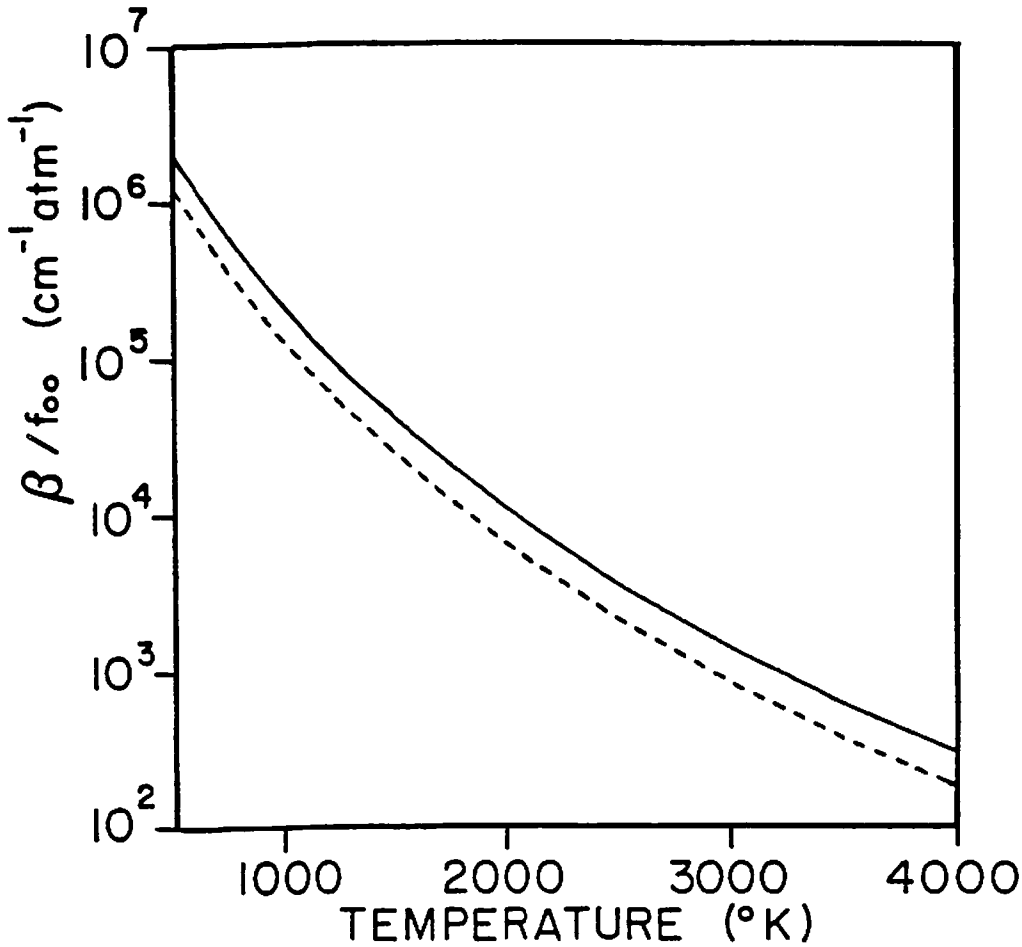

Fig. 4.7 Computed relative NCO absorption coefficient β/f_{00} at 440.479 nm (vac.) vs. temperature, with a Voigt parameter a=0 (solid line), and a=1.0 (dashed line).

4.4 NCO absorption at 305 nm - Analysis and Results

The spectrum of the $[B^2\Pi_i \leftarrow X^2\Pi_i]$ transition of NCO is more complicated than the $[A^2\Sigma^+ \leftarrow X^2\Pi_i]$ spectrum discussed above. Dixon [59] made tentative assignments of the observed band heads and absorption maxima observed in the range $265<\lambda<320$ nm. Many bands were found to be diffuse, indicating a possible predissociation of the upper state. Only the $(10^10) \leftarrow (00^10)$ vibrational band could be analyzed, but uncertain perturbations made it difficult to determine accurate rotational constants. This band, however, is the least perturbed in rotation, and constitutes our best choice for a quantitative UV absorption diagnostic of NCO. Among the four branches available in the band, it is best to use the strong band head of the R_1 branch, which does not overlap with the neighboring R_2, P_1, and P_2 branches. All branches are degraded towards the red.

A computer program was written to calculate the relative absorption coefficient β/f_{10} for the $(10^10) \leftarrow (00^10)$ band. For simplicity, we assumed that the rotational structure obeys the Hill and Van Vleck formula (eq. 4.6) and we used the spectroscopic constants inferred by Dixon [59]. The calculation of β/f_{10} is similar to the one presented above for the $[A^2\Sigma^+ \leftarrow X^2\Pi_i]$ transition. Rotational line strengths were taken directly from Kovacs [26]. No re-normalization to Kovacs' published line strengths was required. Figure 4.8 shows the computed absorption spectrum around the R_1 and R_2 band heads. A summary of spectroscopic constants is given in Table 4.2.

The plateau NCO absorption generated by the C_2N_2 mixtures (see Fig. 4.9) was used to map the relative NCO absorption profile as a function of UV wavelength. The time-resolved traces obtained with this diagnostic at 305 nm were similar to the traces recorded using the previous diagnostic at 440 nm; this indicates an absorption free from the interference of other molecular species present in the shock tube. Under the conditions of our experiments ($T \approx 1470°K$, $p \approx 0.63$ atm), a very broad spectrum was observed, which was fitted using a Voigt a parameter of 9 by matching the experimental and theoretical full widths at half maximum (see Fig. 4.10).

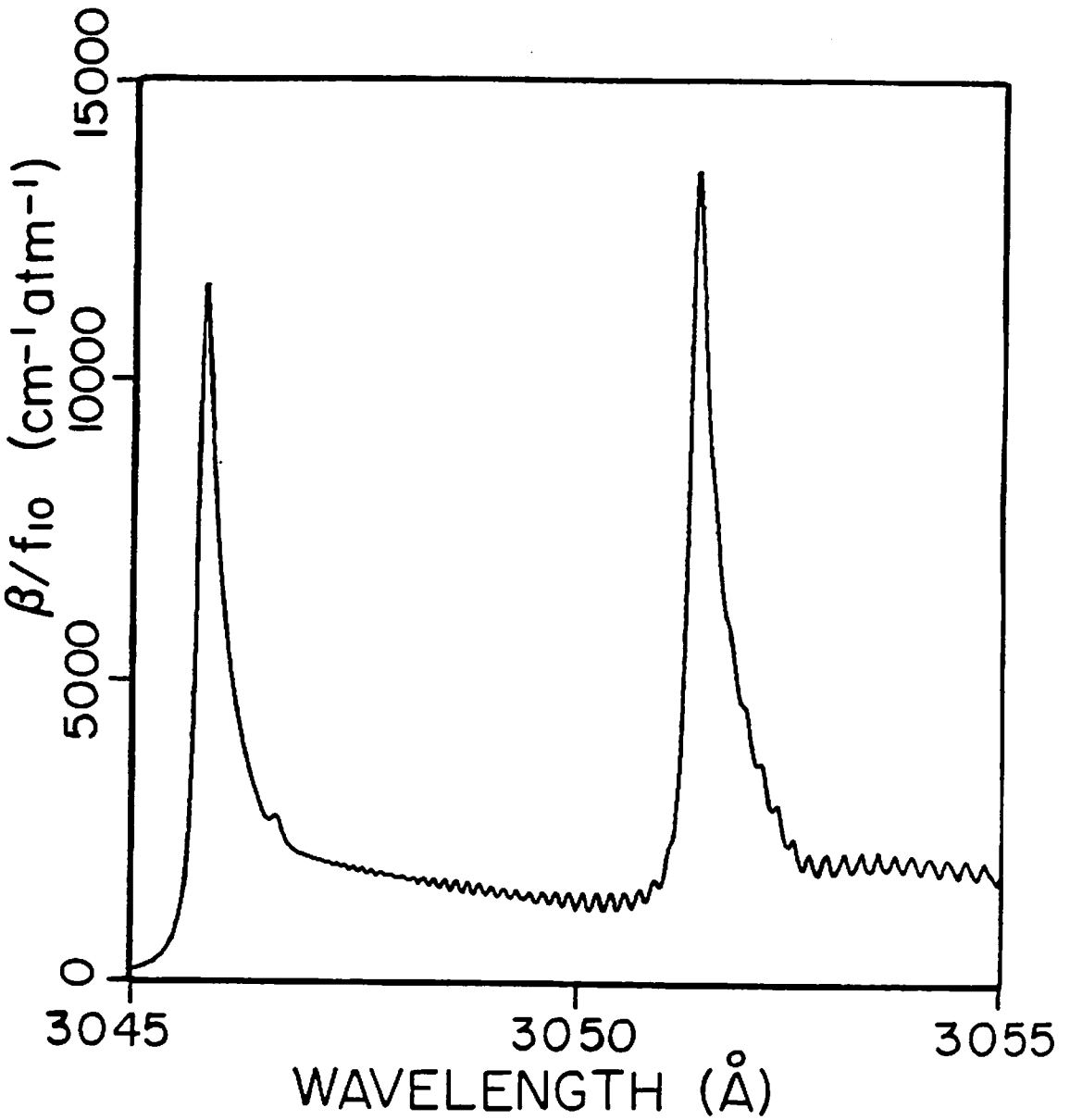

Fig. 4.8 Computed NCO absorption spectrum around 305 nm using an average Voigt parameter a=9. The abscissa shows wavelengths in air. The ordinate shows the relative absorption coefficient β/f_{10}, where f_{10} is the oscillator strength of the $[B^2\Pi_i(10^10)\leftarrow X^2\Pi_i(00^10)]$ band. Note the R_1 bandhead around 3046 Å (air) and the R_2 bandhead around 3051 Å (air).

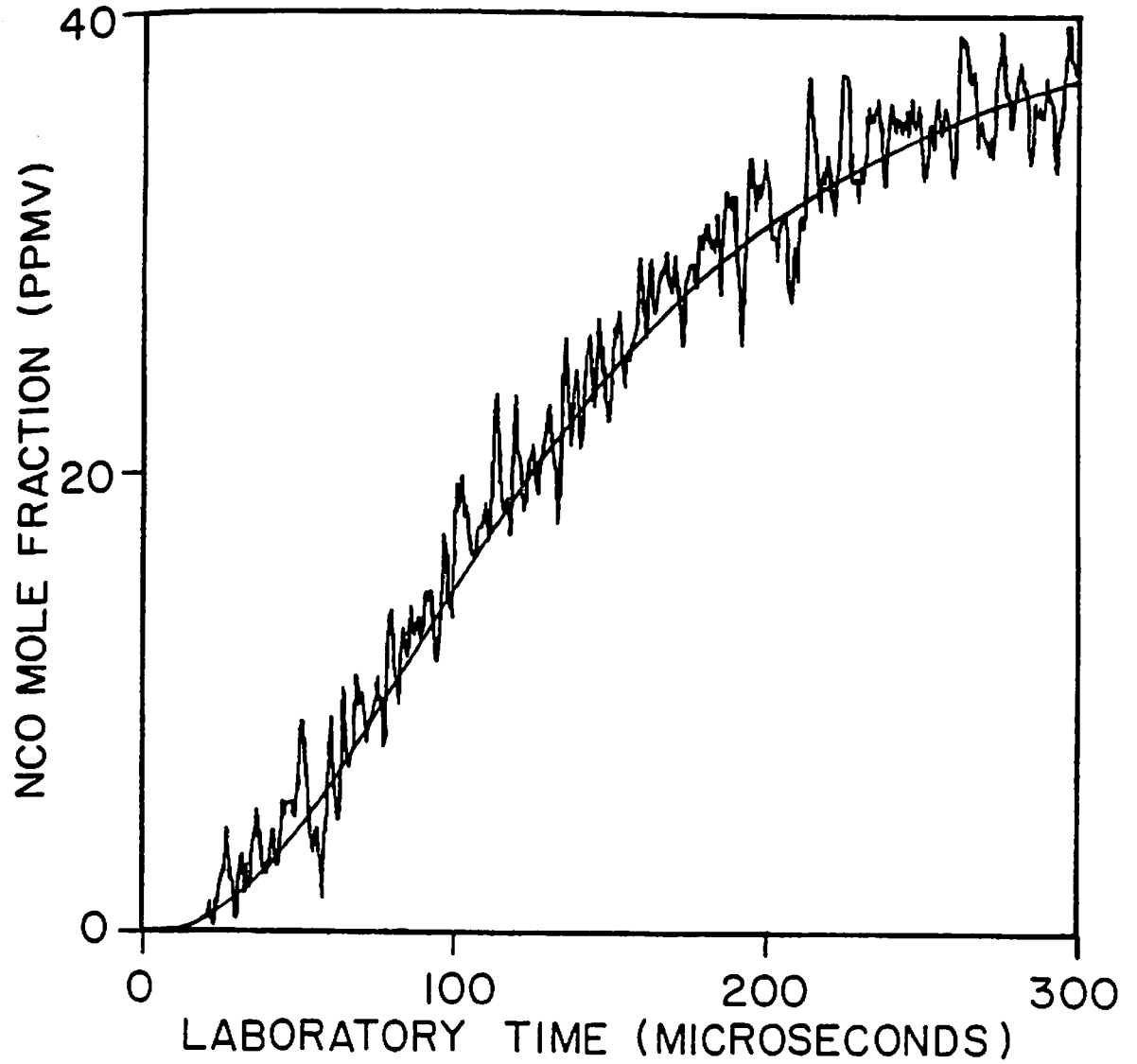

Fig. 4.9 Best computer fit of a typical NCO profile in a $C_2N_2/O_2/N_2O$/argon experiment using the absorption diagnostic at 305 nm. The conditions are T_2=1460°K, p_2=0.61 atm and $N_2O:O_2:C_2N_2:Ar$= 4:1:8:987. The absorption at 300 μsec is 1.3%. The solid line is a best computer fit using rates shown in Table 3.2.

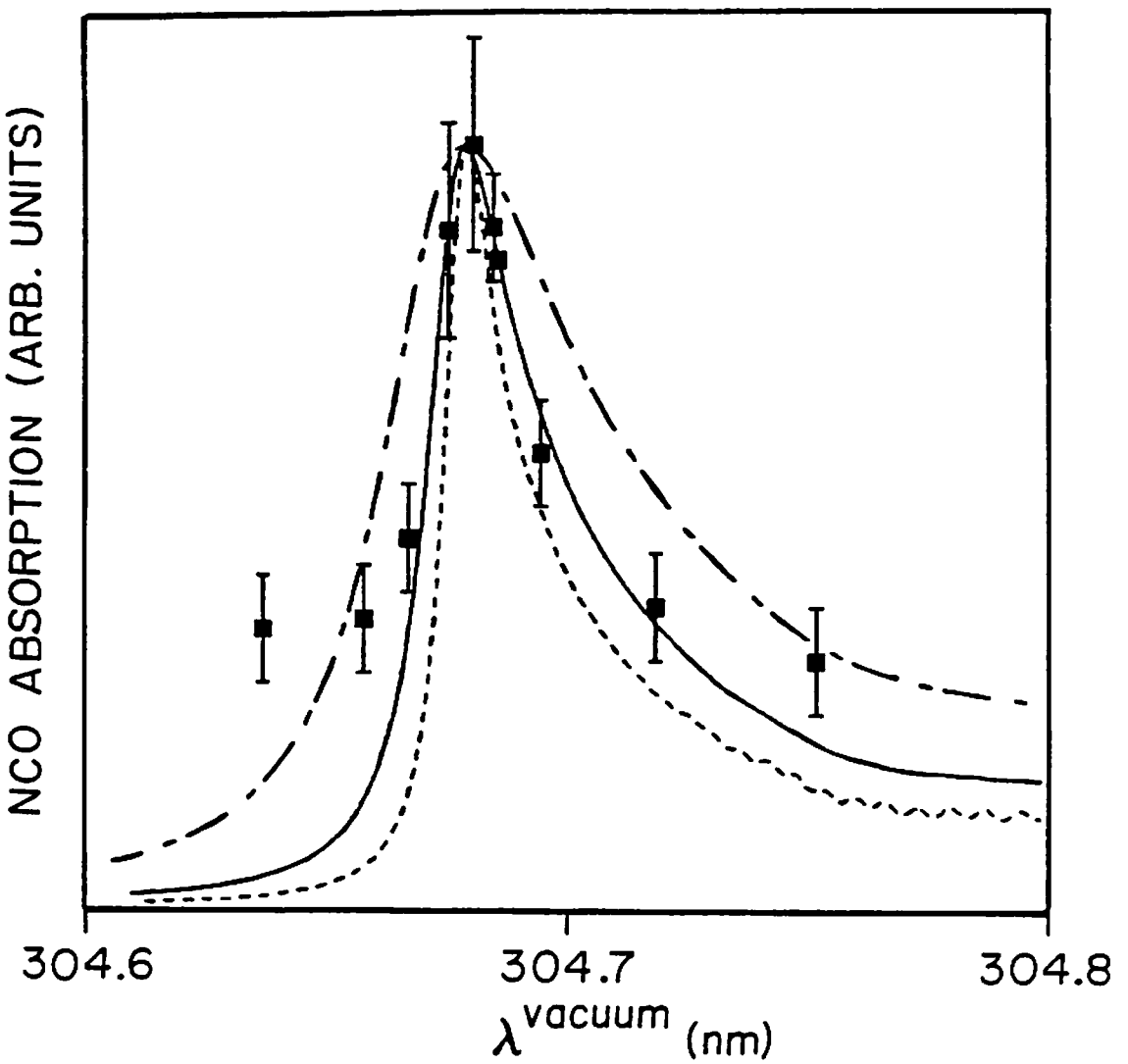

Fig. 4.10 NCO absorption spectrum around 305.681 nm. The vertical error bars on the experimental data correspond to the uncertainties in the measured absorption. The solid line is a best fit to the spectrum using our spectroscopic model and an average Voigt parameter a=9. The dashed lines are computer-generated spectra using a=20 (- · -) and a=5 (···).

The peak absorption was found at 304.681 nm, in reasonable agreement with Dixon's measurement at 304.676 nm (vac). The poor quality of the fit in the wings is attributed to the possible interference of unassigned neighboring vibrational hot bands.

The observation of an exceedingly broad spectrum is consistent with the measurements of Sullivan, et al. [60], who reported a short lifetime and a radiationless decay of the $[B^2\Pi_i(10^10)]$ level of NCO. Two of the three criteria for predissociation of the (10^10) level (Auger process [61]) have therefore been checked (observation of radiationless transitions and excessive natural broadening of discrete levels).

Four experiments were conducted at the measured peak absorption (304.681 nm). As before, a kinetics calculation of the NCO plateau enabled determination of the absolute absorption coefficient. At 304.681 nm,

$$\beta(1470°K,\ 0.63\ atm) = 40\ (-19,+48)\ cm^{-1}atm^{-1},$$

with a=9. Sullivan et al. [60] measured a decay lifetime of 63±3 nsec for the $[B^2\Pi_i(00^10)]$ level of NCO using laser-induced fluorescence. (This lifetime is considerably longer than that of the $[B^2\Pi_i(10^10)]$ level, indicating a dissociation limit lying between the (00^10) and the (10^10) levels of $[B^2\Pi_i]$.) Since this measurement (63 nsec) was carried out in the near absence of added collision partners (zero-pressure limit), the upper state population decayed through a purely radiative transition to all possible vibrational levels of the lower state with $\Delta J=0,\pm1$. Consequently, the total electronic oscillator strength can be estimated from the lifetime of the $[B^2\Pi_i(00^10)]$ state reported by Sullivan, et al. Using a calculation presented in Appendix 4, $f_{el}\approx0.022$.

The complexity of this NCO transition at 305 nm may leave some doubts about the validity of the spectroscopic model. Nevertheless, from the computer-predicted value of $\beta/f_{10}\approx12700\ cm^{-1}atm^{-1}$ at 1470°K with a=9, the oscillator strength of the $(10^10)\leftarrow(00^10)$ band $f_{10}\approx0.0031$ is extracted. Using the above estimate for f_{el}, a Franck-Condon factor for the $(10^10)\leftarrow(00^10)$ band is inferred in the range

$$q_{10}=0.14(-0.06,+0.16).$$

This result is again in agreement with the theoretical calculation described in Appendix 4 ($q_{10}=0.16$).

4.5 Recommendation for the NCO Diagnostic

Quantitative and sensitive absorption measurements of NCO have been demonstrated in high temperature systems, using laser radiation at either 305 or 440 nm. However, the spectrum at 305 nm is highly broadened and cannot entirely be explained in terms of a simple spectroscopic model. By contrast, the spectrum at 440 nm provides a stronger peak absorption coefficient and can be more readily modeled. Therefore the use of the $[A^2\Sigma^+ \leftarrow X^2\Pi_i]$ transition is recommended for a reliable and sensitive high temperature absorption diagnostic of NCO.

4.6 High Temperature Rate of NCO Decomposition

As discussed in the previous paragraph, C_2N_2 mixtures were shock-heated at low temperatures (1450°K) to infer the rate of reaction (5)

$$NCO + O \rightarrow CO + NO, \tag{5}$$

and to predict absolute levels of NCO for quantifying the diagnostic at 440 nm. In this section, further use of the NCO diagnostic will be described to measure the ratio of the rate constants of reaction (5) and (6) at higher temperatures (2240°K)

$$NCO + M \rightarrow N + CO + M. \tag{6}$$

The rate of reaction (6) is important in the data reduction of shock tube experiments at temperatures greater than 2000°K, where NCO decomposition may be faster than other NCO-removing reactions such as reactions (5) or (9). On the other hand, this NCO decomposition reaction is generally unimportant in flames, where free radicals and atoms such as H, O and OH are abundant.

4.6.1 Experimental Considerations

Mixtures of C_2N_2 and N_2O diluted in argon were shock heated to measure the ratio of the rate constants of reactions (5) and (6) at 2240°K, the rate constants for the other reactions significant at early times, reactions (1) and (2), being already well established,

$$N_2O + M \rightarrow N_2 + O + M, \quad (1)$$

$$C_2N_2 + O \rightarrow CN + NCO, \quad (2)$$

$$NCO + O \rightarrow CO + NO, \quad (5)$$

$$NCO + M \rightarrow N + CO + M. \quad (6)$$

Previous work to establish k_5 and k_6 is limited primarily to the present shock tube work in which the ratio k_5/k_6 was determined at 2150°K and 2400°K from measurements of NO and CN (see chapter 3), and k_5 by monitoring NCO using laser absorption.

Six runs were conducted behind incident shock waves with the following mixtures and conditions: $\chi_{C_2N_2}$=0.41%, $0.10<\chi_{N_2O}<0.42\%$, T_2=2240°K, p_2=0.65 atm and ρ_{21}=3.57. (ρ_{21} is the density ratio across the shock and also the ratio of particle time to laboratory time.) Shock speeds varied between 1.48 and 1.50 mm/μsec, with a typical attenuation of 1%/m. Typical leak plus outgassing rates were $3\text{-}5\times10^{-5}$ torr/min. Gases were taken directly from commercial cylinders (Table 2.1), with C_2N_2 (1.01%) dilute in argon. The temperature of the experiments was set by considerations of growing interferences on the NCO absorption system from spontaneous emission at higher temperatures and by insufficient rates of NCO removal from reaction (6) at lower temperatures.

4.6.2 NCO Decomposition in $N_2O/C_2N_2/Ar$ Mixtures

A complete mechanism that encompasses eighteen reactions in the C/N/O system was used in the data reduction (see Table 3.2), but a simplified description, useful in guiding the actual data interpretation, can be given as follows. At early times, N_2O decomposes to provide O-atoms, which rapidly reach a steady-state concentration; C_2N_2 then reacts to form NCO, which in turn is removed either by O-atoms or by

dissociation,

$$N_2O + M \rightarrow N_2 + O + M, \quad (1)$$
$$C_2N_2 + O \rightarrow NCO + CN, \quad (2)$$
$$NCO + O \rightarrow CO + NO, \quad (5)$$
$$NCO + M \rightarrow N + CO + M. \quad (6)$$

At the peak of the NCO concentration,

$$\frac{d[NCO]}{dt} = k_2[C_2N_2][O] - k_5[NCO][O] - k_6[NCO][M] = 0 \ , \quad (4.14)$$

and hence
$$\frac{[C_2N_2]}{[NCO]^{peak}} = \frac{k_5}{k_2} + \frac{k_6}{k_2} \times \frac{[M]}{[O]} \ . \quad (4.15)$$

The mole fraction of O-atoms at steady-state is proportional to the initial N_2O mole fraction,

$$\frac{[O]}{[M]} \propto \left(\chi_{N_2O} \right)_{t=0} \ . \quad (4.16)$$

If $[C_2N_2]$ is nearly constant throughout the time scale of interest, then measurements of the peak NCO concentration for different values of the initial N_2O mole fraction can be plotted as a straight line on a graph showing $[C_2N_2]/[NCO]^{peak}$ as a function of $1/(\chi_{N_2O})_{t=0}$. In the case of this simplified model, the intercept and the slope are respectively proportional to the ratios k_5/k_2 and k_6/k_2. Furthermore, the ratio of the intercept and the slope yields k_5/k_6.

A numerical routine incorporating the mechanism in Table 3.2 was used for the actual data interpretation. Figure 4.11 shows a typical experimental trace, converted to NCO mole fraction. The initial spike results from a Schlieren effect, which is useful in determining the shock arrival time. The NCO mole fraction at the peak (t=14μsec) was used in the data reduction. Values for k_5/k_2 and k_6/k_2 were inferred by varying these quantities in the detailed kinetic mechanism until least-squares agreement was found between the experimental and computer-generated results for $[C_2N_2]/[NCO]^{peak}$ vs. $1/(\chi_{N_2O})_{t=0}$ (see Fig. 4.12).

Finally, the ratio k_5/k_6 was computed from the ratio of the inferred values of k_5/k_2 and k_6/k_2.

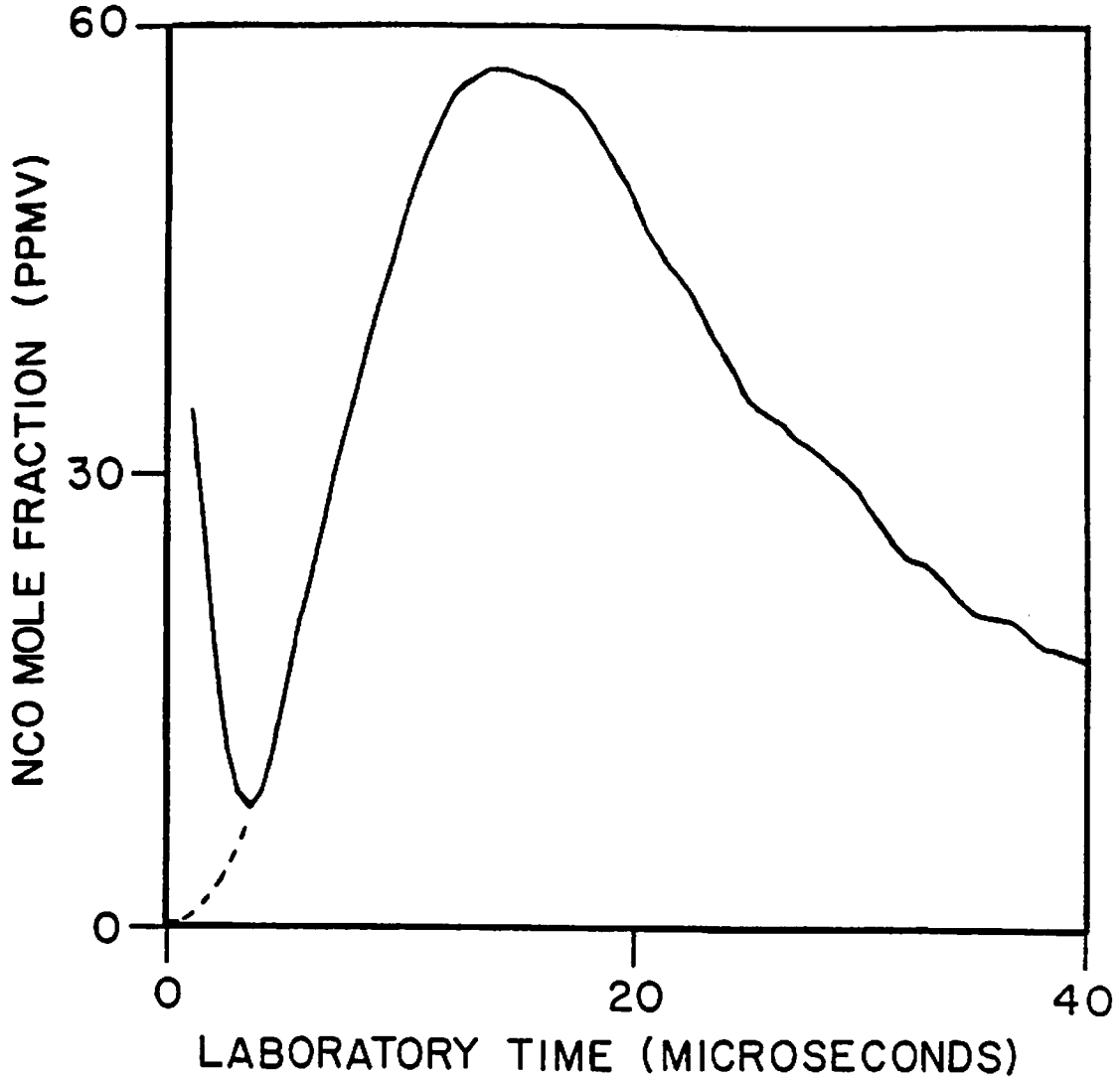

Fig. 4.11 A typical experimental trace in a N_2O/C_2N_2/argon mixture with T_2=2210°K, p_2=0.64 atm, $N_2O:C_2N_2:Ar$=2:4:994 and ρ_{21}=3.56. The initial spike corresponds to a shock-generated Schlieren effect. The dashed line is an estimate of the unperturbed NCO profile at early times. The peak absorption of 1.9% corresponds to χ_{NCO}=57 ppmv, with β(2210°K)≈17 cm^{-1} atm^{-1} (extrapolated value using the spectroscopic model in ¶4.3.1).

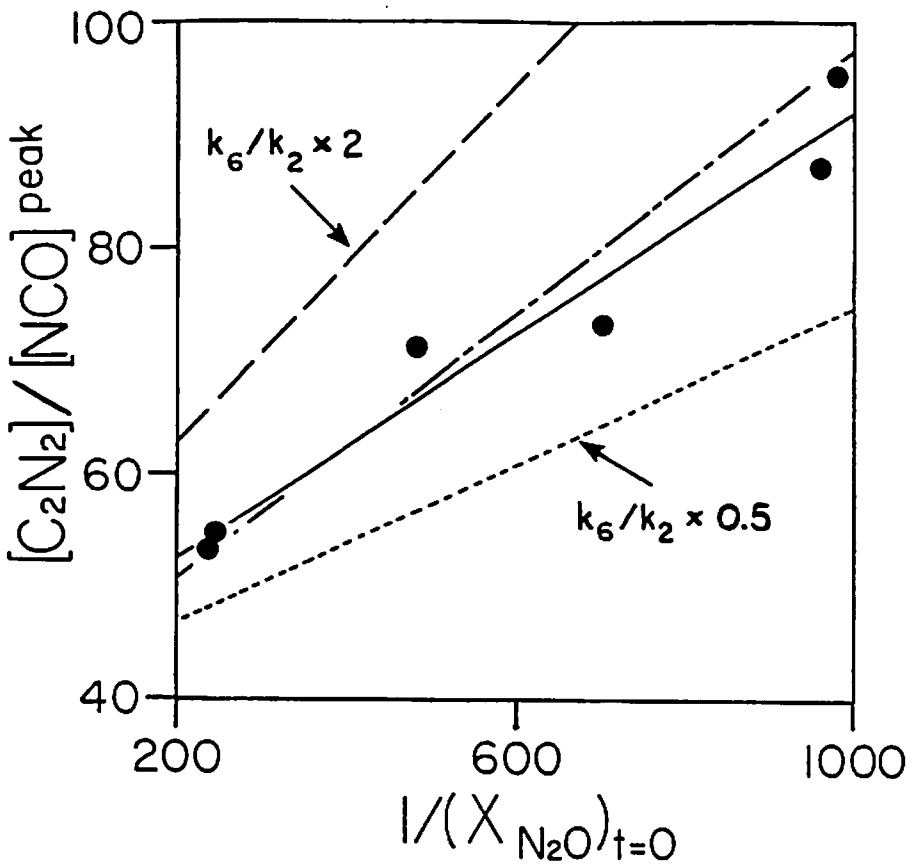

Fig. 4.12 Experimental plot of the concentrations ratio $[C_2N_2]/[NCO]^{peak}$ vs. inverse initial N_2O mole fraction $1/(\chi_{N_2O})_{t=0}$ with $T_2 \simeq 2240°K$ and $p_2 \simeq 0.65$ atm. The peak NCO concentrations are computed using extrapolated absorption coefficients β (see Fig. 4.7). The solid line is a least-squares fit of the experimental data and also a best computer correlation using the mechanism in Table 3.2, $k_5/k_2 \simeq 10^{1.38}$ and $k_6/k_2 \simeq 10^{-2.16}$. The dashed line (- -) corresponds to $k_6/k_2 \times 2.0$ and the dotted line (···) to $k_6/k_2 \times 0.5$ (with k_2 held at the Table 3.2 value). Clearly, neither excursion in k_6/k_2 can adequately fit the experimental slope. The (- · -) line shows insensitivity to the nominal value of k_2 by employing a value of k_2 twice that shown in Table 3.2, but identical values for the ratios $k_5/k_2 \simeq 10^{1.38}$ and $k_6/k_2 \simeq 10^{-2.16}$.

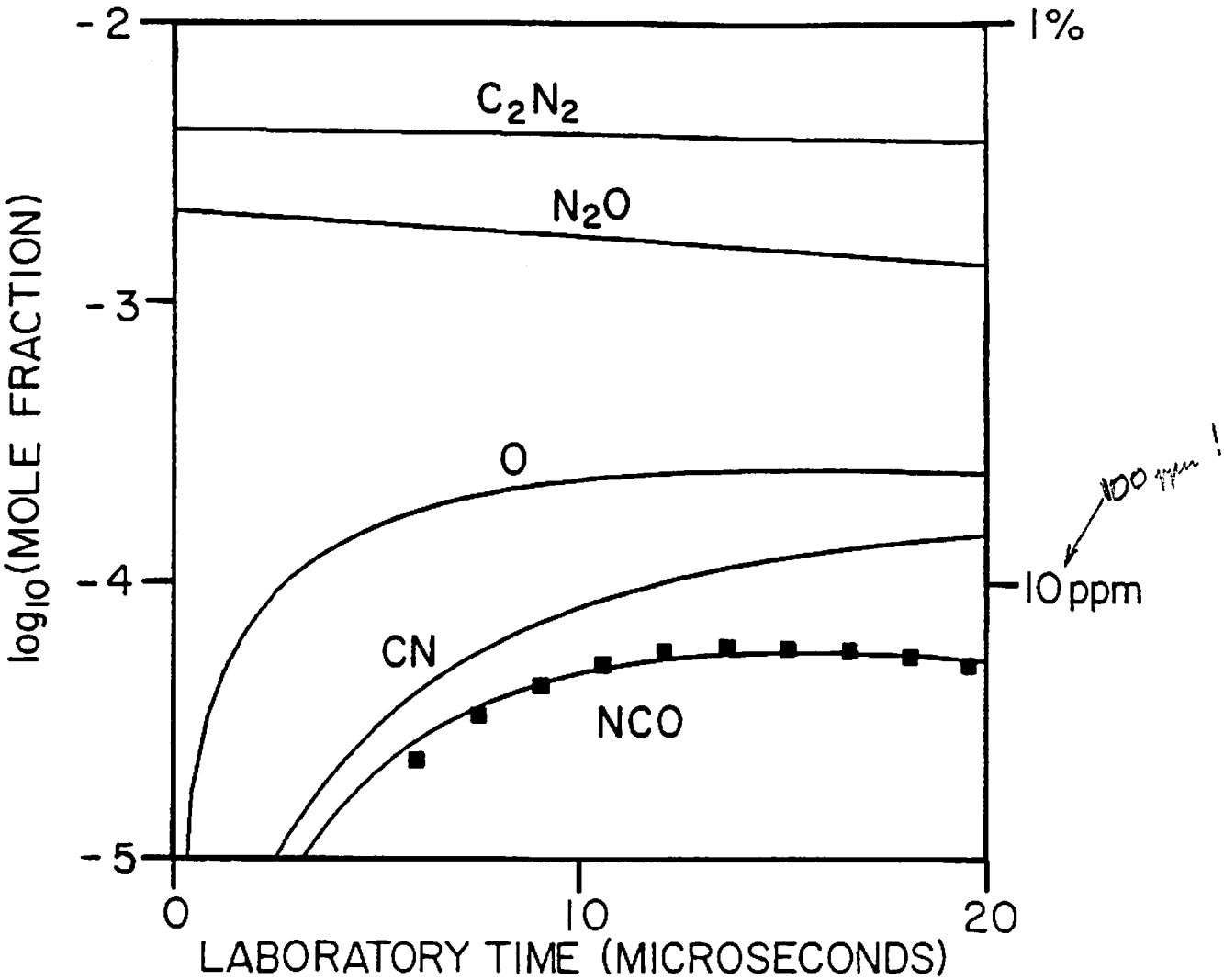

Fig. 4.13 Computer-generated profiles of C_2N_2, N_2O, O, CN and NCO mole fractions using $k_5/k_2=10^{1.38}$ and $k_6/k_2=10^{-2.16}$ from Fig. 4.12, and the conditions of Fig. 4.11. The solid squares are taken from the NCO experimental trace of Fig. 4.11.

Table 4.4 - Uncertainty Analysis for k_5/k_6

Reactions	Uncertainty factors	effect on k_5/k_6	
1 $N_2O+M \rightarrow N_2+O+M$	1.2	-15%	
	0.8		+19%
2 $C_2N_2+O \rightarrow CN+NCO$	1.85		+39%
	0.54	-19%	
3 $CN+O \rightarrow CO+N$	1.85		+8%
	0.54	-6%	
4 $CN+O_2 \rightarrow NCO+O$	1.58	-4%	
	0.63		+5%
7 $C_2N_2+M \rightarrow CN+CN+M$	2.0		+12%
	0.5	-0%	
13 $N_2O+O \rightarrow NO+NO$	1.5		+9%
	0.4	-2%	
14 $N_2O+O \rightarrow N_2+O_2$	1.5		+9%
	0.4	-2%	
15 $N_2+O \rightarrow N+NO$	1.35		+12%
	0.65	-4%	
16 $O+NO \rightarrow N+O_2$	1.3		+5%
	0.7	-4%	
17 $NCO+N \rightarrow N_2+CO$	10.	-8%	
	0.1		+8%
18 $NCO+N \rightarrow CN+NO$	10.	-13%	
	0.1		+8%
19 $CN+N \rightarrow C+N_2$	10.	-11%	
	0.1		+3%
32 $N_2O+CN \rightarrow NCN+NO$	10.		+6%
	0.1	-0%	
Uncertainty in the fit		-75%	+60%
Total uncertainty= $[\Sigma(\text{uncert.})^2]^{1/2}$		-82%	+79%

Computer calculations confirmed that the ratio k_5/k_6 inferred by this procedure is reasonably insensitive to the value of k_2 employed in the detailed model (see Fig. 4.12); hence the value of k_5/k_6 reported is nearly independent of the substantial uncertainties associated with both k_2 and the absorption coefficient $\beta(T=2240°K)$. Residual uncertainties in the ratio result primarily from the uncertain knowledge of other rate constants in the mechanism [×1.7, ×0.6], and the 95% confidence interval on the slope and intercept [62] [×1.8, ×0.5] (see Table 4.4). These two uncorrelated uncertainties can be combined to give an overall uncertainty in k_5/k_6 of [×2.2, ×0.43], which means that the ratio k_5/k_6 is bounded by values 2.2 times and 0.43 times the reported value. Figure 4.13 shows computer-generated profiles of reactants and intermediate species using the values of k_5/k_2 and k_6/k_2 inferred from Fig. 4.12 and other rates reported in the detailed mechanism of Table 3.2.

The result $k_5/k_6 = 10^{3.54(+0.34,-0.37)}$ at (2240°K, 0.65 atm) is plotted in Arrhenius form along with the earlier determinations at (2150°K, 0.65 atm) and (2400°K, 0.6 atm) (Fig. 4.14), which were obtained using two independent experiments based on measurements of NO and CN (see chapter 3). Reasonable agreement is found among the three independent measurements within the size of their individual error bars. Because of these error bars and the narrow range of temperatures studied, it is difficult to estimate a correct temperature dependence of the ratio. For the purpose of reporting a single expression, the activation energy of k_6 was set equal to the NCO dissociation energy, i.e., 47.3 kcal/mole [63], and a number of effective degrees of freedom s=2 was assumed [64]. (The latter assumption implies a temperature exponent in the pre-exponential factor of k_6 equal to $m = \frac{3}{2} - s = -1/2$.) In addition, k_5 was assumed independent of temperature in the range $2150<T<2400°K$. Using a least-squares-fit expression based on the three experimental data points, the result $k_5/k_6 = 10^{-3.1}\ T^{0.5}\ \exp[+24000/T]$ [×2.0, ×0.5] was obtained for ($2150<T<2400°K$, $p\simeq0.65$ atm).

No experimental measurement of k_5 has been performed above 1500°K. However, it is reasonable to assume that k_5 is nearly constant over a large temperature range. Using the earlier measurement of $k_5=10^{13.75}$

cm^3/mole/sec [×1.60, ×0.55] at 1450°K and combining the corresponding uncertainties in k_5 and k_5/k_6, the value $k_6 = 10^{16.8}T^{-0.5}\exp[-24000/T]$ [×2.3, ×0.4] is recommended over the range 2150<T<2400°K and p=0.65 atm. There are no previous data for k_6 available for comparison.

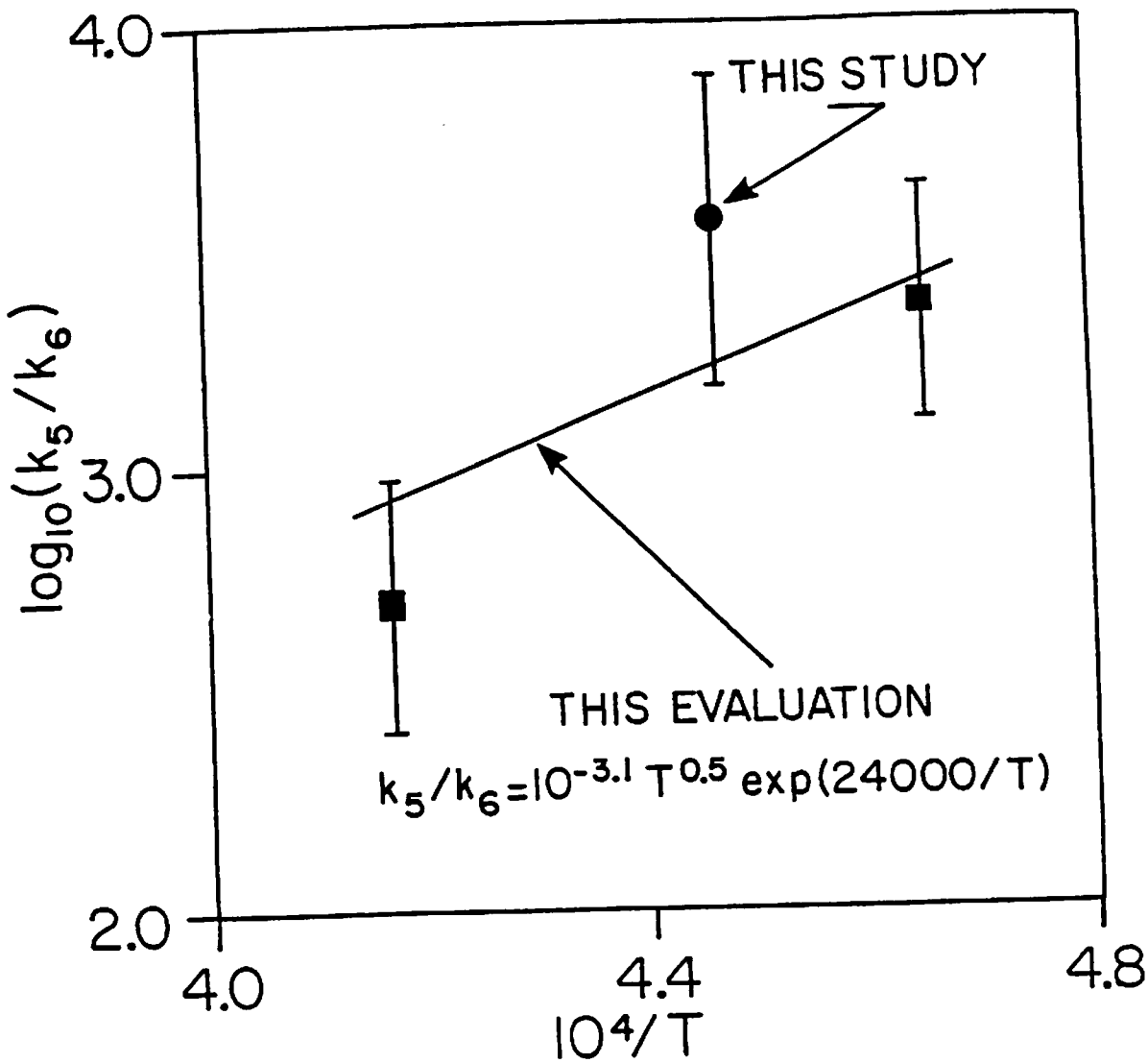

Fig. 4.14 Arrhenius plot for the ratio k_5/k_6. The abscissa shows reciprocal temperatures $10^4/T$ (K^{-1}). The square symbols correspond to experiments reported in chapter 3. Note that these experiments were performed using independent NO and CN measurements.

4.7 Conclusions

The detailed study of cyanogen oxidation kinetics resulted in the development of a novel laser absorption technique to measure NCO concentrations at high temperatures. Using this technique in other cyanogen mixtures, the rates of reactions (5) and (6) were inferred

$$NCO + O \rightarrow CO + NO, \tag{5}$$

$$NCO + M \rightarrow N + CO + M. \tag{6}$$

These results are essential for the reduction of further NCO data from shock tube experiments.

Chapter 5

The Kinetics of NCO Reactions

Chapter 3 reported studies of shock-heated cyanogen mixtures to investigate important fuel-nitrogen reactions involving CN at high temperatures. In chapter 4, a new laser absorption diagnostic of NCO was described for measuring NCO removal rates in an oxidizing medium. Thus far, mixtures of gases containing only three atoms have been shock-heated (C, N and O), in order to simplify the interpretation of the experimental data. In this chapter, we report further use of the NCO diagnostic in four-atom mixtures to infer the rates of

$$HCN + O \rightarrow NCO + H, \tag{8}$$

$$NCO + H \rightarrow CO + NH, \tag{9}$$

$$NCO + H_2 \rightarrow HNCO + H. \tag{10}$$

As discussed in Appendix 8, these reactions contribute to the oxidation of hydrogen cyanide, and thus are important for the fuel-nitrogen mechanism.

5.1 HCN Oxidation in $HCN/N_2O/O_2$/argon Mixtures

In the study of NCO spectroscopy (chapter 4), mixtures of C_2N_2, N_2O and O_2 diluted in argon were shock-heated to determine the rate constant of reaction (5) at 1450°K, the rate constants for (1), (2) and (4) being already well established

$$N_2O + M \rightarrow N_2 + O + M, \tag{1}$$

$$C_2N_2 + O \rightarrow CN + NCO, \tag{2}$$

$$CN + O_2 \rightarrow NCO + O, \tag{4}$$

$$NCO + O \rightarrow CO + NO. \tag{5}$$

In this study, C_2N_2 was replaced by HCN and a comparison of the NCO time-histories in the C_2N_2 and HCN mixtures was used to establish a

value for the rate of reaction (8) at 1440°K

$$HCN + O \rightarrow NCO + H. \tag{8}$$

5.1.1 Experimental Considerations

Three runs were conducted with C_2N_2 mixtures, $N_2O:O_2:C_2N_2:Ar = 4:1:4:991$, $T_2=1450\pm10$°K, $P_2=0.60$ atm, and $\rho_{21}=3.31$. Nine additional runs were conducted with HCN mixtures, $N_2O:O_2:HCN:Ar=8:1:8:983$, $T_2=1430\pm20$°K, $P_2=0.60$atm, and $\rho_{21}=3.32$. Shock speeds varied between 1.14 and 1.17 mm/μsec, with typical attenuation of 1.2%/m for the C_2N_2 mixtures and 2.5%/m for the HCN mixtures. Typical leak plus outgassing rates were 3-5×10^{-5} torr/min. The mole fraction of HCN in the cylinder was checked against known C_2N_2 and HCN mixtures using high-temperature CN emission tests since HCN may slowly decompose in high pressure cylinders (see Appendix 7). The temperature of the experiments was set by considerations of growing interference due to NCO removal by reaction (6) at higher temperatures,

$$NCO + M \rightarrow N + CO + M, \tag{6}$$

and increasing uncertainty in the rate of reaction (1) at lower temperatures. In addition, a few tests were conducted with the laser blocked to monitor possible spontaneous emission interferences from the test gas. These emission levels were found to be insignificant.

5.1.2 Analysis and Results

Data from these experiments were reduced using the complete kinetic mechanism in Table 5.1, but a simplified model based on the following reactions is helpful in appreciating the similarity between the C_2N_2 and HCN experiments

$$N_2O + M \rightarrow N_2 + O + M, \tag{1}$$
$$HCN + O \rightarrow NCO + H, \tag{8}$$
$$NCO + O \rightarrow NO + CO, \tag{5}$$
$$NCO + H \rightarrow NH + CO. \tag{9}$$

Table 5.1 - Reaction Mechanism - H/C/N/O System

	Reactions	ΔH [a]	equil. const [b]	rate constants [c]			Source (Ref #)
				$\log_{10}A$	m	θ(°K)	
1	$N_2O+M \rightarrow N_2+O+M$	+40	-3.8	23.89	-2.5	32710	[22]
2	$C_2N_2+O \rightarrow CN+NCO$	+4	0.3	12.66	0	4440	This study
3	$CN+O \rightarrow CO+N$	-75	10.2	13.31	0	210	This study
4	$CN+O_2 \rightarrow NCO+O$	-2	0.1	12.75	0	0	This study
5	$NCO+O \rightarrow NO+CO$	-105	15.4	13.75	0	0	This study
6	$NCO+M \rightarrow N+CO+M$	+48	-5.8	16.80	-0.5	24000	This study
8	$HCN+O \rightarrow NCO+H$	0	-0.4	8.24	1.47	3775	This study
9	$NCO+H \rightarrow CO+NH$	-39	6.0	14.02	0	1000	This study[d]
10	$NCO+H_2 \rightarrow (HNCO)+H$	-10	1.0	13.23	0	4000	This study[e]
11	$C_2N_2+H \rightarrow CN+HCN$	+4	0.7	14.50	0	4030	This study
12	$CN+H_2 \rightarrow HCN+H$	-16	1.8	11.74	0.7	2460	[6]
13	$N_2O+O \rightarrow NO+NO$	-38	7.1	13.84	0	13400	[22]
14	$N_2O+O \rightarrow N_2+O_2$	-81	12.1	14.00	0	14100	[22]
15	$N_2+O \rightarrow N+NO$	+75	-10.3	14.26	0	38370	[22]
16	$NO+O \rightarrow N+O_2$	+32	-5.3	9.58	1.0	20820	[22]
17	$NCO+N \rightarrow N_2+CO$	-180	25.7	13.30	0	0	[44]
18	$NCO+N \rightarrow CN+NO$	-30	5.2	14.66	0	5530	[45][f]
20	$N_2O+H \rightarrow N_2+OH$	-65	10.8	13.88	0	7600	[22]
21	$NH+NO \rightarrow N_2O+H$	-28	2.3	12.03	0	230	[22]
22	$NO+H \rightarrow N+OH$	+48	-6.6	14.23	0	24560	[22]
23	$O_2+H \rightarrow OH+O$	+16	-1.2	17.57	-1.0	8810	[94]
24	$H_2+O \rightarrow H+OH$	+2	+0.1	10.26	1.0	4480	[94]
25	$H_2O+O \rightarrow OH+OH$	+17	-1.5	9.66	1.3	8605	[94]
26	$OH+H_2 \rightarrow H+H_2O$	-15	1.6	9.07	1.3	1825	[95]
27	$HCN+O \rightarrow NH+CO$	-39	5.6	8.73	1.2	3820	[16]
28	$HCN+O \rightarrow CN+OH$	+18	-1.8	13.70	0	11000	[72][g]
29	$HCN+OH \rightarrow H_2O+CN$	+1	-0.2	12.64	0	4530	[6]
30	$CN+OH \rightarrow NCO+H$	-18	1.4	13.75	0	0	[9]

Table 5.1 (continued)

Reactions	ΔH [a]	equil. const [b]	rate constants [c]			Source (Ref #)
			$\log_{10}A$	m	θ(°K)	
31 $C_2N_2+OH \rightarrow HNCO+CN$	−8	1.3	11.27	0	1450	[96][h]
36 $HNCO+H \rightarrow NH_2+CO$	−17	2.8	14.00	0	4280	[97]
37 $NH+H \rightarrow N+H_2$	−20	2.7	13.70	0	1000	[22]
38 $NH_2+H \rightarrow NH+H_2$	−11	2.2	13.28	0	0	[22]
39 $NCO+OH \rightarrow HNCO+O$	−12	0.9	13.30	0	0	estimate

[a] Heat of reaction at 1500°K (kcal/mole) [63], where $\Delta Hf_0°(CN)=101.2$ kcal/mole [24,63].

[b] $\log_{10}(k_{forward}/k_{backward})$ at 1500°K [63].

[c] Using the notation $k=A\ T^m \exp[-\theta/T]$ (cm^3/mole/sec).

[d] An activation energy of 2 kcal/mole was estimated for this reaction.

[e] An activation energy of 8 kcal/mole was estimated for this reaction. The form of the product (HNCO) is uncertain.

[f] Colket measured $k_{backward}=10^{14}\exp[-21190/T]$ (cm^3/mole/sec); the expression $k_f/k_b=4.54\ \exp[15660/T]$ was assumed.

[g] Upper limit value of k_{28}.

[h] The products of this slow reaction are uncertain.

As with the C_2N_2 mixtures (see ¶4.2.1), the relative NCO trace depends on the rate of NCO removal $k_5[O]+k_9[H]$, and the plateau NCO concentration (normalized by the concentration of the NCO source i.e., [HCN]) is given approximately by the ratio of the rate constants for the formation and removal steps,

$$\frac{[NCO]^{plateau}}{[C_2N_2]} \simeq 2\,\frac{k_2}{k_5} \quad \text{for the } C_2N_2 \text{ mixtures (see ¶4.2.1),} \qquad (5.1)$$

and $$\frac{[NCO]^{plateau}}{[HCN]} \approx \frac{k_8}{k_5 + k_9 \frac{[H]}{[O]}} \quad \text{for the HCN mixtures.} \tag{5.2}$$

Values of the steady-state concentrations of H- and O-atoms can be computed using the complete mechanism in Table 5.1. Under typical conditions for the HCN mixtures, $[H]/[O] \approx 1.6$.

By conducting HCN and C_2N_2 experiments under similar conditions of temperature and pressure, it is therefore possible to infer the ratio k_8/k_2 by comparing the respective NCO absorption plateaus. In the case of the simplified model,

$$\frac{[NCO]^{plateau}/[HCN]}{[NCO]^{plateau}/[C_2N_2]} \approx \frac{k_8}{2\,k_2} \times \frac{1}{1 + \frac{k_9}{k_5} \times \frac{[H]}{[O]}} \,. \tag{5.3}$$

This approach makes the measurement of k_8/k_2 nearly independent of the uncertainties associated with the absorption coefficient β that was reported in chapter 4.

In the actual data reduction, the computer program incorporating the mechanism in Table 5.1 was used to compare the theoretical NCO plateau levels in the HCN and C_2N_2 mixtures. For a given set of rate parameters in the mechanism, a proportionality constant λ was computed to relate the ratio of the theoretical NCO plateau levels in the two mixtures to the corresponding ratio k_8/k_2,

$$\lambda = \frac{k_2(T_1)}{k_8(T_2)} \times \frac{(\chi_{NCO}/\chi_{HCN})^{HCN\ mixt.}}{(\chi_{NCO}/\chi_{C_2N_2})^{C_2N_2\ mixt.}} \,. \tag{5.4}$$

T_1 and T_2 are the temperature of the C_2N_2 and HCN experiments, respectively ($T_1 \approx T_2$). In the case of the simplified model, note the approximate value of λ,

$$\lambda = \frac{0.5}{1 + \frac{k_9}{k_5}\frac{[H]}{[O]}} . \tag{5.5}$$

Using the theoretical value of λ (eq. 5.4), an experimental ratio (k_8^*/k_2^*) was extracted from the observed transmission plateaus (i/i_0) using

$$\frac{k_8^*}{k_2^*}(\bar{T}) = \frac{\ln(i/i_0)^{\text{HCN mixt.}}}{\frac{\beta(T_1)}{f_{00}} P_1 \chi_{HCN}} \times \frac{\frac{\beta(T_2)}{f_{00}} P_2 \chi_{C_2N_2}}{\ln(i/i_0)^{C_2N_2\text{ mixt.}}} \times \frac{1}{\lambda} , \tag{5.6}$$

where $\bar{T}$ is the average temperature $\bar{T}=(T_1+T_2)/2$. The resulting ratio k_8^*/k_2^* was then incorporated in the computer mechanism to calculate a new value of λ (eq. 5.4). Thus, a few iterative steps were required between eqs. (5.4) and (5.6) to extract the final value of k_8/k_2.

A computer analysis was performed to estimate the uncertainties in k_8/k_2 resulting from uncertain reaction rates in the mechanism. To this end, individual rates were adjusted by reasonable factors (Table 5.2), and new estimates of λ were computed that led to new values of k_8/k_2. According to this analysis, the uncertain knowledge of other rates in the mechanism (including k_5 and k_9) introduces an uncertainty of [×0.6, ×2.0] in the ratio k_8/k_2. (Note that the rate of reaction (9) was determined at 1490°K, see ¶5.2.) A reduction of the overall uncertainty in k_8/k_2 could be achieved with further optimization of reactant mixtures. In particular, an increased dilution of the HCN mixtures should result in an easier interpretation of the experiments. Further, oxygen addition should be avoided to prevent excessive OH formation from reaction (23),

$$O_2 + H \rightarrow OH + O, \tag{23}$$

and to limit the substantial uncertainties associated with the rate of reaction (39),

$$NCO + OH \rightarrow HNCO + O. \tag{39}$$

Table 5.2 - Uncertainty Analysis for k_8/k_2

Reactions	Uncertainty factors	effect on k_8/k_2
1 $N_2O+M \rightarrow N_2+O+M$	1.3	-3%
	0.6	+5%
3 $CN+O \rightarrow CO+N$	1.86	-2%
	0.54	+0%
4 $CN+O_2 \rightarrow NCO+O$	1.58	-7%
	0.71	+3%
5 $NCO+O \rightarrow CO+NO$	1.58	-20%
	0.54	+30%
6 $NCO+M \rightarrow N+CO+M$	5.0	-2%
	0.4	+3%
9 $NCO+H \rightarrow CO+NH$	2.6	+32%
	0.54	-17%
10 $NCO+H_2 \rightarrow HNCO+O$	2.5	+3%
	0.2	-3%
11 $C_2N_2+H \rightarrow CN+HCN$	3.2	+10%
	0.32	-20%
12 $CN+H_2 \rightarrow HCN+H$	2.0	-4%
	0.5	+1%
20 $N_2O+H \rightarrow N_2+OH$	1.6	-5%
	0.6	+3%
23 $O_2+H \rightarrow OH+O$	2.0	-7%
	0.5	+3%
27 $HCN+O \rightarrow NH+CO$	3.0	+22%
	0.3	-10%
29 $HCN+OH \rightarrow H_2O+CN$	10.	-16%
	0.1	+10%
37 $NH+H \rightarrow N+H_2$	10.	-20%
	0.1	+7%
39 $NCO+OH \rightarrow HNCO+O$	10.	+40%
	0.1	-13%

Table 5.2 (continued)

Reactions	Uncertainty factors	effect on k_8/k_2	
48 $NH+OH \rightarrow N+H_2O$	10.	-14%	
	0.1		+2%
49 $NH+O \rightarrow NO+H$	10.		+23%
	0.1	-7%	
Total uncertainty$=[\Sigma(\text{uncert.})^2]^{1/2}$		-49%	+70%

At temperatures near 1440°K, $k_8/k_2=2.4(-0.9,+2.4)$. Using the recommended value for $k_2=10^{12.66}\exp[-4440/T]$ cm^3/mole/sec [×0.54, ×1.86], $k_8=10^{11.70(-0.35,+0.40)}$ cm^3/mole/sec at 1440°K. Figure 5.1 shows the fit to a typical experimental trace using the recommended value of k_8 and other rates in Table 5.1. This determination of k_8 is plotted in Fig. 5.2 along with the earlier results of Roth, et al. [14], Davies and Thrush [15], and the recent data of Perry and Melius [16].

5.1.3 Discussion

Melius and Binkley [65] recently showed that the reaction of HCN with O atoms follows two major paths,

$$HCN + O \rightarrow \left({}^{H}_{N}C_{O}\right)^{\ddagger} \rightarrow \begin{cases} NCO + H & (8) \\ (HNCO)^{\ddagger} \rightarrow NH + CO. & (27) \end{cases}$$

A computed activation energy of $E_0^{\ddagger}=11$ kcal/mole at 0°K was also reported. Using transition state theory (TST), the temperature dependence of k_8 can be estimated as follows:

$$k_8 \propto \frac{kT}{h}\frac{Q_{\ddagger}}{Q_O\ Q_{HCN}}\exp[-E_0^{\ddagger}/RT] \ , \qquad (5.7)$$

where k, h and R are respectively the Boltzman, Planck and universal gas constants. $Q_{\ddagger}$ is the activated complex partition function (excluding the vibrational mode along the reaction coordinate); Q_O and Q_{HCN} are the partition functions of O-atoms and HCN, respectively. $E_0^{\ddagger}$ is the energy barrier at 0°K. Using $Q_O^{tr} \propto Q_{HCN}^{tr} \propto Q_{\ddagger}^{tr} \propto T^{3/2}$, $Q_{HCN}^{rot} \propto T^{2/2}$ and $Q_{\ddagger}^{rot} \propto T^{3/2}$ for the translational and rotational partition functions,

$$k_8 \propto \frac{Q_{\ddagger}^{vib}}{Q_{HCN}^{vib}} \exp[-E_0^{\ddagger}/RT] \ . \tag{5.8}$$

Table 5.3 - Estimated Normal Frequencies of $({}_N^H C_O)^{\ddagger}$

Vibrational modes	Frequencies (cm^{-1})	
	$({}_F^H C_O)$	$({}_N^H C_O)^{\ddagger}$
ν_1	2981	2090
ν_2	1837	-
ν_3	1343	940
ν_4	1065	750
ν_5	663	460
ν_6	1175	820

A reasonable estimate of $Q_{\ddagger}^{vib}$ can be obtained by modeling the activated complex $({}_N^H C_O)^{\ddagger}$ using the normal frequencies of the $({}_F^H C_O)$ molecule [66,67]. Table 5.3 summarizes the estimates of the normal frequencies $\nu_i^{\ddagger}$ of the activated complex [67]. Note that ν_2 is the normal mode along the reaction coordinate [66]. $({}_N^H C_O)^{\ddagger}$ is assumed a tight complex with $\nu_i^{\ddagger} \approx 0.7\nu_i$. Using the expression of Varghese for Q_{HCN}^{vib} [38], the temperature dependence of k_8 is calculated,

$$Q_{\ddagger}^{vib}/Q_{HCN}^{vib} \propto T \text{ and } k_8 \propto T \exp[-5540/T].$$

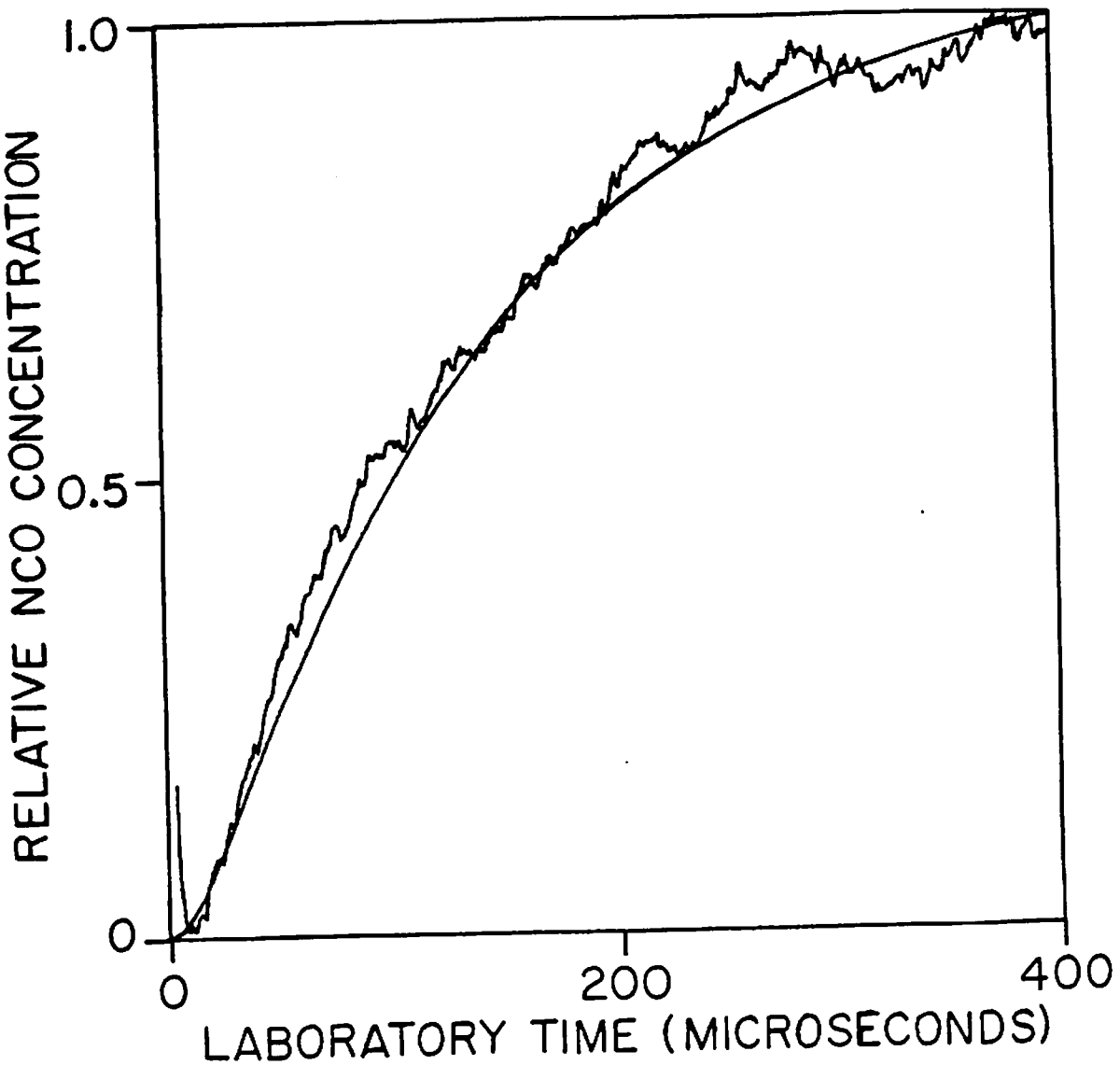

Fig. 5.1 Best computer fit to a typical NCO profile in a $HCN/O_2/N_2O$/argon experiment. The conditions are T_2=1425°K, p_2=0.60 atm, $HCN:O_2:N_2O:Ar$=7:1:8:984 and ρ_{21}=3.32. The plateau absorption of 4.2% corresponds to χ_{NCO}≈20 ppmv. The solid line is a best computer fit using the rates shown in Table 5.1.

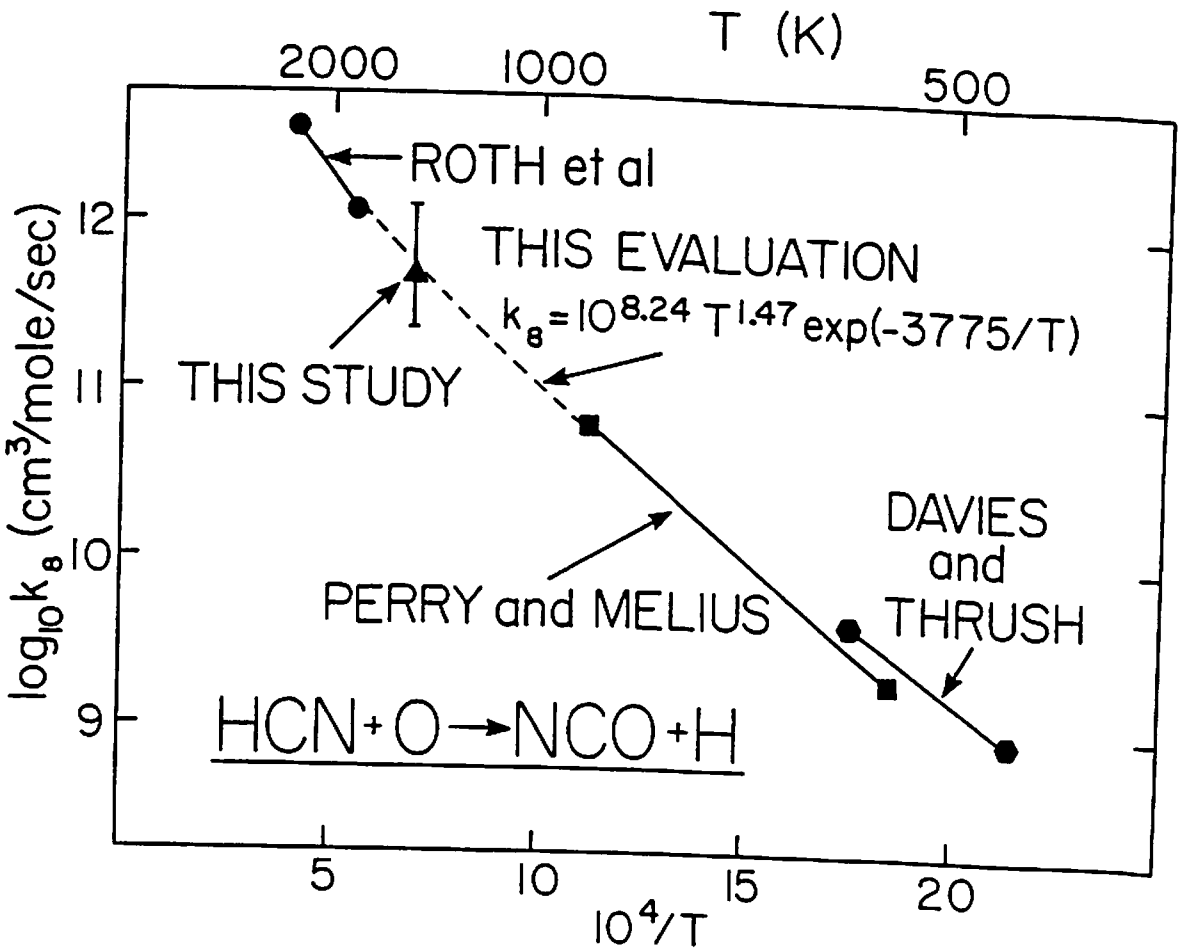

Fig. 5.2 Arrhenius plot for k_8. The abscissa shows reciprocal temperatures $10^4/T$ (K^{-1}).

The effective activation energy, $E=E_0^{\ddagger}+RT$, is therefore about 15.2 kcal/mole at 2100°K. This theoretical estimate agrees well with the reported activation energy of Roth, et al. (14.8 kcal/mole) [14].

Using transition state theory, and the results of Melius and Binkley [65], Perry and Melius [16] calculated the temperature dependence of k_8

$$k_8 \propto T^{1.47} \exp[-3775/T].$$

The corresponding temperature exponent m=1.47 is larger than the present estimate m=1, indicating smaller vibrational frequencies and a looser $({}_N^H C_O)^{\ddagger}$ complex. More importantly, Perry and Melius have assumed an activation energy $E_0^{\ddagger}\simeq 7.5$ kcal/mole to insure agreement with their experimental work in the range 540<T<900°K, a substantially lower value than the calculated $E_0^{\ddagger}=11$ kcal/mole. Nevertheless, the temperature dependence suggested by Perry and Melius is in excellent agreement with the three independent studies of Roth, et al. [14], Perry and Melius [16], and this study. For the purpose of providing a single expression for use over the temperature range 540<T<2500°K, the temperature dependence calculated by Perry and Melius was assumed and a least-squares fit expression was computed using the two end points of Roth, et al., the two end points of Perry and Melius, and one point from this study. On the basis of this analysis, the expression $k_8 \simeq 10^{8.24}\, T^{1.47} \exp[-3775/T]$ cm^3/mole/sec (±30%) is recommended in the range 540<T<2500°K.

It should be noted that this expression does not extrapolate well into the temperature range studied by Davies and Thrush [15]. The present recommended expression is lower than their value by about 50%. However, the value reported by Davies and Thrush should be interpreted as a total reaction rate (k_8+k_{27}) (despite their assumption that NCO and H are the most likely products of this reaction), since they did not treat reaction (8) as a specific path for the (HCN+O) reaction. Thus, the results of Davies and Thrush are in excellent agreement with the total rate (k_8+k_{27}) of Perry and Melius, who found $k_{27}/k_8=0.5$.

5.2 NCO reduction in $N_2O/O_2/H_2/C_2N_2$/argon mixtures

A mixture containing C_2N_2, O_2, H_2 and N_2O diluted in argon was shock heated at 1490°K to measure the rate constant of

$$NCO + H \rightarrow CO + NH, \tag{9}$$

and the ratio k_{11}/k_{12}

$$C_2N_2 + H \rightarrow CN + HCN, \tag{11}$$

$$CN + H_2 \rightarrow H + HCN. \tag{12}$$

In addition, this mixture led to an estimate for the rate constant of

$$NCO + H_2 \rightarrow HNCO + H. \tag{10}$$

5.2.1 Experimental Considerations

The mixture of H_2, O_2, N_2O, C_2N_2 and argon was shock heated with $\chi_{H_2} \approx 0.58\%$, $\chi_{O_2} \approx 0.09\%$, $\chi_{N_2O} \approx 0.41\%$, $\chi_{C_2N_2} \approx 0.40\%$, $T_2 \approx 1490°K$, $p_2 \approx 0.63$ atm, and $\rho_{21} \approx 3.34$. The shock speed was 1.18 mm/μsec, with attenuation of 1.5%/m. The temperature was set by considerations of growing interferences due to NCO removal by reaction (6) at higher temperatures

$$NCO + M \rightarrow N + CO + M, \tag{6}$$

and increasing uncertainty in the rate of reaction (1) at lower temperatures

$$N_2O + M \rightarrow N_2 + O + M. \tag{1}$$

Vibrational equilibrium of NCO was assumed in this experiment.

5.2.2 Reaction Mechanism, Results and Discussion

The mechanism shown in Table 5.1 was used in the data reduction, but a simplified model based on the following reactions is helpful in understanding the influence of k_9 and k_{11}/k_{12} on the measured NCO profile. As

before, N_2O decomposes first to provide O-atoms. The influx of O-atoms is sufficient to trigger reactions in the O/H system that lead to partial equilibrium concentrations of H, O and OH. Because of the relative proportions of O_2 and H_2 in the initial mixture, H is the dominant species in the O/H system [68] and reaction (11) becomes the major sink of C_2N_2

$$C_2N_2 + H \rightarrow CN + HCN. \tag{11}$$

The CN radicals formed by reaction (11) can in turn react with H_2 via reaction (12)

$$CN + H_2 \rightarrow HCN + H, \tag{12}$$

or react with O_2 to form NCO via reaction (4)

$$CN + O_2 \rightarrow NCO + O. \tag{4}$$

Finally, NCO is removed by H-atoms via reaction (9)

$$NCO + H \rightarrow NH + CO. \tag{9}$$

For the purpose of this simplified mechanism, it is assumed that CN has reached steady-state between reactions (11) and (12), and hence

$$\frac{[CN]^{\text{steady-state}}}{[C_2N_2]} \simeq \frac{k_{11}}{k_{12}} \times \frac{[H]^{\text{part.equil.}}}{[H_2]} . \tag{5.9}$$

Further, the rate of change of NCO concentration is given by

$$\frac{d[NCO]}{dt} \simeq k_4[CN][O_2] - k_9[NCO][H] . \tag{5.10}$$

If C_2N_2, O_2 and H_2 are nearly constant throughout the period of interest, the NCO profile peaks at a value ($d[NCO]/dt=0$) where, after substituting the above relation for $[CN]^{\text{steady-state}}$,

$$\frac{[NCO]^{peak}}{[C_2N_2]} = \frac{k_4}{k_9} \times \frac{k_{11}}{k_{12}} \times \frac{[O_2]}{[H_2]} \; . \qquad (5.11)$$

For this simplified model, the relative NCO profile (using the peak as a reference) depends primarily on the rate of reaction (9), since (after substituting the relation for $[CN]^{steady\text{-}state}$ in eq. 5.10)

$$\frac{d[NCO]/[NCO]^{peak}}{dt} = k_9[H][1 - [NCO]/[NCO]^{peak}] \; . \qquad (5.12)$$

The NCO peak concentration thus depends primarily on

$$\frac{k_4}{k_9} \times \frac{k_{11}}{k_{12}} \; ,$$

and the relative time behavior depends on k_9. A record of NCO is therefore sufficient to infer k_9; using the present recommandation for k_4 and the measured NCO peak concentration, the ratio k_{11}/k_{12} can also be inferred.

Table 5.4 - NCO Profile Sensitivity

Rates	Characteristic Features		
	Relative Slope	Peak Concentration	Relative Decay
k_9 ↑ (×2)	↑	↓ (×0.64)	↔
(k_{11}/k_{12}) ↑ (×2)	↑	↑ (×1.42)	↑
k_{10} ↑ (×2)	↓	↓ (×0.82)	↔

Legend
↑ increasing value
↓ decreasing value
↔ no variation.

Despite the apparent simplicity of this model, it was necessary to use a computer fitting technique to further explain the influence of key rate parameters on the NCO profile. In particular, despite the small value of k_{10}, the experimental time histories cannot be adequately fitted without accounting for reaction (10)

$$NCO + H_2 \rightarrow HNCO + H, \tag{10}$$

because of the large quantities of H_2 present in the mixture. It was assumed that the products of reaction (10) are HNCO+H (ΔH=-10 kcal/mole at 1500°K), rather than the thermodynamically favored NH_2+CO (ΔH=-27 kcal/mole at 1500°K), because the path to NH_2+CO requires a complex rearrangement of the molecular bonds. Using the computer, three features of the NCO profile were identified which could be simultaneously fitted to yield the three rate parameters of interest, namely k_9, k_{11}/k_{12} and k_{10}. These three features are the absolute peak NCO concentration, the relative initial slope and the relative decay of the NCO profile (using the peak as a reference). Figure 5.3 shows a best computer fit to the experimental trace. The computed effects of variations in k_9, k_{11}/k_{12} and k_{10} on the three features are illustrated in Table 5.4. For example, this table shows that an increase (↑) in k_{11}/k_{12} would result in increases (↑) in relative initial slope and absolute peak concentration, and to a faster relative decay of the NCO profile.

Figure 5.4 illustrates the effect of k_{11}/k_{12} on the relative NCO profile. Note from Table 5.4 that k_9 and k_{10} both have similar effects on the absolute peak concentration, but opposite effects on the relative initial slope; further, k_9 and k_{10} do not substantially influence the relative decay. It therefore appears possible to determine k_9, k_{11}/k_{12} and k_{10} by fitting the NCO trace alone. A unique value for k_{11}/k_{12} can fit the relative decay and a unique set of values for k_9 and k_{10} can simultaneously fit the relative initial slope and the absolute peak concentration. Figure 5.5 illustrates the effect of k_9 on the relative NCO profile. Additional considerations on the data reduction procedure can be found in Appendix 6.

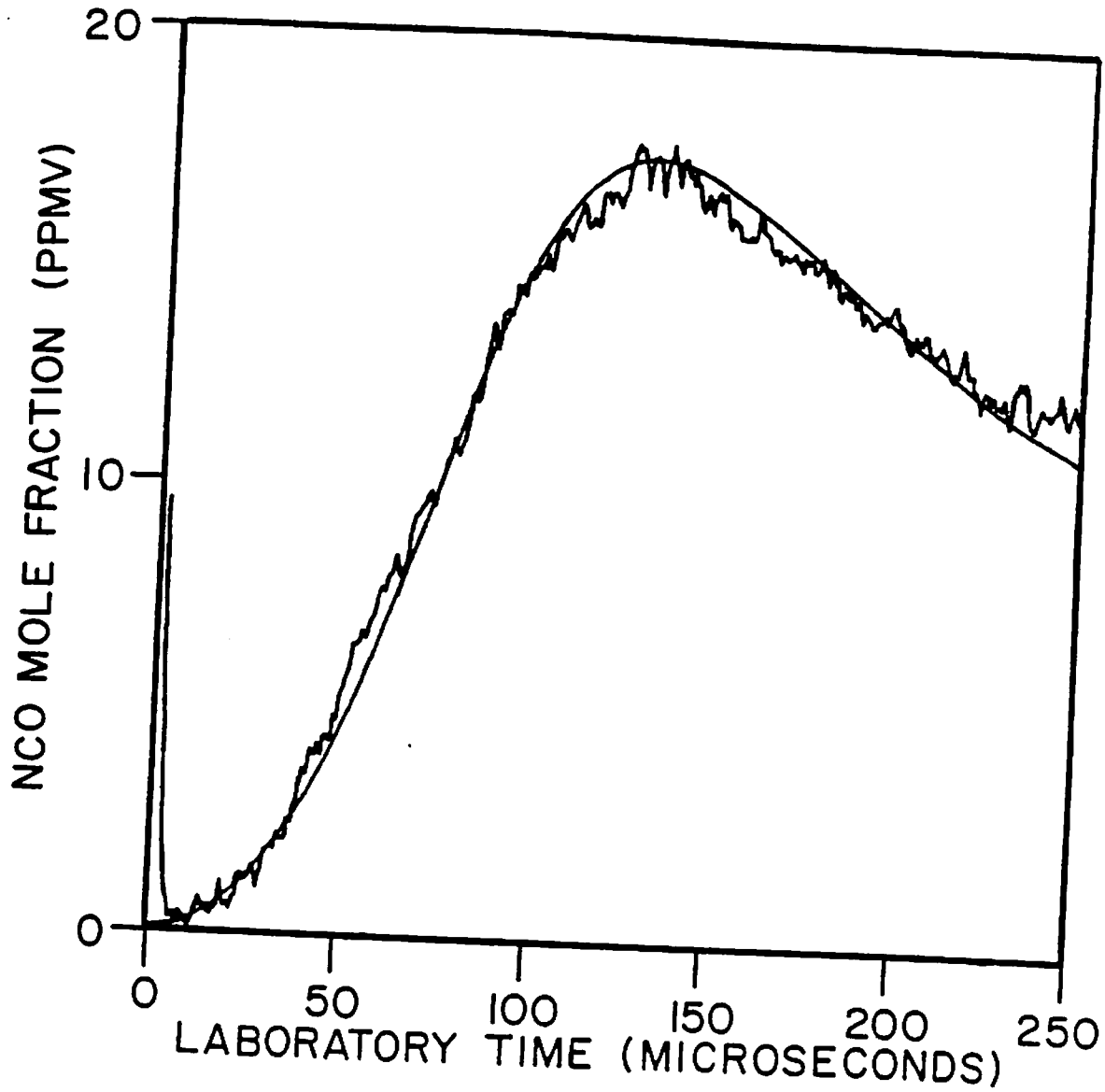

Fig. 5.3 Best computer fit to an NCO profile in a $C_2N_2/O_2/H_2/N_2O$/argon experiment. The conditions are T_2=1490°K, p_2=0.63 atm, N_2O:O_2:H_2:C_2N_2:Ar=4:1:6:4:985 and ρ_{21}=3.34. The peak absorption of 3.3% corresponds to χ_{NCO}=17 ppmv with β=103 cm^{-1} atm^{-1}. The solid line is a best computer fit to the data using k_9= $10^{13.73}$ cm^3/mole/sec, k_{11}/k_{12}=0.81, k_{10}=$10^{12.1}$ cm^3/mole/sec and other rates in Table 5.1.

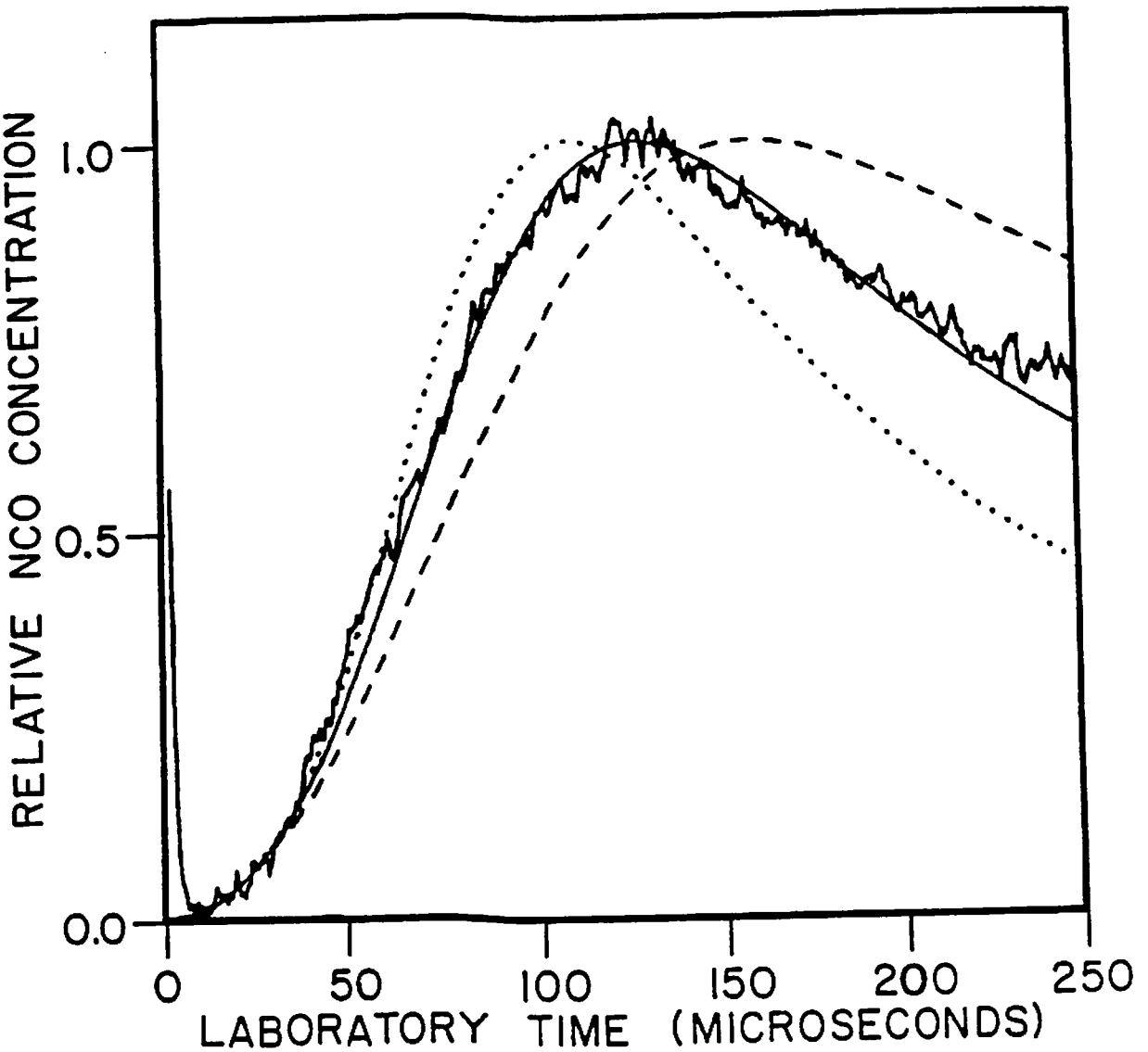

Fig. 5.4 Sensitivity of the relative NCO time-history to excursions in the ratio k_{11}/k_{12}. The conditions are similar to Fig. 5.3. The dotted line (• • •) corresponds to $k_{11}/k_{12} \times 2.0$ and the dashed line (- -) to $k_{11}/k_{12} \times 0.5$.

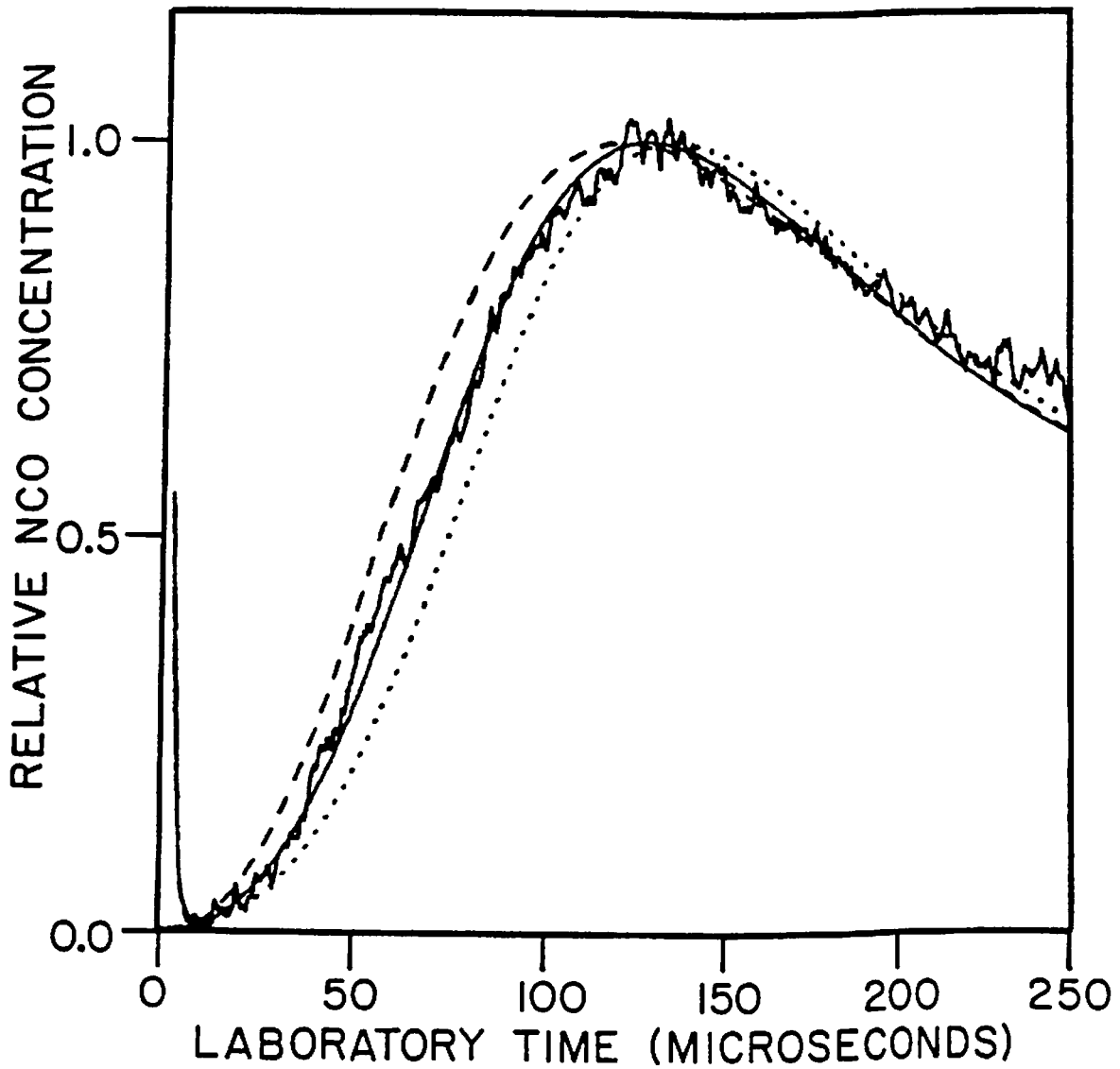

Fig. 5.5 Sensitivity of the relative NCO time-history to excursions in k_9. The conditions are similar to Fig. 5.3. The dotted line (•••) corresponds to $k_9 \times 0.5$ and the dashed line (– –) to $k_9 \times 2.0$.

Table 5.5 - Uncertainty Analysis for k_9, k_{10} and k_{11}/k_{12}

Reactions	Uncert. factors	effect on					
		k_9		k_{10}		k_{11}/k_{12}	
1 $N_2O+M \rightarrow N_2+O+M$	1.3	-11%				-26%	
	0.6		+16%				+25%
2 $C_2N_2+O \rightarrow CN+NCO$	1.86		+10%				
	0.54	-7%					
3 $CN+O \rightarrow CO+N$	1.86	-3%					
	0.54		+2%				
4 $CN+O_2 \rightarrow NCO+O$	1.58		+2%			-51%	
	0.71	-2%					+39%
5 $NCO+O \rightarrow CO+NO$	1.55	-17%					
	0.54		+13%				
6 $NCO+M \rightarrow N+CO+M$	5.0	-2%					
8 $HCN+O \rightarrow NCO+H$	2.5		+9%				
	0.44	-5%					
11 $C_2N_2+H \rightarrow HCN+CN$	0.48 [a]		+15%				+39%
12 $CN+H_2 \rightarrow HCN+H$	6.0 [b]	-36%				-45%	
20 $N_2O+H \rightarrow N_2+OH$	1.6	-5%					
	0.6		+4%				
23 $O_2+H \rightarrow O+OH$	2.0	-9%				-18%	
	0.5		+10%				+18%
24 $H_2+O \rightarrow H+OH$	2.0	-13%				-27%	
	0.5		+14%				+28%

Table 5.5 (continued)

Reactions	Uncert. factors	effect on					
		k_9		k_{10}		k_{11}/k_{12}	
26 $OH+H_2 \rightarrow H+H_2O$	2.0	-13%				-11%	
	0.5		+14%				+11%
30 $CN+OH \rightarrow NCO+H$	10.		+34%				
	0.1	-26%				-18%	
Absorption coeff.	2.1		+73%		+91%		
β	0.55	-29%		-133%			
Total unc.=$[\Sigma(\text{unc.})^2]^{1/2}$		-61%	+89%	-133%	+91%	-82%	+70%

[a] Lower bound from the experimental value of Smith, et al. [98].
[b] Upper bound in Baulch, et al. [13].

On the basis of this analysis, $k_9 = 10^{13.73(+0.42,-0.27)}$ $cm^3/mole/sec$, $k_{11}/k_{12} = 0.81$ (+0.89,-0.47) and $k_{10} = 10^{12.1(+0.4,-0.7)}$ $cm^3/mole/sec$ at 1490°K. Table 5.5 summarizes the uncertainty analysis. Uncertainties in k_9 result from the uncertain knowledge of other reactions in the mechanism [×1.7, ×0.57] and the uncertainty in the measured NCO peak concentration resulting in uncertainty factors in k_9 of [×2.1, ×0.75]. Uncertainties in k_{11}/k_{12} are attributed primarily to the uncertain knowledge of other rates [×2.1, ×0.42], because no absolute knowledge of the NCO concentration was required to fit the relative decay slope to k_{11}/k_{12}. Uncertainties in k_{10} are fairly large [×2.5, ×0.2] and can be attributed mostly to the uncertainty in the absolute peak NCO concentration. A significant reduction in the overall uncertainty on k_9 and k_{10} could be achieved if a more precise value of β(1490°K) were available.

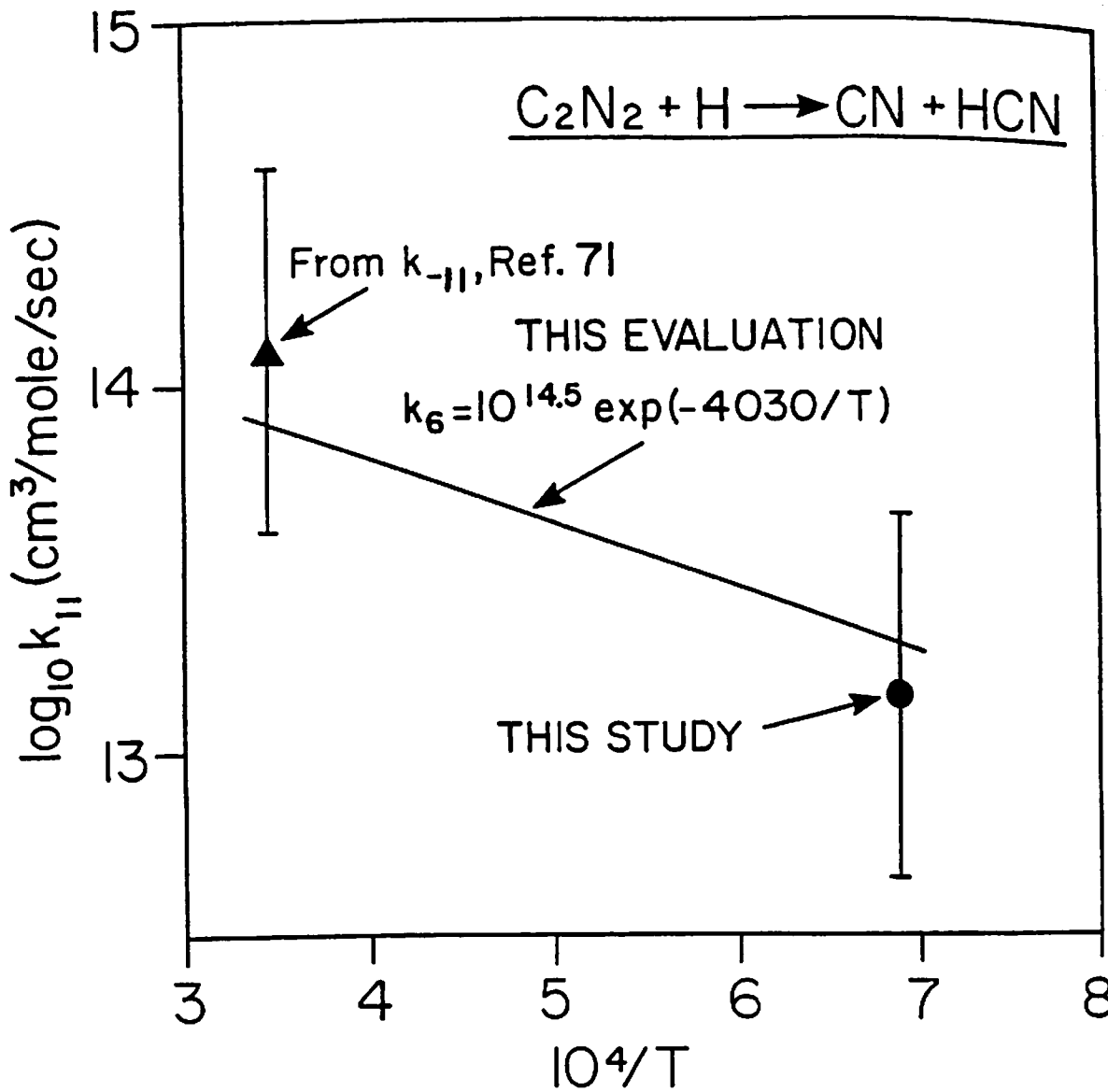

Fig. 5.6 Arrhenius plot for k_{11}. The abscissa shows reciprocal temperatures $10^4/T$ (K^{-1}). The high-temperature data point (solid triangle) was calculated from the measurement of Szekely, et al. [71,72].

There are no previous data of k_9 and k_{10} available for comparison. The Theoretical Chemistry Group at Argonne National Laboratory has recently performed calculations of the temperature dependence of k_{12}, which will be published in the near future. In addition, Miller, et al. [6] proposed the following expression for k_{12} based on the measurements of Szekely, Hanson and Bowman [69] in the range 2700<T<3500°K and Albers, et al. [70] at lower temperatures: $k_{12} = 10^{11.74}T^{0.7}\exp[-2460/T]$ cm^3/mole/sec. Judging from the error bars attached to the high- and low-temperature data, the above expression should be valid within a factor of two at 1490°K. Using the present measurement of k_{11}/k_{12}, this expression leads to $k_{11} = 10^{13.15(\pm 0.5)}$ cm^3/mole/sec at 1490°K. Another estimate of k_{11} can be obtained from the reverse rate k_{-11} measured by Szekely, Hanson and Bowman [71] at high temperatures, with the result $k_{11} = 10^{14.1(\pm 0.5)}$ cm^3/mole/sec at the average temperature of 2900°K [72]. Figure 5.6 is an Arrhenius plot of k_{11}. Using the two values of k_{11} at 2900°K and 1490°K, a straight Arrhenius fit would lead to $k_{11} = 10^{15.1}\exp[-6700/T]$ cm^3/mole/sec. However, the corresponding activation energy and pre-exponential factor of the fit appear too high for this mildly endothermic reaction (ΔH_R<5.3 kcal/mole at 2000°K [24,63]). A more realistic activation energy of 8 kcal/mole leads to the expression $k_{11} = 10^{14.5}\exp[-4030/T]$ cm^3/mole/sec. This straight Arrhenius fit is somewhat arbitrary, since reaction (11) may exhibit a non-Arrhenius behavior. However, the size of the experimental error bars and the uncertainties arising from an unknown $(HC_2N_2)^{\ddagger}$ complex makes a more sophisticated TST calculation superfluous. Further experimental work is clearly needed for this reaction. Until better values are found, the expression $k_{11}=10^{14.5}\exp[-4030/T]$ cm^3/mole/sec is recommended within factors of [×3.2, ×0.32] over the range 1490<T<3070°K.

5.3 Conclusions

A comparison of the plateau levels of NCO resulting from the oxidation of hydrogen cyanide and cyanogen provided a high temperature measurement of the rate of

$$HCN + O \rightarrow NCO + H. \tag{8}$$

By adding molecular hydrogen to the $C_2N_2/N_2O/O_2$/argon mixtures studied in chapters 2 and 3, other experiments were conducted at 1490°K to infer the rates of

$$NCO + H \rightarrow CO + NH, \tag{9}$$

$$NCO + H_2 \rightarrow HNCO + H, \tag{10}$$

and the ratio k_{11}/k_{12}

$$C_2N_2 + H \rightarrow CN + HCN, \tag{11}$$

$$CN + H_2 \rightarrow H + HCN. \tag{12}$$

Reactions (8), (9), (10) and (12) are important in the fuel-nitrogen mechanism (see Appendix 8).

Chapter 6

Conclusions

In an effort to elucidate nitric oxide formation in the combustion of nitrogen-containing fuels, the present study has focused on the measurement of elementary reaction rate constants in the conversion of hydrogen cyanide to amine species. To this end, spectroscopic absorption diagnostics have been developed to measure CN and NCO concentrations in the shock tube. Using these diagnostics, the following reactions have been studied:

$$C_2N_2 + O \rightarrow CN + NCO, \quad (2)$$
$$CN + O \rightarrow CO(v) + N, \quad (3)$$
$$CN + O_2 \rightarrow NCO + O, \quad (4)$$
$$NCO + O \rightarrow CO + NO, \quad (5)$$
$$NCO + M \rightarrow N + CO + M, \quad (6)$$
$$HCN + O \rightarrow NCO + H, \quad (8)$$
$$NCO + H \rightarrow NH + CO, \quad (9)$$
$$NCO + H_2 \rightarrow HNCO + H, \quad (10)$$
$$C_2N_2 + H \rightarrow CN + HCN. \quad (11)$$

Table 6.1 is a summary of the kinetics results and recommended rate expressions.

A computer model incorporating the experimental rate measurements and the best kinetic data available was used to discuss the overall fuel-nitrogen mechanism and formulate recommendations for future research (see Appendix 8). According to the model, a few reactions with little or no available rate data may be important in the HCN to NH_i conversion,

$$HCN + OH \rightarrow CN + H_2O, \quad (29)$$
$$CN + OH \rightarrow HNCO + O, \quad (30)$$
$$NCO + OH \rightarrow HNCO + O, \quad (39)$$

and possibly

$$HCN + OH \rightarrow HOCN + H. \quad (56)$$

Table 6.1 - Summary of Results and Recommended Rate Constants

Reactions	Experiments		Recommendation		
	Temp.	Result [a]	Rate Expression	Uncert. [b]	T-range
2 $C_2N_2+O \rightarrow CN+NCO$	2000	11.70(+0.25,-0.19)	$10^{12.66}\exp[-4440/T]$	±60%	300÷2100
3 $CN+O \rightarrow CO(v=1)+N$	2000	13.26(±0.26)	$10^{13.31}\exp[-210/T]$	±60%	300÷2100
4 $CN+O_2 \rightarrow NCO+O$	2400	12.68(+0.27,-0.19)	$10^{12.75}$	±45%	300÷2400
5 $NCO+O \rightarrow CO+NO$	1450	13.75(+0.20,-0.26)	$10^{13.75}$	±60%	300÷2000
6 $NCO+M \rightarrow N+CO+M$	2150	3.36(±0.27) [c]	$10^{16.8}T^{-0.5}\exp[-24000/T]$	±90%	2150÷2400
	2240	3.54(+0.34,-0.37) [c]			
	2400	2.69(±0.28) [c]			
8 $HCN+O \rightarrow NCO+H$	1440	0.38(+0.30,-0.20) [d]	$10^{8.24}T^{1.47}\exp[-3775/T]$	±30%	500÷2500
9 $NCO+H \rightarrow CO+NH$	1490	13.73(+0.42,-0.27)	$10^{14.02}\exp[-1000/T]$	±80%	≈1500
10 $NCO+H_2 \rightarrow HNCO+H$	1490	12.1(+0.4,-0.7)	$10^{13.23}\exp[-4000/T]$	±100%	≈1500
11 $C_2N_2+H \rightarrow CN+HCN$	1490	-0.09(+0.32,-0.38) [e]	$10^{14.5}\exp[-4030/T]$	±110%	1490÷3000

[a] $\log_{10}k$ (cm^3/mole/sec).
[b] $\ln F$, with F=recommended uncertainty factor, see ¶ A6.3.
[c] $\log_{10}(k_5/k_6)$; experiments were carried out at p_2=0.65 atm.
[d] $\log_{10}(k_8/k_2)$.
[e] $\log_{10}(k_{11}/k_{12})$.

The NCO laser absorption diagnostic should be useful to investigate these reactions. Other unknown reactions control nitric oxide production and thus deserve further experimental work,

$$NH + H \rightarrow N + H_2, \tag{37}$$

$$NH + OH \rightarrow HNO + H, \tag{47}$$

$$NH + OH \rightarrow N + H_2O. \tag{48}$$

In Appendix 8, it was suggested that the formation of HCN in the reaction zone should also contribute to the overall production of nitric oxide. Thus, reactions to form the C≡N triple bond might receive additional attention in an attempt to understand the production of HCN from fuel-nitrogen in the reaction zone.

Further experimental challenges will be encountered on the way to a complete understanding of the fuel-nitrogen mechanism. The shock tube should again prove a valuable tool for studying elementary reactions involved in this important environmental question.

Appendix 1

Experimental Conditions in the Shock Tube

The experimental post-shock pressure and temperature are computed from measurements of the shock velocities using time-interval counters. Control of these conditions can be achieved with reasonable reproducibility by choosing the proper diaphragm thickness and adjusting the initial test gas pressure p_1. In section A1.1 of this appendix, a semi-empirical correlation to determine the value of p_1 that corresponds to the desired post-shock conditions is presented. In section A1.2, an estimate of the uncertainties in T_2 and p_2 that result from the observed attenuation of the shock velocity is provided.

A1.1 Semi-Empirical Correlation for the Post-Shock Conditions

A sketch of a typical incident shock experiment is given in Fig. A1.1. For a one-dimensional shock, the instantaneous ratios of pressure and temperature across the shock wave can be expressed as a function of Mach number using normal shock relations [76]

$$\frac{p_2}{p_1} = p_{21} = \frac{2\gamma_1}{\gamma_1+1} \times M^2 - \frac{\gamma_1-1}{\gamma_1+1}, \tag{A1.1}$$

$$\frac{T_2}{T_1} = T_{21} = \frac{\left(1 + \frac{\gamma_1-1}{2} M^2\right)\left(\frac{2\gamma_1}{\gamma_1-1} M^2 - 1\right)}{\frac{(\gamma_1+1)^2}{2\,(\gamma_1-1)} M^2}. \tag{A1.2}$$

For an ideal shock wave without attenuation or boundary layer effects, the pressure ratio p_{41} across the diaphragm is related to p_{21} using [77]

$$\frac{p_{41}}{p_{21}} = \left(1 - \frac{a_1}{a_4}(\gamma_4-1)\frac{p_{21}-1}{\sqrt{2\gamma_1}\sqrt{\left((\gamma_1+1)\,p_{21} + (\gamma_1-1)\right)}}\right)^{-\frac{2\gamma_4}{\gamma_4-1}}. \tag{A1.3}$$

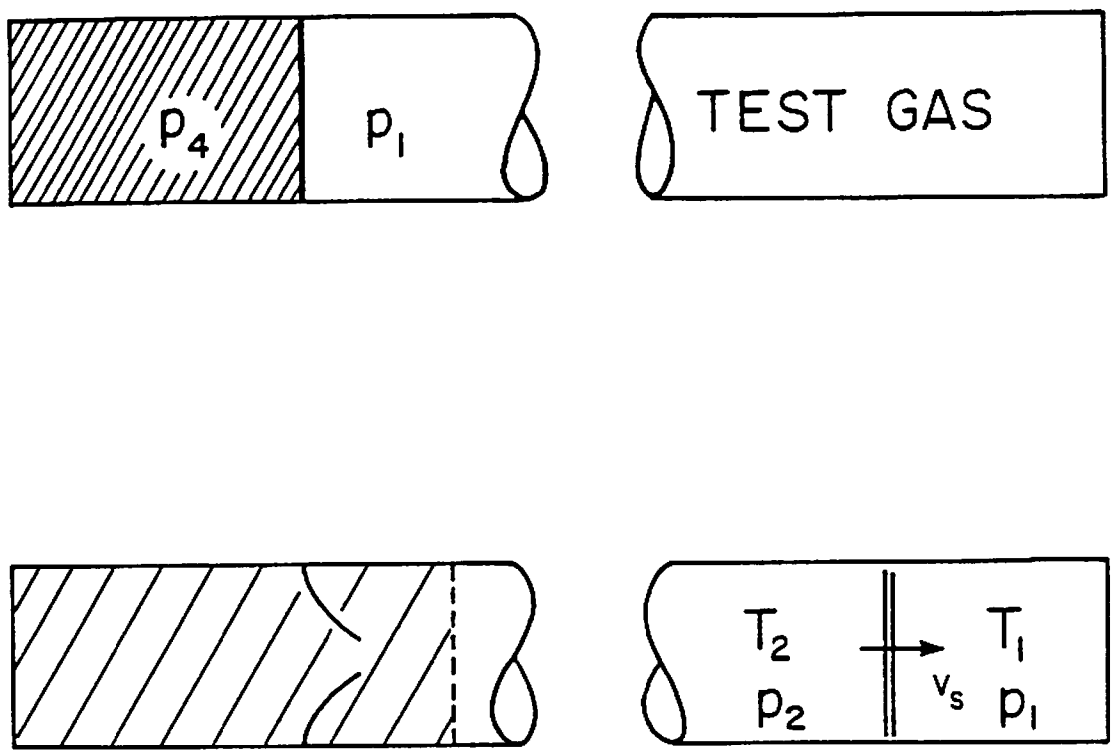

Fig. A1.1 A schematic of a typical incident shock wave experiment.

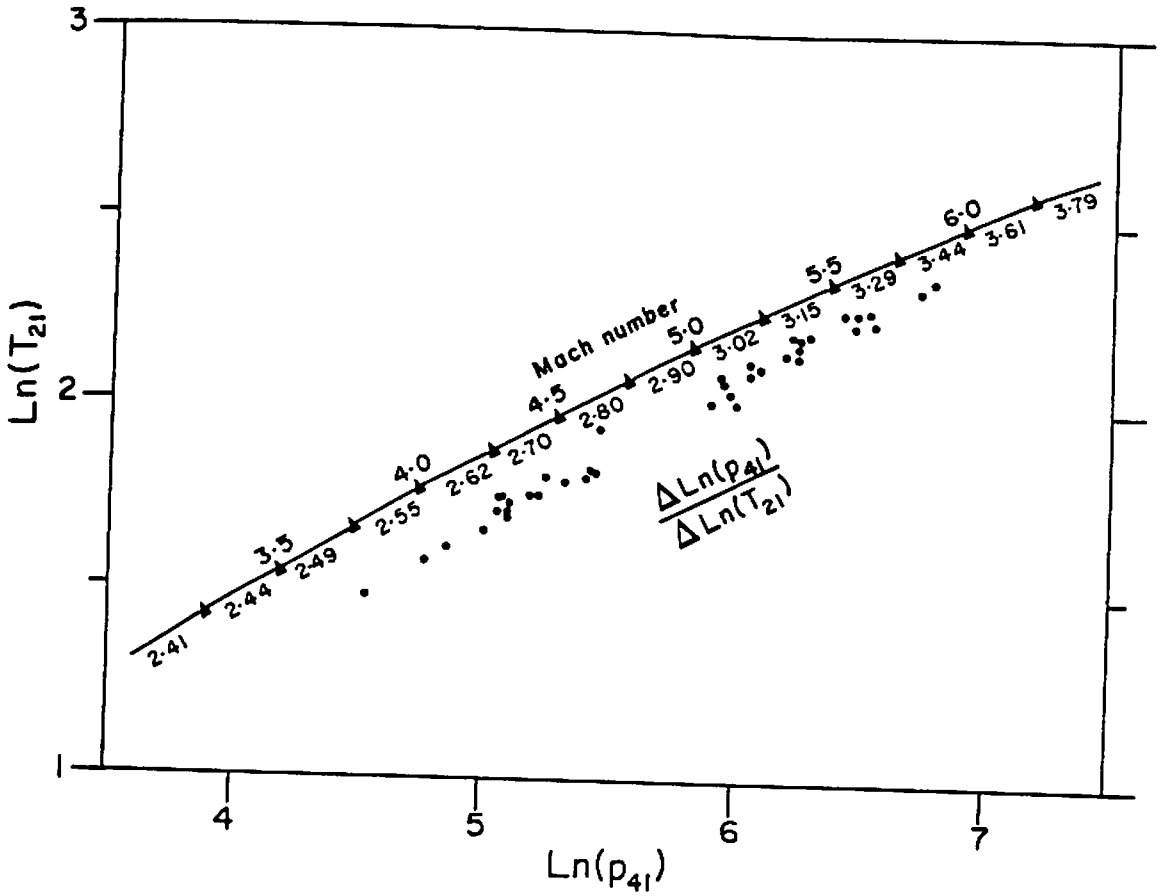

Fig. A1.2 Operating characteristic curve for the shock tube. Plot of the temperature ratio across the incident shock T_{21} vs. pressure ratio across the diaphragm p_{41}. Natural logs have been used on both axes. The Mach numbers M and average slopes $\Delta \ln p_{41}/\Delta \ln T_{21}$ are indicated on the theoretical curve. Note that the experimental points (•) fall on a curve nearly parallel to the theoretical prediction.

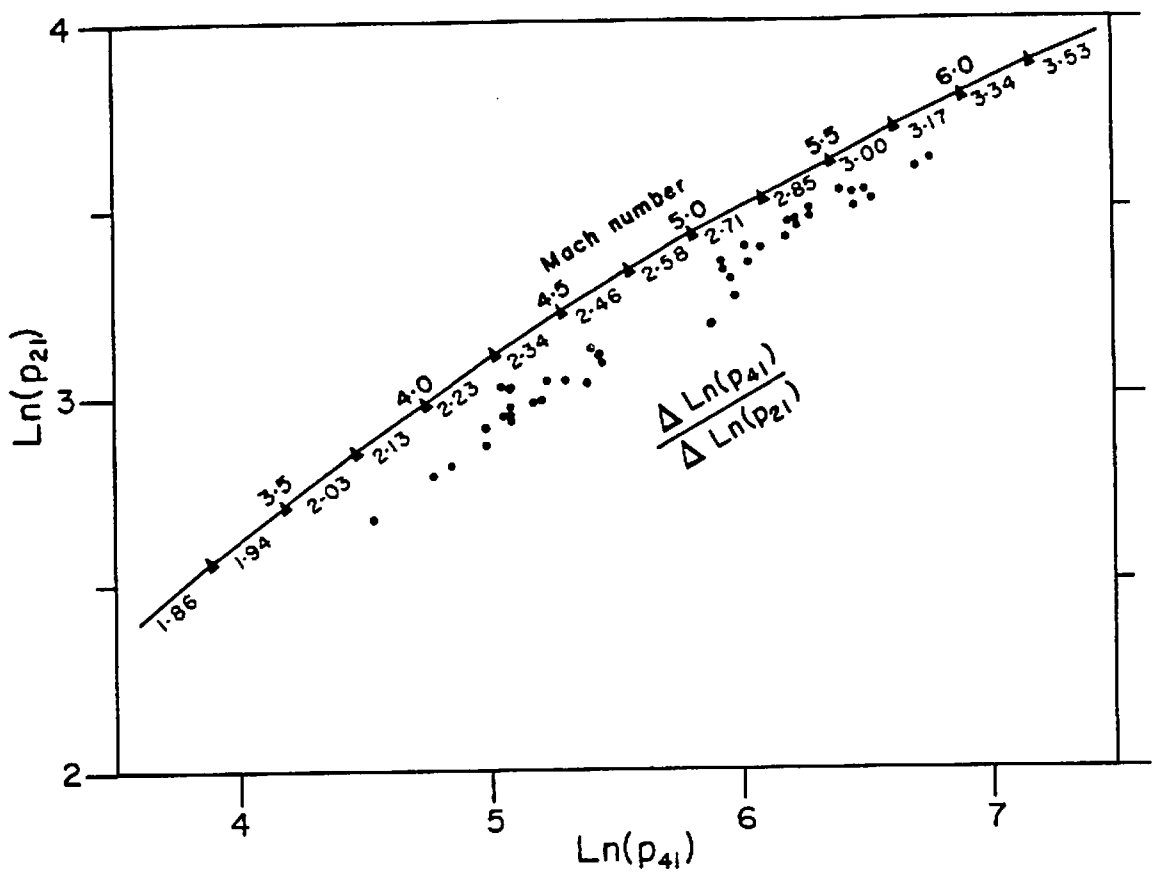

Fig. A1.3 Operating characteristic curve for the shock tube. Plot of the pressure ratio across the incident shock p_{21} vs. pressure ratio across the diaphragm p_{41}. Note the Mach numbers M and the average slopes $\Delta \ln p_{41}/\Delta \ln p_{21}$.

The speed of sound is $a_i=(\gamma_i R_i T_i)^{1/2}$, where $R_i = R/MW_i$ and $T_1=T_4=T_{ambient}$; R is the universal gas constant, MW_i the mixture averaged molecular weight ($MW_i=\Sigma\ X_j\ MW_j$) and γ_i the ratio of specific heats.

For simplicity, it is assumed that helium is the driver gas and argon is the test gas ($\gamma_4=\gamma_1=5/3$, $MW_1=40$ g/mole and $MW_2=4$ g/mole). The resulting theoretical curves for $\ln T_{21}=f(\ln p_{41})$ and $\ln p_{21}=f(\ln p_{41})$ are shown in Fig. A1.2 and A1.3. Each point corresponds to increments of 0.25 in the shock Mach number. Note that individual values for the average slopes $\Delta\ln p_{41}/\Delta\ln T_{21}$ and $\Delta\ln p_{41}/\Delta\ln p_{21}$ are also indicated.

Table A1.1 - Typical Diaphragm Bursting Pressures

Diaphragm Thickness (1/1000")	Typical bursting pressure p_4 (psia)
10	35→40
20	65→75
30	105→120
40	120→145
60	230→250
80	≈260
40+10	160→180
60+10	≈270
20+20	≈140
40+30	≈230

To check the validity of this simple correlation, typical experimental conditions are also shown in Figs. A1.2 and A1.3. Note that p_4 was measured on the driver gauge at the burst of the diaphragm; p_1 was calculated from the relative volumes of the mixing tank and the shock

tube [p_1 (Torr) = 0.309 $p_{mix.tank}$ ("Hg)]; T_1 was measured on a thermometer attached to the test section; p_2 and T_2 were computed using a comprehensive software package that accounts for the initial test gas composition. Despite the great variety of test gas mixtures, the experimental points in Figs. A1.2 and A1.3 consistently fall on curves nearly parallel to the simple correlation of eqs. (A1.1) to (A1.3). The theoretical slopes can therefore be used to adjust p_{41} for better experimental conditions. For example, if a 2% increase in T_{21} ($\Delta \ln T_{21} \simeq 0.02$) is required to adjust the temperature of an experiment with M=4, we need $\Delta \ln p_{41} \simeq 2.62 \times 0.02$ or a 5% increase in p_{41}. Note that the bursting pressures p_4 depend on the precise location of the knife-edge and on the diaphragm thickness. For the current knife-edge configuration, typical bursting pressures are shown in Table A1.1. Together with Figs A1.2 and A1.3, these pressures can be used to adjust p_1.

A1.2 Uncertainties Associated with the Shock Attenuation

Shock attenuation has been observed in nearly all experiments. The weaker the shock, the stronger the attenuation. The average shock speed recorded in consecutive cross-sections bracketed by two thin-film gauges was found to decrease linearly with centerline position of the section, as shown in Fig. A1.4. Theoretical estimates of the uncertainties associated with boundary layer and attenuation effects have been reported by Mirels [20] and De Boer and Miller [21]. However, the following description can provide simple estimates of the effect of attenuation on post-shock temperature and pressure. In this description, the fate of a small collection of molecules is examined from the time it is hit by the shock to the time it traverses the optical diagnostic port (see Fig. A1.5).

The molecules in question are heated by the shock at time t_0. At time $t_1 \simeq t_0 + x/v_s$, the experiment begins as the shock traverses the measurement station. At time $t_2 = t_0 + x/u_2$, the molecules are probed at the diagnostic port. (v_s and u_2 are the average velocities of the shock and the post-shock gases, respectively.) With t_1 as the reference time, the collection of molecules is probed at $t = t_2 - t_1 = x(1/u_2 - 1/v_s)$ after the shock traverses the optical port.

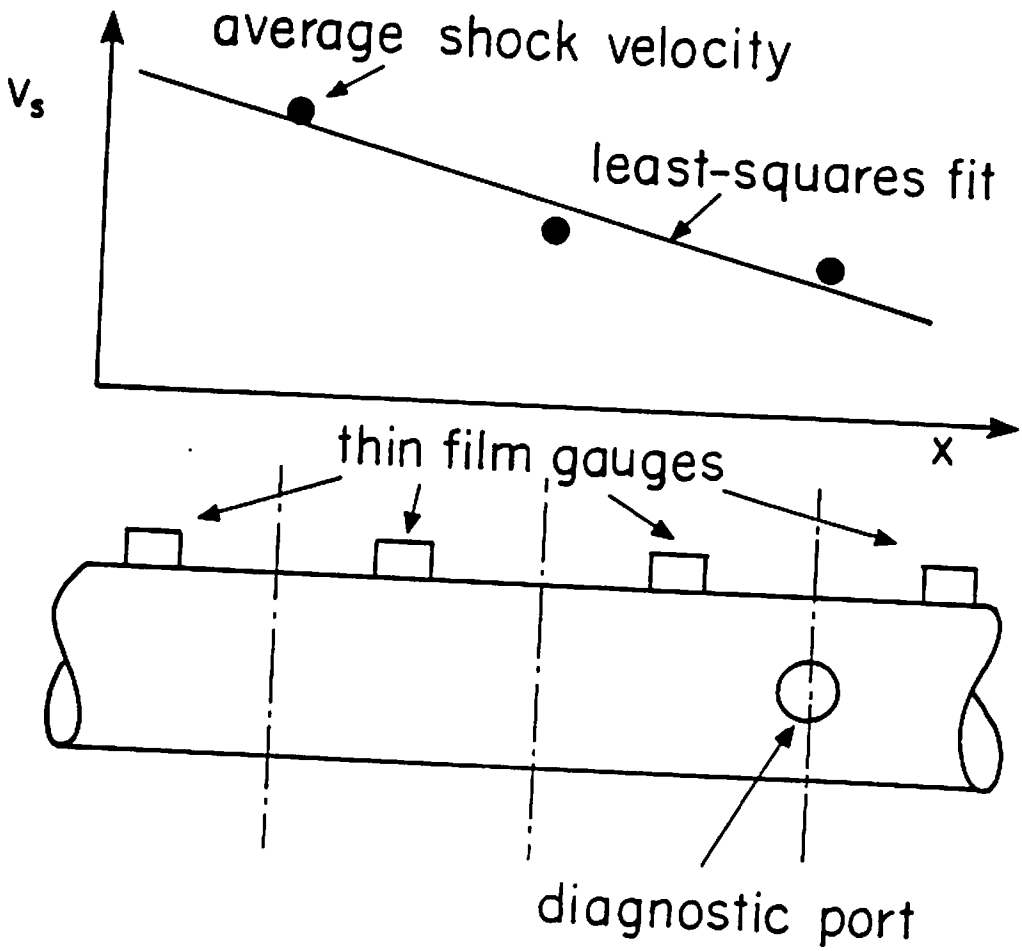

Fig. A1.4 A schematic of the shock attenuation.

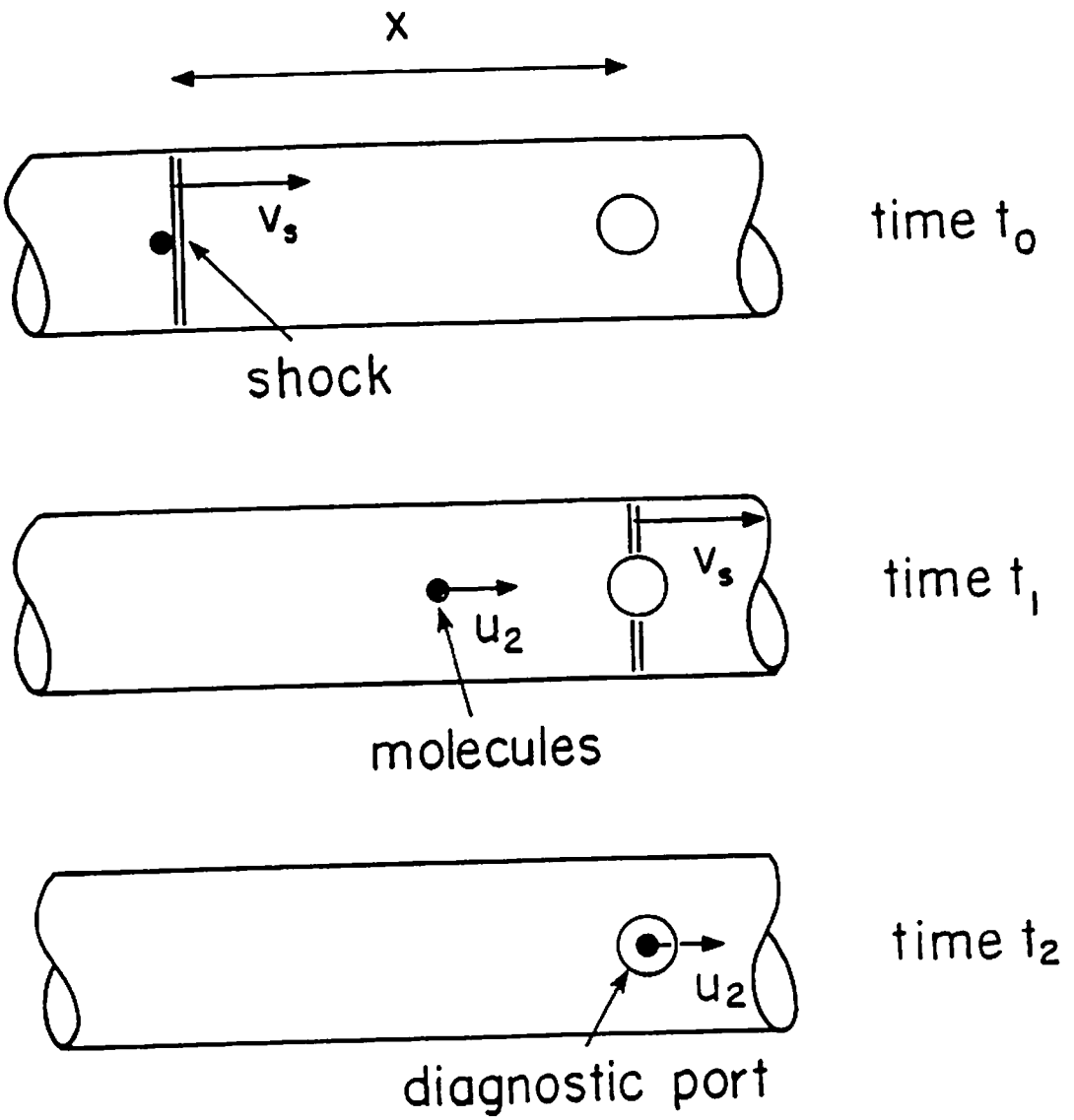

Fig. A1.5 A schematic of the effect of shock attenuation on a collection of molecules.

Nominal experimental conditions (T_2 and p_2) are computed using the measured shock velocity at t_1. However, the collection of molecules were heated at t_0 by a stronger shock that resulted in greater values of T_2 and p_2. Using the measured shock velocities at different locations, the resulting systematic error in p_2 and T_2 can be estimated using the observed shock attenuation. For a linear attenuation, the absolute velocity change Δv_s over the distance x can be written $\Delta v_s = ax$, where a is the slope of the graph shown in Fig. A1.4. Therefore, the shock velocity at t_0 is greater than the nominal velocity by the amount $\Delta v_s / v_s$

$$\frac{\Delta v_s}{v_s} = \frac{ax}{v_s} = \frac{at}{\frac{v_s}{u_2} - 1} = \frac{\Delta M}{M}, \tag{A1.4}$$

where M is the shock Mach number. Using mass conservation,

$$\rho_{21} = v_s/(v_s - u_2), \tag{A1.5}$$

where ρ_{21} is the ratio of densities across the shock. Therefore, a collection of molecules probed at t (post-shock laboratory time) has experienced a stronger shock wave with

$$\frac{\Delta M}{M} = a\ t\ (\rho_{21} - 1)\ . \tag{A1.6}$$

By differentiating eqs. (A1.1) and (A1.2), an estimate of the relative increase in temperature and pressure corresponding to $\Delta M/M$ is obtained

$$\frac{d\ln T_{21}}{d\ln M} = \frac{(\gamma_1 - 1)\ M^2}{1 + \frac{\gamma_1 - 1}{2} M^2} + \frac{\frac{4\ \gamma_1}{\gamma_1 - 1} M^2}{\frac{2\gamma_1}{\gamma_1 - 1} M^2 - 1} - 2\ , \tag{A1.7}$$

$$\frac{d\ln p_{21}}{d\ln M} = \frac{\frac{4\gamma_1}{\gamma_1 + 1} M^2}{\frac{2\gamma_1}{\gamma_1 + 1} M^2 - \frac{\gamma_1 - 1}{\gamma_1 + 1}}\ . \tag{A1.8}$$

For most experiments, M^2 is large and eqs. (A1.7) and (A1.8) can be simplified to read

$$(\Delta T_{21}/T_{21})/(\Delta M/M) = d\ln T_{21}/d\ln M \simeq 2,$$

and

$$(\Delta p_{21}/p_{21})/(\Delta M/M) \simeq d\ln p_{21}/d\ln M \simeq 2.$$

Finally, the relative temperature and pressure attenuations are approximately

$$\frac{\Delta T_2}{T_2} \simeq \frac{\Delta p_2}{p_2} \simeq 2\ a\ t\ (\rho_{21}-1)\ . \qquad \text{(A1.9)}$$

The largest uncertainties in T_2 and p_2 are therefore associated with long lasting experiments and large values of the attenuation, which are both typical of low temperature experiments. For example, experiments to determine k_9 were conducted at 1490°K, with the attenuation rate $a \simeq 1.8\ 10^{-5}\ (\mu sec)^{-1}$, a total experimental time $t \simeq 250\ \mu sec$ and $\rho_{21} \simeq 3.3$. In this case, molecules probed at 250 μsec (lab. time) might have experienced temperatures as high as 1520°K ($\Delta T_2/T_2 \simeq 2\%$). Other experiments to determine k_2 and k_3 were such that $T_2 \simeq 2000$°K, $a \simeq 1.4\ 10^{-5}\ (\mu sec)^{-1}$, $t \simeq 100$ μsec, $\rho_{21} \simeq 3.5$ and $\Delta T_2/T_2 \simeq 0.7\%$. In general, the corresponding uncertainties in the rate measurements were small compared to other uncertainties in the experiments (see Appendix 6).

By failing to address the cause of shock attenuation, and by omitting other simultaneous effects such as boundary layer growth, the above analysis can only provide qualitative estimates of the magnitude of temperature and pressure attenuation. For a more complete description of the comprehensive gas dynamics in the shock tube, the reader is directed to the studies of Mirels [20] and De Boer and Miller [21].

Appendix 2

The CN Broadband Absorption Diagnostic

A2.1 CN Quantitative Absorption Spectroscopy at 388 nm

The broadband absorption from the P_1+P_2 band head of the $[B^2\Sigma^+(v=0) \leftarrow X^2\Sigma^+(v=0)]$ band of CN at 388 nm (air) was used to monitor CN. Under typical experimental conditions, the P_1+P_2 band head is the strongest absorption feature of this electronic system and does not overlap with neighboring branches or other vibrational band [78]. A computer program was written to predict the absorption spectrum of the $(v'=0 \leftarrow v''=0)$ band under specified conditions. The position, strength and shape of each line were computed to generate an absorption coefficient profile $\beta(\nu)$ as a function of frequency

$$\beta(\nu)= \sum_{\text{lines}} \left(\frac{\pi e^2}{m_e c^2}\right) \frac{(2J''+1)\exp\left[-\frac{hc}{kT}\left(T_e(n'')+G(v'')+F(J'')\right)\right]}{Q_e\ Q_v\ Q_r} \times \frac{N}{RT} f_{el}\ q_{v'v''}\ \frac{S_{J'J''}}{(2J''+1)}\ \phi(\nu-\nu_0) \quad (\text{cm}^{-1}\text{atm}^{-1}), \tag{3.1}$$

where $T_e(n'')$, $G(v'')$ and $F(J'')$ are the electronic, vibrational and rotational energies of the lower state (cm^{-1}); R is the universal gas constant (atm cc/mole/°K); N is Avogadro's number; f_{el}, $q_{v'v''}$ and $S_{J'J''}$ are the oscillator strength, the Franck-Condon factor and the rotational line strength, respectively; Q_e, Q_v and Q_r are the electronic, vibrational and rotational partition functions; $\phi(\nu-\nu_0)$ is the lineshape factor (cm). (The quantity $\pi e^2/m_e c^2 = 8.826\ 10^{-13}$ cm.) A recent review of CN spectroscopy was compiled by Colket [24]. The spectroscopic constants used in the program are summarized in Table A2.1. Note that the results of the present spectroscopic program have been checked against the earlier model of Colket [24] in a private communication with the author. Excellent agreement has been found for a variety of typical shock tube conditions and monochromator slit functions.

Table A2.1 - Summary of CN Spectroscopic Constants

Electronic State	$B^2\Sigma^+$	$A^2\Pi_i$	$X^2\Sigma^+$	Ref.
T_e	25751.8	9241.66	0	[101]
ω_e	2164.13		2068.705	[101]
$\omega_e x_e$	20.25		13.144	[101]
B_e	1.9701		1.8996	[101]
α_e	0.02215		0.01735	[101]
B_0	1.95892		1.89118	[24]
D_0	$6.599.10^{-6}$		$6.361.10^{-6}$	[24]
γ	0.015		0.007	[24]
	$\nu_{00}[B\leftarrow X]=25797.85$			[101]
	$q_{00}[B\leftarrow X]=0.9204$			[27]

All units: cm^{-1} except for q_{00} (no units).

A2.1.1 Line positions

Useful details on $^2\Sigma\leftarrow{}^2\Sigma$ electronic transitions can be found in Herzberg [25]. $^2\Sigma$ states belong to Hund's case (b) and the selection rule $\Delta K=\pm 1$ holds, $\Delta K=0$ being forbidden. Each line in the rotational band is split in two components with $J=K\pm 1/2$, but the separation of the two sublevels is small compared with the rotational line spacing. The term components having $J=K+1/2$ are distinguished with the subscript 1 and $J=K-1/2$ with the subscript 2. This subscript is called α for the upper state and β for the lower state. In principle, six rotational branches are possible in any vibrational band,

$$R_1(\alpha=1\leftarrow\beta=1,\ \Delta J=J'-J''=+1),$$
$$R_2(\alpha=2\leftarrow\beta=2,\ \Delta J=+1),$$
$$P_1(\alpha=1\leftarrow\beta=1,\ \Delta J=-1),$$
$$P_2(\alpha=2\leftarrow\beta=2,\ \Delta J=-1),$$
$$R_{Q_{21}}(\alpha=2\leftarrow\beta=1,\ \Delta J=0,\ \Delta K=+1),$$

$$^{P}Q_{12}(\alpha=1\leftarrow\beta=2,\ \Delta J=0,\ \Delta K=-1), \tag{A2.1}$$

but only the R and P branches are sufficiently strong. Line positions are given by the general formula

$$\nu=T_e(n')-T_e(n'')+G(v')-G(v'')+F_\alpha(J')-F_\beta(J'') \quad (cm^{-1}), \tag{A2.2}$$

where $T_e(n')=25751.8\ cm^{-1}$, $T_e(n'')=0\ cm^{-1}$ and

$$G(v)=\omega_e(v+1/2)-\omega_e x_e(v+1/2)^2 \quad (cm^{-1}). \tag{A2.3}$$

To make the individual line positions independent of the uncertainties associated with the vibrational constants ω_e and $\omega_e x_e$, it is helpful to consider each individual band separately. For the ($v'=0\leftarrow v''=0$) band [79],

$$\nu=\nu_{00}+F_\alpha(J')-F_\beta(J''), \tag{A2.4}$$

where

$$F_1(J)=B_v(K+1)K-D_v(K+1)^2K^2+1/2\ \gamma K \tag{A2.5}$$

and

$$F_2(J)=B_v(K+1)K-D_v(K+1)^2K^2-1/2\ \gamma(K+1) \quad (cm^{-1}), \tag{A2.6}$$

where $J=K+1/2$ for F_1 and $J=K-1/2$ for F_2. K is the quantum number of the total angular momentum apart from spin. Values for ν_{00}, B_0 and D_0 are given in Table A2.1. Rotational constants for other bands can be calculated using: $B_v=\beta_e-\alpha_e(v+1/2)$ [25].

A2.1.2 Line strengths

The individual line strengths $f_{n'v'J'\leftarrow n''v''J''}$ of a diatomic molecule are normalization factors which give the relative strengths of transitions to different final levels from a given initial level,

$$f_{n'v'J'\leftarrow n''v''J''} = f_{v'v''}\ \frac{S_{J'J''}}{2J''+1}, \tag{A2.7}$$

where $f_{v'v''}$ is the band oscillator strength and $S_{J'J''}$ the rotational

line strength. For a diatomic molecule such as CN, the electronic, vibrational and rotational energies can be considered separately, according to the Born-Oppenheimer approximation. Further, if the transition frequencies are nearly constant over the whole band system, an electronic oscillator strength f_{el} can be defined such that

$$f_{v'v''}=q_{v'v''}\times f_{el}, \tag{A2.8}$$

where $q_{v'v''}$ is the Franck-Condon factor of the ($v'\leftarrow v''$) band. In this case, the sum of the oscillator strengths originating from a given lower state is equal to f_{el}

$$\sum_{v',J'} f_{n'v'J'\leftarrow n''v''J''} = \sum_{v',J'} f_{el}\, q_{v'v''} \frac{S_{J'J''}}{2J''+1} =$$

$$= f_{el} \sum_{v'} q_{v'v''} \sum_{J'} \frac{S_{J'J''}}{2J''+1} = f_{el} ,$$

since Franck-Condon factors and rotational line strengths are normalized according to

$$\sum_{v'} q_{v'v''} = 1 \quad \text{and} \quad \sum_{J'} \frac{S_{J'J''}}{2J''+1} = 1 . \tag{A2.9}$$

Note that the sum of $S_{J'J''}$ for all possible transitions from a given level equals the degeneracy of that level. The initial level (specific J", K" combination) was consistently defined such that its degeneracy equals the rotational degeneracy (2J"+1). Therefore, for a given J",

$$S(R_1)+S({}^RQ_{21})+S(P_1)=S(R_2)+S({}^PQ_{12})+S(P_2)=2J''+1 , \tag{A2.10}$$

and [80],

$$S(R) = \frac{(J''+1)^2 - \frac{1}{4}}{(J''+1)}$$

$$S(Q)' = \frac{2J''+1}{4J''(J''+1)}$$

$$S(P) = \frac{J''^2 - \frac{1}{4}}{J''} . \qquad (A2.11)$$

As expected, the Q-branches are weak and can be neglected even for small values of J".

A2.1.3 Partition functions

The ground state ($X^2\Sigma^+$, spin multiplicity=2) and the first excited state ($A^2\Pi_1$, spin multiplicity=2, Λ-doubling) contribute to the electronic partition function,

$$Q_e = 2 + 4 \exp[- \frac{hc}{kT} \times 9241.7 \text{ cm}^{-1}] . \qquad (A2.12)$$

The vibration partition function can be calculated using

$$Q_v = \sum_{v''} \exp[- \frac{hc}{kT} G(v'')] , \qquad (A2.13)$$

where $G(v)=\omega_e(v+1/2)-\omega_e x_e(v+1/2)^2$ (cm^{-1}),

and the rotation partition function using

$$Q_r = \frac{kT}{hc} \times \frac{1}{B_v} . \qquad (A2.14)$$

A2.1.4 Line shapes

CN spectral lines are nearly Doppler-broadened for typical shock tube conditions. More generally, Voigt profiles can be used to estimate the spectral line shapes,

$$\phi(\nu-\nu_0) = 2 \frac{\sqrt{\ln 2}}{\sqrt{\pi}} \frac{V(a,x)}{\Delta\nu_D},$$

$$\text{where } V(a,x) = \frac{a}{\pi} \int_{-\infty}^{+\infty} \frac{e^{-y^2} dy}{a^2+(x-y)^2}, \qquad (A2.15)$$

with $$a = \frac{\Delta\nu_C}{\Delta\nu_D}\sqrt{\ln 2} \quad \text{and} \quad x = 2\sqrt{\ln 2}\,\frac{(\nu-\nu_0)}{\Delta\nu_D} \,. \tag{A2.16}$$

$\Delta\nu_D$ is the Doppler width (FWHM),

$$\Delta\nu_D = 7.1623\ 10^{-7}\ \bar{\nu}_0\ \left(\frac{T}{MW_{CN}}\right)^{\frac{1}{2}} \quad (\mathrm{cm}^{-1}) \,, \tag{A2.17}$$

where $\bar{\nu}_0 \approx 25800\ \mathrm{cm}^{-1}$ and $MW_{CN} \approx 26$ gmole. $\Delta\nu_C$ is the dephasing collision width,

$$\Delta\nu_C = \frac{1}{\pi c}\left(\frac{Z'+Z''}{2}\right) = \frac{1}{\pi c}\,N_{Ar}\left(\frac{8\pi kT}{\mu}\right)^{\frac{1}{2}}\sigma^2 = 0.356\ p\ \sigma^2 (T\mu)^{-\frac{1}{2}}\ (\mathrm{cm}^{-1}), \tag{A2.18}$$

where Z' and Z" are the collision frequencies of the lower and upper states, respectively; N_{Ar} is the argon number density, p the pressure (atm), μ=16 g/mole the CN-argon reduced mass and σ=4 Å the optical collision cross-section diameter [24]. The uncertainty resulting from the lack of collision broadening data is negligible, since our technique relies on broad-band absorption and most lines are fully integrated by the monochromator.

A2.2 Sensitivity of the CN broad-band Absorption Diagnostic

Broad-band absorption is inherently more complicated than monochromatic absorption, because a spectral integration must be performed to relate the number density of the absorber to the transmission through the system. The "curves of growth" method [81] can be used to perform this integration for a single absorption line. In the present case, one must rely on the computer to integrate the spectrum over a wide range of frequencies

$$\frac{i}{i_0} = \frac{\int P(\nu)\ M(\nu)\ \exp[-\beta(\nu)\ p_{CN}\ L]\ d\nu}{\int P(\nu)\ M(\nu)\ d\nu} \,. \tag{A2.19}$$

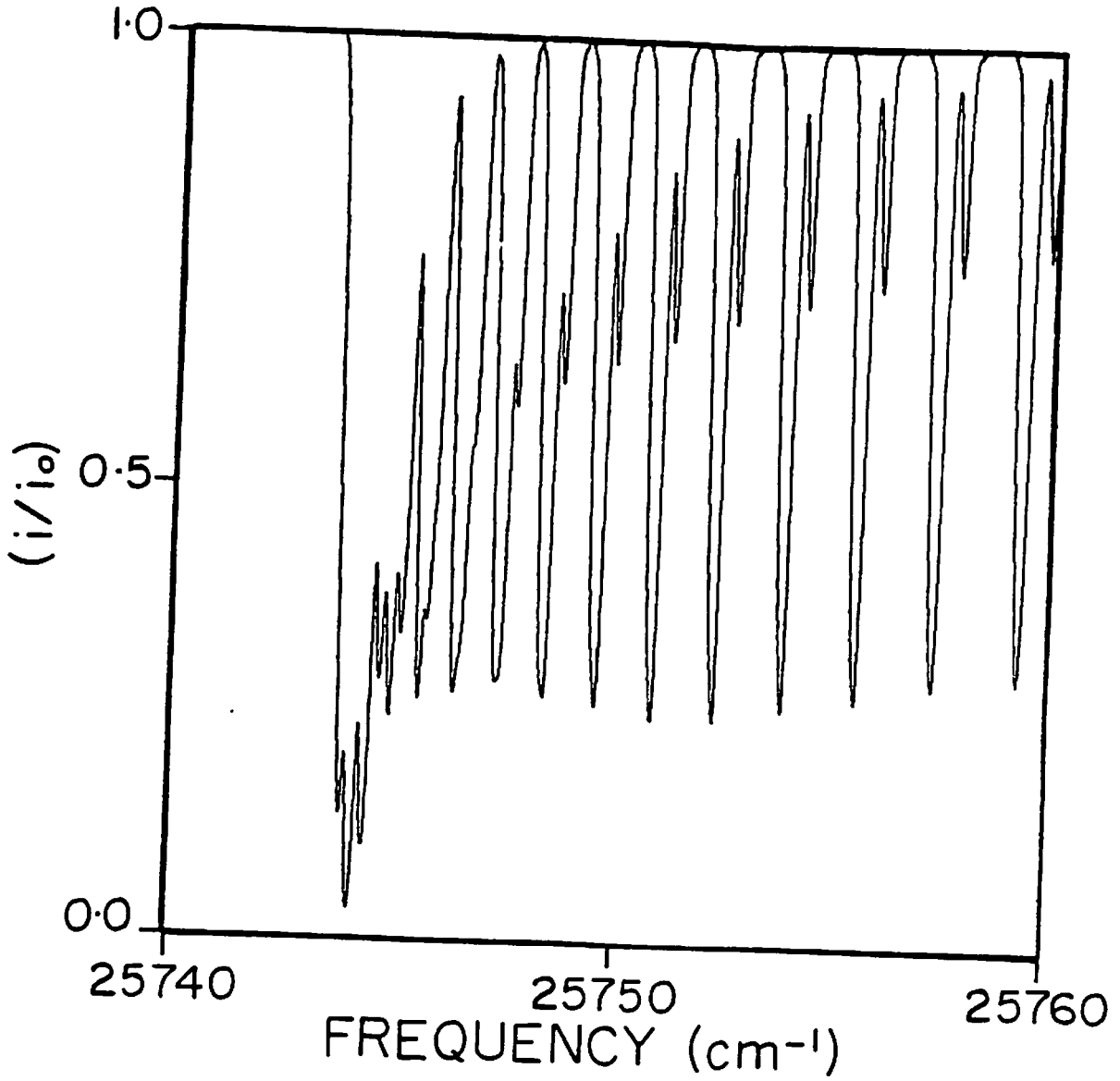

Fig. A2.1 Spectral transmission of CN around 388 nm. The abscissa shows vacuum frequencies in cm^{-1}. The monochromatic spectral transmission $(i/i_0)_\nu \equiv \exp[-\beta(\nu)p_{CN}L]$ is plotted for typical experimental conditions: T_2=2000°K, p_2=0.7 atm, χ_{CN}=30 ppmv, and L=15.24 cm.

Figure A2.1 is a spectral plot of the monochromator transmission function $(i/i_0)_\nu = \exp[-\beta(\nu)p_{CN}L]$ calculated for typical shock tube conditions. Note that this function is nearly saturated at the band head $(i/i_0)_\nu \approx 1$. Figure A2.2 shows the computed absorption $(1-i/i_0)$ as a function of CN mole fraction for typical shock tube conditions, and with the monochromator set at the position that provides maximum absorption (i.e., 3882.6 Å, vac.). For small CN mole fractions, the gas is optically thin over the entire spectrum and the broad-band absorption $(1-i/i_0)$ is proportional to χ_{CN}. For increasing mole fractions, the curve rolls off as the absorption of a few spectral lines becomes saturated. In the linear region of Fig A2.2, a relative change in mole fraction corresponds to an identical change in absorption. In the roll-off region, larger relative variations in χ_{CN} are necessary for similar changes in $(1-i/i_0)$. Expressed in mathematical terms, the "sensitivity" $S(\chi_{CN}) \equiv d\ln(1-i/i_0)/d\ln\chi_{CN}$ is equal to 1 in the linear region and 0 in the roll-off region.

The purpose of this analysis is to design a measurement technique most sensitive to the mole fraction χ_{CN}. Thus, the relative uncertainty $\Delta\chi_{CN}/\chi_{CN}$ must be minimized. In the absence of noise, it would clearly be advantageous to operate in the linear region of Fig. A2.2. Unfortunately, the absorption system is limited by the noise created by the lamp. As a result, the absorption levels in the linear region can fall below the detection limit.

To a good approximation, one can assume a constant relative rms noise $\Delta i/i_0$ independent of the transmission i/i_0. Using the definition of the sensitivity S,

$$\frac{\Delta\chi_{CN}}{\chi_{CN}} = \frac{\dfrac{\Delta(1-i/i_0)}{(1-i/i_0)}}{S(\chi_{CN})} = \frac{\dfrac{\Delta i}{i_0}}{(1-i/i_0)\ S(\chi_{CN})} \cdot \qquad \text{(A2.20)}$$

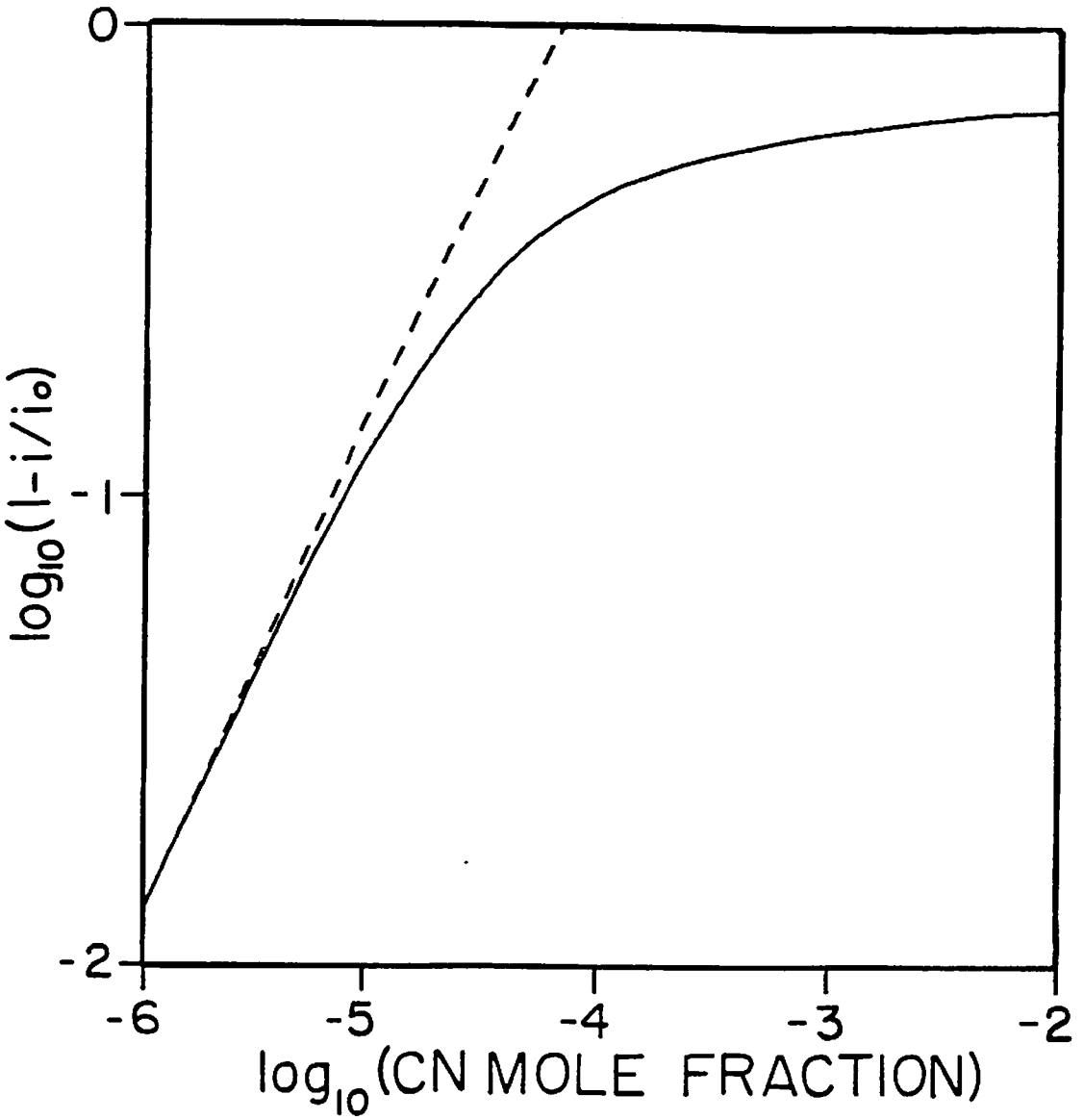

Fig. A2.2 Computed absorption $(1-i/i_0)$ vs. CN mole fraction χ_{CN} for typical experimental conditions: T_2=2000°K, p_2=0.7 atm, L=15.24 cm. The monochromator is set at the position that provides maximum absorption (λ=3882.6 Å, vac.), with the slit widths Δx=190 μm and Δy=103 μm. In addition, a value f_{el}=0.03 is assumed.

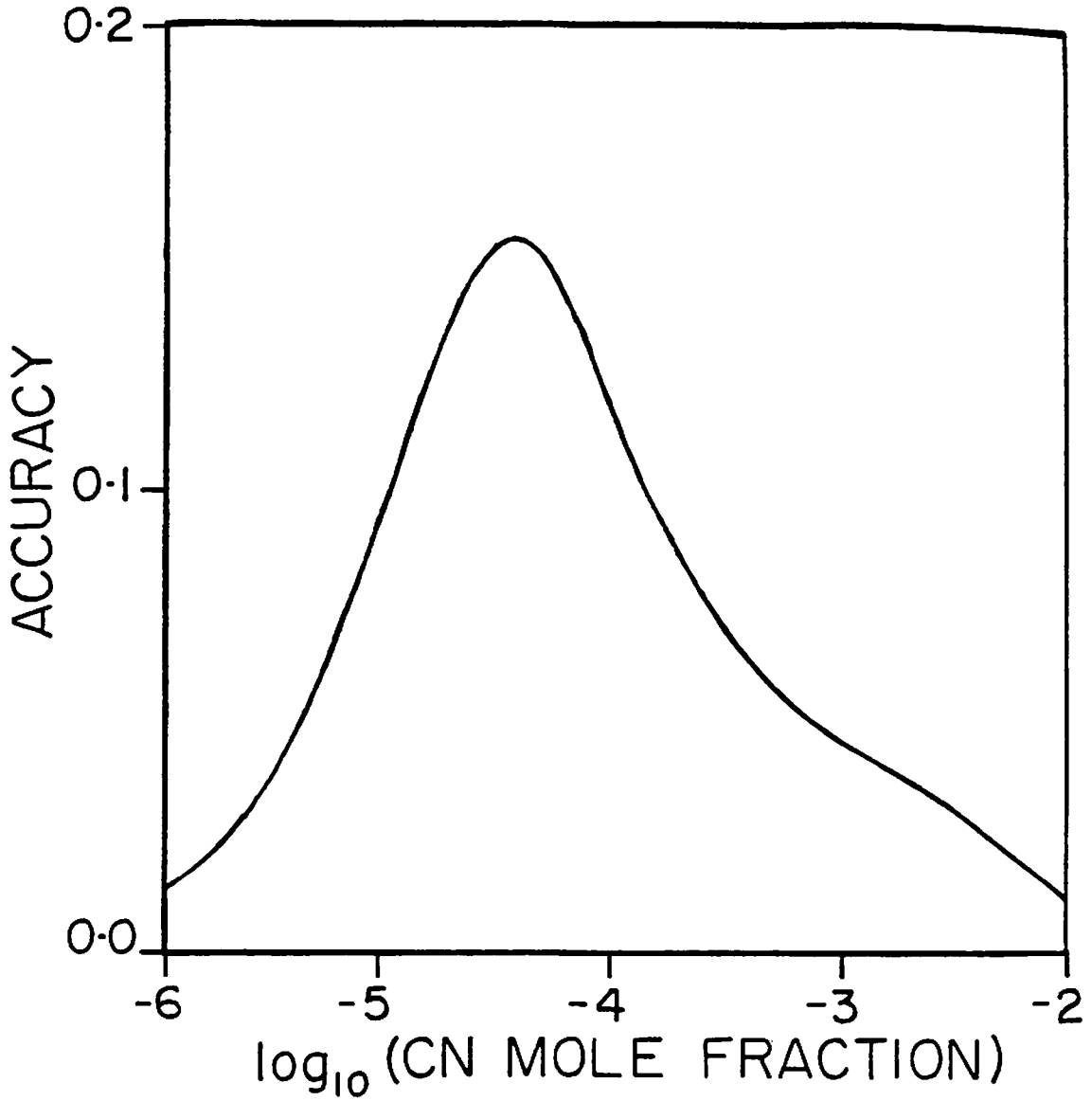

Fig. A2.3 Computed "accuracy" A vs. CN mole fraction χ_{CN}. The conditions are identical to Fig. A2.2.

For a given value of the rms noise $\Delta i/i_0$, minimizing $\Delta\chi_{CN}/\chi_{CN}$ corresponds to maximizing the "accuracy" A, defined as

$$A(\chi_{CN})\equiv(1-i/i_0)\times S(\chi_{CN}). \qquad (A2.21)$$

To illustrate the systematic limitations of an absorption diagnostic, we can briefly derive the "sensitivity" S and the "accuracy" A of a simple monochromatic system. Using Beer's law,

$$i/i_0=\exp(-x), \text{ with } x\equiv\beta(T)p\chi L, \qquad (A2.22)$$

the "sensitivity" S can be found,

$$S(x)=d\ln(1-i/i_0)/d\ln x=xe^{-x}/(1-e^{-x}). \qquad (A2.23)$$

Assuming an rms noise level independent of i/i_0, it follows that the "accuracy" A is a simple function of x,

$$A(x)=(1-i/i_0)S(x)=xe^{-x}. \qquad (A2.24)$$

Therefore, maximum accuracy of a monochromatic absorption system is achieved for an optically thick sample, with x=1 and i/i_0=37%, and the minimum uncertainty on x is $\Delta x/x=2.72\Delta i/i_0$. For the CN broad-band system, the "sensitivity" and the "accuracy" must be evaluated numerically. A computer plot of the accuracy is given in Fig A2.3 for T=2000°K and p=0.7 atm. Maximum accuracy A=0.15 is obtained for χ_{CN}=37 ppmv. For a typical rms signal-to-noise ratio of 100 ($\Delta i/i_0$ = 0.01), the lowest uncertainty in χ_{CN} is 6% for these conditions, and the accuracy is acceptable for χ_{CN} in the range $15<\chi_{CN}<90$ ppmv. Note that the present experiments were performed under conditions that nearly maximize the accuracy.

A2.3 Calibration uncertainties

Calibration runs aimed at characterizing the CN absorption system

were performed by shock heating mixtures of cyanogen diluted in argon and recording the partial equilibrium level of CN from the reaction

$$C_2N_2 + M \rightarrow CN + CN + M. \tag{7}$$

If x_e represents the degree of advancement of reaction (7) at equilibrium, then

$$\chi_{C_2N_2}=(\chi_{C_2N_2})_0\ (1-x_e), \tag{A2.25}$$

$$\chi_{CN}=2(\chi_{C_2N_2})_0\ x_e, \tag{A2.26}$$

and

$$K_p = \frac{\chi_{CN}^{*2}}{\chi_{C_2N_2}^{*}} \times p\ . \tag{A2.27}$$

The asterisk (*) refers to equilibrium conditions. Rearranging eqs. (A2.25) and (A2.27),

$$\frac{x_e^2}{1-x_e} = \frac{K_p}{p} \times \frac{1}{4\ (\chi_{C_2N_2})_0} \equiv \alpha\ , \tag{A2.28}$$

and

$$x_e = \frac{-\alpha + (\alpha^2+4\alpha)^{1/2}}{2}. \tag{A2.29}$$

A significant uncertainty is associated with the heat of formation of CN. In the JANAF tables [63], $\Delta H_f°$=103.2±2.5 kcal/mole. Recently, Colket inferred $\Delta H_f°$=99.2±1.5 kcal/mole [24]. In this study, $\Delta H_f°$=101.2±2 kcal/mole is assumed. Uncertainties in $\Delta H_f°$ can affect the equilibrium constant K_p, since

$$K_p = \frac{K_f(CN)^2}{K_f(C_2N_2)} \quad \text{and} \quad K_f(CN) = \exp[\ \frac{\Delta S_f^0}{R}\ ] \times \exp[-\ \frac{\Delta H_f^0}{RT}\ ]. \tag{A2.30}$$

$\Delta H_f°(CN)$ is known within δ=±2 kcal/mole. Therefore, the relative uncertainty in K_p can be written

$$\frac{dK_p}{K_p} = 2\,\frac{\delta}{RT} = \frac{2010}{T} = \frac{d\alpha}{\alpha}\,. \qquad \text{(A2.31)}$$

Using $\Delta H_f°$=101.2 kcal/mole and other thermochemical data in the JANAF tables, we find $K_p = 10^{7.74}\exp[-63280/T]$ in the range $2300<T<3500$°K. Differentiating equation (A2.29) with α leads to

$$\frac{dx_e}{x_e} = \frac{d\alpha}{\alpha}\times\frac{\alpha}{(\alpha^2+4\alpha)^{1/2}}\times\left(\frac{2}{(\alpha^2+4\alpha)^{1/2}-\alpha} - 1\right) = \frac{d\chi_{CN}^*}{\chi_{CN}^*}\,. \qquad \text{(A2.32)}$$

Calibration uncertainties associated with $\Delta H_f°$ thus go down with increasing temperature or with increasing α. Therefore, the CN system should be calibrated at high temperatures and/or low initial cyanogen mole fraction (i.e., at high values of α).

High temperatures are also desirable to limit the duration of calibration experiments. It can be shown that the time to reach half the CN equilibrium concentration is given by [82]

$$t_{1/2} = \frac{x_e\,\ln(3-x_e)}{(2-x_e)}\,\tau\,, \text{ where } \tau = \frac{1}{k_7[M]} \text{ (particle time).} \qquad \text{(A2.33)}$$

For T=2400°K and p=0.5 atm, $t_{1/2}$≈5 msec; these conditions clearly result in an excessive duration of the experiment. By contrast, $t_{1/2}$≈110 μsec for T=3000°K and p=0.33 atm. Therefore, typical calibration experiments were performed at T≈3000°K, p≈0.33 atm and $(\chi_{C_2N_2})_0$≈80 ppmv, with α≈700, $(1-x_e)\approx10^{-3}$ and $\Delta\chi_{CN}^*/\chi_{CN}^*$≈0.1%. Thus, calibration uncertainties associated with $\Delta H_f°$ were negligible under these conditions.

Appendix 3

The CO(v=1) IR Laser Absorption Diagnostic

The following additional details concerning the CO(v=1) system are discussed in this appendix: Theoretical aspects of the CO(v=1) absorption, calibration procedures and uncertainties in the broadening parameter $2\gamma°$, vibrational relaxation of the CO(v=1) level, and interference from the N_2O absorption background.

A3.1 Laser Absorption by CO(v=1)

The absorption of monochromatic laser radiation by CO(v=1) is given by Beer's law

$$\frac{i}{i_0} = \exp[-\beta\ P_{CO(v=1)}\ L] \ , \tag{3.4}$$

where β is the absorption coefficient ($cm^{-1}atm^{-1}$), $P_{CO(v=1)}$ is the partial pressure of CO in the first excited vibrational level and L is the path length (15.24 cm). The absorption coefficient can be expressed as a product of the line strength and the line shape factor

$$\beta = S_{CO(v=1)}\phi \cdot \tag{3.5}$$

The line shape factor can be described using a Voigt profile (see Appendix 2)

$$\phi = 2\ \frac{\sqrt{\ln 2}}{\sqrt{\pi}}\ \frac{V(a,x)}{\Delta\nu_D} \ , \tag{A2.15}$$

$$\text{where} \quad a = \sqrt{\ln 2}\ \frac{\Delta\nu_C}{\Delta\nu_D} \ \text{(Voigt parameter)},$$

$$\Delta\nu_D = 7.1623\ 10^{-7}\left(\frac{T}{MW_{CO}}\right)^{1/2}\ \bar{\nu}_0\ (cm^{-1})\ \text{(Doppler width)}, \tag{A3.1}$$

In this system, $x = 2\sqrt{\ln 2}\ \delta/\Delta\nu_D$, where δ is the spacing between the laser line and the CO absorption line center. The collision width $\Delta\nu_C$

can be written in the form

$$\Delta\nu_C = 2\gamma p \ (\mathrm{cm}^{-1}), \tag{A3.2}$$

where the collision broadening parameter 2γ depends on temperature. Using the results of Hanson [32] for the P(11) line, the following temperature dependence of 2γ is assumed:

$$2\gamma(300^0\mathrm{K}) = 2\gamma(T) \left(\frac{T}{300}\right)^{0.73} (\mathrm{cm}^{-1}\mathrm{atm}^{-1}) \ . \tag{A3.3}$$

The line strength S at temperature T for a transition [v+1←v, J±1←J] centered at frequency ν can be expressed in terms of the fundamental band strength S_0 at reference temperature T_0 [38],

$$S(\nu,T) = S_0 \frac{T_0}{T} \frac{\nu}{\bar{\nu}_0} \frac{(2J+1) \exp[-\frac{hc}{kT} E(v,J)]}{Q(T)} \left(1-\exp[-\frac{hc}{kT}\nu]\right) \times$$
$$\times (v+1)(1+x_e v) \left(\frac{|m|}{2J+1}(1+Cm+Dm^2)\right) \ (\mathrm{cm}^{-2}\mathrm{atm}^{-1}) \ . \tag{A3.4}$$

S_0=282 $\mathrm{cm}^{-2}\mathrm{atm}^{-1}$ is the band strength at T_0=273.2°K; $\bar{\nu}_0$=2147.36 cm^{-1} is the reference band center frequency. The energy of the lower state can be written in a form suggested by Dunham [83], using the coefficients Y_{ik} measured by Todd, et al. [30],

$$E(v,J) = \sum_i \sum_k Y_{ik}(v+\tfrac{1}{2})^i \left(J(J+1)\right)^k. \tag{A3.5}$$

The partition function can be calculated using

$$Q(T) = \sum_v \sum_J (2J+1) \exp[-\frac{hc}{kT} E(v,J)] \ . \tag{A3.6}$$

Note that x_e=6.124 10^{-3} is a correction for anharmonicity of the vibrational matrix element (v+1); m=-J for P branch lines (ΔJ=-1) and m=J+1 for R branch lines (ΔJ=+1); C=1.73 10^{-4} and D=7.3 10^{-6} are the Herman-Wallis constants for vibration-rotation interaction [38].

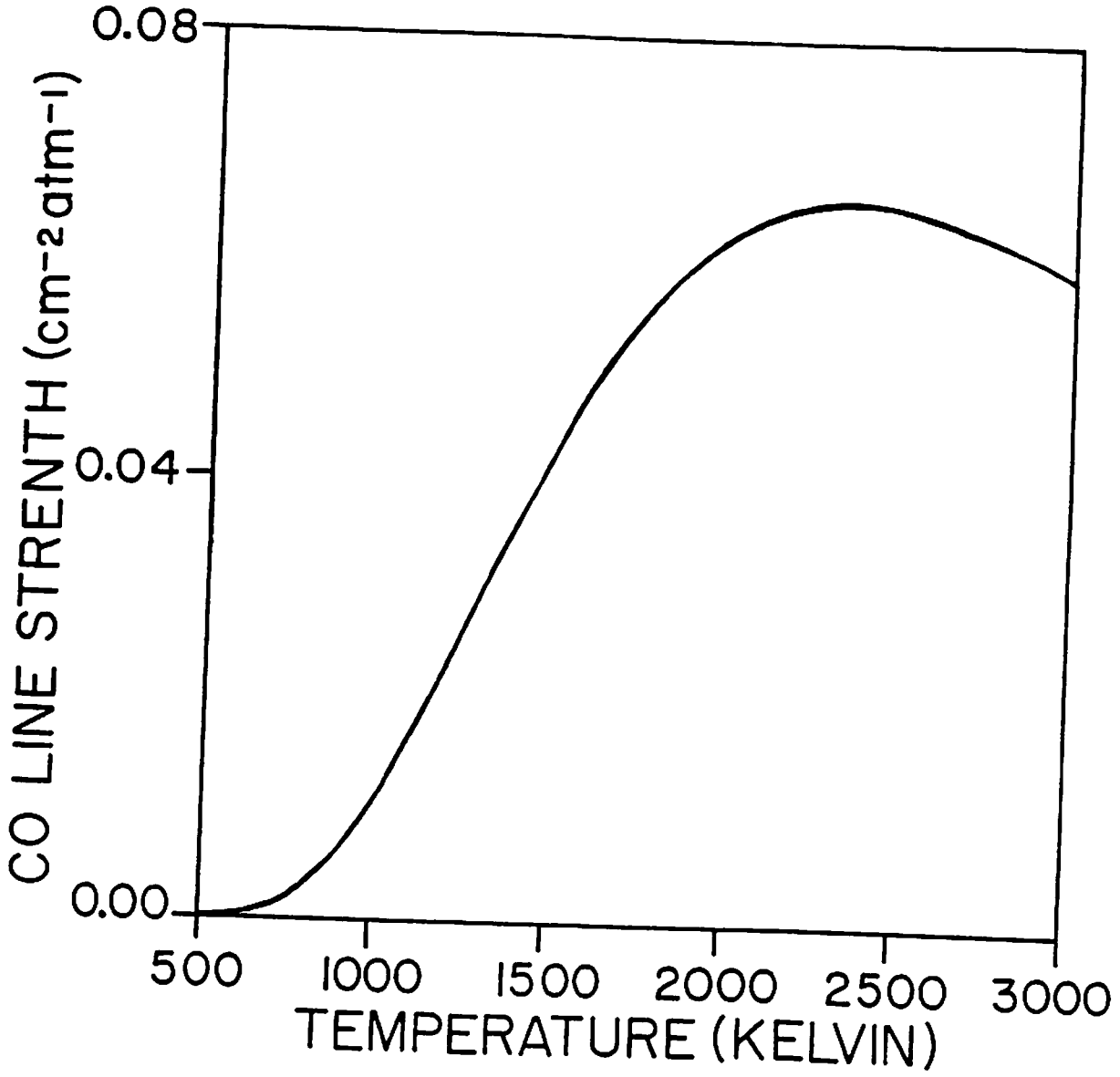

Fig. A3.1 Temperature dependence of the equilibrium CO line strength S_{CO} for the transition CO[v(2←1),J(37←38)].

The expression for $S(\nu,T)$ (eq. A3.4) is convenient to calculate the absorption from a sample of CO at equilibrium,

$$\frac{i}{i_0} = \exp[-S\ p_{CO}\ \phi\ L]\ . \tag{A3.7}$$

A plot of $S(\nu,T)$ vs. temperature is given in Fig. A3.1 for the transition used in this study [v(2←1), J(37←38)]. In the present case, however, vibrational relaxation is not instantaneous and it is more useful to express Beer's law in terms of the partial pressure of CO(v=1). Combining eqs. (3.4) and (3.5),

$$\frac{i}{i_0} = \exp[-S_{CO(v=1)}\ p_{CO(v=1)}\ \phi\ L]\ . \tag{A3.8}$$

Comparing eqs. (A3.7) and (A3.8),

$$S_{CO(v=1)} = S \times \frac{N_{CO}}{N_{CO(v=1)}}\ , \tag{A3.9}$$

$$\frac{N_{CO(v=1)}}{N_{CO}} = \frac{\sum_J (2J+1)\ \exp[-\frac{hc}{kT} E(v,J)]}{Q(T)}$$

where

$$\simeq \exp[-\frac{hc}{kT}\omega_e]\ \left(1-\exp[-\frac{hc}{kT}\omega_e]\right)\ . \tag{A3.10}$$

Note that ω_e=2169.52 cm^{-1} [63], and $hc\omega_e/k$=3121°K. A plot of $S_{CO(v=1)}$ vs. temperature is given in chapter 3 (Fig. 3.3) for the transition used in this study [v(2←1), J(37←38)].

A3.2 Calibration uncertainties

As mentioned in the previous paragraph, the knowledge of 2γ(300°K) and the CO(v=1) line strength is sufficient to calculate the concentration of CO(v=1) from a transmission measurement at known pressure and temperature. Values of $S_{CO(v=1)}$ can be computed at any temperature using eqs. (A3.4), (A3.9) and (A3.10). However, calibration experiments are necessary to determine the broadening parameter 2γ(300°K). To this end, mixtures of CO and argon were shock-heated to infer 2γ(300°K) from the transmissions plateaus of CO(v=1) at vibrational equilibrium. In this

paragraph, the uncertainties in $2\gamma(300°K)$ introduced by a noisy calibration signal will be discussed.

The transmission of a known CO sample at vibrational equilibrium is given by Beer's law,

$$\frac{i}{i_0} = \exp[-S\ p\ \chi_{CO}\ L\ \phi]\ , \tag{A3.11}$$

where S is the line strength of CO at equilibrium (eq. A3.7). Assuming an rms noise level independent of i/i_0,

$$\Delta\left(\frac{i}{i_0}\right) \approx \frac{\Delta i}{i_0} \equiv \frac{1}{\text{S/N ratio}}\ . \tag{A3.12}$$

The corresponding uncertainty in $2\gamma(300°K) \equiv 2\gamma°$ can be estimated using

$$\Delta(2\gamma^0) \approx \frac{\dfrac{\partial(2\gamma^0)}{\partial(i/i_0)}}{\text{S/N ratio}}\ . \tag{A3.13}$$

In addition,

$$\frac{\partial(i/i_0)}{\partial 2\gamma^0} = S\ p\ \chi_{CO}\ L\ \frac{\partial\phi}{\partial 2\gamma^0}\ \frac{i}{i_0}, \tag{A3.14}$$

and, using eq. (A2.15),

$$\frac{\partial\phi}{\partial 2\gamma^0} = \frac{\partial\phi}{\partial a}\ \frac{\partial a}{\partial 2\gamma^0} = 2\ \frac{\sqrt{\ln 2}}{\sqrt{\pi}}\ \frac{1}{\Delta\nu_D}\ \frac{\partial V(a,x)}{\partial a} \times \frac{\partial a}{\partial 2\gamma^0}\ . \tag{A3.15}$$

According to Abramovitz and Stegun [84], the Voigt function can be expressed in terms of the real part of a complex function w(z), with $z=x+ia$, $V(x,a) = \mathrm{Re}[w(x+ia)]$, and

$$\frac{dw}{dz} = -2\ z\ w(z) + \frac{2i}{\sqrt{\pi}} = \frac{\partial V}{\partial x} - i\frac{\partial V}{\partial a}\ . \tag{A3.16}$$

It follows that

$$\frac{\partial V}{\partial a} = 2\ \left(aR + xI - \frac{1}{\sqrt{\pi}}\right),\ \text{where } R \equiv \mathrm{Re}(w) \text{ and } I \equiv \mathrm{Im}(w).$$

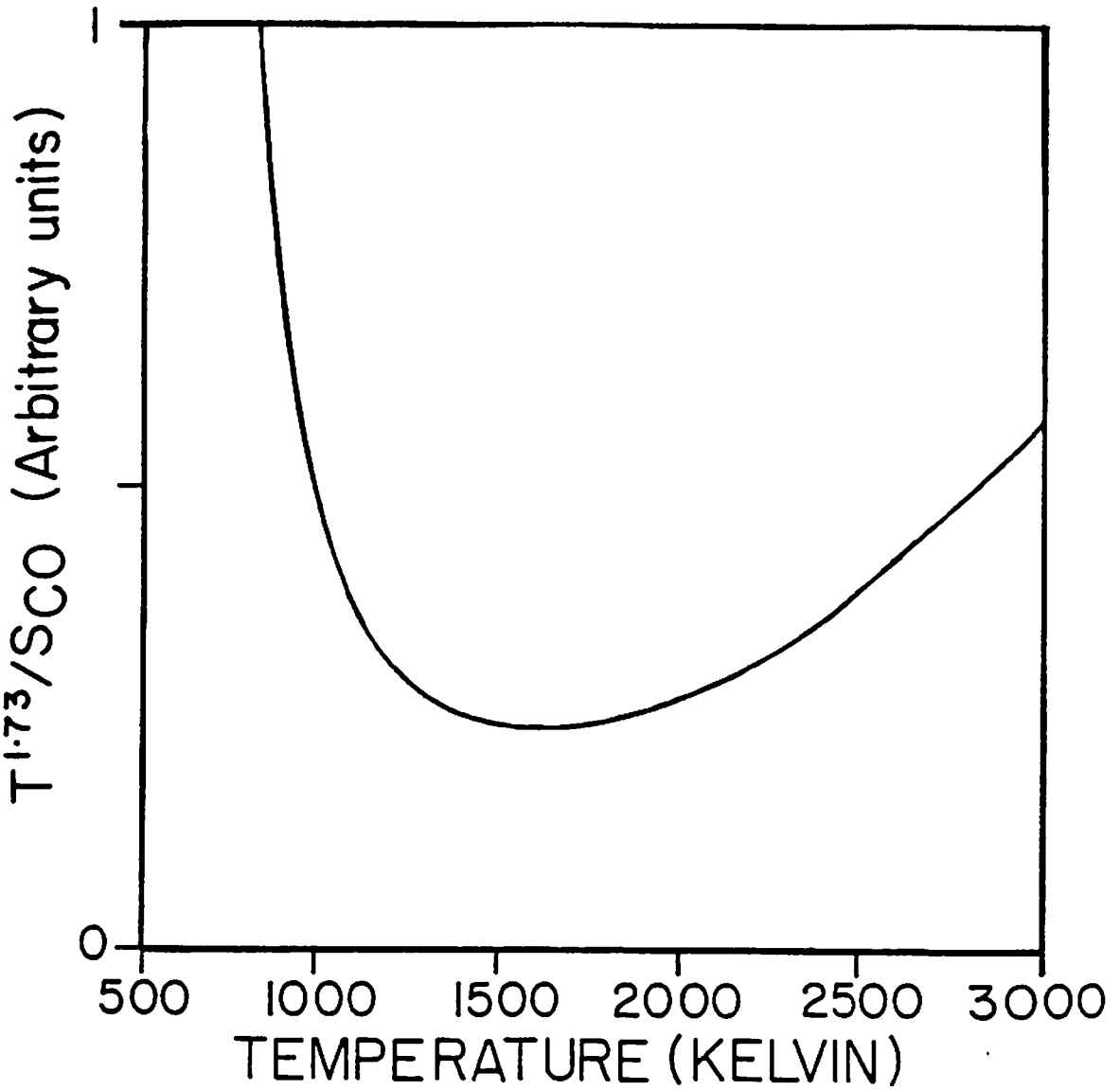

Fig. A3.2 Determination of the optimum calibration temperature for measuring $2\gamma°(300°K)$, the pressure broadening parameter of the CO absorption line [v(2←1),J(37←38)]. Plot of the ratio $T^{1.73}/S_{CO}(T)$ (arbitrary units) vs. temperature.

Using $$\frac{\partial a}{\partial 2\gamma^0} = \frac{\sqrt{\ln 2}}{\Delta\nu_D}\, p \left(\frac{T_0}{T}\right)^{0.73},$$

one obtains

$$\frac{\partial(2\gamma^0)}{\partial(i/i_0)} = \frac{\sqrt{\pi}}{4\ \ln 2}\,\frac{\Delta\nu_D^{\ 2}}{S\ p^2\ \chi\ L}\left(\frac{T}{T_0}\right)^{0.73}\frac{1}{aR + xI - 1/\sqrt{\pi}}\,\frac{i_0}{i}. \qquad \text{(A3.17)}$$

The quantity $(aR+xI-1/\sqrt{\pi})$ is a weak function of p and T. Thus, in the limit of small absorptions $(i/i_0 \simeq 1)$,

$$\frac{\partial(2\gamma^0)}{\partial(i/i_0)} \propto \frac{T^{1.73}}{S(T)} \times \frac{1}{p^2\ \chi}\ . \qquad \text{(A3.18)}$$

For a given noise level, the uncertainty in $2\gamma(300°K)$ is then inversely proportional to p^2 and χ and depends on the ratio $T^{1.73}/S(T)$. A plot of this ratio is given in Fig. A3.2. The minimum uncertainty corresponds to $T \simeq 1600°K$. Unfortunately, the relaxation time for CO is too long at this temperature (for $T=1600°K$, $p\tau \simeq 0.001$ atm sec, particle time). Thus, calibration runs were performed in the range $2040 < T < 2430°K$, where $120 < p\tau < 315$ atm μsec. Using eqs. (A3.13) and (A3.17), we estimated $\Delta(2\gamma°) \simeq 0.03\ cm^{-1}atm^{-1}$. This value is consistent with the experimental scatter in $2\gamma°$. Note that the results of this analysis can be helpful to design optimum calibration experiments for a variety of other molecules.

A3.3 Vibrational non-equilibrium and relaxation of CO

As mentioned, the vibrational relaxation time of CO places a lower bound on the temperature range of our calibration experiments. However, if CO is the product of an elementary reaction, then this slow relaxation process can be useful to keep CO in its original vibrational state, thus providing further experimental insight on the detailed products of the reaction.

In the interpretation of CO(v=1) time histories, vibrational relaxation must be taken into account; to this end, it is convenient to include reaction (3.7) in the reaction mechanism

$$CO(v=1) + M \underset{k_e}{\overset{k_{de}}{\rightleftharpoons}} CO(v\neq 1) + M\ . \qquad (3.7)$$

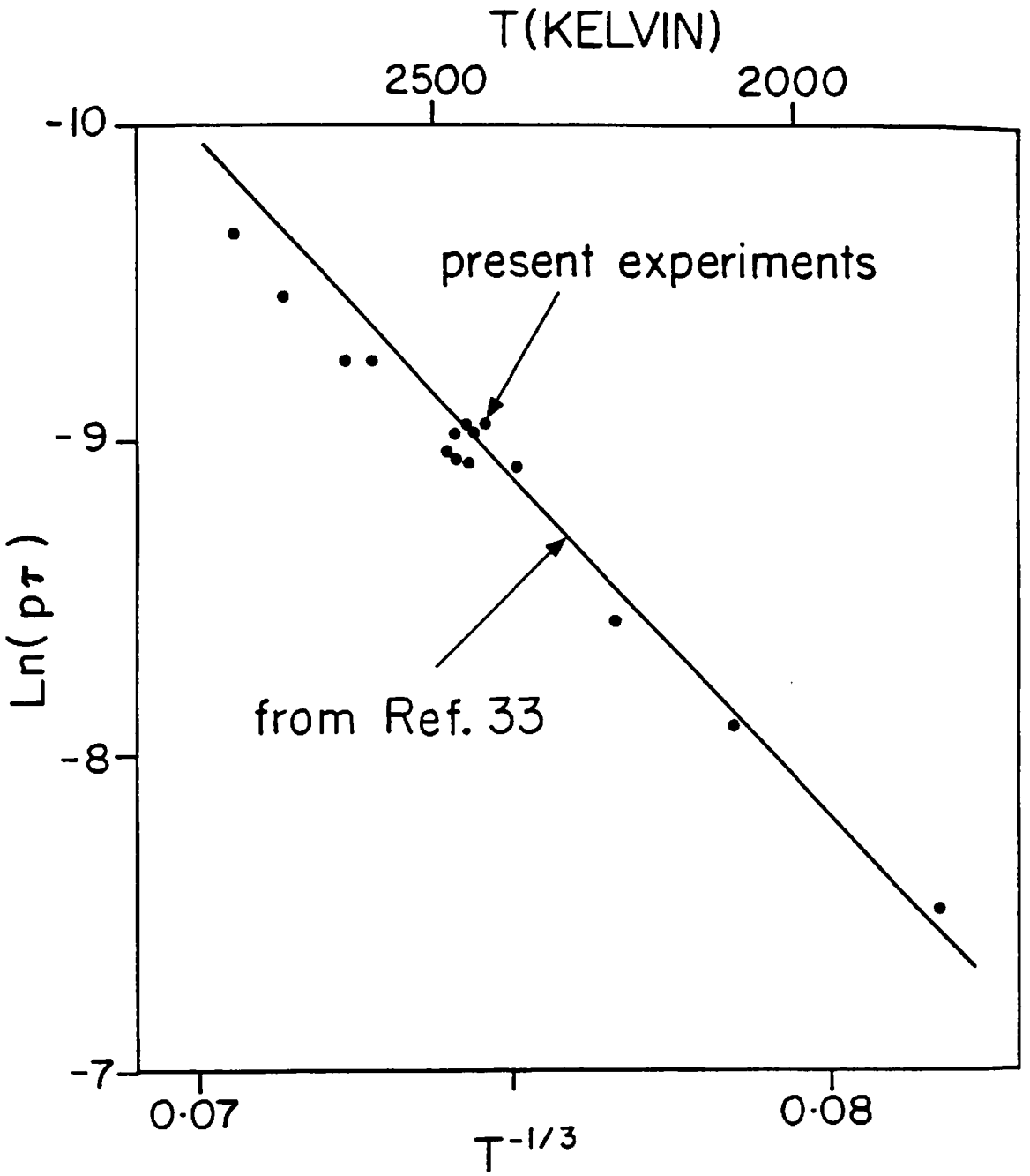

Fig. A3.3 Experimental (•) and recommended (—) vibrational relaxation times of CO(v=1) vs. temperature. The abscissa shows temperatures to the -1/3 power ($K^{-1/3}$), and the ordinate $p\tau$, where p is the gas pressure (atm) and τ is the vibrational relaxation time (μsec, particle time).

Data for the relaxation of CO(v=1→v≠1) has been compiled by Millikan and White [33], who recommended

$$p\tau = 10^{-10.80} \exp[+213\ T^{-\frac{1}{3}}]\ \text{(atm sec)}, \qquad \text{(A3.19)}$$

in the range 1700<T<5000°K. Using the infrared detection system described by Flower [85], experiments were conducted with mixtures of CO and argon and temperatures in the range 1800<T<2900K; these measurements of pτ agreed within 16% with the expression of Millikan and White, which was adopted for further data reduction (see Fig. A3.3).

In order to integrate the vibrational relaxation of CO in the reaction mechanism, expressions for k_e and k_{de} were evaluated from eq. (A3.19) using the simplified two-level model of reaction (3.7) and the following analysis,

$$[CO]_{total} = [CO(v=1)]+[CO(v\neq1)]=[CO(v=1)]^*+[CO(v\neq1)]^*, \qquad \text{(A3.20)}$$

and

$$\frac{[CO(v=1)]^*}{[CO(v\neq1)]^*} = \frac{k_e}{k_{de}}, \qquad \text{(A3.21)}$$

where [CO(v≠1)] is the concentration of CO in all vibrational states but (v=1). Asterisks (*) indicate concentrations at Boltzman equilibrium. The rate of change of CO(v=1) concentrations in a CO/argon mixture is

$$\frac{d[CO(v=1)]}{dt} = -k_{de}[CO(v=1)][M] + k_e[CO(v\neq1)][M], \qquad \text{(A3.22)}$$

Using eqs. (A3.20) and (A3.21), eq. (A3.22) can be rearranged to obtain

$$\frac{d}{dt}\left([CO(v=1)]-[CO(v=1)]^*\right)=-(k_{de}+k_e)[M]\left([CO(v=1)]-[CO(v=1)]^*\right). \qquad \text{(A3.23)}$$

The 1/e vibrational relaxation time is therefore $\tau=1/(k_e+k_{de})[M]$, or $p\tau=RT/(k_e+k_{de})$, where R is the fundamental gas constant. Using the Boltzman relations,

$$\frac{[CO(v=1)]^*}{[CO]_{total}} = \frac{\exp[-\Theta_{vib}/T]}{Q_{vib}} = 1-\frac{[CO(v\neq1)]^*}{[CO]_{total}}, \qquad \text{(A3.24)}$$

where $\theta_{vib}=\omega_e \times hc/k$ is the vibrational temperature and $Q_{vib}=[1-\exp(-\theta_{vib}/T)]^{-1}$ is the vibrational partition function of CO. At vibrational equilibrium,

$$\frac{k_e}{k_{de}} = \frac{[CO(v\neq 1)]^*}{[CO(v=1)]^*} = \frac{\exp[-\Theta_{vib}/T]}{Q_{vib} - \exp[-\Theta_{vib}/T]}, \tag{A3.25}$$

and finally

$$k_{de}=RT/p\tau\ [1-e^{-\theta vib/T}(1-e^{-\theta vib/T})]. \tag{A3.26}$$

In the chemical kinetics code, rate and equilibrium constants must be input in Arrhenius form. Complicated temperature-dependent expressions such as k_e and k_{de}/k_e can be approximated using generalized Arrhenius expressions as suggested by Gardiner [86]. In order to fit the function f(T) to an Arrhenius expression $AT^m\exp[-\theta/T]$ in the temperature range $T_1<T<T_2$, one first calculates an equivalent activation energy E(T) at the two end temperatures T_1 and T_2

$$\theta(T) = \frac{E(T)}{R} = \frac{d\ln f(T)}{d(1/T)}, \tag{A3.27}$$

This expression can be approximated using

$$\theta(T_i) = \frac{\ln f(T_i+\delta) - \ln f(T_i-\delta)}{1/(T_i-\delta) - 1/(T_i+\delta)}, \text{ with } i=1,2 . \tag{A3.28}$$

Then, one determines an average value for the temperature exponent m

$$m = \frac{\theta(T_2) - \theta(T_1)}{T_2 - T_1}, \tag{A3.29}$$

and the average activation energy

$$\theta = \frac{E}{R} = \frac{\theta(T_2)+\theta(T_1)}{2} - m\left(\frac{T_2+T_1}{2}\right) . \tag{A3.30}$$

Finally, an approximation of the average pre-exponential A can be found using a series of discrete temperature points,

$$A = \frac{1}{T_2-T_1}\int_{T_1}^{T_2} \frac{f(T)}{T^m \exp(-\frac{\theta}{T})}\, dT , \tag{A3.31}$$

and
$$A \simeq \frac{1}{n} \sum_{i=1}^{n} \frac{f(T_i)}{T_i^m \exp(-\frac{\theta}{T_i})} . \qquad (A3.32)$$

For CO, we calculated $k_{de}=10^{-5.81}\ T^{4.6}\ \exp[-3610/T]\ cm^3/mole/sec$ and $k_{de}/k_e=10^{-2.49}\ T^{+0.70}\ \exp[+4130/T]$.

A3.4 N_2O Absorption Background

In all experiments, a background absorption was observed which we attributed to N_2O. In this section, spectroscopic arguments will be presented to justify this assumption. At the high temperatures of our experiments, a polyatomic molecule such as N_2O can be significantly populated in many vibrational levels $(v_1 v_2^{\ell} v_3)$ and numerous ν_3 sub-bands can appear around the $(00^01)\leftarrow(00^00)$ fundamental. For example, 125 lower vibrational levels have a population of at least 1% of the ground level (00^00) at 2000°K.

Estimates of the strength and position of significant lines were computed after Gray-Young [34,35], Pliva [36,37] and Varghese [38] to estimate the magnitude of the N_2O absorption spectrum around the ν_3 fundamental. Lines positions are given by

$$\nu=E(v_1,v_2,\ell',v_3+1,J')-E(v_1,v_2,\ell'',v_3,J'')\ (cm^{-1}), \qquad (A3.33)$$

and the energy level of the $(v_1 v_2^{\ell} v_3 J)$ level above the lowest vibrational state is

$$E(v_1,v_2,\ell,v_3,J)=B_{v_1v_2v_3}[J(J+1)-\ell^2]-D_{v_1v_2v_3}[J(J+1)-\ell^2]^2$$
$$+\omega_1{}^\circ v_1+\omega_2{}^\circ v_2+\omega_3{}^\circ v_3+g_{22}\ell^2 \qquad (A3.34)$$
$$+x_{11}{}^\circ v_1{}^2+x_{22}{}^\circ v_2{}^2+x_{33}{}^\circ v_3{}^2+x_{12}{}^\circ v_1v_2+x_{13}{}^\circ v_1v_3+x_{23}{}^\circ v_2v_3\ \ (cm^{-1}),$$

where
$$B_{v_1v_2v_3}=B_o-\alpha_1{}^\circ v_1-\alpha_2{}^\circ v_2-\alpha_3{}^\circ v_3\ \ (cm^{-1}). \qquad (A3.35)$$

Table A3.1 - Spectroscopic Constants for the IR ν_3 Sub-bands of N_2O

Rotational Constants		Vibrational Constants	
B_0	0.41901	$\omega_1{}^\circ$	1276.88
D_0	$1.792.10^{-7}$	$\omega_2{}^\circ$	588.77
$\alpha_1{}^\circ$	$1.965.10^{-3}$	$\omega_3{}^\circ$	2223.76
$\alpha_2{}^\circ$	$-0.569.10^{-3}$	g_{22}	3.0 [a]
$\alpha_3{}^\circ$	$3.449.10^{-3}$	$x_{11}{}^\circ$	-4.195
		$x_{12}{}^\circ$	0.165
		$x_{22}{}^\circ$	-0.279
All units: cm^{-1}		$x_{13}{}^\circ$	-27.177
		$x_{23}{}^\circ$	-14.330
		$x_{33}{}^\circ$	-15.068

[a] Value in Herzberg [66], p.278.

The molecular constants used in the calculations (Pliva [36,37]) are shown in Table A3.1. For simplicity, it was assumed that all levels with identical values of v_2 but different values of ℓ have the same energy and are unresolved. This assumption implies that the (v_2+1) bands with identical $(v_1v_2v_3)$ but different values of ℓ all collapse into a single band, with the following rotational lines strengths

$$S(\nu,T) = S_0 \frac{T_0}{T} \frac{\nu}{\bar{\nu}_0} (v_2+1) \times \frac{(2J+1)\exp[-\frac{hc}{kT} E(v_1,v_2,v_3)]}{Q(T)} \times (v_3+1)\,\Phi, \tag{A3.36}$$

where $$\Phi = \frac{J^2-\ell^2}{J(2J+1)}, \quad \frac{\ell^2}{J(J+1)}, \quad \frac{(J+1)^2-\ell^2}{(J+1)(2J+1)},$$

for the P, Q and R branches, respectively [38]. For simplicity, only two

values of ℓ were used, namely: $\ell=0$ for even values of v_2 and $\ell=1$ for odd values of v_2. $S_0=1600\ cm^{-1}atm^{-1}$ is the N_2O band strength at 300°K [81]. The term (v_3+1) arises from the vibrational matrix element of the ν_3 transition. Q(T) is the total partition function, approximated using

$$Q(T) = \frac{T}{\theta_{rot}} \times Q_{\nu_1} Q_{\nu_2}^2 Q_{\nu_3} , \qquad (A3.37)$$

where $Q_{\nu_i} = \left(1-\exp(-\frac{\theta_i^{vib}}{T})\right)^{-1}$, $\theta_{rot} = \frac{hc}{k} B_0$, and $\theta_i^{vib} = \frac{hc}{k} \omega_i^0$.

For each band, the position of the band gap was used as an approximation for the reference band center frequency $\bar{\nu}_0$.

A computer program was written to calculate the line strengths and positions in the various ν_3 sub-bands. Figure A3.4 shows significant CO and N_2O lines in the vicinity of the laser frequency ($1948<\nu<1950\ cm^{-1}$). CO lines are indicated using the two quantum numbers (v", J") of the ground level. From Fig. A3.4, it is clear that many lines of strength up to $0.001\ cm^{-2}atm^{-1}$ can potentially interfere with the measurement of CO.

Unfortunately, uncertainties in the spectroscopic parameters prohibit any prediction of precise positions for high-lying N_2O lines. It is therefore meaningless to introduce a realistic broadening function, and to compute precisely the N_2O absorption coefficient at the laser frequency. In order to estimate the magnitude of the N_2O background spectrum, it was assumed that each rotational line centered at ν_0 is broadened by a rectangular line shape factor ϕ^* of full width at half maximum $2\times B_\nu$, the average rotational line spacing,

$$\phi^* = \frac{1}{2B_\nu} \text{ for } \nu_0-B_\nu < \nu < \nu_0+B_\nu ,$$
$$\phi^* = 0 \text{ otherwise.} \qquad (A3.38)$$

Note that ϕ^* is properly normalized,

$$\int_{-\infty}^{+\infty} \phi^*(\nu)\, d\nu = 1. \qquad (A3.39)$$

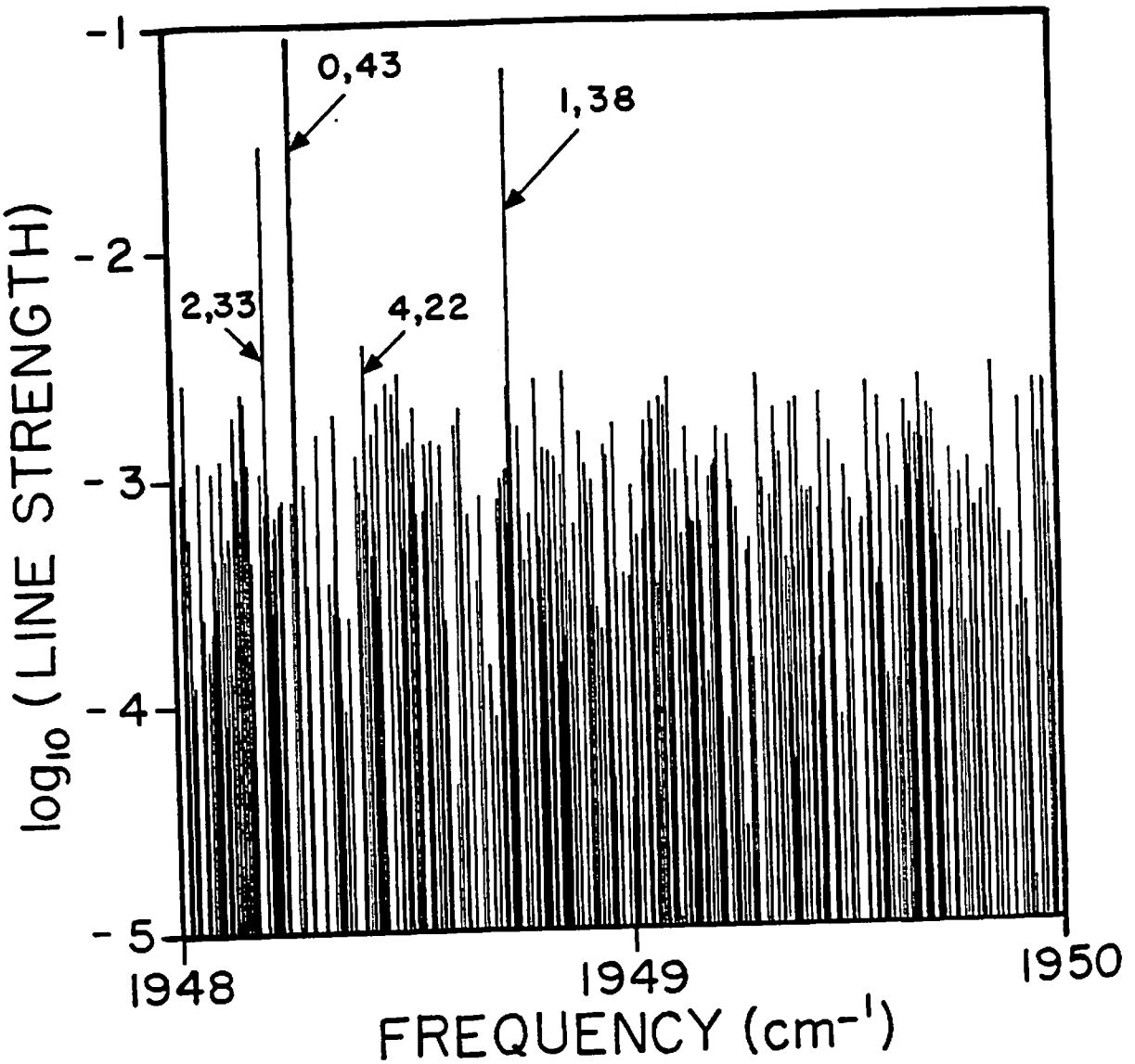

Fig. A3.4 Computed CO and N_2O IR absorption lines around the laser frequency (1948 cm^{-1}) at T=2000°K. The CO absorption lines are indicated using the ground state quantum numbers (v,J). The line used in this study is labeled (v=1,J=38). The abscissa shows vacuum frequencies in cm^{-1} and the ordinate line strengths in cm^{-2} atm^{-1}.

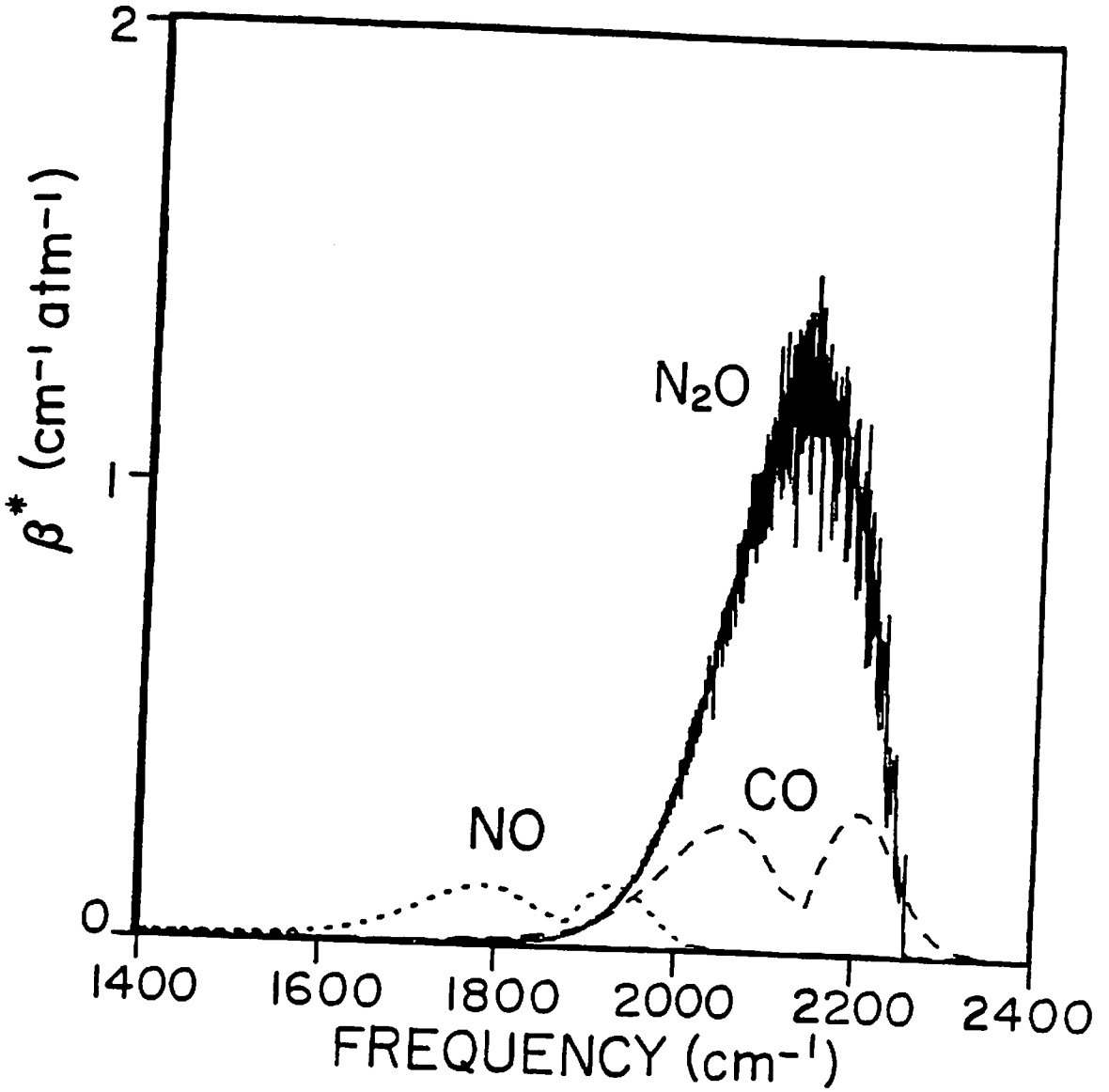

Fig. A3.5 Computed N_2O, CO and NO IR absorption spectra at T=2000°K using ϕ^*, the approximate line shape function of eq. (A3.38).

The simplicity of this broadening function results in a significant reduction of the computing time. The inherent breadth of the function ϕ^* results in the overlap of numerous adjacent lines (see Fig. A3.4). The corresponding absorption coefficient β^* thus provides a crude estimate of the actual absorption spectrum,

$$\beta^* = \sum_{\text{lines}} S(\nu,T)\,\phi^* \quad (\text{cm}^{-1}\text{atm}^{-1}) \,. \tag{A3.40}$$

Figure A3.5 shows a comparison of the CO, NO and N_2O absorption spectra β^* for T=2000°K. The N_2O absorption coefficient β^* at the laser frequency ν=1948 cm^{-1} is $\beta^*(N_2O)$=0.14 $cm^{-1}atm^{-1}$. Thus, the N_2O background absorption can be as high as 1.5% for typical shock tube experiments (T≈2000°K, p≈0.7 atm, χ_{N_2O}≈1%). In fact, interference levels of about 0.6% have been observed. Therefore, N_2O is a probable cause of the observed absorption background. Moreover, this effect could be discerned immediately after the shock arrival. This indicates that the interference can only result from a species present in the initial mixture. C_2N_2 exhibits vibrational bands in the same vicinity, but can be ruled out because of its weak band strength (S_0≈30 $cm^{-1}atm^{-1}$) [81]. Therefore, N_2O is certainly responsible for the observed background interference.

The computed CO(v=1) transmission profiles were corrected for the N_2O background prior to comparison with the experimental traces. The recorded absorption at time zero provided an empirical measurement of the N_2O absorption coefficient β_{N_2O}

$$\left(\frac{i}{i_0}\right)_{t=0} = \exp[-\,\beta_{N_2O}\;\; p_{N_2O}\; L] \,, \tag{A3.41}$$

and the computed transmission was corrected using

$$\begin{aligned}\left(\frac{i}{i_0}\right) &= \exp[-(\beta_{N_2O}\; p_{N_2O} + \beta_{CO(v=1)}\; p_{CO(v=1)})\; L] \\ &= \left(\frac{i}{i_0}\right)_{CO=1} \times \left(\frac{i}{i_0}\right)_{t=0}^{\chi_{N_2O}\,/(\chi_{N_2O})_{t=0}} \,,\end{aligned} \tag{A3.42}$$

where $(i/i_0)_{CO(v=1)}$ is the transmission of CO(v=1), $(i/i_0)_{t=0}$ the observed transmission at t=0 and χ_{N_2O} the computed mole fraction of N_2O.

Appendix 4

Additional Considerations on NCO Spectroscopy

Computational details on NCO spectroscopy, which were previously omitted for clarity, are presented in this appendix. These details include a systematic correction for the wavemeter measurements, a calculation of the electronic oscillator strength f_{el} using observed zero pressure radiative lifetimes, and theoretical estimates of the Franck-Condon factors of a polyatomic XYZ molecule.

A4.1 Systematic Wavemeter Correction

The wavemeter is an automatic interferometer which compares the number of interference fringes N_0 created by a reference wavelength λ_0 to the number of fringes N created by an unknown laser wavelength λ. The number of fringes per unit displacement of the interferometer mirrors is inversely proportional to the wavelength, and

$$\frac{\lambda}{\lambda_0} = \frac{N_0}{N} . \tag{A4.1}$$

The quantity displayed on the digital readout is automatically computed using

$$\lambda^{meas} = \left(\frac{N_0}{N}\right) \times \lambda_0^{vac}. \tag{A4.2}$$

For a vacuum wavemeter,

$$\frac{N_0}{N} = \frac{\lambda^{vac}}{\lambda_0^{vac}}, \text{ thus } \lambda^{meas} = \lambda^{vac}. \tag{A4.3}$$

By contrast, if the wavemeter is held at atmospheric pressure,

$$\frac{N_0}{N} = \frac{\lambda^{air}}{\lambda_0^{air}}, \text{ and } \lambda^{meas} = \frac{\lambda^{air}}{\lambda_0^{air}} \times \lambda_0^{vac}. \tag{A4.4}$$

Using the index of refraction of air $n(\lambda)$, $\lambda^{vac} = \lambda^{air} \times n(\lambda)$, and

$$\lambda^{meas} = \lambda_0^{vac} \times \frac{\lambda^{vac}}{\lambda_0^{vac}} \times \frac{n(\lambda_0)}{n(\lambda)} = \lambda^{vac} \times \frac{n(\lambda_0)}{n(\lambda)} \ . \qquad (A4.5)$$

To infer the true vacuum wavelength λ^{vac} from the measured quantity λ^{meas}, a correction

$$\frac{\Delta\lambda}{\lambda} = \frac{\lambda^{meas} - \lambda^{vac}}{\lambda^{vac}} = \varepsilon(\lambda_0) - \varepsilon(\lambda) \ , \qquad (A4.6)$$

where $\varepsilon(\lambda)=n(\lambda)-1$, is computed. This correction is negligible for wavelengths near the reference λ_0 (e.g., for most wavelengths accessible with the R6G dye). However, the correction can be substantial for values of λ further away from λ_0. Using Cauchy's formula for $n(\lambda)$ (with λ in Å) [87],

$$\varepsilon(\lambda) \times 10^7 = 2726.43 + \frac{12.288\ 10^8}{\lambda^2} + \frac{3.555\ 10^{15}}{\lambda^4} \ . \qquad (A4.7)$$

It follows that

$$\frac{\Delta\lambda}{\lambda} \doteq 122.88 \left(\frac{1}{\lambda_0^2} - \frac{1}{\lambda^2}\right) + 3.555\ 10^8 \left(\frac{1}{\lambda_0^4} - \frac{1}{\lambda^4}\right) \ . \qquad (A4.8)$$

For λ_0=6329.91 Å (He-Ne wavelength, vac.) and λ=4404.79 Å (NCO band head), $\Delta\lambda/\lambda=-4\ 10^{-6}$, which corresponds to about two increments of the last wavemeter digit. Note that the peak absorption of the $P_2+{}^PQ_{12}$ bandhead of NCO was observed at $\lambda^{meas}=440.477_5$. The resulting correction indicates that the true peak lies at $\lambda^{vac}=440.479_3$ nm; this value agrees well with the prediction of the spectroscopic model (see Fig. 4.6).

In principle, an additional correction should be introduced to account for the temperature dependence of $n(\lambda)$. Using a correlation available in the CRC handbook [87],

$$\frac{\varepsilon(\lambda,T)}{\varepsilon(\lambda,T_0)} = \frac{1}{[1+\alpha(T-T_0)]} = \frac{(\Delta\lambda/\lambda)_T}{(\Delta\lambda/\lambda)_{T_0}} \ . \qquad (A4.9)$$

Using the average value $\bar{\alpha}=3690.10^{-6}\ K^{-1}$ in the range $4400<\lambda<6350$ Å and T_0=15°K, the additional temperature correction corresponding to an

excursion of ±50°C in the room temperature is less than 2/10th of the last wavemeter digit and can therefore be neglected.

A4.2 Electronic Oscillator Strength and Lifetime Measurements

Laser-induced fluorescence experiments (LIF) can provide measurements of excited state lifetimes, if the duration of the laser pulse is much shorter than the decay of the fluorescence signal. Such measurements have been performed for both electronic transitions of NCO at 305 and 440 nm. In this paragraph, the extraction of electronic oscillator strengths f_{el} from these lifetime measurements will be examined.

Laser-induced fluorescence can be regarded as a two-step process consisting of a fast pumping of the molecule to an upper state, followed by a spontaneous fluorescence decay of finite lifetime τ. A plot of τ vs. pressure can be extrapolated to provide a zero pressure radiative lifetime of the upper state. At zero pressure, and in the absence of predissociation or curve-crossing, fluorescence can only occur from the spontaneous decay of the original upper state, since collisions are otherwise required to redistribute the energy among the various upper levels. On the other hand, transitions to the lower electronic state are restricted by selection rules (eg: $\Delta J = J' - J'' = 0, \pm 1$). An example of zero pressure LIF has been sketched in Fig. A4.1. In general, the inverse lifetime τ^{-1} can be written as a function of the Einstein A-coefficients for the allowed transitions ($\ell \equiv$lower state, $u \equiv$upper state),

$$\tau^{-1} = \sum_{\ell} A_{u \to \ell}. \qquad \text{(A4.10)}$$

The Einstein A-coefficients are related to the absorption oscillator strength using

$$A_{u \to \ell} = \frac{g_\ell}{g_u} \frac{2\Pi e^2}{\varepsilon_0 mc} \nu_{u\ell}^2 f_{u \leftarrow \ell} = 0.667 \frac{g_\ell}{g_u} \nu_{u\ell}^2 f_{u \leftarrow \ell}, \qquad \text{(A4.11)}$$

where g is the population degeneracy, $\nu_{u\ell}$ is the transition frequency (cm^{-1}), $f_{u \leftarrow \ell}$ is the absorption oscillator strength and $A_{u\ell}$ is the Einstein A-coefficient (sec^{-1}). For NCO, a particular rovibronic state has

a degeneracy $g=2(v_2+1)(2J+1)$; there are two levels arising from the possible orientation of the electronic angular momentum, (v_2+1) degenerate bendings and $(2J+1)$ degenerate rotational levels. In this case, the absorption oscillator strength can be written $f_{u\leftarrow\ell}=f_{v''\leftarrow v'',J'\leftarrow J''}$, where v is a short hand notation for $(v_1 v_2^K v_3)$. Assuming that the transition frequencies are nearly constant over the whole band system $(\nu_{u\ell} \approx \bar{\nu})$, and that the electronic transition moments R_e are independent of the vibrational state [88], the oscillator strength of a vibrational progression can be related to a common "electronic oscillator strength" f_{el} using

$$f_{v'v''J'J''} \approx f_{el} \frac{q_{v'v''}}{(v_2''+1)} \frac{S_{J'J''}}{(2J''+1)} , \qquad (A4.12)$$

where $q_{v'v''}$ is the Franck-Condon factor for the $(v'_1 v'^{K'}_2 v'_3) \leftarrow (v''_1 v''^{K''}_2 v''_3)$ band and $S_{J'J''}$ the rotational line strength. Substituting eqs. (A4.11) and (A4.12) in eq. (A4.10),

$$\tau^{-1} \approx 0.667 \sum_{v''J''} \frac{2(v_2''+1)(2J''+1)}{2(v_2'+1)(2J'+1)} \bar{\nu}^2 f_{el} \frac{q_{v'v''}}{v_2''+1} \frac{S_{J'J''}}{2J''+1} . \qquad (A4.13)$$

Note that an average transition frequency $\bar{\nu}$ was used to ensure consistency with the corresponding assumption on f_{el}. Factorizing eq. (A4.13),

$$\tau^{-1} \approx 0.667 \bar{\nu}^2 f_{el} \frac{\sum_{v''} q_{v'v''}}{v_2'+1} \frac{\sum_{J''} S_{J'J''}}{(2J'+1)} . \qquad (A4.14)$$

By convention, Franck-Condon factors and rotational line strengths are normalized according to

$$\sum_{v'} q_{v'v''} = v''_2+1, \text{ or } \sum_{v''} q_{v'v''} = v'_2+1 , \qquad (A4.15)$$

and

$$\sum_{J'} S_{J'J''} = 2J''+1, \text{ or } \sum_{J''} S_{J'J''} = 2J'+1 . \qquad (A4.16)$$

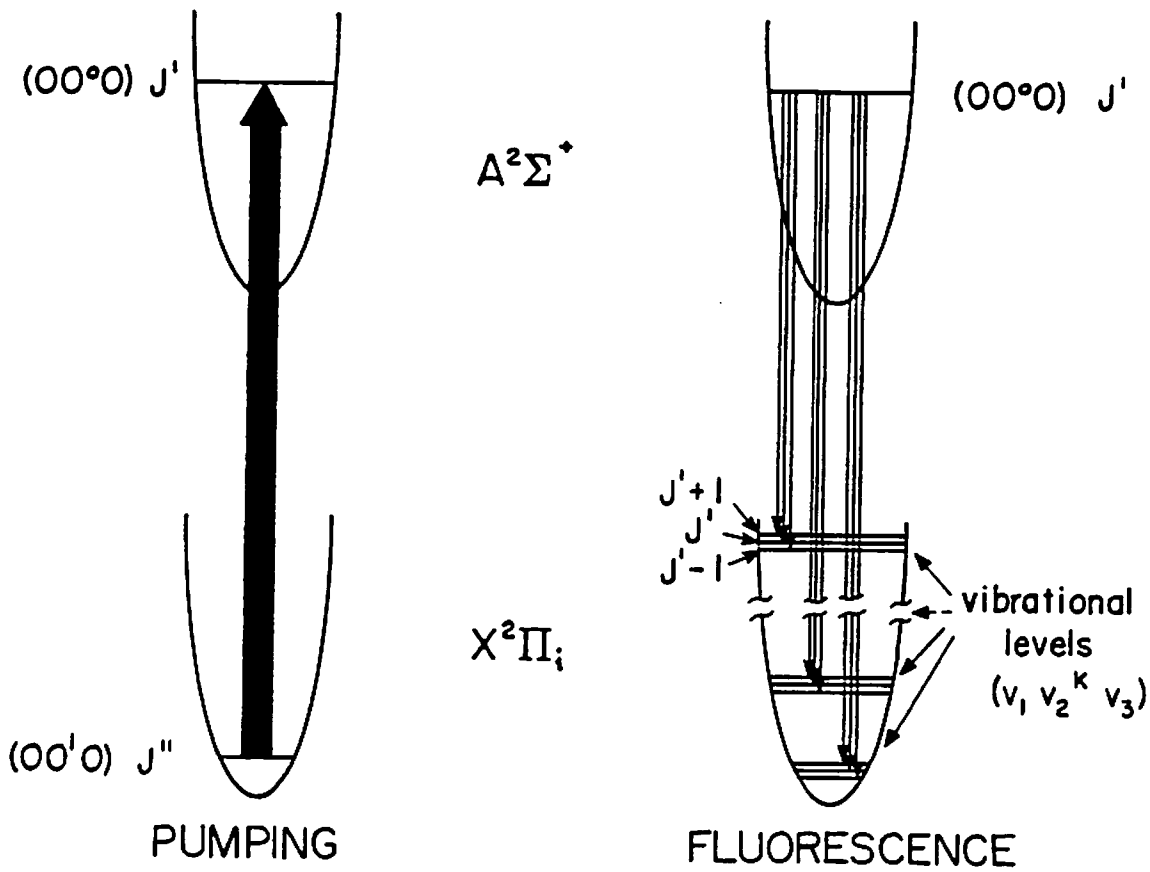

Fig. A4.1 A schematic of a zero pressure laser-induced-fluorescence (LIF) experiment, in the absence of predissociation or curve-crossing effects.

It follows that eq. (A4.14) can be simplified to read

$$\tau^{-1} \approx 0.667\ \bar{\nu}^{\,2}\ f_{el}\ . \qquad \text{(A4.17)}$$

This expression is valid at zero pressure for any upper level pumped, as long as it is meaningful to define an electronic oscillator strength f_{el}. Thus, the measured lifetimes of different excited upper states are expected to be inversely proportional to the average fluorescence frequency squared $\bar{\nu}^{\,2}$ and to be independent of vibrational progressions and Franck-Condon factors. This unintuitive fact has been confirmed by experimental observation. For example, note the measurements of Charlton, et al. [56] for the lifetimes of the $A^2\Sigma^+$ state of NCO (Table A4.1).

Using eq. (A4.17) and the fluorescence measurements of Sullivan, et al. [60] for the $B^2\Pi_1$ state of NCO (τ=63±3 nsec), the oscillator strength for the $[B^2\Pi_1 \leftarrow X^2\Pi_1]$ transition at 305 nm is

$$f_{el} = \frac{\tau^{-1}}{0.667\ \bar{\nu}^{\,2}} = 1/(0.667 \times 32822^2 \times 63\ 10^{-9}) \approx 0.022\ .$$

This value was utilized in chapter 4 to extract an experimental Franck-Condon factor q_{10} for the $(10^10) \leftarrow (00^10)$ band of NCO ($q_{10} \approx 0.14$).

Table A4.1 - Lifetimes of the $A^2\Sigma^+$ State of NCO

Vibronic level	$\bar{\nu}(cm^{-1})$	Lifetimes (nsec)
$00^00\ ^2\Sigma^+$	22700	361
$01^10\ ^2\Pi$	23380	357
$10^00\ ^2\Sigma^+$	23990	322
$02^00\ ^2\Sigma^+$	24090	328
$00^01\ ^2\Sigma^+$	25040	351

A4.3 Theoretical Estimates of NCO Franck-Condon Factors

In the Born-Oppenheimer approximation, the intensity of an electric dipole transition is proportional to the square of the vibrational overlap integral

$$\left|\int \Psi'^{*}_{vib}\, \Psi''_{vib}\, dR\right|^2 = \left|\langle v'|v''\rangle\right|^2, \tag{A4.18}$$

which is also known as the Franck-Condon factor for the $v' \leftarrow v''$ band [89]. Franck-Condon factors have been extensively studied both theoretically and experimentally for a variety of diatomic molecules, but limited attention has been devoted to the more complex polyatomic molecules. Smith and Warsop [57] provided formulae for estimating Franck-Condon factors of vibrational progressions originating from the vibrationless ground state of polyatomic molecules. Assuming no interaction among normal modes of vibration, Smith and Warsop reported overlap integrals for non-degenerate vibrational transitions [e.g., $NCO(v'_1 \leftarrow v''_1=0)$],

$$\langle v|0\rangle = R(v,0) = \frac{(-i)^v\, 2^{-(v-1)/2}}{(v!)^{1/2}} \left(\frac{\beta}{1+\beta^2}\right)^{1/2} \left(\frac{1-\beta^2}{1+\beta^2}\right)^{v/2} \times \exp\left(-\frac{1}{2}\frac{\gamma^2\beta^2}{1+\beta^2}\right) \times H_v\left(i\beta^2\gamma(1-\beta^4)^{-1/2}\right) \tag{A4.19}$$

where H_v is the Hermite polynomial of degree v, $\beta=\alpha''/\alpha'=(\nu_i''/\nu_i')^{1/2}$, $\gamma=\alpha' d_i$ and $\alpha^2=4\pi^2\nu_i c/h$, ν_i is the vibration frequency (cm^{-1}), d_i is the projection of vector **d** along the vibrational coordinate of interest (see below). Using eq. (A4.18), the Franck-Condon factors for the $(v \leftarrow 0)$ band can be written

$$q_{v0} = R^{*}(v,0)\, R(v,0)\ , \tag{A4.20}$$

where R^* is the complex conjugate of R. Calculation of the overlap integrals of eq. (A4.19) require an evaluation of **d**, the vectorial separation of the origins of normal coordinates in the upper and lower levels. From Sharp and Rosenstock [58],

$$d = (\mathbf{L})^{-1}\mathbf{R} \ , \tag{A4.21}$$

where **L** is a matrix of rank (3N-6) and R is the vector of changes in equilibrium positions from the initial to the final states,

$$\mathbf{R} = \mathbf{S}''-\mathbf{S}' \ ; \tag{A4.22}$$

S is the vector of internal displacement coordinates. The matrix L satisfies the general relation [58]

$$\mathbf{L}^{\dagger}\ \mathbf{G}^{-1}\ \mathbf{L} = \mathbf{E} \ , \tag{A4.23}$$

where $\mathbf{L}^{\dagger}$ is the Hermitian conjugate of **L**, **E** is the identity matrix, and G is the kinetic energy matrix (see below). Following the choice of Sharp and Rosenstock [58], S represents the set of internal symmetry coordinates in the calculation of **G** and **R**.

For a linear molecule such as NCO, these coordinates can be written as a function of Δr_1 and Δr_2, the linear displacements from the equilibrium position, and $\Delta\phi$, the angular displacement (see Fig. A4.2),

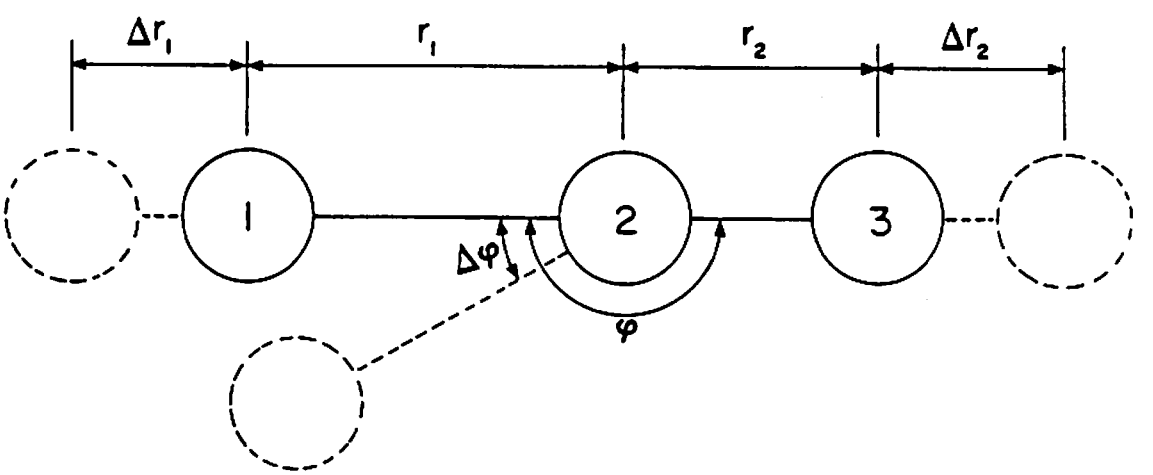

Fig. A4.2 A schematic of the three internal symmetry coordinates of a linear XYZ molecule.

$$S = \begin{vmatrix} \frac{\sqrt{2}}{2}(\Delta r_1+\Delta r_2) \\ (r_1 r_2)^{1/2}\ \Delta\phi \\ \frac{\sqrt{2}}{2}(\Delta r_1-\Delta r_2) \end{vmatrix} . \qquad (A4.24)$$

The matrix G and the normal vibration modes of the XYZ molecule can be found using the "effectiveness vectors" [89] $\mathbf{s}_{t\alpha}$ (α is the atom index and t is the index of the normal vibration). Note that s_t are the three coordinates of the vector **S**. The vectors $\mathbf{s}_{t\alpha}$ are defined such that

- $\mathbf{s}_{t\alpha}$ points in the direction in which moving atom α causes the largest increase in the internal coordinate s_t. (In this case, only atom α is moving.)
- the magnitude of $\mathbf{s}_{t\alpha}$ equals the maximum change in s_t produced by moving atom α a unit distance.

Figure A4.3 illustrates the calculation of $\mathbf{s}_{t\alpha}$. Note the cartesian coordinates ($\mathbf{e}_1$, $\mathbf{e}_2$). The vertical bars attached to an atom indicate that the atom is "frozen" in its equilibrium position for the purpose of estimating $\mathbf{s}_{t\alpha}$. Using the "effectiveness vectors" $\mathbf{s}_{t\alpha}$, the normal modes of vibration of an XYZ molecule are sketched in Fig. A4.4. The matrix G can be calculated using [89]

$$G_{tt'} = \sum_{\alpha} \mu_\alpha\, s_{t\alpha}\, s_{t'\alpha} , \qquad (A4.25)$$

where $\mu_\alpha = 1/m_\alpha$ is the inverse mass of atom α (amu^{-1}),

$$G = \begin{vmatrix} (\mu_1+\mu_3)/2 & 0 & (\mu_1-\mu_3)/2 \\ 0 & \mu_1 \frac{r_2}{r_1} + \mu_2 (\frac{r_2}{r_1}) \left(1+\frac{r_1}{r_2}\right)^2 + \mu_3 \frac{r_1}{r_2} & 0 \\ (\mu_1-\mu_3)/2 & 0 & 2\mu_2+(\mu_1+\mu_3)/2 \end{vmatrix} \qquad (A4.26)$$

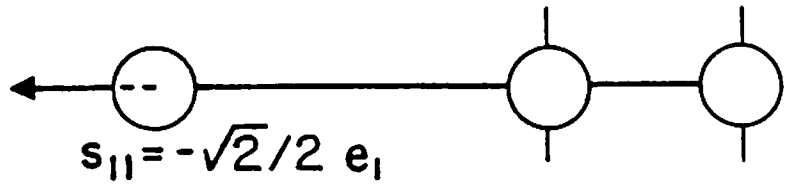

Maximum change in Δr_1 is obtained by moving atom 1 in the $-e_1$ direction; displacement of atom 1 over a unit distance results in a $\sqrt{2}/2$ change in s_1.

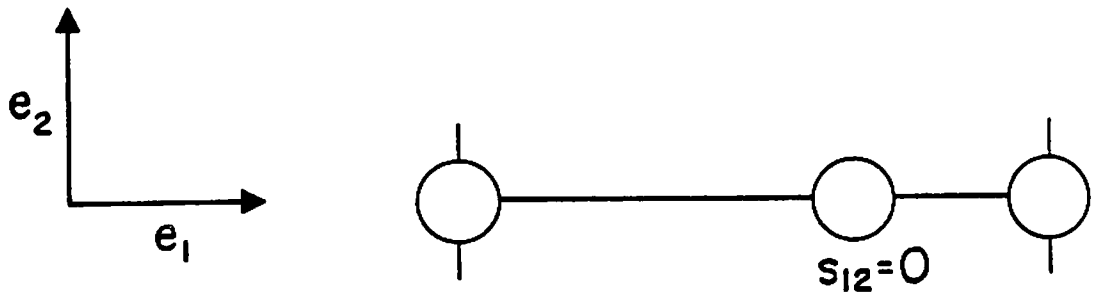

With atoms 1 and 2 "frozen" in their equilibrium position, no change in atom 2 can affect the sum $\Delta r_1 + \Delta r_2$.

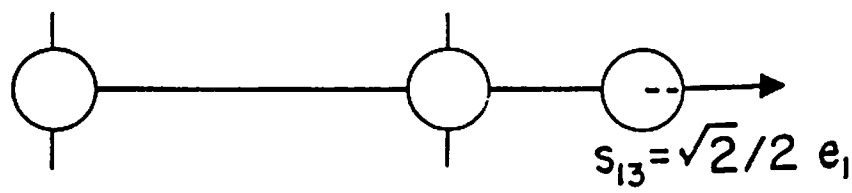

Fig. A4.3 Calculation of the effectiveness vectors $s_{t\alpha}$ of a linear XYZ molecule.

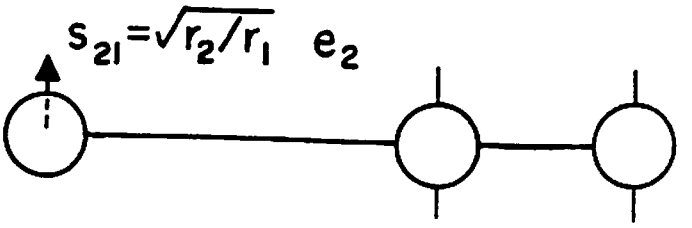

Maximum change in $\Delta\phi$ is obtained by moving atom 1 in the e_2 direction. Displacement of atom 1 over a unit distance corresponds to $\Delta\phi=1/r_1$.

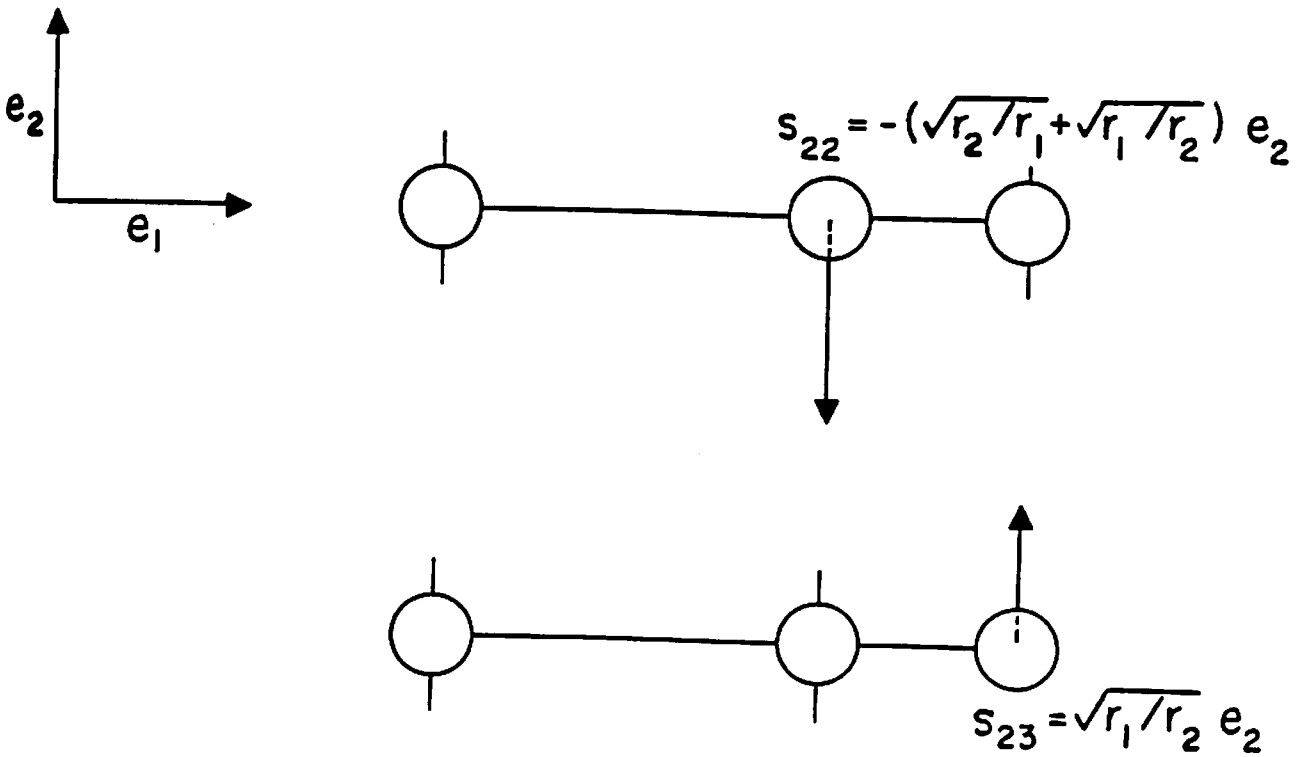

Fig. A4.3 Calculation of the effectiveness vectors $s_{t\alpha}$ of a linear XYZ molecule (continued).

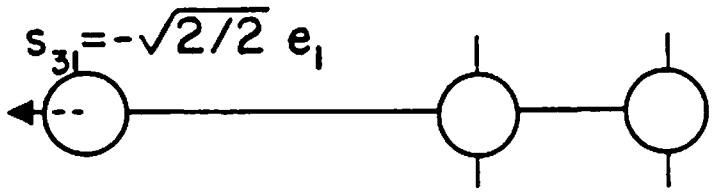

Maximum change in Δr_1 is obtained by moving atom 1 in the e_1 direction.

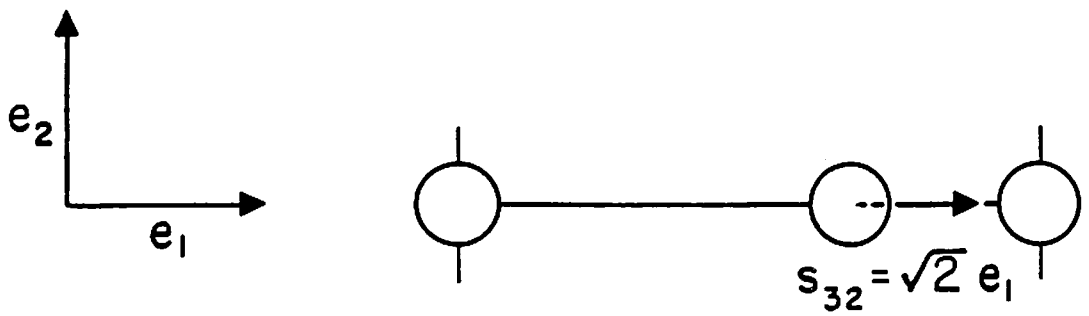

Maximum change in $\Delta r_1 - \Delta r_2$ is obtained by moving atom 2 in the e_1 direction. Displacement of atom 2 over a unit distance corresponds to a $2 \times \sqrt{2}/2$ change of s_3.

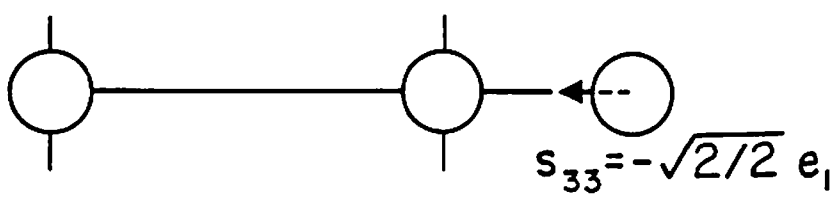

Fig. A4.3 Calculation of the effectiveness vectors $s_{t\alpha}$ of a linear XYZ molecule (continued).

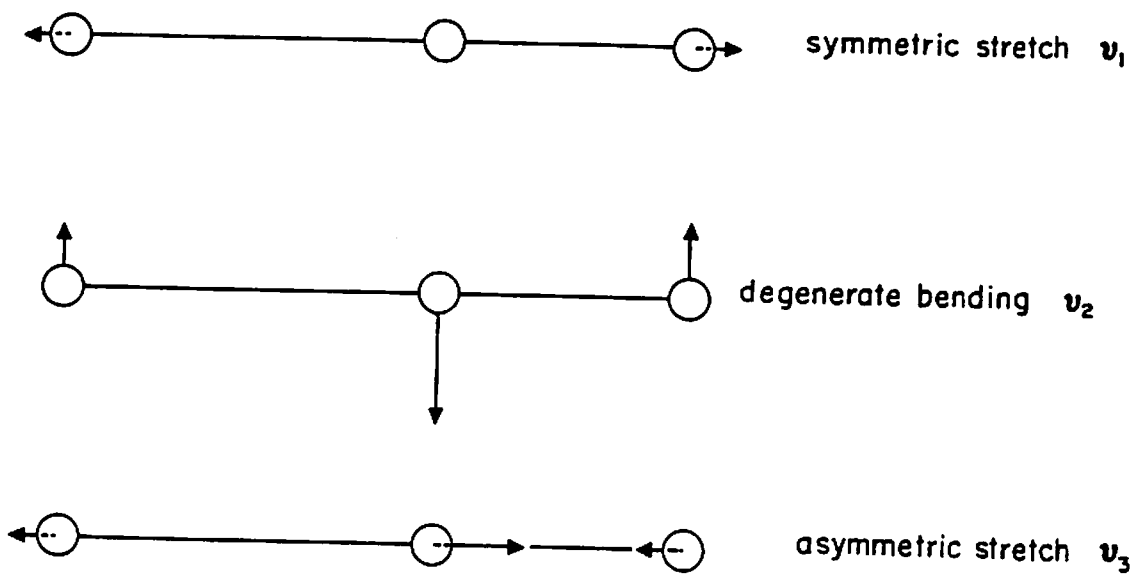

Fig. A4.4 A schematic of the three normal modes of vibration of a linear XYZ molecule.

To find **L**, the matrix eq. (A4.23) $\mathbf{L}^{\dagger}\ \mathbf{G}^{-1}\ \mathbf{L} = \mathbf{E}$ must be solved. Since **G** is a real matrix, **L** is real and eq. (A4.23) is equivalent to ${}^{t}\mathbf{L}\ \mathbf{G}^{-1}\ \mathbf{L} = \mathbf{E}$, where ${}^{t}\mathbf{L}$ is the transpose of **L**. To solve for **L**, **G** is diagonalized by looking for a matrix **U** such that $\mathbf{G} = \mathbf{U}\ \mathbf{G}_d\ \mathbf{U}^{-1}$ with $\mathbf{G}_d$ a diagonal matrix. Since **G** is symmetric, **U** can be chosen orthonormal, with ${}^{t}\mathbf{U} = \mathbf{U}^{-1}$. In this case, the matrix $\mathbf{L} = \mathbf{U}\ \mathbf{G}_d^{1/2}\ {}^{t}\mathbf{U}$ satisfies the equation ${}^{t}\mathbf{L}\ \mathbf{G}^{-1}\ \mathbf{L} = \mathbf{E}$, since:

$$ {}^{t}\mathbf{L}\ \mathbf{G}^{-1}\ \mathbf{L} = \mathbf{U}\ \mathbf{G}_d^{1/2}\ {}^{t}\mathbf{U}\ \mathbf{U}\ \mathbf{G}_d^{-1}\ {}^{t}\mathbf{U}\ \mathbf{U}\ \mathbf{G}_d^{1/2}\ {}^{t}\mathbf{U} = \mathbf{E}. \qquad \text{(A4.27)} $$

To find $\mathbf{G}_d$ and **U**, the secular equation in the **G** eigenvalues is solved

$$ \left(\left(\frac{\mu_1+\mu_3}{2} - \lambda\right)\left(\frac{\mu_1+\mu_3}{2} + 2\mu_2 - \lambda\right) - \left(\frac{\mu_1-\mu_3}{2}\right)^2\right)(G_{22} - \lambda) = 0. \qquad \text{(A4.28)} $$

Thus, the eigenvalues of **G** are

$$ \lambda_1 = \lambda_0 + \delta,\ \lambda_2 = G_{22} \text{ and } \lambda_3 = \lambda_0 - \delta, \qquad \text{(A4.29)} $$

where $$ \lambda_0 = \mu_2 + (\mu_1+\mu_3)/2 \text{ and } \delta^2 = \mu_2^2 + (\mu_1-\mu_3)^2/4. \qquad \text{(A4.30)} $$

A set of eigenvectors is chosen, and

$$ \mathbf{U} = \begin{vmatrix} \dfrac{\mu_1-\mu_3}{2\Delta_1} & 0 & \dfrac{\mu_1-\mu_3}{2\Delta_2} \\ 0 & 1 & 0 \\ \dfrac{\mu_2+\delta}{\Delta_1} & 0 & \dfrac{\mu_2-\delta}{\Delta_2} \end{vmatrix} \qquad \text{(A4.31)} $$

where $$ \Delta_1^2 = \left(\frac{\mu_1-\mu_3}{2}\right)^2 + (\mu_2+\delta)^2 \text{ and } \Delta_2^2 = \left(\frac{\mu_1-\mu_3}{2}\right)^2 + (\mu_2-\delta)^2. \qquad \text{(A4.32)} $$

The matrix **L** is given by

$$ \mathbf{L} = \begin{vmatrix} L_{11} & 0 & L_{13} \\ 0 & L_{22} & 0 \\ L_{31} & 0 & L_{33} \end{vmatrix}, \qquad \text{(A4.33)} $$

where
$$L_{11} = \left(\frac{\mu_1-\mu_3}{2}\right)^2 \left(\frac{\lambda_1^{1/2}}{\Delta_1^2} + \frac{\lambda_3^{1/2}}{\Delta_2^2}\right) , \tag{A4.34}$$

$$L_{31} = L_{13} = \left(\frac{\mu_1-\mu_3}{2}\right) \left(\frac{\lambda_1^{1/2}}{\Delta_1^2} (\mu_2+\delta) + \frac{\lambda_3^{1/2}}{\Delta_2^2} (\mu_2-\delta)\right) , \tag{A4.35}$$

$$L_{33} = \frac{\lambda_1^{1/2}}{\Delta_1^2} (\mu_2+\delta)^2 + \frac{\lambda_3^{1/2}}{\Delta_2^2} (\mu_2-\delta)^2 , \tag{A4.36}$$

and
$$L_{22} = \sqrt{G_{22}} . \tag{A4.37}$$

Finally,

$$\mathbf{L}^{-1} = \begin{vmatrix} \frac{L_{33}}{\Theta} & 0 & -\frac{L_{31}}{\Theta} \\ 0 & \frac{1}{\sqrt{G_{22}}} & 0 \\ -\frac{L_{13}}{\Theta} & 0 & \frac{L_{11}}{\Theta} \end{vmatrix} . \tag{A4.38}$$

where
$$\Theta^2 = (L_{11}L_{33}-L_{13}L_{31})^2 = \mu_2(\mu_1+\mu_3)+\mu_1\mu_3 .$$

To evaluate the vector **d**, one calculates **R**, the change in equilibrium positions from the initial to the final states. Since NCO maintains a linear configuration in its electronic transition,

$$\mathbf{R} = \frac{\sqrt{2}}{2} \begin{vmatrix} (r_1''+r_2'') - (r_1'+r_2') \\ 0 \\ (r_1''-r_2'') - (r_1'-r_2') \end{vmatrix} . \tag{A4.39}$$

Using $\rho \equiv r_1+r_2$ and assuming that the ratio (r_1/r_2) is conserved in the electronic transition,

$$\mathbf{R} = \frac{\sqrt{2}}{2} (\rho''-\rho') \begin{vmatrix} 1 \\ 0 \\ c \end{vmatrix} , \text{ with } c = \frac{(r_1/r_2) - 1}{(r_1/r_2) + 1} . \tag{A4.40}$$

Finally,

$$\mathbf{d} = \mathbf{L}^{-1}\mathbf{R} = \frac{\sqrt{2}}{2}(\rho''-\rho') \begin{vmatrix} \frac{L_{33}-L_{31}c}{\theta} \\ 0 \\ \frac{-L_{13}+L_{11}c}{\theta} \end{vmatrix} . \qquad (A4.41)$$

Note the dimensions of the following variables:

vector **R**	L
matrix **L**	$M^{-1/2}$
matrix **G**	M^{-1}
vector **d**	$M^{1/2}L$
scalar α	$M^{-1/2}L^{-1}$
γ, β, R(v,0)	no units

If d_i is evaluated in Å.amu$^{1/2}$, and ν_i' is the vibrational frequency of the upper state (cm^{-1}), then

$$\gamma = 0.1722\ \nu'_i{}^{1/2}(\mathrm{cm}^{-1/2})\ d_i(\text{Å.amu}^{1/2}). \qquad (A4.42)$$

To calculate the Franck-Condon factor of the transition [$B^2\Pi_i(10^10)$← $X^2\Pi_i(00^10)$], the quantities $d_1 = \sqrt{2}/2\ (\rho''-\rho')\ (L_{33}-L_{31}c)/\theta$, which corresponds to the symmetric stretch ν_1, are evaluated. Assigning the indices 1,2 and 3 to the N, C and O atoms, respectively, $\mu_1=1/14$, $\mu_2=1/12$ and $\mu_3=1/16$ (amu^{-1}), $L_{33}=0.4833$ amu$^{-1/2}$, $L_{31}=0.0060$ amu$^{-1/2}$, and $\theta=0.125$ amu^{-1}. Dixon [59] calculated upper bounds of (r_1+r_2) for the X, A and B states of NCO: $\rho'(B^2\Pi_i)<2.45$ Å, $\rho''(X^2\Pi_i)<2.408$ Å. Since d_1 depends only on the difference $(\rho''-\rho')$, these upper bounds can provide reasonable estimates of $(\rho''-\rho') \approx 2.408-2.45= -0.042$ Å. Note that Milligan and Jacox [54] found $r_1''=1.23$ Å and $r_2''=1.18$ Å for the lower state. Assuming that the ratio r_1/r_2 is conserved in the transition,

$$c = \frac{(r_1/r_2)-1}{(r_1/r_2)+1} \approx 0.0207 \text{ and } d_1 \approx -0.1148 \text{ Å.amu}^{1/2}. \tag{A4.43}$$

Using $\nu''_1 = 1047$ cm^{-1} [59] and $\nu_1' = 1275$ cm^{-1} [54], it follows that $\gamma \approx -0.7059$, $\beta \approx 0.9062$, and

$$R(1,0) = -i \left(\frac{\beta}{1+\beta^2}\right)^{1/2} \left(\frac{1-\beta^2}{1+\beta^2}\right)^{1/2} \exp\left(-\frac{1}{2}\frac{\gamma^2\beta^2}{1+\beta^2}\right)$$
$$\times\ 2i\ \beta^2\gamma(1-\beta^4)^{-1/2} = -0.4013\ . \tag{A4.44}$$

Finally,

$$q_{10} = R(1,0)^2 = 0.1611.$$

This theoretical estimate agrees within 15% with the present experimental value $q_{10} \approx 0.14(-0.06,+0.16)$.

A similar calculation can be performed for the $[A^2\Sigma^+(00^00) \leftarrow X^2\Pi_i(00^10)]$ transition of NCO. With $\nu_1' = 1324$ cm^{-1} [48], $\rho''-\rho' \approx 2.408-2.369 \approx 0.039$ Å, it follows that $d_1 \approx 0.1066$ Å.amu$^{1/2}$, $\beta \approx 0.8893$ and $\gamma \approx 0.6679$. Using

$$R(0,0) = \sqrt{2}\left(\frac{\beta}{1+\beta^2}\right)^{1/2} \exp\left(-\frac{1}{2}\frac{\gamma^2\beta^2}{1+\beta^2}\right), \tag{A4.45}$$

then

$$R(0,0) \approx 0.90$$

and

$$q_{00} \approx 0.81.$$

This estimate is again in good agreement with the experimental determination in chapter 4,

$$q_{00} \approx 0.70(\pm 0.30).$$

Appendix 5

Spectroscopic Programs

This appendix contains four computer programs written in Fortran. The input/output calls are compatible with the Hewlett-Packard 1000 MX series computers. The reader is directed to the program comments for computational details.

Program LCN calculates the broad-band absorption of CN around 388 nm. Program PART computes the partition function of NCO using the complete formulation of Hougen [49] (see eq. 4.10). Programs LNCOA and LNCOB calculate the semi-quantitative spectroscopy of NCO around 440 and 305 nm, respectively.

Program LCN

```
 2:59 PM  THU.,  2  AUG., 1984
LSLCN  T=ØØØØ4 IS ON CR GØ   USING ØØØ24 BLKS R=ØØØØ

ØØØ1  FTN4,L
ØØØ2  SEMA (XYZ,Ø)
ØØØ3        PROGRAM LCN
ØØØ4  CCCCCCCCCCCCCCCCCCCCCCCCCCCCCCCCCCCCCCCCCCCCCCCCCCCCCCCCCCCCCCCCCCCC
ØØØ5  C
ØØØ6  C This program calculates the broad band absorption of the CN transition
ØØØ7  C B2sigma+ <-- X2sigma+. It takes into account the v"=Ø to v'=Ø
ØØØ8  C and v"=1 to v'=1 vibrational bands.
ØØØ9  C The optical setup includes a high pressure mercury lamp,the shock
ØØ1Ø  C tube and a monochromator.
ØØ11  C
ØØ12  CCCCCCCCCCCCCCCCCCCCCCCCCCCCCCCCCCCCCCCCCCCCCCCCCCCCCCCCCCCCCCCCCCCC
ØØ13  C
ØØ14  C  MICHEL LOUGE 1982
ØØ15  C
ØØ16  CCCCCCCCCCCCCCCCCCCCCCCCCCCCCCCCCCCCCCCCCCCCCCCCCCCCCCCCCCCCCCCCCCCC
ØØ17  C
ØØ18  C The following data is currently incorporated in the program:
ØØ19  C
ØØ2Ø  C   MWCN............... CN molecular weight (gmole)
ØØ21  C   MWCP............... Collision partner mol.weight (gmole)
ØØ22  C   SIG................Collision cross-section diameter (Angstroms)
ØØ23  C   TE..................B2sigma+ electronic energy (cm-1)
ØØ24  C   LØ..................Monochromator dial setting in air (Angstroms)
ØØ25  C   DX..................Entrance slit width (mm)
ØØ26  C   DY..................Exit slit width (mm)
ØØ27  C   ALPHA...............Monochromator dispersion (Angstrom/mm)
ØØ28  C   L ..................Shock tube diameter (cm)
ØØ29  C   NREF ...............Air index of refraction
ØØ3Ø  C
ØØ31  CCCCCCCCCCCCCCCCCCCCCCCCCCCCCCCCCCCCCCCCCCCCCCCCCCCCCCCCCCCCCCCCCCCC
ØØ32        DIMENSION S(5ØØØ), VO(2ØØ),NA1(3),NA2(3),NA3(3),IDCB(144)
ØØ33       *,IPRAM(5)
ØØ34        REAL L,INC,MWCN,MWCP,LØ,INCØ,JP,KJJ,KMAX,NREF,MONO,INC1
ØØ35        COMMON LØ,DX,DY,ALPHA
ØØ36        COMMON /XYZ/ AMON (5ØØØ)
ØØ37        CALL RMPAR (IPRAM)
ØØ38        CALL LUERR (ITERM)
ØØ39        ITERW=ITERM
ØØ4Ø        IF (IPRAM(1).EQ.5) ITERM=5
ØØ41        IF (IPRAM(1).EQ.5) ITERW=9
ØØ42  CCCCCCCCCCCCCCCCCCCCCCCCCCCCCCCCCCCCCCCCCCCCCCCCCCCCCCCCCCCCCCCCCCCC
ØØ43  C
ØØ44  C The following set of lines can be included to plot the
ØØ45  C transmission spectrum of CN.
ØØ46  C
ØØ47  CCCCCCCCCCCCCCCCCCCCCCCCCCCCCCCCCCCCCCCCCCCCCCCCCCCCCCCCCCCCCCCCCCCC
ØØ48  C     NA1(1)=2HLC
ØØ49  C     NA1(2)=2HN
ØØ5Ø  C     NA1(3)=2H
ØØ51  C     CALL CREAT (IDCB,IER,NA1(1),59Ø,4)
ØØ52  C     CALL CLOSE (IDCB)
ØØ53  CCCCCCCCCCCCCCCCCCCCCCCCCCCCCCCCCCCCCCCCCCCCCCCCCCCCCCCCCCCCCCCCCCCC
ØØ54        NFLAG=Ø
ØØ55        WRITE (ITERW,1Ø4)
ØØ56  1Ø4   FORMAT (//,5X,"If you want to calculate:",//,
ØØ57       *1ØX,"the transmission resulting from",/,
ØØ58       *1ØX,"a given CN mole fraction ........... enter Ø",
ØØ59       *//,
ØØ6Ø       *1ØX,"the effective oscillator strength fel",/,
ØØ61       *1ØX,"resulting from a calibration run ... enter 1",
```

```
      *//,
      *10X,"the CN mole fraction corresponding",/,
      *10X,"to a given transmission I/I0 ....... enter 2",
      *//)
       READ (ITERM,*) NADINE
       IF (NADINE.NE.0) GO TO 20
       WRITE (ITERW,100)
100    FORMAT (10X,"Please input:",/,
      *15X,"Pressure..........atm",/,
      *15X,"Temperature.......Kelvins",//)
       READ (ITERM,*) P,T
       WRITE (ITERW,112)
112    FORMAT (//,5X,"Individual calculation ... enter 0",/,
      *            5X,"Conversion of a mole fraction file",/
      *            5X,"to a transmission file ... enter 1",//)
       READ (ITERM,*) NAD
       IF (NAD.NE.1) WRITE (ITERW,116)
116    FORMAT (//,5X,"Enter the CN mole fraction....ppm",//)
       IF (NAD.NE.1) READ (ITERM,*) CHI
       IF (NAD.NE.1) WRITE (ITERW,118)
       IF (NAD.NE.1) READ (ITERM,*) NAD1
       IF (NAD1.EQ.1) NFLAG=3
118    FORMAT (//,5X,"Do you want an uncertainty analysis ?",/,
      *10X,"yes....enter 1",/,
      *10X,"no.....enter 0",//)
       IF (NAD.NE.1) GO TO 23
       WRITE (ITERW,113)
113    FORMAT (//,5X,"Enter kinetics file name...",//)
115    FORMAT (//,5X,"Output file name?...",//)
       READ (ITERM,114) (NA2(I),I=1,3)
114    FORMAT (3A2)
       WRITE (ITERW,115)
       READ (ITERM,114) (NA3(I),I=1,3)
       CALL CREAT (IDCB,IER,NA3(1),48,4)
       CALL CLOSE (IDCB)
       GO TO 23
20     IF (NADINE.NE.1) GO TO 21
       WRITE (ITERW,108)
108    FORMAT (10X,"Please input:",/,
      *15X,"Pressure...............atm",/,
      *15X,"Temperature............Kelvins",/,
      *15X,"Mole fraction..........ppm",/,
      *15X,"Experimental I/I0 .....per cent",//)
       READ (ITERM,*) P,T,CHI,TR0
       GO TO 23
21     IF (NADINE.NE.2) GO TO 22
       WRITE (ITERW,109)
109    FORMAT (10X,"Please input:",/,
      *15X,"Pressure...............atm",/,
      *15X,"Temperature............Kelvins",/,
      *15X,"Experimental I/I0 .....per cent",//)
       READ (ITERM,*) P,T,TR0
       GO TO 23
22     STOP
23     CONTINUE
       TR0=TR0*1.E-2
       HC=1.438789/T
       MWCN=26.0177
       MWCP=39.9480
       SIG=4.0
       TE=25751.8
       WRITE (ITERW,120)
120    FORMAT (5X,"Do you wish to enter the monochromator",
      *" characteristics ?",/,
```

```
      *10X,"yes.... enter 1",/,
      *10X,"no .... enter 0",//)
       READ (ITERM,*) NAD2
       IF (NAD2.NE.1) GO TO 121
29     WRITE (ITERW,122)
122    FORMAT (5X,"Please input :",/,
      *15X,"Monochromator dial setting.......Angstroms  ",/,
      *15X,"Entrance slit width .............microns",/,
      *15X,"Exit slit width .................microns",/,
      *15X,"Reciprocal linear dispersion ....Angstroms/mm",//)
       READ (ITERM,*) L0,DX,DY,ALPHA
       DX=DX*1E-3
       DY=DY*1E-3
       GO TO 123
121    CONTINUE
       L0=3882.62
       DX=0.190
       DY=0.103
       ALPHA=12.5
123    L=15.24
       NREF=1.0002817
       RMASS=MWCN*MWCP/(MWCN+MWCP)
       CO=0.35621*P*SIG**2/SQRT(T*RMASS)
       DO=7.1623E-7*TE*SQRT(T/MWCN)
       A=0.832555*CO/DO
       INC0=WIDV(A)/5.*DO/1.665109
       OMAX=1.E8/(L0-ALPHA*(DX+DY)/2.)/NREF
       OMIN=1.E8/(L0+ALPHA*(DX+DY)/2.)/NREF
CCCCCCCCCCCCCCCCCCCCCCCCCCCCCCCCCCCCCCCCCCCCCCCCCCCCCCCCCCCCCCCCCCCCCCCCCCCC
C
C The program divides the frequency range viewed by the monochromator
C in  5000 intervals, and issues a warning if the grid does not allow for
C at least 10 intervals in one full line width.
C
CCCCCCCCCCCCCCCCCCCCCCCCCCCCCCCCCCCCCCCCCCCCCCCCCCCCCCCCCCCCCCCCCCCCCCCCCCCC
       INC=(OMAX-OMIN)/FLOAT(4999)
       IF (INC.GT.INC0) WRITE (ITERW,101) INC,INC0
101    FORMAT (//,5X,"Warning!  The increment wavenumber is: ",F8.6,
      *" cm-1",/,
      * 5X,"but 1/10-th of the full line width is: ",F8.6," cm-1",//)
       X=INC*1.6651/DO
       I0=0
       VOI=VOIGT(0,A)*0.939437/DO
1      I0=I0+1
       VO(I0)=VOIGT(X*(I0-1),A)*0.939437/DO
       TEST=VO(I0)/VOI
       IF (TEST.GT.1.E-2.AND.I0.LT.200) GO TO 1
       QE=2.+4.*EXP(-HC*9241.7)+2.*EXP(-HC*TE)
       NV=-1
       QV=0.0
12     NV=NV+1
       GV=GX(NV)*HC
       IF (GV.GT.50..OR.NV.GE.75) GO TO 13
       QV=QV+EXP(-GV)
       GO TO 12
13     CONTINUE
CCCCCCCCCCCCCCCCCCCCCCCCCCCCCCCCCCCCCCCCCCCCCCCCCCCCCCCCCCCCCCCCCCCCCCCCCCCC
C
C The following spectroscopic constants for CN are taken from:
C
C   Herzberg [Spectra of Diatomic Molecules]
C   Colket [J. Quant. Spectrosc. Radiat. Transfer, 31,7 (1984)]
C   Engleman [J. Mol. Spec., 49, 106 (1974)]
C   Spindler [J. Quant. Spectrosc. Radiat. Transfer, 5, 165 (1967)]
```

```
C
C
C  prgm name        variable                      value               reference
C
C   TE              Te                            25751.8 cm-1        Herzberg
C                   Nu00                          25797.35 cm-1       Herzberg
C   MWCN            CN mol.weight                  26.0177 gm
C   MWCP            Col.partner m.w.               39.9480 gm
C   SIG             Col.cross-section             4.0 angstroms        Colket
C   NREF            Air index of ref.             1.0002817            CRC handb.
C                   Omega e(X)                     2071.1 cm-1        Engleman
C                   OmegaeXe (X)                     13.8 cm-1           "
C                   Omega e(B)                     2144.8 cm-1           "
C                   OmegaeXe (B)                     12.2 cm-1           "
C   BEX             Be(X2sigma+)                   1.8985 cm-1         Herzberg
C   AEX             alpha e (X2s+)                 1.735e-2 cm-1        "    "
C   BEB             Be(B2sigma+)                   1.9701 cm-1          "    "
C   AEB             alpha e (B2s+)                 2.215e-2 cm-1        "    "
C   MVER            m(vertex) for v"=0            27      )           Herzberg
C                   m(vertex) for v"=1            29      )           page 171
C   DVX      (      Dv for v"=0                   6.414e-6 cm-1       Engleman
C            (      Dv for v"=1                   6.42 e-6 cm-1        "      "
C   GAX      (      gamma for v"=0                6.16 e-3 cm-1        "      "
C            (      gamma for v"=1                5.96 e-3 cm-1        "      "
C
C   DVB      (      Dv for v'=0                   6.58 e-6 cm-1        "      "
C            (      Dv for v'=1                   6.69 e-6 cm-1        "      "
C   GAB      (      gamma for v'=0                15.65e-3 cm-1        "      "
C            (      gamma for v'=1                16.90e-3 cm-1        "      "
C
C   QVV             Franck-Condon factor
C                    v"=v'=0                      0.9204              Spindler
C                    v"=v'=1                      0.7900               "    "
C
C   FEL             oscillator strenght            0.028
C
CCCCCCCCCCCCCCCCCCCCCCCCCCCCCCCCCCCCCCCCCCCCCCCCCCCCCCCCCCCCCCCCCCCCCC
      BEX=1.8996
      AEX=1.735E-2
      BEB=1.9701
      AEB=2.215E-2
      IF(NADINE.NE.1) WRITE (ITERW,220)
220   FORMAT (5X,"Do you input the value of fel?",/,
     *10X,"yes...enter 1",/,
     *10X,"no ...enter 0",/)
      IF (NADINE.NE.1) READ (ITERM,*) NAD5
      IF (NADINE.NE.1.AND.NAD5.NE.1) FEL=0.02239
      IF (NADINE.NE.1.AND.NAD5.EQ.1) WRITE (ITERW,221)
      IF (NADINE.NE.1.AND.NAD5.EQ.1) READ (ITERM,*) FEL
221   FORMAT (5X,"Please input fel:",/,)
      DO 10 N=1,2
      KMAX=0.0
      NV=N-1
      IF (NV.EQ.0) MVER=27
      IF (NV.EQ.1) MVER=29
      IF (NV.EQ.0) DVX=6.414E-6
      IF (NV.EQ.1) DVX=6.42 E-6
      IF (NV.EQ.0) GAX=6.16 E-3
      IF (NV.EQ.1) GAX=5.96 E-3
      IF (NV.EQ.0) DVB=6.58 E-6
      IF (NV.EQ.1) DVB=6.69 E-6
      IF (NV.EQ.0) GAB=15.65E-3
      IF (NV.EQ.1) GAB=16.9 E-3
      BVX=BEX-AEX*(NV+0.5)
```

```
      BVB=BEB-AEB*(NV+Ø.5)
      GB=2144.8*(NV+Ø.5)-12.2*(NV+Ø.5)**2
      IF (NV.EQ.Ø) QVV=Ø.92Ø4
      IF (NV.EQ.1) QVV=Ø.79ØØ
      QR=1./HC/BVX
      DO 1Ø ND=1,2
      NDJ=-2*ND+3
      DO 1Ø NA=1,2
      K=-1
11    K=K+1
CCCCCCCCCCCCCCCCCCCCCCCCCCCCCCCCCCCCCCCCCCCCCCCCCCCCCCCCCCCCCCCCCCCCCCCCCCC
C
C Only R and P branches are considered in this program. Doublet splitting
C is taken into account. Rotational line strengths are twice the values
C reported by Schadee [Bull. Astron. Inst. Netherlands, 17, 311 (1964)].
C The factor of two results from our normalization convention:
C
C     S(R1)+S(P1)=S(R2)+S(P2)=2J"+1
C
C
C The program first computes line strengths and positions for the two
C bands (Ø-Ø and 1-1) until it encounters a line that either falls out
C of the monochromator spectral range or is 1ØØ times weaker than the
C strongest line so far. If the first line out of the monochromator
C range belongs to a P-branch and has an index m smaller than the
C band head vertex, the program jumps to the first observable line
C after the band head, and resumes its calculation until the lines
C are too weak.
C
CCCCCCCCCCCCCCCCCCCCCCCCCCCCCCCCCCCCCCCCCCCCCCCCCCCCCCCCCCCCCCCCCCCCCCCCCCC
      IF((NDJ.EQ.-1.AND.NA.EQ.1.AND.K.EQ.Ø).OR.
     *   (NDJ.EQ.-1.AND.NA.EQ.2.AND.K.EQ.Ø).OR.
     *   (NDJ.EQ.-1.AND.NA.EQ.2.AND.K.EQ.1).OR.
     *   (NDJ.EQ.+1.AND.NA.EQ.2.AND.K.EQ.Ø)) GO TO 11
      IF (NV.EQ.Ø) OM=25797.85+F(BVB,DVB,GAB,K+NDJ,NA)-
     *F(BVX,DVX,GAX,K,NA)
      IF (NV.EQ.1)
     *OM=TE+GB-GX(NV)+F(BVB,DVB,GAB,K+NDJ,NA)-F(BVX,DVX,GAX,K,NA)
      IF (OM.GT.OMAX.AND.NDJ.EQ.+1) GO TO 1Ø
      IF (OM.LT.OMIN.AND.NDJ.EQ.+1) GO TO 16
      IF (OM.GT.OMAX.AND.NDJ.EQ.-1.AND.K.GT.MVER) GO TO 1Ø
      IF (OM.LT.OMIN.AND.NDJ.EQ.-1.AND.K.GT.MVER) GO TO 16
      IF (OM.GT.OMAX.AND.NDJ.EQ.-1.AND.K.LE.MVER) GO TO 16
      IF (OM.LT.OMIN.AND.NDJ.EQ.-1.AND.K.LE.MVER) K=2*MVER-K
      IF (OM.LT.OMIN.AND.NDJ.EQ.-1.AND.K.LE.MVER) GO TO 11
16    IF (NA.EQ.1) JP=FLOAT (K) + Ø.5
      IF (NA.EQ.2) JP=FLOAT (K) - Ø.5
      IF (NDJ.EQ.-1) STR=(JP**2-.25)/JP
      IF (NDJ.EQ.+1) STR=(JP+.5)*(JP+1.5)/(JP+1)
      IF (NADINE.EQ.Ø.OR.NADINE.EQ.2)
     *STR=STR/(2.*JP+1.)*QVV*FEL
      IF (NADINE.EQ.1)
     *STR=STR/(2.*JP+1.)*QVV
      EX=HC*(GX(NV)+F(BVX,DVX,GAX,K,NA))
      IF ( EX.GT.5Ø.) EX=Ø.Ø
      IF ( EX.LE.5Ø.) EX=EXP(-EX)
      IF ((NADINE.EQ.Ø.AND.NAD.EQ.Ø).OR.NADINE.EQ.1)
     *KJJ=CHI*1E-6*P/T*6.476353E9*(2.*JP+1.)/QE/QV/QR*EX*STR
      IF (NADINE.EQ.2.OR. (NADINE.EQ.Ø.AND.NAD.EQ.1))
     *KJJ=    1E-6*P/T*6.476353E9*(2.*JP+1.)/QE/QV/QR*EX*STR
      IF (KJJ.GT.KMAX) KMAX=KJJ
      IF (KMAX.NE.Ø.Ø) TEST=KJJ/KMAX
      IF (KMAX.NE.Ø.Ø.AND.TEST.LE.1E-3) GO TO 1Ø
      IF (OM.LT.OMIN.OR.OM.GT.OMAX) GO TO 11
```

```
      TEST=OM-INC*INT((OM-OMIN)/INC)-OMIN-INC/2.
      IF (TEST.LE.0.0) INDEX=INT((OM-OMIN)/INC)+1
      IF (TEST.GT.0.0) INDEX=INT((OM-OMIN)/INC)+2
      S(INDEX)=S(INDEX)+KJJ*VO(I)*L
CCCCCCCCCCCCCCCCCCCCCCCCCCCCCCCCCCCCCCCCCCCCCCCCCCCCCCCCCCCCCCCCCCCCCCCCCC
C
C  Once a line is accepted, its center is assigned to the closest
C  grid point. 200 adjacent points on each side of the center line
C  are then affected by the broadened line shape.
C
CCCCCCCCCCCCCCCCCCCCCCCCCCCCCCCCCCCCCCCCCCCCCCCCCCCCCCCCCCCCCCCCCCCCCCCCCC
      DO 14 I=1,I0-1
      J=INDEX+I
      IF (J.LE. 5000) S(J)=S(J)+KJJ*VO(I+1)*L
      J=INDEX-I
      IF (J.GE.1) S(J)=S(J)+KJJ*VO(I+1)*L
14    CONTINUE
      GO TO 11
10    CONTINUE
CCCCCCCCCCCCCCCCCCCCCCCCCCCCCCCCCCCCCCCCCCCCCCCCCCCCCCCCCCCCCCCCCCCCCCCCCC
C
C  The following set of instructions can be used to plot the monochromatic
C  transmission spectrum of CN as a function of vacuum frequency (see Fig.
C  A2.1). The spectral range is limited by the monochromator slit function.
C
CCCCCCCCCCCCCCCCCCCCCCCCCCCCCCCCCCCCCCCCCCCCCCCCCCCCCCCCCCCCCCCCCCCCCCCCCC
C
C The user is encouraged to purge the output file "LCN" after use,
C because it uses in excess of 590 blocks of disk space...
C
CCCCCCCCCCCCCCCCCCCCCCCCCCCCCCCCCCCCCCCCCCCCCCCCCCCCCCCCCCCCCCCCCCCCCCCCCC
C
C     IF (NADINE.NE.0) GO TO 99
C     CALL LFOUT (NA1,LUOUT)
C     WRITE (LUOUT,103)
C 103 FORMAT (4H1000)
C     DO 97 I=1, 5000
C     OM=OMIN+(I-1)*INC
C     TRANS=EXP(-S(I))
C     IF (I.EQ.1001.OR.
C    *    I.EQ.2001.OR.
C    *    I.EQ.3001.OR.
C    *    I.EQ.4001) WRITE (LUOUT,103)
C     WRITE (LUOUT,96) OM,TRANS
C 97  CONTINUE
C     CALL LFCLS (LUOUT)
C 99  CONTINUE
C
CCCCCCCCCCCCCCCCCCCCCCCCCCCCCCCCCCCCCCCCCCCCCCCCCCCCCCCCCCCCCCCCCCCCCCCCCC
96    FORMAT (E14.9,1H,,E12.7)
      ITER=0
      IF (NAD.EQ.1) CALL LFIN (NA2,LUIN)
      IF (NAD.EQ.1) CALL LFOUT(NA3,LUO )
      IF (NAD.EQ.1) READ (LUIN,*) NUM
      IF (NAD.EQ.1) WRITE (LUO ,117 ) NUM
117   FORMAT (I4)
      UNK=0.0
      IF (NADINE.EQ.0) UNK=1.0
      IF (NADINE.EQ.1) UNK=0.02239
      IF (NADINE.EQ.2) WRITE (ITERW,111)
111   FORMAT (//,5X,"Do you have an initial guess?...",/,
     *5X,"If not,enter 0",//)
      IF (NADINE.EQ.2) READ (ITERM,*) UNK
      SUM0=0.0
```

```
      FAC=1.0
      DO 32 I=1,5000
      IF (I.EQ.1.OR.I.EQ.5000) FAC=2.0
      OM=OMIN+(I-1)*INC
      WL0=1.E8/OM/NREF
      SUM0=SUM0+MONO(WL0)/FAC
      AMON(I)=MONO(WL0)
32    CONTINUE
      SUM0=SUM0*INC
      IF (NAD.NE.1)  GO TO 25
      DO 17 J=1,NUM
      READ (LUIN,*) TIME,UNK
      UNK=UNK*1E6
25    CONTINUE
      SUM=0.0
      IF (NADINE.NE.0) SUMD=0.0
CCCCCCCCCCCCCCCCCCCCCCCCCCCCCCCCCCCCCCCCCCCCCCCCCCCCCCCCCCCCCCCCCCCC
C
C To solve for the effective oscillator strength or for the mole fraction
C corresponding to a given experimental transmission, the program computes
C the first derivative of the transmission in respect to the unknown
C quantity and uses a Newton-Raphson iteration scheme.
C The program allows for 10 iterations, and the criterion for conver-
C gence is a relative error of 1e-10.
C The initial guess for the unknown value is zero.
C
CCCCCCCCCCCCCCCCCCCCCCCCCCCCCCCCCCCCCCCCCCCCCCCCCCCCCCCCCCCCCCCCCCCC
      FAC=1.0
      DO 15 I=1,5000
      IF (I.EQ.1.OR.I.EQ.5000) FAC=2.0
      OM=OMIN+INC*(I-1)
      S0=S(I)*UNK
      IF (S0  .GT.50.) EX0 = 0.0
      IF (S0  .LE.50.) EX0 = EXP (-S0   )
      SUM=SUM+AMON(I)*EX0/FAC
      IF (NADINE.NE.0) SUMD=SUMD+AMON(I)*EX0*S(I)/FAC
15    CONTINUE
      SUM=SUM*INC
      IF (NADINE.EQ.0) GO TO 24
      SUMD=SUMD*INC
      UNK=UNK+(SUM-TR0*SUM0)/SUMD
      TEST=ABS(SUM-TR0*SUM0)/ABS(SUM0-SUM)
      IF (TEST.LT..001) GO TO 24
      ITER=ITER+1
      IF (ITER.GT.10) WRITE (ITERW,105)
105   FORMAT (5X,"WARNING! No convergence after 10 iterations.",//)
      IF (ITER.GT.10) STOP
      GO TO 25
24    CONTINUE
      TRANS=SUM/SUM0*100.
      IF (NAD.EQ.1) TRANS=TRANS*1.E-2
      IF (NAD.EQ.1) WRITE (LUO,96) TIME,TRANS
      IF (NAD.EQ.1) WRITE (ITERW,223) J
223   FORMAT (5X,"J= ",I3)
17    CONTINUE
      IF (NADINE.NE.0) WRITE (ITERW,110) ITER
110   FORMAT(//,5X,"Convergence after ",I1," iterations",//)
      IF (NADINE.EQ.0.AND.NAD.NE.1.AND.(NFLAG.EQ.0.OR.NFLAG.EQ.3))
     *WRITE (ITERW,102) TRANS
102   FORMAT (//,5X,"Total transmission = ", F7.4," per cent",//)
      IF (NAD2.EQ.1.AND.(NFLAG.EQ.0.OR.NFLAG.EQ.3)) WRITE (ITERW,124)
      IF (NAD2.EQ.1.AND.(NFLAG.EQ.0.OR.NFLAG.EQ.3))READ(ITERM,*)NAD3
124   FORMAT (5X,"Do you want new monochromator settings?",/,
     *10X,"yes....enter 1",/,
```

```
     *10X,"no ....enter 0",//)
      IF (NAD3.NE.1) GO TO 28
      SUM=0.0
      SUM0=0.0
      SUMD=0.0
      DO 30 I=1,5000
      S(I)=0.0
   30 CONTINUE
      GO TO 29
   28 CONTINUE
      IF (NADINE.NE.0.OR.NAD1.NE.1) GO TO 26
      NFLAG=NFLAG-2
      IF (NFLAG.EQ.1) TRA=TRANS
      IF (NFLAG.EQ.-1) TRANS1=TRANS
      IF (NFLAG.EQ.-3) TRANS0=TRANS
      IF (NFLAG.EQ.-3) GO TO 26
      UNK=SQRT(1.5)**NFLAG
      GO TO 25
   26 CONTINUE
      IF (NAD1.NE.1) GO TO 27
      UNFA=ALOG((100.-TRANS1)/(100.-TRANS0))/ALOG(1.5)*(100.-TRA)
      UNFA=UNFA*1.E-2
      WRITE (ITERW,119) UNFA
  119 FORMAT (//,5X,"The uncertainty on the CN mole fraction is:",//,
     *30X,1H1,/,20X,20(1H-),/,20X,"S/N ratio *",F9.7,///)
   27 CONTINUE
      IF (NADINE.EQ.1) WRITE (ITERW,106) UNK
  106 FORMAT (//,5X,"Oscillator strength =",F8.6,//)
      IF (NADINE.EQ.2) WRITE (ITERW,107) UNK
  107 FORMAT (//,5X,"CN mole fraction= ",F7.1 ," ppm",//)
      IF (NAD.EQ.1) CALL LFCLS (LUIN)
      IF (NAD.EQ.1) CALL LFCLS (LUO )
      STOP
      END
      FUNCTION F (BV,DV,GA,K,NA)
      F=BV*(K+1)*K-DV*K**2*(K+1)**2
      IF (NA.EQ.1) F=F+0.5*GA*K
      IF (NA.EQ.2) F=F-0.5*GA*(K+1)
      RETURN
      END
      FUNCTION GX (NV)
      GX=2071.1*(NV+0.5)-13.8*(NV+0.5)**2
      RETURN
      END
CCCCCCCCCCCCCCCCCCCCCCCCCCCCCCCCCCCCCCCCCCCCCCCCCCCCCCCCCCCCCCCCCCCCCC
      REAL FUNCTION MONO ( WL )
CCCCCCCCCCCCCCCCCCCCCCCCCCCCCCCCCCCCCCCCCCCCCCCCCCCCCCCCCCCCCCCCCCCCCC
C
C This routine defines the monochromator slit function. It computes
C the relative power transmitted by the instrument as a function of
C wavelength in air. This function is accurately described by a simple
C trapezoid.
C
CCCCCCCCCCCCCCCCCCCCCCCCCCCCCCCCCCCCCCCCCCCCCCCCCCCCCCCCCCCCCCCCCCCCCC
      REAL L0
      COMMON L0,DX,DY,ALPHA
      X=ABS(WL-L0)
      X0=ALPHA*ABS(DX-DY)/2.
      X1=ALPHA*    (DX+DY)/2.
      IF (X.LE.X0) MONO=1.0
      IF (X.GE.X1) MONO=0.0
      IF (X.GT.X0.AND.X.LT.X1) MONO=1.-(X-X0)/(X1-X0)
      RETURN
      END
```

```
CCCCCCCCCCCCCCCCCCCCCCCCCCCCCCCCCCCCCCCCCCCCCCCCCCCCCCCCCCCCCCCCCCCCCCC
      FUNCTION VOIGT(X,Y)
C************************************************************************
C     THIS ROUTINE COMPUTES THE VOIGT FUNCTION :Y/PI*INTEGRAL FROM
C     - TO + INFINITY OF EXP(-T*T)/(Y**2+(X-T)**2)DT
C************************************************************************
      REAL B(22),RI(15),XN(15),YN(15),D0(25),D1(25),D2(25),D3(25),
     1D4(25),HN(25),XX(3),HH(3),NBY2(19),C(21)
      LOGICAL TRU
      DATA B/0.,.7093602E-7/,XN/10.,9.,2*8.,7.,6.,5.,4.,7
     1*3./,YN/3*.6,.5,2*.4,4*.3,1.,.9,.8,2*.7/,
     2H/.201/,XX/.5246476,1.65068,.7071068/,
     3HH/.2562121,.2588268E-1,.2820948/,NBY2/9.5,9.,8.5,8.,7.5,7.,6.5
     4,6.,5.5,5.,4.5,4.,3.5,3.,2.5,2.,1.5,1.,.5/,C/.7093602E-7,-.2518434
     5E-6,.8566874E-6,-.2787638E-5,.860774E-5,-.2565551E-4,.7228775E-4
     6,-.1933631E-3,.4899520E-3,-.1173267E-2,.2648752E-2,-.5623190E-2,
     7.1119601E-1,-.2084976E-1,.3621573E-1,-.5851412E-1,.8770816E-1,
     8-.121664,.15584,-.184,.2/
      DATA  TRU/.FALSE./
      IF (TRU) GO TO 104
C************************************************************************
C     REGION I: COMPUTE DAWSON'S FUNCTION AT MESH POINTS.
C************************************************************************
      TRU=.TRUE.
      DO 101 I=1,15
101   RI(I)=-I/2.
      DO 103 I=1,25
      HN(I)=H*(I-.5)
      CO=4.*HN(I)*HN(I)/25.-2.
      DO 102 J=2,21
102   B(J+1)=CO*B(J)-B(J-1)+C(J)
      D0(I)=HN(I)*(B(22)-B(21))/5.
      D1(I)=1.-2.*HN(I)*D0(I)
      D2(I)=(HN(I)*D1(I)+D0(I))/RI(2)
      D3(I)=(HN(I)*D2(I)+D1(I))/RI(3)
103   D4(I)=(HN(I)*D3(I)+D2(I))/RI(4)
104   IF (X-5.) 105,112,112
105   IF (Y-1.) 110,110,106
106   IF (X.GT.1.85*(3.6-Y)) GO TO 112
C************************************************************************
C     REGION II:CONTINUED FRACTION. COMPUTE NUMBER OF TERMS NEEDED.
C************************************************************************
      IF (Y.LT.1.45) GO TO 107
      I=Y+Y
      GO TO 108
107   I=11.*Y
108   J=X+X+1.85
      MAX=XN(J)*YN(I)+.46
      MIN=MIN0(16,21-2*MAX)
C************************************************************************
C     EVALUATE CONTINUED FRACTION
C************************************************************************
      UU=Y
      VV=X
      DO 109 J=MIN,19
      U=NBY2(J)/(UU*UU+VV*VV)
      UU=Y+U*UU
109   VV=X-U*VV
      VOIGT=UU/(UU*UU+VV*VV)/1.77454
      RETURN
110   Y2=Y*Y
      IF (X+Y.GE.5.) GO TO 113
C************************************************************************
C     REGION I: COMPUTE DAWSON'S FUNCTION AT X FROM TAYLOR SERIES.
```

```
C*********************************************************************
      N=X/H
      DX=X-HN(N+1)
      U=(((D4(N+1)*DX+D3(N+1))*DX+D2(N+1))*DX+D1(N+1))*DX+DØ(N+1)
      V=1.-2.*X*U
C*********************************************************************
C     TAYLOR SERIES EXPANSION ABOUT Y=Ø.Ø
C*********************************************************************
      VV=EXP(Y2-X*X)*COS(2.*X*Y)/1.128379-Y*V
      UU=-Y
      MAX=5.+(12.5-X)*.8*Y
      DO 111 I=2,MAX,2
      U=(X*V+U)/RI(I)
      V=(X*U+V)/RI(I+1)
      UU=-UU*Y2
111   VV=VV+V*UU
      VOIGT=1.128379*VV
      RETURN
112   Y2=Y*Y
      IF (Y.LT.11-.6875*X) GO TO 113
C*********************************************************************
C     REGION IIIB: 2-POINT GAUSS-HERMITE QUADRATURE.
C*********************************************************************
      U=X-XX(3)
      V=X+XX(3)
      VOIGT=Y*(HH(3)/(Y2+U*U)+HH(3)/(Y2+V*V))
      RETURN
C*********************************************************************
C     REGION IIIA: 4-POINT GAUSS-HERMITE QUADRATURE.
C*********************************************************************
113   U=X-XX(1)
      V=X+XX(1)
      UU=X-XX(2)
      VV=X+XX(2)
      VOIGT=Y*(HH(1)/(Y2+U*U)+HH(1)/(Y2+V*V)+HH(2)/(Y2+UU*UU)+HH(2)/
     1(Y2+VV*VV))
      RETURN
      END
      FUNCTION WIDV(A)
CCCCCCCCCCCCCCCCCCCCCCCCCCCCCCCCCCCCCCCCCCCCCCCCCCCCCCCCCCCCCCCCCCCCCCC
C
C  This function gives an approximate non-dimensional
C  value for the half-width at half maximum of a
C  Voigt profile of parameter a.
C
CCCCCCCCCCCCCCCCCCCCCCCCCCCCCCCCCCCCCCCCCCCCCCCCCCCCCCCCCCCCCCCCCCCCCCC
      DATA PI/3.1415926/,AC/Ø.18121/
      RL=SQRT(ALOG(2.))
      D=(A-RL)/(A+RL)
      BD=Ø.Ø23665*EXP(Ø.6*D)+Ø.ØØ418*EXP(-1.9*D)
      RD=1.-(AC*(1.-D*D))-(BD*SIN(PI*D))
      WIDV=RD*(A+RL)
      RETURN
      END
```

Program PART

```
 3:Ø2 PM  THU.,  2  AUG., 1984
LSPART T=ØØØØ4 IS ON CR GØ   USING ØØØ11 BLKS R=ØØØØ

ØØØ1  FTN4,L
ØØØ2          PROGRAM PART
ØØØ3  CCCCCCCCCCCCCCCCCCCCCCCCCCCCCCCCCCCCCCCCCCCCCCCCCCCCCCCCCCCCCCCCCCCCCCC
ØØØ4  C
ØØØ5  C    MICHEL LOUGE 1983
ØØØ6  C
ØØØ7  CCCCCCCCCCCCCCCCCCCCCCCCCCCCCCCCCCCCCCCCCCCCCCCCCCCCCCCCCCCCCCCCCCCCCCC
ØØØ8          INTEGER VMAX,V
ØØØ9          REAL JMAX,J,LA1,LA2,LA3
ØØ1Ø          DATA E,A /-.1591,-96.2Ø/
ØØ11          DATA B,D /.3894,.149E-6/
ØØ12          DATA O1,O2,O3 /1Ø47.,538.94,23Ø3./
ØØ13          DATA L /1/
ØØ14          DATA X2,XK /Ø.69,Ø.77/
ØØ15          CALL LUERR (ITERM)
ØØ16          WRITE (ITERM,1ØØ)
ØØ17  1ØØ     FORMAT (5X,"Please enter temperature (K) _")
ØØ18          READ (ITERM,*) T
ØØ19          HC=1.4388/T
ØØ2Ø          QV1=1./(1.-EXP(-HC*O1))
ØØ21          QV3=1./(1.-EXP(-HC*O3))
ØØ22          VMAX=INT(T/1ØØ.)+15
ØØ23          JMAX=3.*SQRT(T)+5Ø.
ØØ24          Q=Ø.Ø
ØØ25          DO 1 I=1,VMAX+1
ØØ26          V=I-1
ØØ27          KMAX=V+L
ØØ28          K=KMAX+2
ØØ29          C1=-E**2*O2/8.*FLOAT(V+1)
ØØ3Ø          C=C1*FLOAT(V+2)
ØØ31  2       K=K-2
ØØ32          IF (K.LT.Ø) GO TO 1
ØØ33          R=Ø.5*SQRT(A**2+FLOAT(V+1-K)*FLOAT(V+1+K)
ØØ34         **E**2*O2**2)
ØØ35          SB=Ø.5*E*O2*SQRT(FLOAT(V+1-K)*FLOAT(V+1+K))/R
ØØ36          ANH=X2*FLOAT(V)**2+XK*(K**2-1.)+O2*FLOAT(V)
ØØ37          IF (K.NE.KMAX) GO TO 3
ØØ38          AEFF=A*(1.-E**2/8.*FLOAT(K)*FLOAT(K+1))
ØØ39          J=FLOAT(K)-Ø.5
ØØ4Ø          F=C+B*FLOAT(K)-Ø.5*A+ANH
ØØ41          Q=Q+(2.*J+1.)*2.*EXP(-F*HC)
ØØ42  4       J=J+1.
ØØ43          F=C+B*((J+Ø.5)**2-FLOAT(K)**2)+ANH
ØØ44          F1=Ø.5*SQRT(4.*B**2*(J+Ø.5)**2
ØØ45         *+AEFF*(AEFF-4.*B*FLOAT(K)))
ØØ46          Q=Q+(2.*J+1.)*2.*(EXP(-HC*(F+F1))+EXP(-HC*(F-F1)))
ØØ47          IF (J.LT.JMAX) GO TO 4
ØØ48          GO TO 2
ØØ49  3       CONTINUE
ØØ5Ø          IF (K.EQ.Ø) GO TO 5
ØØ51          W=FLOAT(V+1)*FLOAT(K)*A*E**2*O2/16./R
ØØ52          CB=Ø.5*A/R
ØØ53          J=FLOAT(K)-Ø.5
ØØ54          F=C1+B*FLOAT(K)+ANH
ØØ55          F1=R+W
ØØ56          Q=Q+(2.*J+1.)*2.*(EXP(-HC*(F+F1))+EXP(-HC*(F-F1)))
ØØ57  6       J=J+1.
ØØ58          LA1=R+CB**2*B**2/2./R*(J+Ø.5-FLOAT(K))*(J+Ø.5+FLOAT(K))
ØØ59          LA2=SQRT((W+B*FLOAT(K))**2+SB**2*B**2*
ØØ6Ø         *(J+Ø.5-FLOAT(K))*(J+Ø.5+FLOAT(K)))
ØØ61          LA3=SQRT((W-B*FLOAT(K))**2+SB**2*B**2*
```

```
      *(J+Ø.5-FLOAT(K))*(J+Ø.5+FLOAT(K)))
       F=C1+B*(J+Ø.5-FLOAT(K))*(J+Ø.5+FLOAT(K))+ANH
       Q=Q+(2.*J+1.)*2.*(EXP(-HC*(F+LA1+LA2))+
      *                  EXP(-HC*(F+LA1-LA2))+
      *                  EXP(-HC*(F-LA1+LA3))+
      *                  EXP(-HC*(F-LA1-LA3)))
       IF (J.LT.JMAX) GO TO 6
       GO TO 2
 5     CONTINUE
       J=Ø.5
 8     CONTINUE
       F=C1+B*(J+Ø.5)**2+ANH
       F1=R**2+B**2*(J+Ø.5)**2
       F2=2.*B*(J+Ø.5)*R*SB
       Q=Q+(2.*J+1.)*(EXP(-HC*(F+SQRT(F1+F2)))+
      *               EXP(-HC*(F+SQRT(F1-F2)))+
      *               EXP(-HC*(F-SQRT(F1+F2)))+
      *               EXP(-HC*(F-SQRT(F1-F2))))
       J=J+1.
       IF (J.LT.JMAX) GO TO 8
 1     CONTINUE
       Q=Q*QV1*QV3
       WRITE (ITERM,1Ø1) T,Q
 1Ø1   FORMAT (5X,"The partition function at ",F7.2," is:",
      *E12.7)
       STOP
       END
```

Program LNCOA

```
 3:01 PM  THU.,  2  AUG., 1984
LSNCOA T=00004 IS ON CR G0   USING 00111 BLKS R=0000

FTN4,L
SEMA (XYZ,0)
      PROGRAM LNCOA
CCCCCCCCCCCCCCCCCCCCCCCCCCCCCCCCCCCCCCCCCCCCCCCCCCCCCCCCCCCCCCCCCCCCCC
C
C  MICHEL LOUGE 1983
C
CCCCCCCCCCCCCCCCCCCCCCCCCCCCCCCCCCCCCCCCCCCCCCCCCCCCCCCCCCCCCCCCCCCCCC
C
C This program calculates the semi-quantitative spectroscopy of the
C NCO[A2Sigma+i(100) <-- X2PIi(000)] band around 440nm.
C It evaluates line strengths and positions of the twelve possible
C branches of the band. References for the calculations are:
C
C   Author     reference   content
C
C   Dixon      48          spectr.csts.of X2PIi,Renner effect,etc...
C   Hougen     49          Rovibronic levels of a 2PIi linear XYZ mol.
C   Herzberg   25,66,67    spectr.review
C   Kovacs     26          rotational line strengths for 2Sig <-- 2PI
C   Lucht      102         background on diatomic mol.spectra
C
C The input and output of the program are:
C
C      mode                          input,units       output, units
C
C    line position,                temperature (K)   relative line
C    relative strength                               strength (cm-2*atm-1),
C   (mode 1)                                         line pos. (cm-1 or Angs.),
C                                                    and J"
C
C    line position,                temperature (K),  relative absorption
C    relative strength,            Voigt factor,     coeff. (cm-1*atm-1)
C    broadening                    spectral region   as a funct. of posit.
C   (mode 2)                       cm-1 or Angstroms (cm-1 or Angstroms)
C
C
C The formulae associated with the two modes are:
C
C   mode 1:
C
C   I/I0=exp[-K*f10*Phi*Pnco*L]
C
C   mode 2:
C
C   I/I0=exp[-S*f10*Pnco*L]
C
C   where:
C              K..... relative result of mode 1 (cm-2*atm-1)
C              f10... fel*qv"v'
C              fel... electronic oscillator strength
C              qv"v'  Franck-Condon factor
C              Phi... lineshape factor (cm)
C              Pnco.. partial pressure of NCO (atm)
C              L..... absorption cell length (cm)
C              S..... relative strength (mode 2 output) (cm-1*atm-1)
C              I/I0.. transmission (Beer's law)
C
CCCCCCCCCCCCCCCCCCCCCCCCCCCCCCCCCCCCCCCCCCCCCCCCCCCCCCCCCCCCCCCCCCCCCC
      IMPLICIT DOUBLE PRECISION (A-H,O-Z)
      DIMENSION IDCB(144),NAME(3)
```

```
      INTEGER NP(4,12)
      COMMON /XYZ/ ST(5000),VO(2000)
      DOUBLE PRECISION  J,K,KMAX
      DOUBLE PRECISION INDEX
      NAME(1)=2HLN
      NAME(2)=2HCO
      NAME(3)=2HSA
      DATA NP /
CCCCCCCCCCCCCCCCCCCCCCCCCCCCCCCCCCCCCCCCCCCCCCCCCCCCCCCCCCCCCCCCCCCCCCCCCCCCCCC
C
C The array NP describes the possible branches in the spectrum.
C We have:
C                NP(1,i) ....  Delta(J)=J'-J"
C                NP(2,i) ....  Alpha (Upper state)
C                NP(3,i) ....  Beta  (Lower state)
C                NP(4,i) ....  J0-0.5 (J0=lowest possible J")
C
C Note that Alpha (or Beta) =1 means that J=K+1/2 and F1=rot.energy
C  "     "    "        "     2   "     "  J=K-1/2  "  F2= "    "
C
C The branches described by NP(i,j) are:
C
C       R1  Q1  P1  qR12  pQ12  oP12  sR21  rQ21  qP21  R2  Q2  P2
C        1,  0, -1,    1,    0,   -1,    1,    0,   -1,  1,  0, -1,
C        1,  1,  1,    1,    1,    1,    2,    2,    2,  2,  2,  2,
C        1,  1,  1,    2,    2,    2,    1,    1,    1,  2,  2,  2,
C        1,  1,  0,    1,    1,    0,    1,    1,    2,  1,  1,  2 /
CCCCCCCCCCCCCCCCCCCCCCCCCCCCCCCCCCCCCCCCCCCCCCCCCCCCCCCCCCCCCCCCCCCCCCCCCCCCCCC
     * 1, 1, 1, 1,
     * 0, 1, 1, 1,
     *-1, 1, 1, 0,
     * 1, 1, 2, 1,
     * 0, 1, 2, 1,
     *-1, 1, 2, 0,
     * 1, 2, 1, 1,
     * 0, 2, 1, 1,
     *-1, 2, 1, 2,
     * 1, 2, 2, 1,
     * 0, 2, 2, 1,
     *-1, 2, 2, 2/
      CALL CREAT (IDCB,IER,NAME,144,4)
      CALL CLOSE (IDCB)
CCCCCCCCCCCCCCCCCCCCCCCCCCCCCCCCCCCCCCCCCCCCCCCCCCCCCCCCCCCCCCCCCCCCCCCCCCCCCCC
C
C The program names and creates its output file LNCOSA. The format is
C compatible with GRAPH. In mode 1, the output file contains 5 blocks
C of 1000 points each to describe the broadened spectrum. In mode 2,
C the output file lists line strengths and positions for the 12 branches
C R1 through P2. Note that in mode 2, the number of lines in each
C individual band is automatically adjusted by the program to account
C for different rotational progressions at different temperatures.
C For simplicity of programming, the number of lines in each branch is
C omitted in the output file, and it is replaced by a row of (*).
C Before graphing, the output file of mode 2 should be edited accordingly.
C
CCCCCCCCCCCCCCCCCCCCCCCCCCCCCCCCCCCCCCCCCCCCCCCCCCCCCCCCCCCCCCCCCCCCCCCCCCCCCCC
      CALL LFOUT (NAME,LUOUT)
      CALL LUERR (IT)
      WRITE (IT,103)
103   FORMAT (5X,"If you want wavenumbers in vacuum, enter 0",/,
     *        5X,"                 wavelengths in air, enter 1... _")
      READ (IT,*) NAD
      WRITE (IT,100)
```

```
100   FORMAT (5X,"Please enter the temperature: _")
      READ (IT,*) T
      WRITE (IT,104)
104   FORMAT (5X,"Do you consider broadening ?",/,
     *10X,"yes ... enter 1",/,
     *10X,"no  ... enter 0  _")
      READ (IT,*) NAD1
      IF (NAD1.NE.1) GO TO 4
      IF (NAD.EQ.0) WRITE (IT,105)
105   FORMAT (5X,"Please enter the spectral region:",/,
     *10X,"Omin,Omax ... cm-1 in vacuum  _")
      IF (NAD.EQ.1) WRITE (IT,106)
106   FORMAT (5X,"Please enter the spectral region:",/,
     *10X,"Lamb.min,lamb.max ... Angstroms in air  _")
      READ (IT,*) WMIN,WMAX
      WRITE (IT,107)
107   FORMAT (5X,"Please enter the Voigt parameter a:  _")
      READ (IT,*) A
      WRITE (IT,112)
112   FORMAT (5X,"Do you intend to calculate Omax only?",/,
     *10X,"yes... enter 1",/,
     *10X,"no ... enter 0  _")
      READ (IT,*) NAD2
      IF (NAD.EQ.1) WMIN=1.D8/INDEX(WMIN)/WMIN
      IF (NAD.EQ.1) WMAX1=1.D8/INDEX(WMAX)/WMAX
      IF (NAD.EQ.1) WMAX=WMIN
      IF (NAD.EQ.1) WMIN=WMAX1
CCCCCCCCCCCCCCCCCCCCCCCCCCCCCCCCCCCCCCCCCCCCCCCCCCCCCCCCCCCCCCCCCCCCCC
C
C Note that the line positions have been computed using frequencies
C in vacuo (cm-1) or wavelength in air (Angstroms). The function INDEX
C is called to perform the appropriate corrections.
C
CCCCCCCCCCCCCCCCCCCCCCCCCCCCCCCCCCCCCCCCCCCCCCCCCCCCCCCCCCCCCCCCCCCCCC
      AINC=DABS(WMAX-WMIN)/4.999D3
CCCCCCCCCCCCCCCCCCCCCCCCCCCCCCCCCCCCCCCCCCCCCCCCCCCCCCCCCCCCCCCCCCCCCC
C
C In mode 2, the program divides the spectral region of in-
C terest in 5000 increments (variable AINC). Note that the line posi-
C tions are calculated in double precision.
C
CCCCCCCCCCCCCCCCCCCCCCCCCCCCCCCCCCCCCCCCCCCCCCCCCCCCCCCCCCCCCCCCCCCCCC
      DO=7.1623D-7*22750.*DSQRT(T/42.)
CCCCCCCCCCCCCCCCCCCCCCCCCCCCCCCCCCCCCCCCCCCCCCCCCCCCCCCCCCCCCCCCCCCCCC
C
C To calculate Doppler widths, a molecular weigth of 42 amu and an
C average transition frequency of 22750 cm-1 have been assumed.
C
CCCCCCCCCCCCCCCCCCCCCCCCCCCCCCCCCCCCCCCCCCCCCCCCCCCCCCCCCCCCCCCCCCCCCC
C
C Some variables used in this program:
C
C      variable name                   meaning
C
C        DO                            Doppler width (cm-1)
C        A                             Voigt factor
C        ST(5000)                      relative absorption coeff. (cm-1*atm-1)
C        WMIN                          lower bound of the spectral region
C        WMAX                          upper bound of the spectral region
C                                      The user's input of WMIN and WMAX
C                                      should be consistent with the
C                                      choice of cm-1 in vacuum or Angstrom
C                                      in air. Note that the program always
C                                      converts to frequencies in cm-1 (vac.)
```

```
C        T                                 Temperature (K)
C        AINC                              Elementary increment for S-calc. (cm-1)
C        [illegible]                       Relative line strength (cm-2*atm-1)
C        KMAX                              [illegible] K in the branch so far.
C        VOIGT(X,Y)                        Voigt function
C        VO(2000)                          Voigt line shape func. array (cm)
C        O                                 Transition wave number in vac. (cm-1)
C        OM(J,M,I,LEVEL)                   Energy level (cm-1)
C        DJ                                J'-J"
C        J                                 Ground state J"
C        Q(T)                              Total partition function
C        IND                               Index for the S(5000) array
C        INDEX(WL)                         Air index of refraction func.of wav.le.
C
CCCCCCCCCCCCCCCCCCCCCCCCCCCCCCCCCCCCCCCCCCCCCCCCCCCCCCCCCCCCCCCCCCCCCCCCC
      X=AINC*1.6651/DO
      DO 9 I=1,5000
      ST(I)=0.0
9     CONTINUE
      DO 10 I=1,2000
      VO(I)=0.0
CCCCCCCCCCCCCCCCCCCCCCCCCCCCCCCCCCCCCCCCCCCCCCCCCCCCCCCCCCCCCCCCCCCCCCCCC
C
C After setting the increment in mode 2, the program computes Voigt
C lineshapes (cm) which are valid for any line in the band.
C The integer I0 is the total number of points considered in a half
C lineshape. (The complete lineshape function is therefore sampled using
C 2*I0 points.)
C
CCCCCCCCCCCCCCCCCCCCCCCCCCCCCCCCCCCCCCCCCCCCCCCCCCCCCCCCCCCCCCCCCCCCCCCCC
10    CONTINUE
      I0=0
      VOI=VOIGT(0,A)*0.939437/DO
 5     I0=I0+1
      VO(I0)=VOIGT(X*(I0-1),A)*0.939437/DO
      TEST=VO(I0)/VOI
      IF (TEST.GT.5.D-4.AND.I0.LT.2000) GO TO 5
CCCCCCCCCCCCCCCCCCCCCCCCCCCCCCCCCCCCCCCCCCCCCCCCCCCCCCCCCCCCCCCCCCCCCCCCC
C
      WMIN=WMIN-(I0-1)*AINC
      WMAX=WMAX+(I0-1)*AINC
C
CCCCCCCCCCCCCCCCCCCCCCCCCCCCCCCCCCCCCCCCCCCCCCCCCCCCCCCCCCCCCCCCCCCCCCCCC
C
C Note that the computer automatically extends the spectral range used
C in mode 2 to account for all possible lines that can influence the
C spectral region of interest.
C
CCCCCCCCCCCCCCCCCCCCCCCCCCCCCCCCCCCCCCCCCCCCCCCCCCCCCCCCCCCCCCCCCCCCCCCCC
      I00=I0+4999
4     CONTINUE
      IF (I0.EQ.2000) WRITE (IT,113)
113   FORMAT (5X,"Warning: The number of points to describe",/,
     *5X,"the Voigt profile is unsufficient.")
CCCCCCCCCCCCCCCCCCCCCCCCCCCCCCCCCCCCCCCCCCCCCCCCCCCCCCCCCCCCCCCCCCCCCCCCC
C
C loop over 12 possible branches
C
      DO 1 I=1,12
C
CCCCCCCCCCCCCCCCCCCCCCCCCCCCCCCCCCCCCCCCCCCCCCCCCCCCCCCCCCCCCCCCCCCCCCCCC
      KMAX=0.0
      J=NP(4,I)+.5
CCCCCCCCCCCCCCCCCCCCCCCCCCCCCCCCCCCCCCCCCCCCCCCCCCCCCCCCCCCCCCCCCCCCCCCCC
```

```
C
C implicit loop over all relevant values of J"
C
 3    CONTINUE
C
CCCCCCCCCCCCCCCCCCCCCCCCCCCCCCCCCCCCCCCCCCCCCCCCCCCCCCCCCCCCCCCCCCCC
      O=OM(J+NP(1,I),NP(2,I),I,2)-OM(J,NP(3,I),I,1)
      IF (NAD.EQ.1.AND.NAD1.NE.1) O=1.D8/O
      IF (NAD.EQ.1.AND.NAD1.NE.1) O=O/INDEX(O)
      K=6.477D9/T*2.*DEXP(-1.4388*OM(J,NP(3,I),I,1)/T)/Q(T)
CCCCCCCCC        I            CCCCCCCCCCCCCCCCCCCCCCCCCCCCCCCCCCCCC
C                I
C This factor of 2 has been introduced to respect the normalization
C convention of the rotational line strengths. We assume that each
C lambda singlet is an initial level of degeneracy 2J"+1, despite the
C small energy difference. Therefore, we have:
C
C                sR21+Q1+qP21=
C                R1+rQ21+P1  =
C                R2+pQ12+P2  =
C                qR12+Q2+oP12= 2J"+1
C
C Kovacs, however, quotes rotational line strengths with:
C
C  sR21+Q1+qP21+R1+rQ21+P1=R2+pQ12+P2+qR12+Q2+oP12=2J"+1
C
C In other words, Kovacs considers each initial level as a
C Lambda doublet. Consequently, Kovacs' line strengths must be
C multiplied by a factor of 2.
C
CCCCCCCCCCCCCCCCCCCCCCCCCCCCCCCCCCCCCCCCCCCCCCCCCCCCCCCCCCCCCCCCCCCC
     **S(J,NP(1,I),NP(2,I),NP(3,I))
      IF (NAD1.NE.1) WRITE (LUOUT,101) O,K,J
101   FORMAT (2X,D12.7,1H,,D12.7,1H,,D9.4)
      IF (K.GT.KMAX) KMAX=K
      TEST=K/KMAX
      IF (NAD1.NE.1.OR.O.GT.WMAX.OR.O.LT.WMIN) GO TO 6
CCCCCCCCCCCCCCCCCCCCCCCCCCCCCCCCCCCCCCCCCCCCCCCCCCCCCCCCCCCCCCCCCCCC
C
C In mode 2, after checking that a line falls within the spectral range
C of interest, the program calculates the contribution of the line to
C the relative absorption coefficient.
C To this end, it first computes the closest index for line center
C (variable IND) then proceeds to fill I0 adjacent S(I) on both
C sides. Note that 1<IND<2*I0+4998.
C
CCCCCCCCCCCCCCCCCCCCCCCCCCCCCCCCCCCCCCCCCCCCCCCCCCCCCCCCCCCCCCCCCCCC
      TEST1=O-AINC*IDINT((O-WMIN)/AINC)-WMIN-AINC/2.
      IF (TEST1.LE.0.0) IND=IDINT((O-WMIN)/AINC) +1
      IF (TEST1.GT.0.0) IND=IDINT((O-WMIN)/AINC) +2
      IF (IND.GE.I0.AND.IND.LE.I00) ST(IND-I0+1)=ST(IND-I0+1)
     *+K*VO(1)
      DO 7 I1=1,I0-1
      J1=IND+I1
      IF (J1.GE.I0.AND.J1.LE.I00) ST(J1-I0+1)=ST(J1-I0+1)+K*VO(I1+1)
      J1=IND-I1
      IF (J1.GE.I0.AND.J1.LE.I00) ST(J1-I0+1)=ST(J1-I0+1)+K*VO(I1+1)
7     CONTINUE
6     CONTINUE
      IF (TEST.GT.0.01) J=J+1.
CCCCCCCCCCCCCCCCCCCCCCCCCCCCCCCCCCCCCCCCCCCCCCCCCCCCCCCCCCCCCCCCCCCC
C
C The program considers all possible lines in a given branch until the
C relative line strength is 1% of the strongest value in the branch so
```

```
C far.
C
CCCCCCCCCCCCCCCCCCCCCCCCCCCCCCCCCCCCCCCCCCCCCCCCCCCCCCCCCCCCCCCCCCCCCCCCCCCC
      IF (TEST.GT.Ø.Ø1) GO TO 3
      IF (NAD1.NE.1) WRITE (LUOUT,1Ø2)
1Ø2   FORMAT(5(1H*))
1     CONTINUE
      IF (NAD1.NE.1) GO TO 12
      STM=Ø.Ø
      DO 8 I=IØ,IØØ
      O=WMIN+(I-1)*AINC
      IF (NAD.EQ.1) O=1.D8/O
      IF (NAD.EQ.1) O=O/INDEX(O)
      I1=I-(IØ-1)
      IF (I1.EQ.1ØØ1.OR.
     *    I1.EQ.2ØØ1.OR.
     *    I1.EQ.3ØØ1.OR.
     *    I1.EQ.ØØØ1.OR.
     *    I1.EQ.4ØØ1.AND.NAD2.NE.1) WRITE (LUOUT,11Ø)
11Ø   FORMAT (4H1ØØØ)
      IF (ST(I1).LE.STM) GO TO 11
      STM=ST(I1)
      OMAX=O
11    IF (NAD2.NE.1) WRITE (LUOUT,1Ø9) O,ST(I1)
1Ø9   FORMAT (D14.9,1H,,D12.7)
8     CONTINUE
12    CONTINUE
      IF (NAD1.NE.Ø) WRITE (IT,111) OMAX,STM
111   FORMAT (5X,"The position of the max. abs. coeff. is: ",D14.9,
     */,1ØX,"and Beta/FØØ = ",D14.9)
      CALL LFCLS(LUOUT)
      STOP
      END
      DOUBLE PRECISION FUNCTION OM(J,M,I,LEVEL)
      IMPLICIT DOUBLE PRECISION (A-H,O-Z)
      COMMON /XYZ/ ST(5ØØØ),VO(2ØØØ)
CCCCCCCCCCCCCCCCCCCCCCCCCCCCCCCCCCCCCCCCCCCCCCCCCCCCCCCCCCCCCCCCCCCCCCCCCCCC
C
C This function calculates the rotational energy levels of the X2PI1
C electronic level according to the formula of Hill and Van Vleck.
C
C It calculates the energy of the 2Sigma+ rot. levels according to
C Dixon [Phil. Trans. Roy. Soc. London, A252, 165 (1963Ø)].
C
C The constants used in this function are:
C
C  prgm name      meaning     value (cm-1)          source and remarks
C
C  B              B"          .3894                 Dixon  table 7 p.178
C                 B'          .4Ø211                Dixon  table 6 p.175
C  D              D"          .149 e-6              Dixon
C  D              D'          .177 e-6              Dixon
C  A              A"          -95.5Ø                Dixon  p.173 table 7
C                 A'            Ø.Ø
C  P              P            .ØØ2                 Dixon  table 7 p.178
C  DBL                                              Lambda-doubling term energy
C  NDBL                        +1                    for upper Lamb. doubl. comp.
C                                                    (pQ12, R2 and P2 branches)
C                              -1                    for lower Lamb. doubl. comp.
C                                                    (qR12, Q2 and oP12 branches)
C  O              nuØ"           Ø                  By convention,Dixon
C                 nuØ'       22753.98                considers the zero point
C                              I                    energy above the potential
```

```
C                          Dixon table 4          well (TØ instead of Te)
C
C  Note that the 2Pi1/2 level of the ground electronic state exhibits a
C  small Lambda-doubling, according to Dixon. We have the selection rule
C  + <--> - and the following symmetry rules for rotational levels:
C
C       For 2Sigma+ states:  Rotational levels are + for even N
C                                 "    "      "    "  - for odd  N
C
C
C       For 2Pi 1/2 states:
C
C For even N, rot. states are + for the upper component of Lamb. doubl.
C                             and - for the lower component of Lamb. doubl.
C  For odd N, rot. states are - for the upper component of Lamb. doubl.
C                             and + for the lower component of Lamb. doubl.
C
C (N is the total angular momentum apart from spin.)
C
C Consequently, R2, PQ12 and P2 branches always originate from the upper
C component of a Lambda-doublet in the X2Pi 1/2 state (Beta=2).
C Similarly, QR12, Q2 and OP12 always originate from the lower
C Lambda-doublet component.
C
CCCCCCCCCCCCCCCCCCCCCCCCCCCCCCCCCCCCCCCCCCCCCCCCCCCCCCCCCCCCCCCCCCCCCCCCCC
      DOUBLE PRECISION J,K
      IF (LEVEL.EQ.2) GO TO 1
      O=Ø.ØDØ
      B=Ø.3894DØ
      D=.149D-6
      A=-95.59DØ
      P=Ø.ØØ2DØ
      NDBL=Ø
      IF (I.EQ.5.OR.I.EQ.1Ø.OR.I.EQ.12) NDBL=+1
      IF (I.EQ.4.OR.I.EQ.6.OR.I.EQ.11) NDBL=-1
      DBL=NDBL*Ø.5*P*(J+Ø.5)
      OM=O+B*(J-Ø.5)*(J+1.5)+(-1.Ø)**M*DSQRT(
     *B**2*(J+Ø.5)**2+Ø.25*A*(A-4.*B))-
     *D*((J-Ø.5)*(J+Ø.5)**2*(J+1.5)+1.)+DBL
      GO TO 2
1     CONTINUE
      O=22753.98DØ
      B=Ø.4Ø211DØ
      D=.177D-6
      K=J+(-1.)**M*Ø.5
      OM=O+B*K*(K+1.)-D*K**2*(K+1.)**2
2     CONTINUE
      RETURN
      END
      DOUBLE PRECISION FUNCTION Q(T)
      IMPLICIT DOUBLE PRECISION (A-H,O-Z)
      COMMON /XYZ/ ST(5ØØØ),VO(2ØØØ)
CCCCCCCCCCCCCCCCCCCCCCCCCCCCCCCCCCCCCCCCCCCCCCCCCCCCCCCCCCCCCCCCCCCCCCCCCC
C
C This function calculates the total partition function for NCO. The
C complete calculation has been carried out elsewhere (prgm PART).
C In that program, all rovibronic levels of the ground electronic
C state were summed up, according to the expressions of Hougen [J. Chem.
C Phys., 36, 519 (1962)].
C Contributions of the A- and B- energy levels to the total partition
C function were neglected. Spectroscopic constants were taken from Dixon
C or Hougen. In addition, Omega1=1922 cm-1 and Omega2=1275 cm-1 were taken
C from Millikan and Jacox [J. Chem. Phys., 47, 5157 (1967)].
C
```

```
C The total partition function can adequately be described by the simpler
C formula given in this routine. A minor correction factor (variable F)
C was introduced to provide better agreement with the more complete
C computation of PART.
C
C Note that the bending vibration Omega2 has multiple degeneracies equal
C to 2*(v2+1). In addition, Lambda doubling occurs in all vibronic states
C with non zero K. Therefore, the global degeneracy of a given bending
C vibrational level is 4*(v2+1). The factor of 4 here explains the
C factor of 4 in Q(T), and the (v2+1) term explains the squared contri-
C bution of Omega2 to Q(T). Note that the introduction of a lambda
C doubling degeneracy (factor of 2) is consistent with our definition
C of the lower levels of a rotational transition, and the normalization
C rule Sum[Sj"j']=2*J"+1.
C
CCCCCCCCCCCCCCCCCCCCCCCCCCCCCCCCCCCCCCCCCCCCCCCCCCCCCCCCCCCCCCCCCCCCCCCC
      IF (T.LT.1000.) F=1.003+15./T
      IF (T.GE.1000.) F=1.0309-1.36D-5*T
      Q=F*4.*T/1.4388/0.3894/(1.-DEXP(-1.4388*1922./T))/
     *(1.-DEXP(-1.4388*538.94/T))**2/
     *(1.-DEXP(-1.4388*1275.0/T))
      RETURN
      END
      DOUBLE PRECISION FUNCTION S(J0,DJ,NA,NB)
CCCCCCCCCCCCCCCCCCCCCCCCCCCCCCCCCCCCCCCCCCCCCCCCCCCCCCCCCCCCCCCCCCCCCCCC
C
C The functions S, U and C are taken from Kovacs ["Rotational Structure
C in the Spectra of Diatomic Molecules", Elsevier, NY (1969)]. Kovacs'
C expressions apply to diatomic molecules, and to polyatomics that
C satisfy the Born-Oppenheimer approximation.
C Note that in his tables of rotational line strengths, Kovacs uses the
C following notation:
C
C        J .......... J"
C        Lambda ..... Min(Lamb.",Lamb.') ==> in our case, Lambda=0
C
C We have the following variables:
C
C        J .......... J"
C        DJ ......... J'-J"
C        NA ......... Alpha (upper level index)
C        NB ......... Beta (lower level index)
C        LEVEL ...... Upper level ==> 2
C                     Lower level ==> 1
C        IFLAG ...... Superscript in U and C  + ==> 1
C                                             - ==> 2
CCCCCCCCCCCCCCCCCCCCCCCCCCCCCCCCCCCCCCCCCCCCCCCCCCCCCCCCCCCCCCCCCCCCCCCC
      IMPLICIT DOUBLE PRECISION (A-H,O-Z)
      COMMON /XYZ/ ST(5000),VO(2000)
      DOUBLE PRECISION J,J0
      INTEGER DJ,NA,NB
      J=J0
      IF (DJ.EQ.+1.AND.NA.EQ.1.AND.NB.EQ.1) GO TO 1
      IF (DJ.EQ. 0.AND.NA.EQ.1.AND.NB.EQ.1) GO TO 2
      IF (DJ.EQ.-1.AND.NA.EQ.1.AND.NB.EQ.1) GO TO 3
      IF (DJ.EQ.+1.AND.NA.EQ.1.AND.NB.EQ.2) GO TO 4
      IF (DJ.EQ. 0.AND.NA.EQ.1.AND.NB.EQ.2) GO TO 5
      IF (DJ.EQ.-1.AND.NA.EQ.1.AND.NB.EQ.2) GO TO 6
      IF (DJ.EQ.+1.AND.NA.EQ.2.AND.NB.EQ.1) GO TO 7
      IF (DJ.EQ. 0.AND.NA.EQ.2.AND.NB.EQ.1) GO TO 8
      IF (DJ.EQ.-1.AND.NA.EQ.2.AND.NB.EQ.1) GO TO 9
      IF (DJ.EQ.+1.AND.NA.EQ.2.AND.NB.EQ.2) GO TO 10
      IF (DJ.EQ. 0.AND.NA.EQ.2.AND.NB.EQ.2) GO TO 11
```

```
      IF (DJ.EQ.-1.AND.NA.EQ.2.AND.NB.EQ.2) GO TO 12
      GO TO 13
1     J=J-1.
      S=(J-1.5)*(J-.5)/8./J/C(J-1.,2,2)/C(J,1,2)*
     *(U(J-1.,2,2)*U(J,1,2)+4.*(J+.5)**2)**2
      GO TO 13
2     S=(J-.5)*(J+.5)*(J+1.5)/4./J/(J+1.)/C(J,2,2)/C(J,1,2)*
     *(U(J,2,2)*U(J,1,2)+4.*(J+.5)**2)**2
      GO TO 13
3     J=J-1.
      S=(J+1.5)*(J+2.5)/8./(J+1.)/C(J+1.,2,2)/C(J,1,2)*
     *(U(J+1.,2,2)*U(J,1,2)+4.*(J+.5)**2)**2
      GO TO 13
4     J=J+1.
      S=(J-1.5)*(J-.5)/8./J/C(J-1.,2,1)/C(J,1,2)*
     *(U(J-1.,2,1)*U(J,1,2)-4.*(J+.5)**2)**2
      GO TO 13
5     S=(J-.5)*(J+.5)*(J+1.5)/4./J/(J+1.)/C(J,2,1)/C(J,1,2)*
     *(U(J,2,1)*U(J,1,2)-4.*(J+.5)**2)**2
      GO TO 13
6     J=J-1.
      S=(J+1.5)*(J+2.5)/8./(J+1.)/C(J+1.,2,1)/C(J,1,2)*
     *(U(J+1.,2,1)*U(J,1,2)-4.*(J+.5)**2)**2
      GO TO 13
7     J=J+1.
      S=(J-1.5)*(J-.5)/8./J/C(J-1.,2,2)/C(J,1,1)*
     *(U(J-1.,2,2)*U(J,1,1)-4.*(J+.5)**2)**2
      GO TO 13
8     S=(J-.5)*(J+.5)*(J+1.5)/4./J/(J+1.)/C(J,2,2)/C(J,1,1)*
     *(U(J,2,2)*U(J,1,1)-4.*(J+.5)**2)**2
      GO TO 13
9     J=J-1.
      S=(J+1.5)*(J+2.5)/8./(J+1.)/C(J+1.,2,2)/C(J,1,1)*
     *(U(J+1.,2,2)*U(J,1,1)-4.*(J+.5)**2)**2
      GO TO 13
10    J=J+1.
      S=(J-1.5)*(J-.5)/8./J/C(J-1.,2,1)/C(J,1,1)*
     *(U(J-1.,2,1)*U(J,1,1)+4.*(J+.5)**2)**2
      GO TO 13
11    S=(J-.5)*(J+.5)*(J+1.5)/4./J/(J+1.)/C(J,2,1)/C(J,1,1)*
     *(U(J,2,1)*U(J,1,1)+4.*(J+.5)**2)**2
      GO TO 13
12    J=J-1.
      S=(J+1.5)*(J+2.5)/8./(J+1.)/C(J+1.,2,1)/C(J,1,1)*
     *(U(J+1.,2,1)*U(J,1,1)+4.*(J+.5)**2)**2
13    RETURN
      END
      DOUBLE PRECISION FUNCTION C(J,LEVEL,IFLAG)
      IMPLICIT DOUBLE PRECISION (A-H,O-Z)
      COMMON /XYZ/ ST(5000),VO(2000)
      DOUBLE PRECISION  J,L
      IF (LEVEL.EQ.1) L=1.0
      IF (LEVEL.EQ.2) L=0.0
      C=0.5*(U(J,LEVEL,IFLAG)**2+4.*(J+0.5-L)*(J+0.5+L))
      RETURN
      END
      DOUBLE PRECISION FUNCTION U(J,LEVEL,IFLAG)
      IMPLICIT DOUBLE PRECISION (A-H,O-Z)
      COMMON /XYZ/ ST(5000),VO(2000)
      DOUBLE PRECISION J,L
      IF (LEVEL.EQ.1) L=1.0
      IF (LEVEL.EQ.2) L=0.0
      IF (LEVEL.EQ.1) Y=-95.59/0.3894
      IF (LEVEL.EQ.2) Y=0.0
```

```
      U=DSQRT(L**2*Y*(Y-4.)+4.*(J+0.5)**2)
     *+(-1.0)**(IFLAG+1)*L*(Y-2.)
      RETURN
      END
      DOUBLE PRECISION  FUNCTION INDEX ( WL  )
      IMPLICIT DOUBLE PRECISION (A-H,O-Z)
      COMMON /XYZ/ ST(5000),VO(2000)
CCCCCCCCCCCCCCCCCCCCCCCCCCCCCCCCCCCCCCCCCCCCCCCCCCCCCCCCCCCCCCCCCCCCC
C
C This function is given in the CRC handbook p. E-224. It uses the Cauchy
C formula for the air index of refraction. The fit is
C valid for all UV wavelengths. Note that the temperature dependence of the
C index has been omitted here.
C
CCCCCCCCCCCCCCCCCCCCCCCCCCCCCCCCCCCCCCCCCCCCCCCCCCCCCCCCCCCCCCCCCCCCCCC
      INDEX=2726.43D0+12.288D6/WL**2+.3555D16/WL**4
      INDEX=1.+INDEX*1.D-7
      RETURN
      END
      DOUBLE PRECISION FUNCTION VOIGT (X,Y)
      IMPLICIT DOUBLE PRECISION (A-H,O-Z)
      COMMON /XYZ/ ST(5000),VO(2000)
C*********************************************************************
C
C     THIS ROUTINE COMPUTES THE REAL  (WR) AND IMAGINARY (WI) PARTS OF
C     THE COMPLEX PROBABILITY FUNCTION w(z),
C
C     w(z) = exp(-z*z) * erfc(-i*z),
C
C     WHERE erfc IS THE COMPLEMENTARY ERROR FUNCTION.  THE COMPUTATION
C     IS VALID FOR THE UPPER HALF PLANE OF z = x + iy , ie y > 0.
C
C     MAXIMUM RELATIVE ERROR FOR WR IS < 2.E-6 AND FOR WI IS < 5.E-6.
C
C     SUBROUTINE ADAPTED FROM:
C     J. HUMLICEK. J. QUANT. SPECTROSC. RADIAT. TRANSFER 21, 309 (1979)
C
C
C*********************************************************************
      DIMENSION T(6), C(6), S(6)
      DATA T/0.314240376D00,0.947788391D00,0.159768264D01,
     * 0.227950708D01,0.302063703D01,0.38897249D01/
      DATA C/0.101172805D01,-0.75197147D00,0.12557727D-01,
     * 0.100220082D-01,-0.242068135D-03,0.500848061D-06/
      DATA S/0.1393237D01,0.231152406D00,-0.155351466D00,
     * 0.621836624D-02,0.919082986D-04,-0.627525958D-06/
      WR=0.
      WI=0.
      Y1=Y+1.5
      Y2=Y1*Y1
C*********************************************************************
C
C     BRANCH TO REGION I OR II DEPENDING ON VALUES OF X AND Y.
C
C*********************************************************************
      IF(Y.GT.0.85.OR.DABS(X).LT.(18.1*Y+1.65)) GO TO 20
C*********************************************************************
C
C     CALCULATIONS FOR REGION II
C
      IF (DABS(X).LT.12.) WR=DEXP(-X*X)
      Y3=Y+3.
      DO 10 I=1,6
      R=X-T(I)
```

```
      R2=R*R
      D=1./(R2+Y2)
      D1=Y1*D
      D2=R*D
      WR=WR+Y*(C(I)*(R*D2-1.5*D1)+S(I)*Y3*D2)/(R2+2.25)
      R=X+T(I)
      R2=R*R
      D=1./(R2+Y2)
      D3=Y1*D
      D4=R*D
      WR=WR+Y*(C(I)*(R*D4-1.5*D3)-S(I)*Y3*D4)/(R2+2.25)
10    WI=WI+C(I)*(D2+D4)+S(I)*(D1-D3)
      VOIGT=WR
      RETURN
C
C     END OF CALCULATIONS FOR REGION II
C
C*********************************************************************
C
C      CALCULATIONS FOR REGION I
C
20    DO 30 I=1,6
      R=X-T(I)
      D=1./(R*R+Y2)
      D1=Y1*D
      D2=R*D
      R=X+T(I)
      D=1./(R*R+Y2)
      D3=Y1*D
      D4=R*D
      WR=WR+C(I)*(D1+D3)-S(I)*(D2-D4)
30    WI=WI+C(I)*(D2+D4)+S(I)*(D1-D3)
      VOIGT=WR
      RETURN
C
C     END OF CALCULATIONS FOR REGION I
C
C*********************************************************************
      END
S
```

Program LNCOB

```
 3:ØØ PM  THU.,  2  AUG., 1984
LSNCOB T=ØØØØ4 IS ON CR GØ   USING ØØØ98 BLKS R=ØØØØ

ØØØ1  FTN4,L
ØØØ2  SEMA (XYZ,Ø)
ØØØ3        PROGRAM LNCOB
ØØØ4  CCCCCCCCCCCCCCCCCCCCCCCCCCCCCCCCCCCCCCCCCCCCCCCCCCCCCCCCCCCCCCCCCCCCCCCC
ØØØ5  C
ØØØ6  C  MICHEL LOUGE 1983
ØØØ7  C
ØØØ8  CCCCCCCCCCCCCCCCCCCCCCCCCCCCCCCCCCCCCCCCCCCCCCCCCCCCCCCCCCCCCCCCCCCCCCCC
ØØØ9  C
ØØ1Ø  C This program calculates the semi-quantitative spectroscopy of the
ØØ11  C NCO[B2PIi(1ØØ) <-- X2PIi(ØØØ)] band around 3Ø5nm.
ØØ12  C It evaluates the line strengths and positions for the P1,Q1,R1 and
ØØ13  C the P2,Q2,R2 branches. References for the calculations are:
ØØ14  C
ØØ15  C   Author     reference     content
ØØ16  C
ØØ17  C   Dixon        48          spectr.csts.of X2PIi,Renner effect,etc...
ØØ18  C   Dixon        59          spectr.csts.of B2PIi,bands,etc...
ØØ19  C   Hougen       49          Rovibronic levels of a 2PIi linear XYZ mol.
ØØ2Ø  C   Herzberg     25,66,67    spectr.review
ØØ21  C   Kovacs       26          rotational line strengths for 2PI <-- 2PI
ØØ22  C   Lucht        1Ø2         background on diatomic mol.spectra
ØØ23  C   Sullivan     6Ø          lifetimes in the B2PIi <-- X2PIi trans.
ØØ24  C
ØØ25  C The input and output of the program are:
ØØ26  C
ØØ27  C      mode                      input,units        output, units
ØØ28  C
ØØ29  C    line position,            temperature (K)     relative line
ØØ3Ø  C    relative strength                            strength (cm-2*atm-1),
ØØ31  C   (mode 1)                                      line pos. (cm-1 or Angs.),
ØØ32  C                                                 and J"
ØØ33  C
ØØ34  C    line position,            temperature (K),    relative absorption
ØØ35  C    relative strength,        Voigt factor,       coeff. (cm-1*atm-1)
ØØ36  C    broadening                spectral region     as a funct. of posit.
ØØ37  C   (mode 2)                   cm-1 or Angstroms   (cm-1 or Angstroms)
ØØ38  C
ØØ39  C
ØØ4Ø  C The formulae associated with the two modes are:
ØØ41  C
ØØ42  C   mode 1:
ØØ43  C
ØØ44  C   I/IØ=exp[-K*flØ*Phi*Pnco*L]
ØØ45  C
ØØ46  C   mode 2:
ØØ47  C
ØØ48  C   I/IØ=exp[-S*flØ*Pnco*L]
ØØ49  C
ØØ5Ø  C   where:
ØØ51  C              K..... relative result of mode 1 (cm-2*atm-1)
ØØ52  C              flØ... fel*qv"v'
ØØ53  C              fel... electronic oscillator strength
ØØ54  C              qv"v'  Franck-Condon factor
ØØ55  C              Phi... lineshape factor (cm)
ØØ56  C              Pnco.. partial pressure of NCO (atm)
ØØ57  C              L..... absorption cell length (cm)
ØØ58  C              S..... relative strength (mode 2 output) (cm-1*atm-1)
ØØ59  C              I/IØ.. transmission (Beer's law)
ØØ6Ø  C
ØØ61  CCCCCCCCCCCCCCCCCCCCCCCCCCCCCCCCCCCCCCCCCCCCCCCCCCCCCCCCCCCCCCCCCCCCCCCC
```

```
      IMPLICIT DOUBLE PRECISION (A-H,O-Z)
      DIMENSION IDCB(144),NAME(3)
      COMMON /XYZ/ ST(5000),VO(2000)
      INTEGER DJ
      DOUBLE PRECISION  J0,J,K,KMAX
      DOUBLE PRECISION INDEX
      NAME(1)=2HLN
      NAME(2)=2HCO
      NAME(3)=2HSB
      CALL CREAT (IDCB,IER,NAME,144,4)
      CALL CLOSE (IDCB)
CCCCCCCCCCCCCCCCCCCCCCCCCCCCCCCCCCCCCCCCCCCCCCCCCCCCCCCCCCCCCCCC
C
C The program names and creates its output file LNCOSB. The format is
C compatible with GRAPH. In mode 1, the output file contains 5 blocks
C of 1000 points each to describe the broadened spectrum. In mode 2,
C the output file lists line strengths and positions for the 12 branches
C R1 through P2. Note that in mode 2, the number of lines in each
C individual band is automatically adjusted by the program to account
C for different rotational progressions at different temperatures.
C For simplicity of programming, the number of lines in each branch is
C omitted in the output file, and it is replaced by a row of (*).
C Before graphing, the output file of mode 2 should be edited accordingly.
C
CCCCCCCCCCCCCCCCCCCCCCCCCCCCCCCCCCCCCCCCCCCCCCCCCCCCCCCCCCCCCCCC
      CALL LFOUT (NAME,LUOUT)
      CALL LUERR (IT)
      WRITE (IT,103)
  103 FORMAT (5X,"If you want wavenumbers in vacuum, enter 0",/,
     *       5X,"              wavelengths in air, enter 1... _")
      READ (IT,*) NAD
      WRITE (IT,100)
  100 FORMAT (5X,"Please enter the temperature: _")
      READ (IT,*) T
      WRITE (IT,104)
  104 FORMAT (5X,"Do you consider broadening ?",/,
     *10X,"yes ... enter 1",/,
     *10X,"no  ... enter 0  _")
      READ (IT,*) NAD1
      WRITE (IT,114)
  114 FORMAT (5X,"Please enter the new values of B'v and D'v",/,
     *5X,"(if Dixon's values are O.K., enter a negative number)  _")
      READ (IT,*) BN,DN
      IF (BN.LT.0.0) BN=0.3765
      IF (DN.LT.0.0) DN=15.D-3
      IF (NAD1.NE.1) GO TO 4
      IF (NAD.EQ.0) WRITE (IT,105)
  105 FORMAT (5X,"Please enter the spectral region:",/,
     *10X,"Omin,Omax ... cm-1 in vacuum  _")
      IF (NAD.EQ.1) WRITE (IT,106)
  106 FORMAT (5X,"Please enter the spectral region:",/,
     *10X,"Lamb.min,lamb.max ... Angstroms in air  _")
      READ (IT,*) WMIN,WMAX
      WRITE (IT,107)
  107 FORMAT (5X,"Please enter the Voigt parameter a:  _")
      READ (IT,*) A
      WRITE (IT,112)
  112 FORMAT (5X,"Do you intend to calculate Omax only?",/,
     *10X,"yes... enter 1",/,
     *10X,"no ... enter 0  _")
      READ (IT,*) NAD2
      IF (NAD.EQ.1) WMIN=1.D8/INDEX(WMIN)/WMIN
      IF (NAD.EQ.1) WMAX1=1.D8/INDEX(WMAX)/WMAX
      IF (NAD.EQ.1) WMAX=WMIN
```

```
      IF (NAD.EQ.1) WMIN=WMAX1
CCCCCCCCCCCCCCCCCCCCCCCCCCCCCCCCCCCCCCCCCCCCCCCCCCCCCCCCCCCCCCCCCCCCCCCC
C
C Note that the positions have been computed using frequencies in vacuo
C (cm-1) or wavelengths in air (Angstroms). The function INDEX is called
C to perform the appropriate corrections.
C
CCCCCCCCCCCCCCCCCCCCCCCCCCCCCCCCCCCCCCCCCCCCCCCCCCCCCCCCCCCCCCCCCCCCCCCC
      AINC=DABS(WMAX-WMIN)/4.999D3
CCCCCCCCCCCCCCCCCCCCCCCCCCCCCCCCCCCCCCCCCCCCCCCCCCCCCCCCCCCCCCCCCCCCCCCC
C
C In mode 2, the program divides the spectral region of in-
C terest in 5000 increments (variable AINC). Note that the line posi-
C tions are calculated in double precision.
C
CCCCCCCCCCCCCCCCCCCCCCCCCCCCCCCCCCCCCCCCCCCCCCCCCCCCCCCCCCCCCCCCCCCCCCCC
      DO=7.1623D-7*32781.*DSQRT(T/42.)
CCCCCCCCCCCCCCCCCCCCCCCCCCCCCCCCCCCCCCCCCCCCCCCCCCCCCCCCCCCCCCCCCCCCCCCC
C
C To calculate Doppler widths, a molecular weigth of 42 amu and an
C average transition frequency of 32781 cm-1 have been assumed.
C
CCCCCCCCCCCCCCCCCCCCCCCCCCCCCCCCCCCCCCCCCCCCCCCCCCCCCCCCCCCCCCCCCCCCCCCC
C
C Some variables used in this program:
C
C     variable name                    meaning
C
C       DO                             Doppler width (cm-1)
C       A                              Voigt factor
C       ST(5000)                       relative absorption coeff. (cm-1*atm-1)
C       WMIN                           lower bound of the spectral region
C       WMAX                           upper bound of the spectral region
C                                      The user's input of WMIN and WMAX
C                                      should be consistent with the choice
C                                      of cm-1 in vacuum or Angstroms in air.
C                                      Note that the program always converts
C                                      to frequencies (cm-1) in vacuum.
C       T                              Temperature (K)
C       AINC                           Elementary increment for S-calc. (cm-1)
C       K                              Relative line strength (cm-2*atm-1)
C       KMAX                           Largest  K in the branch so far.
C       VOIGT(X,Y)                     Voigt function
C       VO(2000)                       Voigt line shape func. array (cm)
C       O                              Transition frequency in vac. (cm-1)
C       OM(J,N,LEVEL)                  Energy level (cm-1)
C       DJ                             J'-J"
C       N                              Branch index (alpha, beta= 1 or 2)
C       J0                             Initial rotational quantum number
C       J                              Ground state J"
C       Q(T)                           Total partition function
C       IND                            Index for the S(5000) array
C       INDEX(WL)                      Air index of refraction func.of wav.le.
C
CCCCCCCCCCCCCCCCCCCCCCCCCCCCCCCCCCCCCCCCCCCCCCCCCCCCCCCCCCCCCCCCCCCCCCCC
      X=AINC*1.6651/DO
      DO 9 I=1,5000
      ST(I)=0.0
9     CONTINUE
      DO 10 I=1,2000
      VO(I)=0.0
CCCCCCCCCCCCCCCCCCCCCCCCCCCCCCCCCCCCCCCCCCCCCCCCCCCCCCCCCCCCCCCCCCCCCCCC
C
C After setting the increment in mode 2, the program computes Voigt
```

```
C lineshapes (cm) which are valid for any line in the band.
C The integer IØ is the total number of points considered in a half
C lineshape. (The complete lineshape function is therefore sampled using
C 2*IØ points.)
C
CCCCCCCCCCCCCCCCCCCCCCCCCCCCCCCCCCCCCCCCCCCCCCCCCCCCCCCCCCCCCCCCCCCCCCCC
1Ø      CONTINUE
        IØ=Ø
        VOI=VOIGT(Ø,A)*Ø.939437/DO
5       IØ=IØ+1
        VO(IØ)=VOIGT(X*(IØ-1),A)*Ø.939437/DO
        TEST=VO(IØ)/VOI
        IF (TEST.GT.5.D-4.AND.IØ.LT.2ØØØ) GO TO 5
        WMIN=WMIN-(IØ-1)*AINC
        WMAX=WMAX+(IØ-1)*AINC
        IØØ=IØ+4999
4       CONTINUE
        IF (IØ.EQ.2ØØØ) WRITE (IT,113)
113     FORMAT (5X,"Warning: The number of points to describe",/,
       *5X,"the Voigt profile is unsufficient.")
CCCCCCCCCCCCCCCCCCCCCCCCCCCCCCCCCCCCCCCCCCCCCCCCCCCCCCCCCCCCCCCCCCCCCCCC
C
C Loop over three branches (P,Q,R)
C
        DO 1 I=1,3
C
CCCCCCCCCCCCCCCCCCCCCCCCCCCCCCCCCCCCCCCCCCCCCCCCCCCCCCCCCCCCCCCCCCCCCCCC
        DJ=I-2
C
CCCCCCCCCCCCCCCCCCCCCCCCCCCCCCCCCCCCCCCCCCCCCCCCCCCCCCCCCCCCCCCCCCCCCCCC
C
C Loop over the branch index N (alpha or beta).
C
        DO 2 N=1,2
C
CCCCCCCCCCCCCCCCCCCCCCCCCCCCCCCCCCCCCCCCCCCCCCCCCCCCCCCCCCCCCCCCCCCCCCCC
C
CCCCCCCCCCCCCCCCCCCCCCCCCCCCCCCCCCCCCCCCCCCCCCCCCCCCCCCCCCCCCCCCCCCCCCCC
C
C DJ=-1 ==> P-branch
C DJ= Ø ==> Q-branch
C DJ=+1 ==> R-branch
C
C Sign in the            Omega=Lambda+/-S     index
C Hill and Van Vleck
C formula:
C
C     (+)                      1/2                F2
C     (-)                      3/2                F1
C
C Note that both states are inverted (A<Ø).
C
CCCCCCCCCCCCCCCCCCCCCCCCCCCCCCCCCCCCCCCCCCCCCCCCCCCCCCCCCCCCCCCCCCCCCCCC
        KMAX=Ø.Ø
        JØ=1.5
        IF (N.EQ.1.AND.DJ.EQ.Ø) JØ=Ø.5
        IF (DJ.EQ.-1) JØ=2.5
        J=JØ
CCCCCCCCCCCCCCCCCCCCCCCCCCCCCCCCCCCCCCCCCCCCCCCCCCCCCCCCCCCCCCCCCCCCCCCC
C
C Note the missing lines at the initial rotational transitions:
C
C   branch     JØ
C
```

```
C     P2          2.5
C     Q2          1.5
C     R2          1.5
C     P1          2.5
C     Q1          Ø.5
C     R1          1.5
C
CCCCCCCCCCCCCCCCCCCCCCCCCCCCCCCCCCCCCCCCCCCCCCCCCCCCCCCCCCCCCCCCCCCCCCCCCC
3     CONTINUE
      O=OM(J+DJ.N,2,BN,DN)-OM(J,N,1,BN,DN)
      IF (NAD.EQ.1.AND.NAD1.NE.1) O=1.D8/O
      IF (NAD.EQ.1.AND.NAD1.NE.1) O=O/INDEX(O)
      K=6.477D9/T*2.*DEXP(-1.4388*OM(J,N,1,BN,DN)/T)/Q(T)
CCCCCCCCC          I            CCCCCCCCCCCCCCCCCCCCCCCCCCCCCCCCCCCCCCC
C                  I
C This factor of 2 has been introduced because Lambda doubling cannot be
C resolved. Since NCO is asymmetrical, both components are equally strong.
C
CCCCCCCCCCCCCCCCCCCCCCCCCCCCCCCCCCCCCCCCCCCCCCCCCCCCCCCCCCCCCCCCCCCCCCCCCC
     **S(J,DJ,N)
      IF (NAD1.NE.1) WRITE (LUOUT,1Ø1) O,K,J
1Ø1   FORMAT (2X,D12.7,1H,,D12.7,1H,,D9.4)
      IF (K.GT.KMAX) KMAX=K
      TEST=K/KMAX
      IF (NAD1.NE.1.OR.O.GT.WMAX.OR.O.LT.WMIN) GO TO 6
CCCCCCCCCCCCCCCCCCCCCCCCCCCCCCCCCCCCCCCCCCCCCCCCCCCCCCCCCCCCCCCCCCCCCCCCCC
C
C In mode 2, after checking that a line falls within the spectral range
C of interest, the program calculates the contribution of the line to
C the relative absorption coefficient.
C To this end, it first computes the closest index for line center
C (variable IND) then proceeds to fill IØ adjacent S(I) on both
C sides. Note that 1<IND<2*IØ+4998.
C
CCCCCCCCCCCCCCCCCCCCCCCCCCCCCCCCCCCCCCCCCCCCCCCCCCCCCCCCCCCCCCCCCCCCCCCCCC
      TEST1=O-AINC*IDINT((O-WMIN)/AINC)-WMIN-AINC/2.
      IF (TEST1.LE.Ø.Ø) IND=IDINT((O-WMIN)/AINC) +1
      IF (TEST1.GT.Ø.Ø) IND=IDINT((O-WMIN)/AINC) +2
      IF(IND.GE.IØ.AND.IND.LE.IØØ) ST(IND-IØ+1)=ST(IND-IØ+1)+K*VO(1)
      DO 7 I1=1,IØ-1
      J1=IND+I1
      IF (J1.GE.IØ.AND.J1.LE.IØØ) ST(J1-IØ+1)=ST(J1-IØ+1)+K*VO(I1+1)
      J1=IND-I1
      IF (J1.GE.IØ.AND.J1.LE.IØØ) ST(J1-IØ+1)=ST(J1-IØ+1)+K*VO(I1+1)
7     CONTINUE
6     CONTINUE
      IF (TEST.GT.Ø.Ø1) J=J+1.
CCCCCCCCCCCCCCCCCCCCCCCCCCCCCCCCCCCCCCCCCCCCCCCCCCCCCCCCCCCCCCCCCCCCCCCCCC
C
C The program considers all possible lines in a given branch until the
C relative line strength is 1% of the strongest value in the branch so
C far.
C
CCCCCCCCCCCCCCCCCCCCCCCCCCCCCCCCCCCCCCCCCCCCCCCCCCCCCCCCCCCCCCCCCCCCCCCCCC
      IF (TEST.GT.Ø.Ø1) GO TO 3
      IF (NAD1.NE.1) WRITE (LUOUT,1Ø2)
1Ø2   FORMAT(5(1H*))
2     CONTINUE
1     CONTINUE
      IF (NAD1.NE.1) GO TO 12
      STM=Ø.Ø
      DO 8 I=IØ,IØØ
      O=WMIN+(I-1)*AINC
      IF (NAD.EQ.1) O=1.D8/O
```

```
      IF (NAD.EQ.1) O=O/INDEX(O)
      I1=I-(I0-1)
      IF (I1.EQ.1001.OR.
     *    I1.EQ.2001.OR.
     *    I1.EQ.3001.OR.
     *    I1.EQ.0001.OR.
     *    I1.EQ.4001.AND.NAD2.NE.1) WRITE (LUOUT,110)
 110  FORMAT (4H1000)
      IF (ST(I1).LE.STM) GO TO 11
      STM=ST(I1)
      OMAX=O
 11   IF (NAD2.NE.1) WRITE (LUOUT,109) O,ST(I1)
 109  FORMAT (D14.9,1H,,D12.7)
 8    CONTINUE
 12   CONTINUE
      IF (NAD1.NE.0) WRITE (IT,111) OMAX,STM
 111  FORMAT (5X,"The position of the max. abs. coeff. is: ",D14.9,
     */,5X,"(Beta/F10)max=",D14.9,/)
      CALL LFCLS(LUOUT)
      STOP
      END
      DOUBLE PRECISION FUNCTION OM(J,N,LEVEL,BN,DN)
      IMPLICIT DOUBLE PRECISION (A-H,O-Z)
      COMMON /XYZ/ ST(5000),VO(2000)
CCCCCCCCCCCCCCCCCCCCCCCCCCCCCCCCCCCCCCCCCCCCCCCCCCCCCCCCCCCCCCCCCCCCCC
C
C This function calculates the rotational energy levels of both 2PIi
C electronic states using the Hill and Van Vleck formula.
C
C The spectroscopic constants for NCO are:
C
C  References: Dixon [Phil.Trans.Roy.Soc.London, A252, 165 (1960)]
C              Dixon [Can.J.Phys., 38, 10 (1960)].
C
C                                                   source and remarks
C  prgm name      meaning      value (cm-1)
C                                                 Dixon table 7 p.178
C  B              B"           .3894              Dixon (3) p.14
C                 B'           .3765              Dixon p.14
C  D              D",D'        15.e-8             Dixon p.178 table 7
C  A              A"           -95.59             Dixon p.14
C                 A'           -30.8              By convention,Dixon
C  O              nu0"             0              considers the zero point
C                 nu0'         32781.13           energy above the potential
C                                                 well (T0 instead of Te)
C
C
CCCCCCCCCCCCCCCCCCCCCCCCCCCCCCCCCCCCCCCCCCCCCCCCCCCCCCCCCCCCCCCCCCCCCCCCC
      DOUBLE PRECISION J
      IF (LEVEL.EQ.2) GO TO 1
      O=0.0D0
      B=0.3894D0
      D=15.D-8
      A=-95.59D0
      GO TO 2
 1    CONTINUE
      O=32781.13D0
      B=BN
      D=DN
      A=-30.8D0
 2    CONTINUE
      OM=O+B*(J-0.5)*(J+1.5)+(-1.0)**N*DSQRT(
     *B**2*(J+0.5)**2+0.25*A*(A-4.*B))-
     *D*((J-0.5)*(J+0.5)**2*(J+1.5)+1.)
      RETURN
```

```
      END
      DOUBLE PRECISION FUNCTION Q(T)
      IMPLICIT DOUBLE PRECISION (A-H,O-Z)
      COMMON /XYZ/ ST(5000),VO(2000)
CCCCCCCCCCCCCCCCCCCCCCCCCCCCCCCCCCCCCCCCCCCCCCCCCCCCCCCCCCCCCCCCCCCCCCCC
C
C This function calculates the total partition function for NCO. The
C complete calculation has been carried out elsewhere (prgm PART).
C In that program, all rovibronic levels of the ground electronic
C state were summed up, according to the expressions of Hougen [J. Chem.
C Phys., 36, 519 (1962)].
C Contributions of the A- and B- energy levels to the total partition
C function were neglected. Spectroscopic constants were taken from Dixon
C or Hougen. In addition, Omega1=1922 cm-1 and Omega2=1275 cm-1 were taken
C from Millikan and Jacox [J. Chem. Phys., 47, 5157 (1967)].
C
C The total partition function can adequately be described by the simpler
C formula given in this routine. A minor correction factor (variable F)
C was introduced to provide better agreement with the more complete
C computation of PART.
C
C Note that the bending vibration Omega2 has multiple degeneracies equal
C to 2*(v2+1). In addition, Lambda doubling occurs in all vibronic states
C with non zero K. Therefore, the global degeneracy of a given bending
C vibrational level is 4*(v2+1). The factor of 4 here explains the
C factor of 4 in Q(T), and the (v2+1) term explains the squared contri-
C bution of Omega2 to Q(T). Note that the introduction of a lambda
C doubling degeneracy (factor of 2) is consistent with our definition
C of the lower levels of a rotational transition, and the normalization
C rule Sum[Sj"j']=2*J"+1.
C
CCCCCCCCCCCCCCCCCCCCCCCCCCCCCCCCCCCCCCCCCCCCCCCCCCCCCCCCCCCCCCCCCCCCCCCC
      IF (T.LT.1000.) F=1.003+15./T
      IF (T.GE.1000.) F=1.0309-1.36D-5*T
      Q=F*4.*T/1.4388/0.3894/(1.-DEXP(-1.4388*1922./T))/
     *(1.-DEXP(-1.4388*538.94/T))**2/
     *(1.-DEXP(-1.4388*1275.0/T))
      RETURN
      END
      DOUBLE PRECISION FUNCTION S(J,DJ,N)
      IMPLICIT DOUBLE PRECISION (A-H,O-Z)
      COMMON /XYZ/ ST(5000),VO(2000)
CCCCCCCCCCCCCCCCCCCCCCCCCCCCCCCCCCCCCCCCCCCCCCCCCCCCCCCCCCCCCCCCCCCCCCCC
C
C The functions S,U and C are taken directly from Kovacs [Rotational
C Structure in the Spectra of Diatomic Molecules. Elsevier, NY (1969)].
C Kovacs' expressions apply to diatomic molecules and to polyatomics
C that satisfy the Born-Oppenheimer approximation.
C
C We have the following variables:
C
C     J ........... J"
C     L ........... Lambda
C     DJ .......... J'-J"
C     LEVEL ...... Upper level ==> 2
C                  Lower level ==> 1
C     IFLAG ...... Superscript in U and C  + ==> 1
C                                          - ==> 2
C
CCCCCCCCCCCCCCCCCCCCCCCCCCCCCCCCCCCCCCCCCCCCCCCCCCCCCCCCCCCCCCCCCCCCCCCC
C
C Rotational line strengths are normalized according to Sum(Sj"j')=2J"+1.
C Lower levels are chosen with degeneracy 2J"+1. Therefore, we have, eg:
C
```

```
C    S(P1c)+S(Q1c)+S(R1c)=2*J"+1 (respec. index 2,c,d)
C
C This description implicitely assumes that Lambda doubling can be
C resolved. A lower level is therefore defined by J, N and the Lambda
C doubling quantum number. This is consistent with the introduction of
C K-doubling in the total partition function. In practice however,
C Lambda doubling cannot be resolved. The individual components of the
C doublet therefore add up in the line strength calculation. This explains
C our earlier introduction of a factor of 2, since both components of the
C Lambda doublet of an asymmetrical molecule are equal in strength (see
C line 266).
C
CCCCCCCCCCCCCCCCCCCCCCCCCCCCCCCCCCCCCCCCCCCCCCCCCCCCCCCCCCCCCCCCCCCCCCCCCCCCCCCC
      DOUBLE PRECISION  J,L
      INTEGER DJ
      L=1.Ø
      IF (N.NE.1) GO TO 1Ø
      IF (DJ.NE.-1) GO TO 1
      S=(J-L-Ø.5)*(J+L+Ø.5)/4./J/C(J-1.,2,2)/C(J,1,2)*
     *(U(J-1.,2,2)*U(J,1,2)+4.*(J-L+Ø.5)*(J+L-Ø.5))**2
      GO TO 2Ø
1     CONTINUE
      IF (DJ.NE.Ø) GO TO 2
      S=(J+Ø.5)/2./J/(J+1.)/C(J,2,2)/C(J,1,2)*
     *((L+Ø.5)*U(J,2,2)*U(J,1,2)+4.*(L-Ø.5)*
     *(J-L+Ø.5)*(J+L+Ø.5))**2
      GO TO 2Ø
2     CONTINUE
      S=(J-L+Ø.5)*(J+L+1.5)/4./(J+1.)/C(J+1.,2,2)/
     *C(J,1,2)*(U(J+1.,2,2)*U(J,1,2)+
     *4.*(J-L+1.5)*(J+L+Ø.5))**2
      GO TO 2Ø
1Ø    CONTINUE
      IF (DJ.NE.-1) GO TO 3
      S=(J-L-Ø.5)*(J+L+Ø.5)/4./J/C(J-1.,2,1)/C(J,1,1)*
     *(U(J-1.,2,1)*U(J,1,1)+4.*(J-L+Ø.5)*(J+L-Ø.5))**2
      GO TO 2Ø
3     CONTINUE
      IF (DJ.NE.Ø) GO TO 4
      S=(J+Ø.5)/2./J/(J+1.)/C(J,2,1)/C(J,1,1)*
     *((L+Ø.5)*U(J,2,1)*U(J,1,1)+
     *4.*(L-Ø.5)*(J-L+Ø.5)*(J+L+Ø.5))**2
      GO TO 2Ø
4     CONTINUE
      S=(J-L+Ø.5)*(J+L+1.5)/4./(J+1.)/C(J+1.,2,1)
     */C(J,1,1)*(U(J+1.,2,1)*U(J,1,1)+
     *4.*(J-L+1.5)*(J+L+Ø.5))**2
2Ø    RETURN
      END
      DOUBLE PRECISION FUNCTION C(J,LEVEL,IFLAG)
      IMPLICIT DOUBLE PRECISION (A-H,O-Z)
      COMMON /XYZ/ ST(5ØØØ),VO(2ØØØ)
      DOUBLE PRECISION  J,L
      L=1.Ø
      C=Ø.5*(U(J,LEVEL,IFLAG)**2+4.*(J+Ø.5-L)*(J+Ø.5+L))
      RETURN
      END
      DOUBLE PRECISION FUNCTION U(J,LEVEL,IFLAG)
      IMPLICIT DOUBLE PRECISION (A-H,O-Z)
      COMMON /XYZ/ ST(5ØØØ),VO(2ØØØ)
      DOUBLE PRECISION J,L
      L=1.Ø
      IF (LEVEL.EQ.1) Y=-95.59/Ø.3894
      IF (LEVEL.EQ.2) Y=-3Ø.8Ø/Ø.3765
```

```
      U=DSQRT(L**2*Y*(Y-4.)+4.*(J+0.5)**2)
     *+(-1.0)**(IFLAG+1)*L*(Y-2.)
      RETURN
      END
      DOUBLE PRECISION  FUNCTION INDEX ( WL )
      IMPLICIT DOUBLE PRECISION (A-H,O-Z)
      COMMON /XYZ/ ST(5000),VO(2000)
CCCCCCCCCCCCCCCCCCCCCCCCCCCCCCCCCCCCCCCCCCCCCCCCCCCCCCCCCCCCCCCCCCCCCCCCCCCC
C
C This function is found in the CRC handbook p. E-224. It is the Cauchy
C index of refraction of air as a function of wavelength. The fit is
C valid for all UV wavelengths.
C
CCCCCCCCCCCCCCCCCCCCCCCCCCCCCCCCCCCCCCCCCCCCCCCCCCCCCCCCCCCCCCCCCCCCCCCCCCCC
      INDEX=2726.43D0+12.288D8/WL**2+0.3555D16/WL**4
      INDEX=1.+INDEX*1.D-7
      RETURN
      END
      DOUBLE PRECISION FUNCTION VOIGT (X,Y)
      IMPLICIT DOUBLE PRECISION (A-H,O-Z)
      COMMON /XYZ/ ST(5000),VO(2000)
C*********************************************************************
C
C     THIS ROUTINE COMPUTES THE REAL  (WR) AND IMAGINARY (WI) PARTS OF
C     THE COMPLEX PROBABILITY FUNCTION w(z),
C
C     w(z) = exp(-z*z) * erfc(-i*z),
C
C     WHERE erfc IS THE COMPLEMENTARY ERROR FUNCTION.  THE COMPUTATION
C     IS VALID FOR THE UPPER HALF PLANE OF z = x + iy , ie y > 0.
C
C     MAXIMUM RELATIVE ERROR FOR WR IS < 2.E-6 AND FOR WI IS < 5.E-6.
C
C     SUBROUTINE ADAPTED FROM:
C     J. HUMLICEK, J. QUANT. SPECTROSC. RADIAT. TRANSFER 21, 309 (1979)
C
C
C*********************************************************************
      DIMENSION T(6), C(6), S(6)
      DATA T/0.314240376D00,0.947788391D00,0.159768264D01,
     * 0.227950708D01,0.302063703D01,0.38897249D01/
      DATA C/0.101172805D01,-0.75197147D00,0.12557727D-01,
     * 0.100220082D-01,-0.242068135D-03,0.500843361D-06/
      DATA S/0.1393237D01,0.231152406D00,-0.155351456D00,
     * 0.621836624D-02,0.919082986D-04,-0.627525953D-06/
      WR=0.
      WI=0.
      Y1=Y+1.5
      Y2=Y1*Y1
C*********************************************************************
C
C     BRANCH TO REGION I OR II DEPENDING ON VALUES OF X AND Y.
C
C*********************************************************************
      IF(Y.GT.0.85.OR.DABS(X).LT.(18.1*Y+1.65)) GO TO 20
C*********************************************************************
C
C     CALCULATIONS FOR REGION II
C
      IF (DABS(X).LT.12.) WR=DEXP(-X*X)
      Y3=Y+3.
      DO 10 I=1,6
      R=X-T(I)
      R2=R*R
```

```
      D=1./(R2+Y2)
      D1=Y1*D
      D2=R*D
      WR=WR+Y*(C(I)*(R*D2-1.5*D1)+S(I)*Y3*D2)/(R2+2.25)
      R=X+T(I)
      R2=R*R
      D=1./(R2+Y2)
      D3=Y1*D
      D4=R*D
      WR=WR+Y*(C(I)*(R*D4-1.5*D3)-S(I)*Y3*D4)/(R2+2.25)
10    WI=WI+C(I)*(D2+D4)+S(I)*(D1-D3)
      VOIGT=WR
      RETURN
C
C     END OF CALCULATIONS FOR REGION II
C
C*********************************************************************
C
C      CALCULATIONS FOR REGION I
C
20    DO 30 I=1,6
      R=X-T(I)
      D=1./(R*R+Y2)
      D1=Y1*D
      D2=R*D
      R=X+T(I)
      D=1./(R*R+Y2)
      D3=Y1*D
      D4=R*D
      WR=WR+C(I)*(D1+D3)-S(I)*(D2-D4)
30    WI=WI+C(I)*(D2+D4)+S(I)*(D1-D3)
      VOIGT=WR
      RETURN
C
C     END OF CALCULATIONS FOR REGION I
C
C*********************************************************************
      END
S
```

Appendix 6

Data Reduction Procedure and Uncertainty Analysis

In this appendix, a systematic approach to the experimental and data reduction procedures is presented and a method to estimate the uncertainties associated with shock tube experiments is discussed.

A6.1 Determination of Experimental Conditions

Shock tube experiments are generally aimed at measuring fundamental kinetic data by comparing measured and calculated profiles of selected species. Before running an experiment, a comprehensive study is performed to choose reactant mixtures, conditions and species diagnostics that render the measured profile most sensitive to the kinetic data of interest. To analyze each problem, it is useful to reduce the chemical mechanism to a handful of key reactions and to perform a steady-state analysis of the simplified reaction set. In addition to simplifying the kinetic problem, this approach provides a convenient frame for discussing the data interpretation. Moreover, computer experiments based on a comprehensive chemical mechanism can be used to validate the conclusions of the simple analysis and carry out an optimization of the kinetics experiments.

If posed in general terms, the problem of optimizing shock tube measurements becomes a task with a confusing range of choices. Fortunately, a few rules of thumb can reduce the number of acceptable options.

First, reactant mixtures must be tailored to limit the influence of interfering reactions in the kinetics mechanism, and to promote the reactions of interest in the very first stages of the experiment. If elementary radicals and atoms are involved in the reaction studied, then the test mixtures should include a well known and direct source of these species. For example, N_2O can be used as a reliable source of O-atoms; a mixture of N_2O and H_2 can provide known amounts of H-atoms, etc... Further, it is important to restrict the induction mechanism to a single

rate-limiting step, because new uncertainties are added with each new initiation reaction.

The precision of a rate measurement depends also on the careful choice of the species diagnostic. In general, it is better to measure an intermediate species than a final product, because the concentration of the former is more dependent on the kinetics of the system than the concentration of the latter. For example, mixtures of C_2N_2 and N_2O diluted in argon at moderate temperatures (T≈1800°K) can be described using the simplified three reactions model

$$N_2O + M \rightarrow N_2 + O + M, \quad (1)$$

$$C_2N_2 + O \rightarrow CN + NCO, \quad (2)$$

$$CN + O \rightarrow CO + N. \quad (3)$$

It was shown in chapter 3 that $[CN]^{peak}/[C_2N_2] \approx k_2/k_3$. Further, $[CO]^{peak} \approx [CO]_{t\rightarrow\infty} \approx 2[C_2N_2]_{t=0}$. It follows that plateau CO concentrations are independent of the reaction kinetics. By contrast, peak CN concentrations are directly proportional to the ratio k_2/k_3. It is clear that a measurement of the intermediate radical CN provides better kinetics insight than a measurement of the stable product CO.

Finally, acceptable experiments usually correspond to a narrow range of conditions. In general, it is better to work with maximum dilution to prevent excessive kinetics interference from unknown reactions. On the other hand, spectroscopic diagnostics usually dictate the conditions of the experiment. In particular, detection limits often impose high reactant mole fractions to achieve suitable post-shock species concentrations. For example, an upper bound on temperature must be set to collect a detectable absorption signal (absorption levels decrease with increasing temperature). Note that detection limits are closely related to the size of the molecular partition functions. For example, the partition function and detection limits of a polyatomic molecule are equally dependent on temperature. Further, experimental temperatures are often restricted by possible optical interferences (spontaneous emission from the test gas), or by reaction rate considerations. In practice, experi-

mental conditions are frequently adjusted by trial and error because of conflicting and possibly unknown diagnostic and kinetics considerations.

A6.2 Development of a Chemical Kinetics Model

The successful interpretation of measured species time-histories depends on the careful choice of a chemical kinetics mechanism. The failure to include certain reactions in a comprehensive model can result in erroneous measurements of the rate constants of interest. The consequences of such mistakes can be greatly reduced by diluting the reactant mixtures. However, further dilution can be prevented by detection limits considerations, and a correct interpretation of the chemical mechanism becomes essential.

To construct a reasonable mechanism, it is helpful to envision the reactions in the shock tube as a simple chemical sequence. Each step of the sequence is found by determining which species are most likely to react with the products of the previous step. Consider for example the mechanism in Fig. 3.10. The initial step is the thermal decomposition of C_2N_2. The resulting CN radicals will undoubtedly react with O_2, giving rise to NCO and O. At this stage, it is essential to recognize that the resulting O-atoms will react with C_2N_2, thus accelerating the production of CN, and the production of O-atoms. Clearly, the failure to include reaction (2)

$$C_2N_2 + O \rightarrow CN + NCO, \qquad (2)$$

would render the data interpretation impossible, since the model would predict an excessive rise time of CN. More subtle mistakes can arise from the omission of other critical reactions. For example, omitting reaction (3) from the C_2N_2/O_2/argon mechanism

$$CN + O \rightarrow CO + N, \qquad (3)$$

would not prevent a fit of the initial slope of CN; however, it would certainly result in an erroneous measurement of k_4

$$CN + O_2 \rightarrow NCO + O. \quad (4)$$

In the absence of a known chemical mechanism, postulating an excessive number of reactions is better than failing to include a few important steps. If it necessary to reduce the size of the mechanism, then the computer can be used to evaluate the importance of each reaction. However, such an analysis can only be performed if reasonable data is available for all reaction rates.

In the absence of any published data, it is therefore useful to estimate the magnitude of selected reaction rate constants. Unfortunately, such theoretical predictions are limited. Benson [103] and Gardiner [86] surveyed a great variety of elementary reactions, proposed a few semi-empirical correlations, and reviewed the available theories. They also mentioned the serious limitations associated with each theoretical analysis. In particular, they indicated that the collision theory of reaction rates depends on unknown steric factors in the range $10^{-5}<p<1$ [86], and fails to predict activation energies. In addition, the transition state theory (TST) requires two uncertain procedures i.e., estimating the set of vibrational frequencies of the activated complex and estimating the barrier height [103]. In an attempt to overcome these limitations, Binkley and Frisch [104] have applied quantum mechanical techniques to compute the vibrational frequencies, equilibrium geometries and total energies of any H/N/C/O molecular species, including activation complexes. Using empirically determined corrections, and transition state theory, this method proved successful in predicting the temperature dependence of the reaction of O-atoms with HCN [16]. Unfortunately, this sophisticated technique is not readily available; to perform a TST calculation, most researchers must make various assumptions about the intrinsic properties of the transition state. To this end, known molecules of comparable shape can provide approximate frequencies and bond lengths (see ¶ 5.1.3). Additional assumptions about the tightness of the transition state are made to relate the properties of the parent molecule to the properties of the transition state. Tight

transition states have interatomic distances about twice the distances in the corresponding stable molecules [103]; in addition, their bending and stretching frequencies are about 30% lower than comparable stable frequencies [103]. On the other hand, loose complexes have longer distances (2.9 times the stable bond distance) and smaller frequencies [103]. Most atom metathesis reactions such as reactions (2), (3), (4), (5), (8), (9), (10) and (11) have tight transition states [103]. Note that the uncertainties associated with these assumptions increase with increasing complexity of the transition state. In general, simple theoretical estimates based on transition state theory predict the temperature dependence of pre-exponential factors with reasonable accuracy, and are useful to correlate the observed curvature of non-Arrhenius rate constants (see ¶ 5.1.3). To this date however, no simple theory can reliably predict the barrier height of an elementary reaction. In general, endothermic reactions have a barrier height at least equal to their heat of reaction, and strongly exothermic reactions commonly exhibit small activation energies. In addition, limited correlations for simple reactions such as abstraction reactions are available (see Benson [103]). In the present study, barrier heights $E=\Delta H_R+\delta$ have been observed for endothermic reactions, with $2<\delta<6$ kcal/mole (see Table A6.1).

Upper bounds for the magnitude of unknown rate constants are given by the line-of-center collision rate,

$$k_c = 10^{12.44} \left(\frac{T}{\mu}\right)^{1/2} \bar{\sigma}^{\,2} \exp[-E_0/RT] \text{ cm}^3/\text{mole/sec} \ . \qquad \text{(A6.1)}$$

μ is the reduced mass of the reactants (g/mole). $\bar{\sigma}$ is the collision cross-section diameter (Å) [86], and is presumably known from experimental transport properties measurements [105]. $E_0=0$ for exothermic reactions and $E_0=\Delta H_R$ for endothermic reactions. Around the average temperature $\bar{T}$, k_c can be approximated using a standard Arrhenius expression [86],

$$k_c = A_c \exp[-E/RT], \qquad \text{(A6.2)}$$

where $$A_c = 10^{12.44} \left(\frac{e\bar{T}}{\mu}\right)^{1/2} \bar{\sigma}^2 \ (cm^3/mole/sec), \tag{A6.3}$$

and $$E=E_0+1/2\ R\bar{T}. \tag{A6.4}$$

As mentioned above, the collision rate k_c is an upper bound for k, the actual rate constant of interest. To relate further k_c to k around the average temperature $\bar{T}$, a steric factor p can be introduced to relate A_c to A_a, the respective Arrhenius pre-exponential factors of k_c and k; for

$$k=A\ T^m \exp[-\theta/T]\ (cm^3/mole/sec),$$

the approximate Arrhenius pre-exponential factor A_a around $\bar{T}$ is [86]

$$A_a=A\ (e\bar{T})^m, \tag{A6.5}$$

and, by definition, $$p=A_a/A_c \tag{A6.6}$$

In general, steric factors decrease with increasing complexity of the reactants. Table A6.1 shows estimates of the steric factors for the reaction rates measured in the present study. To evaluate p from eqs. (A6.2) to (A6.6), average temperatures $\bar{T}$ were set equal to the average experimental temperatures in Table 6.1; in addition, the present recommended rate expressions (Table 6.1) were used to estimate the "actual" rate constants k and the corresponding values of A_a (eq. A6.5). Note the coupling between the value of p inferred and the activation energy specified or assumed. The resulting steric factors are high for the reactions of radicals and atoms ($0.05<p<0.1$), and lower for the reactions of stable molecules and radicals ($p\approx0.01$). A greater disparity is observed for the reactions of stable molecules and atoms ($0.01<p<0.2$); such disparity has also been observed by Gardiner [86]. Table A6.1 and other reported values of p (see Gardiner [86]) are useful to assume reasonable steric factors for unknown elementary reactions. Thus, rough estimates of unknown rate constants can be found using eq. (A6.1) and

$$k^{estimated}=p^{estimated} \times k_c. \tag{A6.7}$$

Table A6.1 - Experimental Steric Factors

	Reaction	Type [a]	$\bar{T}$ [b]	μ [c]	$\bar{\sigma}$	$\log_{10}A$ [d]	p	$\Delta H(\bar{T})$ [e]	E [f]
2	$C_2N_2+O \rightarrow CN+NCO$	A-S	2000	12.2	3.05	14.73	0.009	+3	+9
3	$CN+O \rightarrow CO+N$	R-A	2000	9.90	2.51	14.61	0.05	-75	0
4	$CN+O_2 \rightarrow NCO+O$	R-S	2400	14.3	3.37	14.82	0.009	-1	0
5	$NCO+O \rightarrow CO+NO$	R-A	1450	11.6	3.26	14.73	0.1	-105	0[g]
8	$HCN+O \rightarrow NCO+H$	A-S	1440	10.0	3.06	14.71	0.06	0	+2
9	$NCO+H \rightarrow CO+NH$	R-A	1490	0.977	3.13	15.24	0.06	-39	+2[g]
10	$NCO+H_2 \rightarrow HNCO+H$	R-S	1490	1.91	3.86	15.28	0.009	-10	+8[g]
11	$C_2N_2+H \rightarrow CN+HCN$	A-S	1490	0.981	2.92	15.18	0.2	+4	+8

[a] R-A=Radical+Atom; $0.05<p<0.1$.
R-S=Radical+Stable species; $p=0.009$.
A-S=Atom+Stable species; $0.009<p<0.2$.

[b] Average experimental temperature (°K).

[c] Collision cross-section of the reactants A and B. $\bar{\sigma}=(\sigma_A+\sigma_B)/2$ (Å).

[d] A-factor of k_c in Arrhenius form, $A=10^{12.44}\left(\frac{e\bar{T}}{\mu}\right)^{1/2}\bar{\sigma}^2$(cc/mol/sec).

[e] Heat of reaction at $\bar{T}$ (kcal/mole).

[f] Activation energy at $\bar{T}$ in Arrhenius form. $E=(\theta+m\bar{T})R$ (kcal/mole).

[g] Estimated activation energy (kcal/mole).

In general, absolute estimates based on transition state theory or the line-of-center approach must be used with great caution, and shock tube experiments should be designed to minimize their influence on the final result.

A6.3 Data Reduction Procedure

The reduction of experimental shock tube data consists in minimizing the quantity $|\chi-\chi_0|/\chi_0$ in a given time interval $[t_0,t_f]$ by adjusting a few selected rate parameters. $\chi_0=g_0[t;\beta]$ is the mole fraction profile derived from an experimental record using the calibration parameter β,

and $\chi=g[t;k_j]$ is the theoretical mole fraction computed using a complete reaction mechanism and the set of rate constants k_j. The data reduction can prove very complex, if it is posed in these general terms, since $\chi=g[t;k_j]$ is often a complicated parametric function of k_j. Only limited systematic treatments of this kind have been reported in the literature. In particular, Miller and Frenklach applied a statistical analysis to the study of the thermal decomposition of propane [90]. Despite several attempts to generalize these techniques, only simple mechanisms have been investigated. Further, these methods are often aimed at minimizing the quantity $|\chi-\chi_0|/\chi$ at a single characteristic time, rather than over a complete time interval $[t_0,t_f]$.

In practice, it appears convenient to fit the selected kinetics parameters to a few specific features that can be easily identified on the theoretical profile. Such features include absolute peak concentrations, plateau levels, relative initial slopes, relative decays, times-to-peak, etc... If these features can be quantified, then the data reduction consists in solving the set of N equations

$$a_i=a_i^0 \quad i=1,N, \tag{A6.8}$$

where

$$a_i=g_i[K_j;I_n;\beta], \quad j=1,N \; ; \; n=1,M \; ; \tag{A6.9}$$

a_i are N features of the theoretical profile, K_j are N selected kinetics parameters, I_n are M uncertain rate constants that can interfere with the data reduction, β is a calibration parameter, and g is a real parametric function. (The quantities K_j may be rate constants of combinations thereof). To obtain a unique solution to eq. (A6.8), N features a_i must be identified to determine uniquely the N quantities K_j. In principle, eq. (A6.8) can be solved numerically using a Newton-Raphson technique based on a first order expansion of eq. (A6.9),

$$a_i-a_i^0 = \sum_j \frac{\partial g_i}{\partial K_j}(K_j-K_j^0) \; , \; i=1,N \; . \tag{A6.10}$$

K_j° is the solution to eq. (A6.8); a_i are N features computed using the N estimates K_j. Equation (A6.10) can be written in matrix form

$$\mathbf{A} = \mathbf{J}\,\mathbf{K}, \tag{A6.11}$$

where J is the Jacobian of the set of functions g_i. A unique solution to eq. (A6.11) can only be found if the determinant of J is different than zero.

In practice, it is often difficult to quantify the characteristic features a_i or to find the function g_i in closed form. In this case, a solution to eq. (A6.8) is found by adjusting the set of N parameters K_j until a simultaneous visual match of the N features a_i is obtained. The systematic treatment outlined above remains useful to establish the feasibility of the data reduction procedure. For example, in the data reduction of the $C_2N_2/O_2/H_2/N_2O/Ar$ experiments described in ¶5.2, the following profile features and kinetics parameters have been used (see Table 5.4): a_1=relative slope, a_2=absolute peak concentration, a_3=relative decay; $K_1=k_9$, $K_2=k_{11}/k_{12}$, $K_3=k_{10}$, with the reactions

$$NCO + H \rightarrow CO + NH, \tag{9}$$

$$C_2N_2 + H \rightarrow CN + HCN, \tag{11}$$

$$CN + H_2 \rightarrow HCN + H, \tag{12}$$

$$NCO + H_2 \rightarrow HNCO + H. \tag{10}$$

Using Table 5.4, the corresponding Jacobian matrix is written

$$J = \begin{vmatrix} a_{11} & a_{12} & -a_{13} \\ -a_{21} & a_{22} & -a_{23} \\ 0 & a_{32} & 0 \end{vmatrix}, \text{ with } a_{ij}>0.$$

It follows that the Jacobian determinant is strictly positive,

$$\det(\mathbf{J})=a_{32}(a_{11}a_{23}+a_{21}a_{13})>0.$$

In principle, all three parameters K_j can be extracted using the three characteristic features found in Table 5.4, and the data reduction procedure is feasible.

A6.4 Uncertainty Analysis

Like other experimental techniques, shock tube measurements contain inherent uncertainties. Since the resulting kinetics data is often used in other experiments to extract further fundamental parameters, careful estimates of the experimental uncertainties should be reported with the recommended rate constants. These uncertainties usually fall in two categories. First, the uncertainties associated with the spectroscopic diagnostics can be distinguished. They result in the uncertain measurement of the species concentrations, and are related to detection limits and the accuracy of calibration parameters. Other significant uncertainties result from the uncertain knowledge of the rates of interfering reactions in the mechanism. In principle, theoretical estimates of all uncertainties can be obtained using the first-order analysis introduced in ¶A6.3. If the nominal interfering rates $I_n°$ and calibration parameter $\beta°$ are adjusted by the amounts $(I_n-I_n°)$ and $(\beta-\beta°)$, then the recommended parameters $K_j°$ must be adjusted by $(K_j-K_j°)$ to ensure the return to an optimum fit. To first order,

$$a_i-a_i^0 = \sum_j \frac{\partial g_i}{\partial K_j}(K_j-K_j^0) + \sum_n \frac{\partial g_i}{\partial I_n}(I_n-I_n^0) + \frac{\partial g_i}{\partial \beta}(\beta-\beta^0) \ . \qquad \text{(A6.12)}$$

An optimum fit is obtained with $a_i-a_i°=0$. Thus, eq. (A6.12) can be solved for $(K_j-K_j°)$. For j=1,N,

$$(K_j-K_j^0) = \sum_i (J^{-1})_{ji} \left(\sum_n \frac{\partial g_i}{\partial I_n}(I_n-I_n^0) + \frac{\partial g_i}{\partial \beta}(\beta-\beta^0)\right) , \qquad \text{(A6.13)}$$

where $(J^{-1})_{ji}$ is the (j,i) component of the inverse Jacobian. Equation (A6.13) can be rearranged to read

$$(K_j-K_j^0) = \sum_n \left(\sum_i (J^{-1})_{ji} \frac{\partial g_i}{\partial I_n}\right)(I_n-I_n^0) + \sum_j (J^{-1})_{ij} \frac{\partial g_i}{\partial \beta}(\beta-\beta^0)$$

$$= \sum_n a_{jn}(I_n-I_n^0) + b_j(\beta-\beta^0) \ . \qquad \text{(A6.14)}$$

Assuming that $(I_n-I_n°)$ and $(\beta-\beta°)$ are N+1 normally distributed independent random variables with variance $\sigma(I_n)$ and $\sigma(\beta)$,

$$\sigma^2(K_j) = \sum_n a_{jn}^2 \, \sigma^2(I_n) + b_j^2 \, \sigma^2(\beta) \; . \qquad \text{(A6.15)}$$

Since absolute uncertainties in K_j are proportional to the variance $\sigma(K_j)$,

$$\frac{\Delta K_i}{K_i} = \sqrt{\sum_n \left(\frac{\Delta K_i}{K_i}\right)_n^2} \, , \qquad \text{(A6.16)}$$

where $(\Delta K_i/K_i)_n$ is the nth component of the uncertainty, associated with the nth interfering rate constant (or with the calibration parameter β). As mentioned earlier, it is difficult in practice to evaluate the Jacobian J or the functions g_i. Usually, it is convenient to estimate the quantities $(\Delta K_i/K_i)_n$ by modifying each individual rate I_n (or β) by a factor F_n, and to adjust the parameters $K_i°$ by the factors F_i^n to ensure the return to an optimum fit of all characteristic features a_i. Then the values of $(\Delta K_i/ K_i)_n$ can be estimated using

$$\left(\frac{\Delta K_i}{K_i}\right)_n = (\Delta \ln K_i)_n = \ln F_i^n \; . \qquad \text{(A6.17)}$$

(In the uncertainty tables of chapters 2 to 5, the quantities $\ln F_i^n$ are expressed as a percentage.)

In general, if an excursion $I_n° \times F_n$ results in the adjusted rate $K_i° \times F_i^n$, then the excursion $I_n°/F_n$ does not necessarily result in $K_i°/F_i^n$. Therefore, it is useful to consider separately the factors resulting in an increase in K_i $(K_i \times F_i^n)$ and the factors resulting in a decrease in K_i $(K_i \times f_i^n)$, and

$$\ln F_i = \sqrt{\sum_n (\ln F_i^n)^2} \text{ and } \ln f_i = \sqrt{\sum_n (\ln f_i^n)^2} \; . \qquad \text{(A6.18)}$$

F_i^n and f_i^n are the upper and lower factors necessary to adjust $K_i°$ for the return to an optimal fit, given the maximum excursions of I_n. F_i and f_i are the resulting excursion factors for $K_i°$. Thus, the estimated error bar attached to the result $K_i = K_i°$ is given by

$$(K_i^{min} = f_i K_i°) < K_i < (K_i^{max} = F_i K_i°). \qquad \text{(A6.19)}$$

Appendix 7

Analysis of an HCN/argon Cylinder

Hydrogen cyanide may slowly decompose in high-pressure HCN/Ar cylinders by surface reactions on the cylinder walls. In the kinetics experiments of chapter 5, the precise composition of a cylinder mixture was required to extract absolute values of elementary reaction rate constants. In particular, eq. (5.6) shows that the experimental ratio k_8^*/k_2^* is inversely proportional to the mole fraction of HCN in the reactant mixture. In this appendix, a comparative method to check the HCN composition of an unknown cylinder (C_1) using another cylinder of known composition (C_2) is examined.

Shortly after completing our experiments with the original cylinder (C_1; initial composition, 8.9% HCN dilute in argon), the manufacturer (Airco) delivered a recently calibrated cylinder (C_2) containing a mixture of 9.116% HCN dilute in argon. To check the composition of (C_1) against the known composition of (C_2), mixtures of the cylinder gases dilute in argon were shock-heated, with the conditions T_2=4050±130°K and p_2=0.33±0.01 atm. The respective plateau emission levels of CN at 388 nm were compared to infer the composition of C_1, the unknown cylinder. The CN emission system was described in detail by Szekely [72]. It consists of aligning and focusing optics, a monochromator and a photomultiplier tube. To ensure nearly complete conversion of HCN to CN, the experiments were conducted in highly diluted mixtures of HCN (see Szekely, et al. [91]). Table A7.1 summarizes the experimental conditions and results. The dilution parameter d is the fraction of cylinder gas in the experimental mixture. If x is the mole fraction of HCN in the cylinder, then the HCN mole fraction in the experiment is x×d. V is the observed voltage corresponding to the CN emission plateau. It is proportional to the plateau CN mole fraction and to the pressure p. The CN mole fraction is in turn proportional to the initial HCN mole fraction, and

$$V=F(T)\ x\ d\ p, \qquad (A7.1)$$

where F(T) is a constant independent of the cylinder composition and function of temperature. Six runs were performed with the original cylinder (C_1) and F(T) showed no significant temperature dependence within the limited temperature range of these experiments ($3963<T<4368°K$). After a statistical analysis of the data using a t-distribution [62], it was found

$$(x_2F)=(5.97\pm0.34)\ 10^4\ \text{mV/atm}$$
$$(x_1F)=(4.83\pm0.04)\ 10^4\ \text{mV/atm}, \qquad \text{(A7.2)}$$

at 95% degree of confidence. Using eqs. (A7.1) and (A7.2), the dilution of the original cylinder (C_1) was extracted using

$$x_1 = x_2 \frac{(x_1F)}{(x_2F)} = 9.116\% \times \frac{4.83}{5.97} = 7.4\pm0.4\% \ , \qquad \text{(A7.3)}$$

at 95% degree of confidence. The magnitude of x_1 indicates that a significant amount of HCN had decomposed in cylinder C_1 (18%).

Table A7.1 - Analysis of an HCN Cylinder

Cylinder	p(atm)	T(°K)	d(%)	V(mV)	$xF\times10^{-4}$(mV/atm)
C_2	0.329	4058	0.261	55.4	6.45
C_2	0.357	4368	0.263	52.0	5.54
C_2	0.321	3980	0.242	48.4	6.23
C_2	0.320	3963	0.291	54.4	5.84
C_2	0.334	4113	0.292	56.9	5.83
C_2	0.327	4048	0.368	71.4	5.93
C_1	0.325	4039	0.274	43.0	4.83
C_1	0.321	3961	0.279	43.2	4.82

An additional experiment was conducted to check the accuracy of this method using a known cylinder containing a mixture of C_2N_2 (1.01%) dilute in argon. Under the conditions of the experiment (T_2=3940°K, p_2=0.328 atm, d=1.224%), C_2N_2 is rapidly converted to 2 CN (see Appendix 2), and the observed voltage plateau (V=50.5 mV) is given by

$$V=2\ F\ x\ d\ p. \qquad (A7.4)$$

Using $F=(x_2F)/x_2=5.97\times10^4/0.09116$ mV/atm, this method predicts the following composition of the C_2N_2/Ar cylinder:

$$x=50.5\times0.09116/2\times5.97.10^4\times0.01224\times0.328=0.96\%.$$

This value agrees within 5% with the actual composition of the C_2N_2/Ar cylinder (x=1.01%). The method described in this appendix is therefore reliable and it can be used to check the composition of HCN/Ar gas cylinders.

Appendix 8

The Fuel-Nitrogen Mechanism

A8.1 Introduction

The mechanism of fuel-nitrogen chemistry has drawn considerable attention in the combustion community. In a study of rich atmospheric pressure flames (CH_4, C_2H_4 or C_2H_2), Morley [3] observed nearly quantitative conversion of fuel-nitrogen to hydrogen cyanide in the reaction zone, regardless of the actual source of fuel-nitrogen (NO, NH_3, CH_3CN or pyridine). Acknowledging Morley's results, and implicitly assuming a fast, quantitative and therefore not rate-limiting production of HCN, other workers subsequently studied the conversion of HCN to NO and N_2 in the post-flame gases. For example, Haynes [9] considered the fate of HCN in a key paper on HCN oxidation in fuel-rich flames. Morley [74] detected intermediate species such as OH, NH, CN and NO in premixed H_2/O_2/argon flames doped with CH_3CN to elucidate NO and N_2 formation. Using a more direct approach, Miller, et al. [6] recently studied low pressure premixed H_2/O_2/argon flames seeded with HCN, and successfully developed the first comprehensive model of fuel-nitrogen chemistry coupled with a complete flame structure analysis. Finally, the present shock tube work was aimed at characterizing the detailed kinetics of the conversion of HCN to NH_i species.

In this appendix, implications of the present reaction rate measurements for the overall kinetics of the fuel-nitrogen mechanism are discussed. A simplified model of the combustion of H_2/CO mixtures seeded with HCN is used to assess the relative importance of the major paths in the conversion of HCN to NO and N_2 under post-flame conditions. The computer results are then compared with available experimental data to discuss the limitations of the model.

Table A8.1 - Kinetic Model of $H_2/O_2/CO$/argon/HCN Combustion

	Reactions	Rate Constant [a]			Source (Ref. #)
		$\log_{10}A$	m	θ(°K)	
3	$CN+O \rightarrow CO+N$	13.31	0	210	This study
4	$CN+O_2 \rightarrow NCO+O$	12.75	0	0	This study
5	$NCO+O \rightarrow CO+NO$	13.75	0	0	This study
6	$NCO+M \rightarrow N+CO+M$	16.80	-0.5	24000	This study
8	$HCN+O \rightarrow NCO+H$	8.24	1.47	3775	This study
9	$NCO+H \rightarrow CO+NH$	14.02	0	1000	This study
10	$NCO+H_2 \rightarrow HNCO+H$	13.23	0	4000	This study
12	$CN+H_2 \rightarrow HCN+H$	11.74	0.7	2460	[6]
15	$N_2+O \rightarrow N+NO$	14.26	0	38370	[22]
16	$NO+O \rightarrow N+O_2$	9.58	1.0	20820	[22]
22	$NO+H \rightarrow N+OH$	14.23	0	24560	[22]
23	$H+O_2 \rightarrow OH+O$	17.57	-1.0	8810	[94]
24	$O+H_2 \rightarrow H+OH$	10.26	1.0	4480	[94]
25	$H_2O+O \rightarrow OH+OH$	9.66	1.3	8605	[94]
26	$H_2+OH \rightarrow H_2O+H$	9.07	1.3	1825	[95]
27	$HCN+O \rightarrow NH+CO$	8.73	1.2	3820	[16]
29	$HCN+OH \rightarrow CN+H_2O$	12.64	0	4530	[6]
30	$CN+OH \rightarrow NCO+H$	13.75	0	0	[9]
36	$HNCO+H \rightarrow NH_2+CO$	14.00	0	4280	[97]
37	$NH+H \rightarrow N+H_2$	13.70	0	1000	[22]
38	$NH_2+H \rightarrow NH+H_2$	13.28	0	0	[22]
39	$NCO+OH \rightarrow HNCO+O$	13.3	0	0	estimate
40	$CH_4+1/2\,O_2 \rightarrow CO+2H_2$	-	-	-	[73] [b]
41	$H_2+O_2 \rightarrow OH+OH$	13.23	0	24230	[99]
42	$H_2+M \rightarrow H+H+M$	12.35	0.5	46600	[6]
43	$CO+OH \rightarrow CO_2+H$	7.18	1.3	-385	[100]
44	$NH_2+OH \rightarrow NH+H_2O$	11.7	0.5	1000	[22]
45	$NH_2+O \rightarrow HNO+H$	14.8	-0.5	0	[22]
46	$NH_2+O \rightarrow NH+OH$	14.1	-0.5	0	[22]

Table A8.1 (continued)

Reactions	Rate Constant[a]			Source (Ref. #)
	$\log_{10}A$	m	θ(°K)	
47 $NH+OH \rightarrow HNO+H$	12.0	0.5	1000	[22]
48 $NH+OH \rightarrow N+H_2O$	11.7	0.5	1000	[22]
49 $NH+O \rightarrow NO+H$	11.8	0.5	0	[22]
50 $NH+N \rightarrow N_2+H$	11.8	0.5	0	[22]
51 $HNO+M \rightarrow H+NO+M$	16.5	0	24500	[22]
52 $HNO+OH \rightarrow NO+H_2O$	12.1	0.5	1000	[22]
53 $HNO+O \rightarrow NO+OH$	11.7	0.5	1000	[22]
54 $HNO+H \rightarrow NO+H_2$	13.1	0	2000	[22]
55 $NH_2+NO \rightarrow N_2+H_2O$	19.8	-2.5	950	[22]

[a] Using the notation $k=A\ T^m \exp[-\theta/T]$ (cm^3/mole/sec).

[b] Global reaction (see eq. A8.1).

A8.2 Simplified Model of the Fuel-Nitrogen Mechanism

A zero dimension, diffusion-free, constant pressure and temperature model of the combustion of H_2/CO mixtures seeded with HCN was incorporated in a standard shock tube kinetics code [40]. The initial proportions of H_2, O_2 and CO corresponded to selected methane/air flames stoichiometries, in an attempt to approximate the relative proportions of H, O and OH species in the post-flame gases of a CH_4/air flame. Accordingly, an additional step was introduced to produce CO and H_2 from the global oxidation of CH_4,

$$CH_4 + 1/2\ O_2 \rightarrow CO + 2\ H_2. \tag{40}$$

Note that reaction (40) is several orders of magnitude faster than reaction (41), the rate-limiting step of the detailed kinetics,

$$H_2 + O_2 \rightarrow OH + OH. \tag{41}$$

Thus, reaction (40) does not significantly influence the kinetics of the model, and is merely a convenient way to incorporate the correct H_2, O_2 and CO proportions corresponding to methane combustion.

Despite the introduction of reaction (40), this calculation does not adequately model a typical premixed hydrocarbon flame. Bowman has shown that, upon choosing a judicious quasi-global rate, a model can successfully predict the distribution of temperature in the flame, but generally fails to reproduce the NO concentration profiles based on more detailed hydrocarbon kinetics [106]. In fact, the substitution of a quasi-global step for the detailed kinetics of methane oxidation results in a significant overshoot of active radical and atom concentrations that lead to increased rates of NO formation [106].

Reaction (40) is followed by elementary reactions in the H/O system, leading to partial equilibrium levels of O, H and OH

$$H_2 + O_2 \rightarrow OH + OH, \tag{41}$$

$$H_2 + M \rightarrow H + H + M, \tag{42}$$

$$H_2 + OH \rightarrow H_2O + H, \tag{26}$$

$$O_2 + H \rightarrow OH + O, \tag{23}$$

$$H_2 + O \rightarrow OH + H, \tag{24}$$

$$H_2O + O \rightarrow OH + OH, \tag{25}$$

and by the CO oxidation reaction

$$CO + OH \rightarrow CO_2 + H. \tag{43}$$

Duterque, et al. measured the rate of reaction (40) in a well-stirred reactor [73]

$$RR_{40}=10^{16.85} \exp[-23500/T]\ [CH_4][O_2]\ \text{mole/cm}^3\text{/sec}, \tag{A8.1}$$

where RR_{40} represents the rate of reaction (40). Note that the choice of Duterque's expression for RR_{40} is arbitrary. Quasi-global models developed for well-stirred reactors are not generally suitable to model shock

tube ignition delays or flame speeds. However, in the present case, reaction (40) is several orders of magnitude faster than reaction (41), the rate-limiting step of the detailed kinetics, regardless of the specific expression for RR_{40}. Thus, the present model conveniently incorporates Duterque's expression, which, unlike more complicated quasi-global rates, is first order in the reactant concentrations.

For this simplified model, the conversion of fuel-nitrogen to HCN is assumed to be instantaneous; thus, HCN is introduced with the premixed reactants [6], with a mole fraction corresponding to typical fuel-nitrogen contents (χ_{HCN}/χ_{CO}=1%). At the temperature of the calculations (T=1800°K), the direct oxidation of N_2 does not contribute significantly to nitric oxide formation, and the amount of molecular nitrogen in the premixed reactants does not influence the kinetics of the model. Thus, in order to monitor the formation of molecular nitrogen, argon has been used as a diluent in the "air", with the stoichiometric equation

$$\phi\ CH_4 + 2(O_2+3.76\ Ar) \rightarrow \phi\ CO + 2\phi\ H_2 + (2-\phi/2)O_2 + 7.52\ Ar \rightarrow \text{products} \qquad \text{(A8.2)}$$

A 38-reaction model shown in Table A8.1 was utilized in the calculations. A base case was computed with the nominal conditions T=1800°K, p=1 atm, ϕ=1, χ_{HCN}/χ_{CO}=1%. Time histories of the major/minor species mole fractions are given in Figs. A8.1 and A8.2.

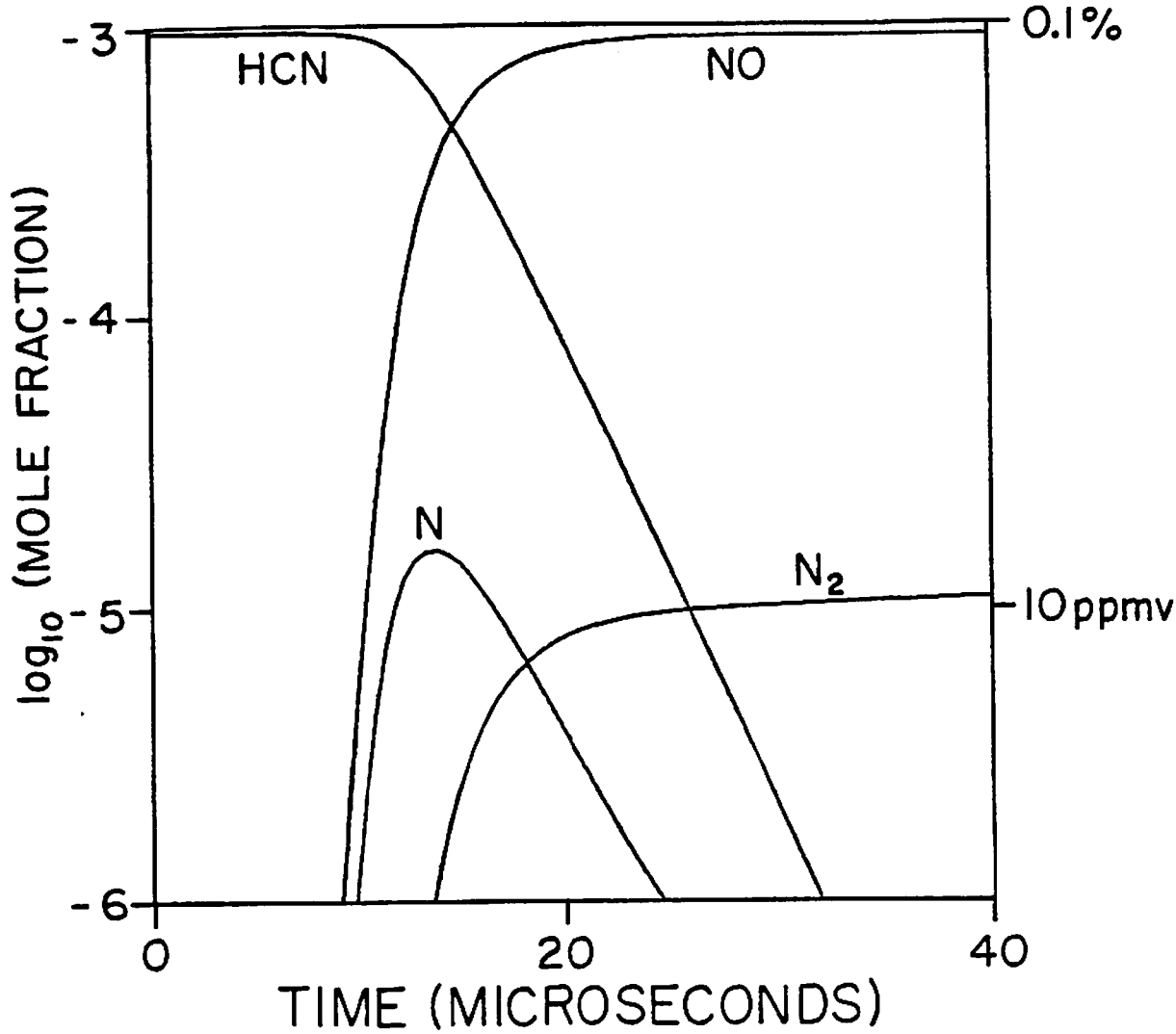

Fig. A8.1 Computer-predicted major species time-histories in a zero-dimensional model of premixed $CO/H_2/O_2/Ar/HCN$ combustion. The conditions are T=1800°K, p=1 atm, ϕ=1 (based on CH_4/air combustion) and HCN=1% of CO by volume. Note the rapid establishment of steady NO and N_2 mole fractions and the corresponding disappearance of HCN.

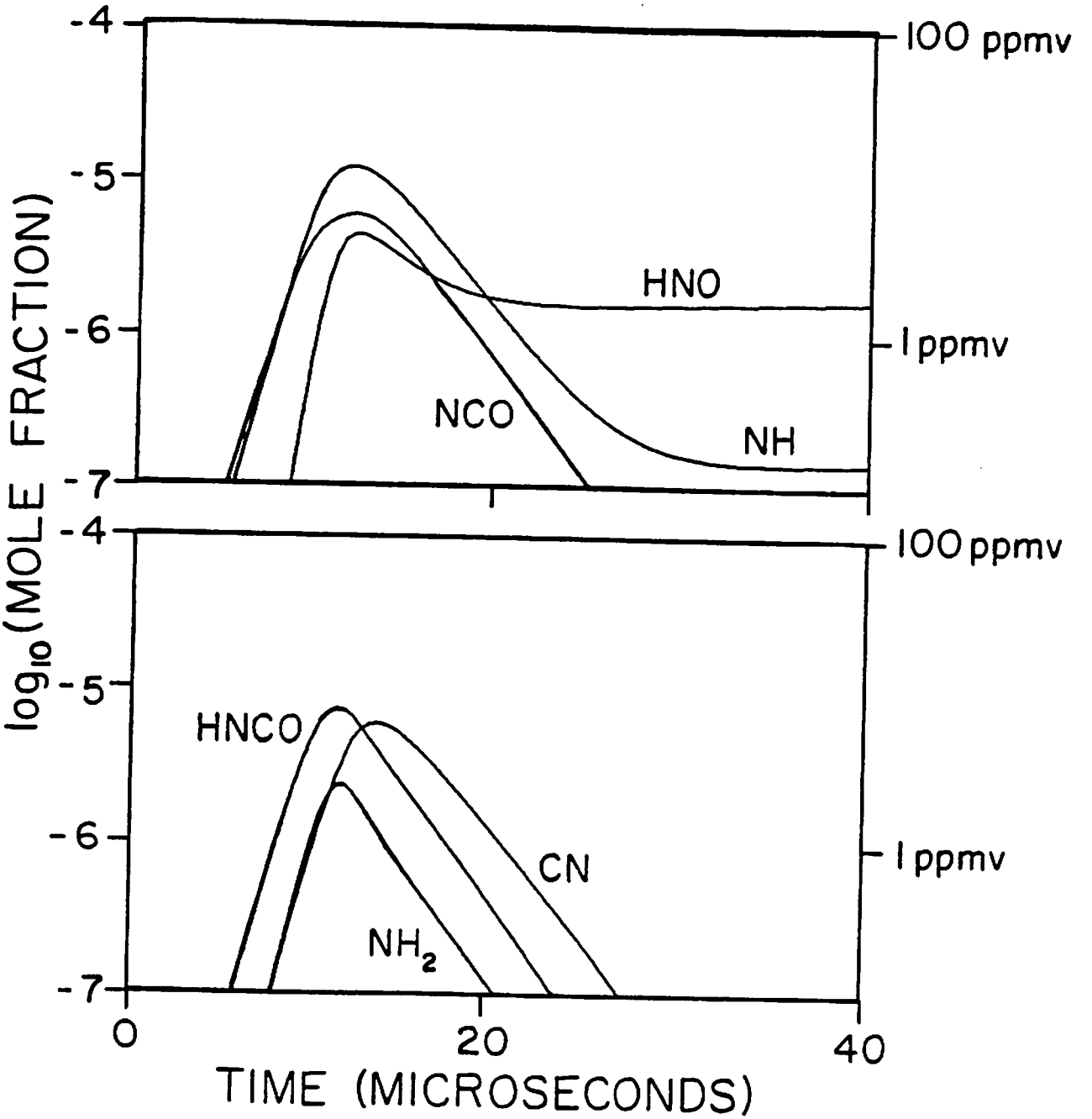

Fig. A8.2 Computer-predicted minor species time-histories. The conditions are identical to Fig. A8.1.

Figure A8.3 shows the relative importance of significant reaction paths in the HCN to NO and N_2 conversion. The numbers on each path represent the fraction of fuel-nitrogen which participates in a given reaction. These fractional numbers are subsequently called $P_j^{i\to k}$, where subscript (j) is the index of reaction (j), and superscripts (i) and (k) indicate which intermediate species in Fig. A8.3 are respectively removed (i) and formed (k) by reaction (j). Figure A8.3 can be interpreted as a current flow diagram, where the nodes (e.g., i or k) are the intermediate species, and the current (e.g., $P_j^{i\to k}$) is the amount of fuel-nitrogen involved in the reaction (e.g., j). For example, 9.6% of the fuel-nitrogen is involved in reaction (3).

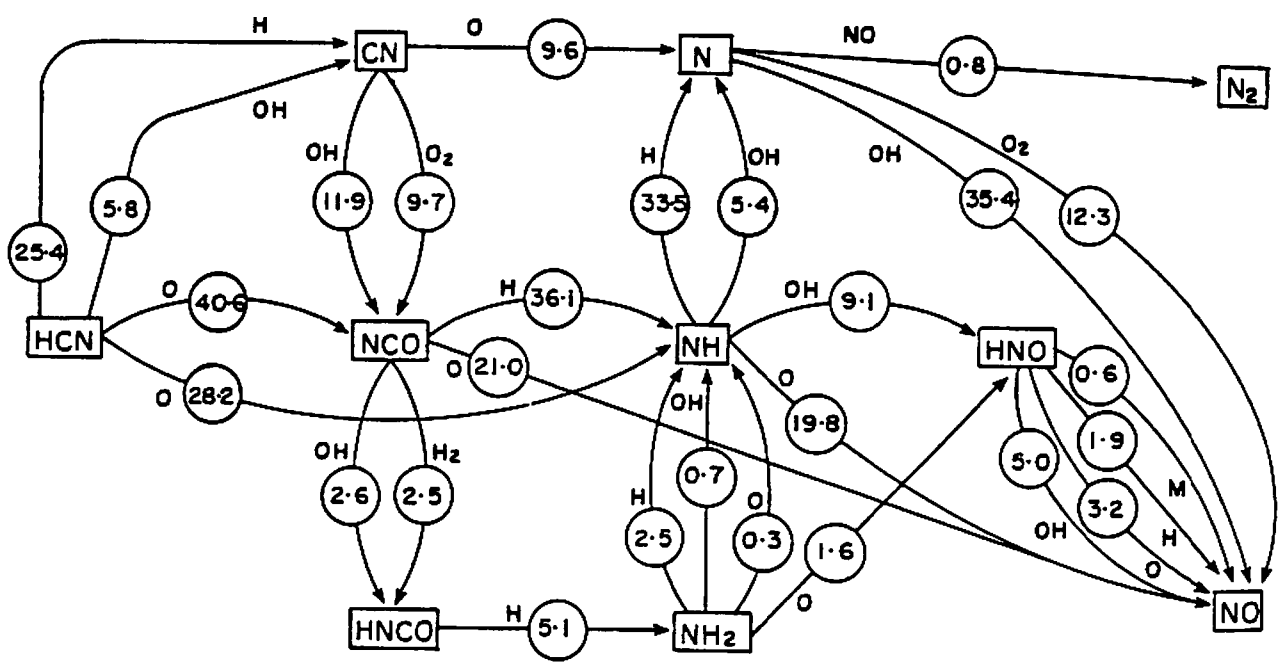

Fig. A8.3 Major reaction paths in the conversion of HCN to NO and N_2. The conditions are identical to Fig. A8.1. The numbers on each path represent the instantaneous fraction (%) of fuel-nitrogen which participates in a given reaction($P_j^{i\to k}$).

The fractional numbers $P_j^{i\to k}$ were computed for each intermediate species (i) using

$$P_j^{i\to k} = \left(\sum_n P_n^{l\to i}\right) \frac{RR_j^{i\to k}}{\sum_m RR_m^{i\to p}}, \tag{A8.3}$$

where $RR_m^{i\to p}$ represents the rate of reaction (m), which removes (i) and forms (p). For each node in Fig. A8.3 (e.g., CN), the total fraction of fuel-nitrogen coming to the node is equal to the total fraction leaving the node,

$$\sum_n P_n^{l\to i} = \sum_m P_m^{i\to p}. \tag{A8.4}$$

Note that Fig. A8.3 was constructed from left to right i.e., the numbers $P_j^{i\to k}$ were computed using removal rates only,

$$RR_m^{i\to p} = -k_m[i][x] + k_{-m}[p][y] < 0. \tag{A8.5}$$

For example, reaction (3) removes 30.8% of CN, since

$$\frac{RR_3^{CN\to N}}{RR_3^{CN\to N} + RR_4^{CN\to NCO} + RR_{30}^{CN\to NCO}} = \frac{RR_j^{i\to k}}{\sum_m RR_m^{i\to p}} = 30.8\%,$$

with

$$CN + O \to CO + N \tag{3}$$

$$CN + O_2 \to NCO + O, \tag{4}$$

$$CN + OH \to NCO + H. \tag{30}$$

Further, the total fraction of fuel-nitrogen converted to CN is given by

$$P_{-12}^{HCN\to CN} + P_{29}^{HCN\to CN} = \sum_n P_n^{l\to i} = 31.2\%,$$

with

$$HCN + H \to CN + H_2, \tag{-12}$$

$$HCN + OH \to CN + H_2O. \tag{29}$$

Therefore, the fraction of fuel-nitrogen involved in reaction (3) is

$$P_3^{CN\to N} = 31.2\% \times 30.8\% = 9.6\%.$$

All removal rates $RR_m^{i\to p}$ were computed at the peak of species (i) or, in the case of monotonic time-histories (e.g. for (i)=HCN, NO or N_2), at the 1/e time. This convention results in an instantaneous picture of the relative reaction paths (Fig. A8.3). Note that a more sophisticated algorithm could be used to integrate eq. (A8.3) and obtain the total fraction of fuel-nitrogen involved in reaction (j), during the entire conversion of HCN to NO and N_2,

$$\bar{P}_j^{i\to k} = \left(\sum_n \bar{P}_n^{l\to i}\right) \frac{\int RR_j^{i\to k} dt}{\sum_m \int RR_m^{i\to p} dt} . \qquad \text{(A8.6)}$$

Thus, under the assumptions of the present model, Fig. A8.3 indicates the major paths in the conversion of HCN to NO and N_2,

HCN + H → CN + H_2 (25%),	(-12)
HCN + O → NCO + H (41%),	(8)
HCN + O → NH + CO (28%),	(27)
NCO + H → CO + NH (36%),	(9)
NCO + O → CO + NO (21%),	(5)
NH + H → N + H_2 (34%).	(37)

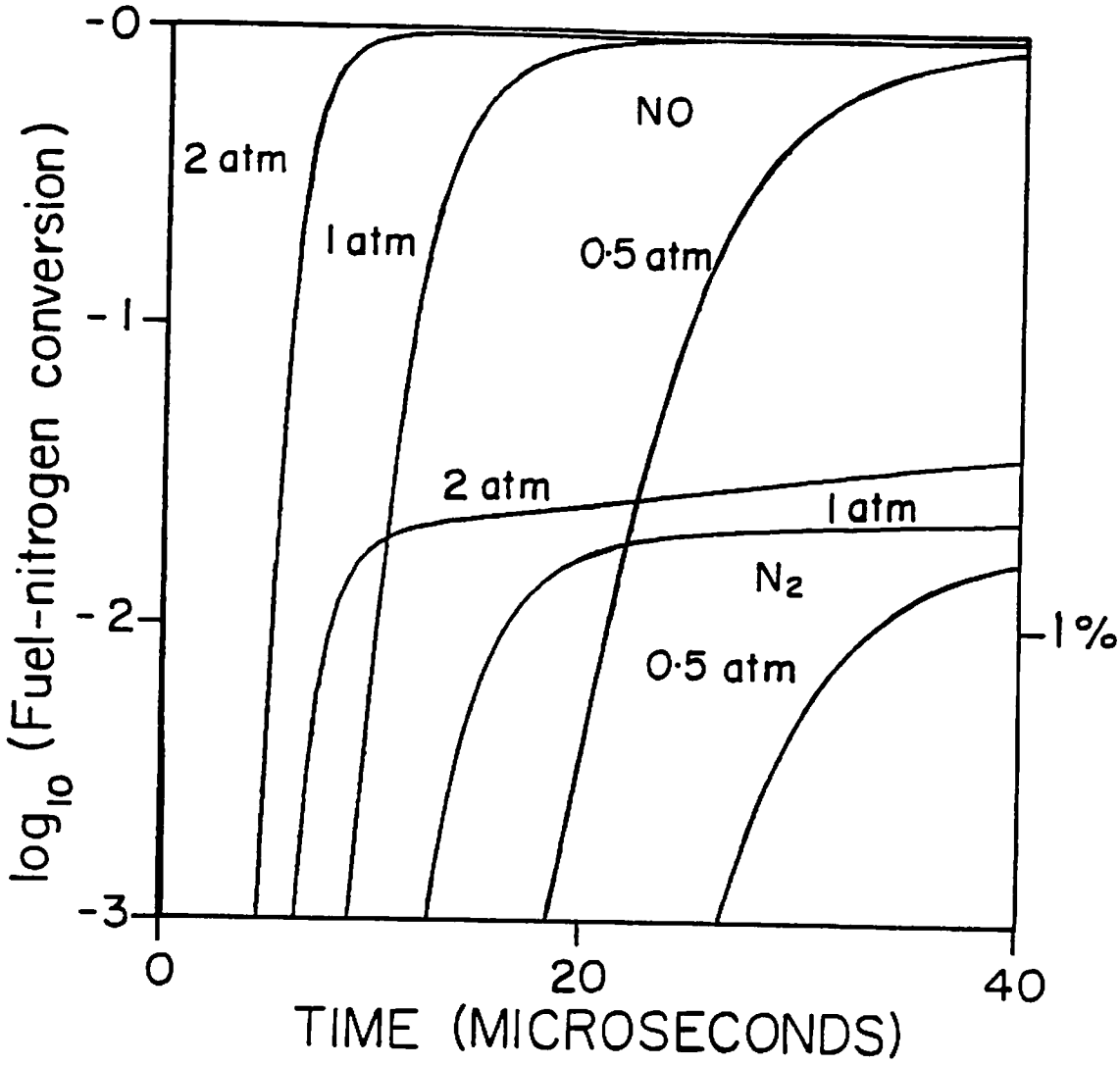

Fig. A8.4 Effect of pressure on the fraction of fuel-nitrogen converted to NO and N_2. The time-dependent conversion is defined as $2\chi_{N_2}/(\chi_{HCN})_{t=0}$ for N_2 and $\chi_{NO}/(\chi_{HCN})_{t=0}$ for NO.

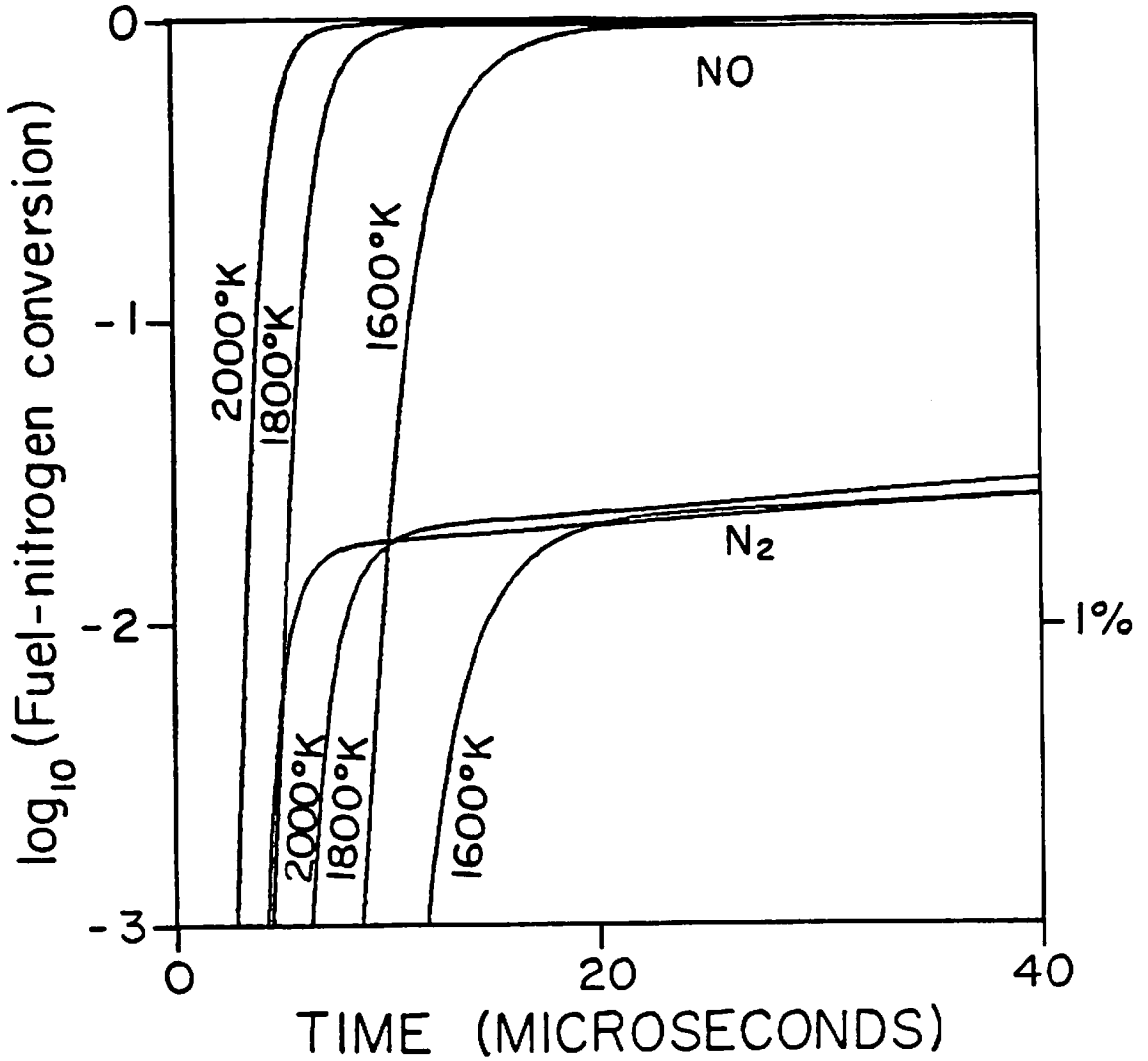

Fig. A8.5 Effect of temperature on the fraction of fuel-nitrogen converted to NO and N_2.

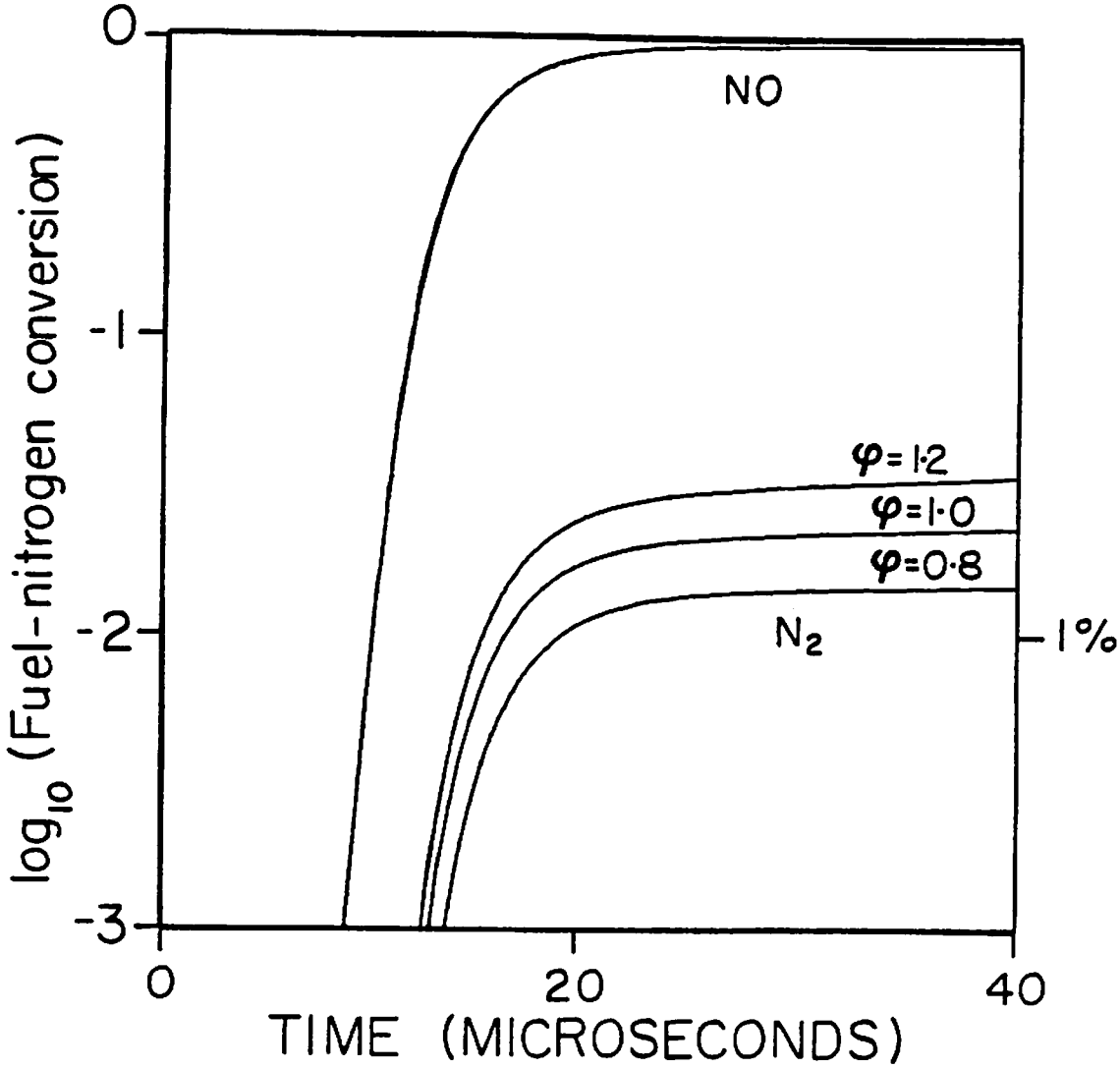

Fig. A8.6 Effect of equivalence ratio ϕ on the fraction of fuel-nitrogen converted to NO and N_2. Stoichiometric coefficients are based on methane/air combustion.

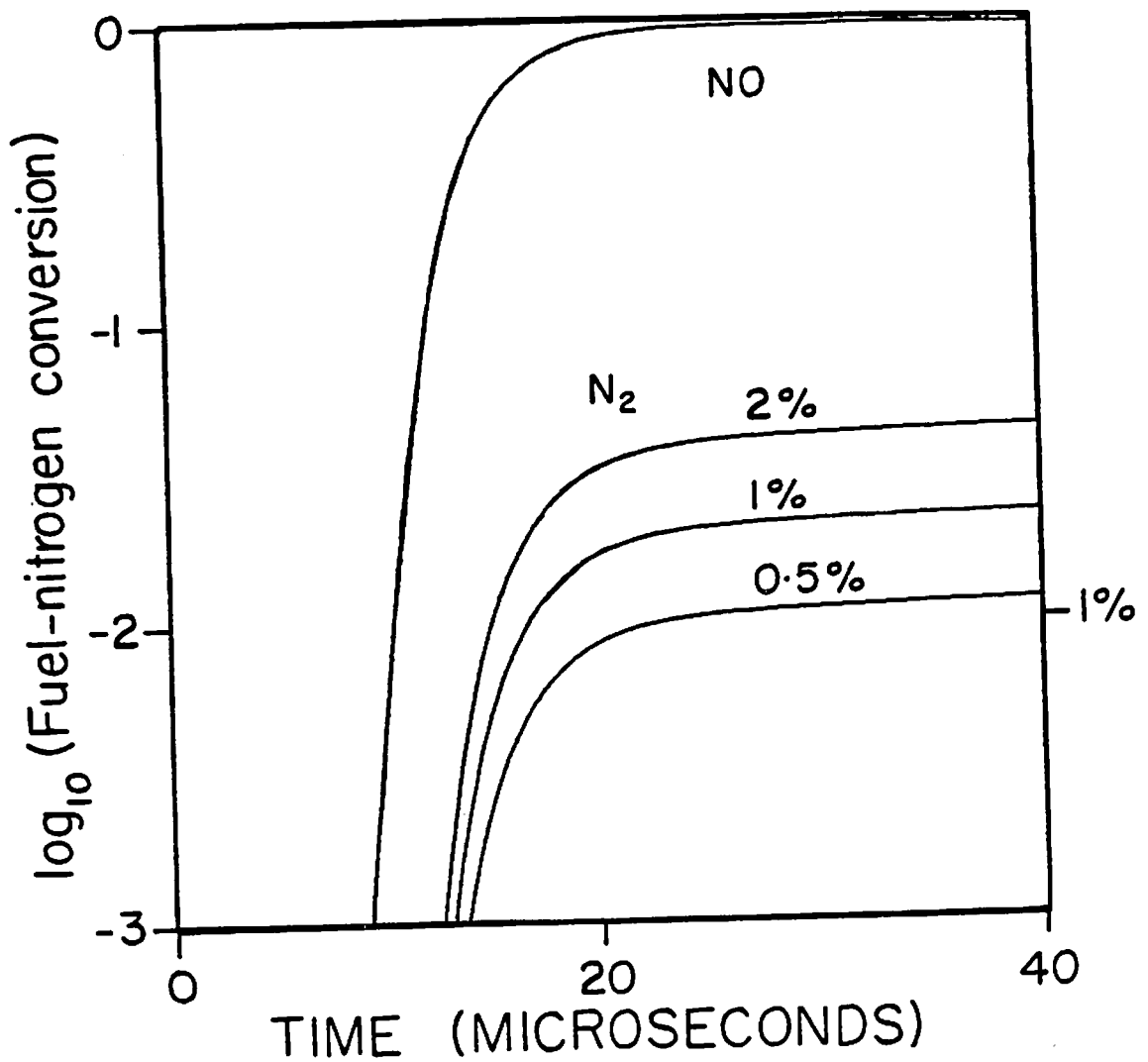

Fig. A8.7 Effect of fuel-nitrogen content (χ_{HCN}/χ_{CO}) on the fraction converted to NO and N_2.

Effects of excursions in p, T, ϕ and the ratio χ_{HCN}/χ_{CO} are shown in Figs. A8.4 to A8.7, where the fraction of fuel-nitrogen converted to NO ($\chi_{NO}/\chi_{HCN,t=0}$) or N_2 ($2\chi_{N_2}/\chi_{HCN,t=0}$) are plotted as a function of time. Pressure and temperature have a significant influence on the time behavior, but have a smaller effect on the overall conversion to N_2 and NO (Figs. A8.4 and A8.5). On the other hand, richer stoichiometries and higher fuel-nitrogen contents enhance the conversion of NO to N_2 (Figs. A8.6 and A8.7). Figures A8.8 and A8.9 show the main reaction paths corresponding to ϕ=0.8 and ϕ=1.2. Only the paths that involve more than 20% fuel-nitrogen have been shown. From Figs. A8.3, A8.8 and A8.9, it is clear that nitrogen formation follows the production of nitric oxide and occurs mostly via reaction (-15)

$$N + NO \rightarrow N_2 + O, \qquad (-15)$$

and that NO is produced mostly by reactions (-22) and (-16)

$$N + OH \rightarrow NO + H, \qquad (-22)$$

$$N + O_2 \rightarrow NO + O. \qquad (-16)$$

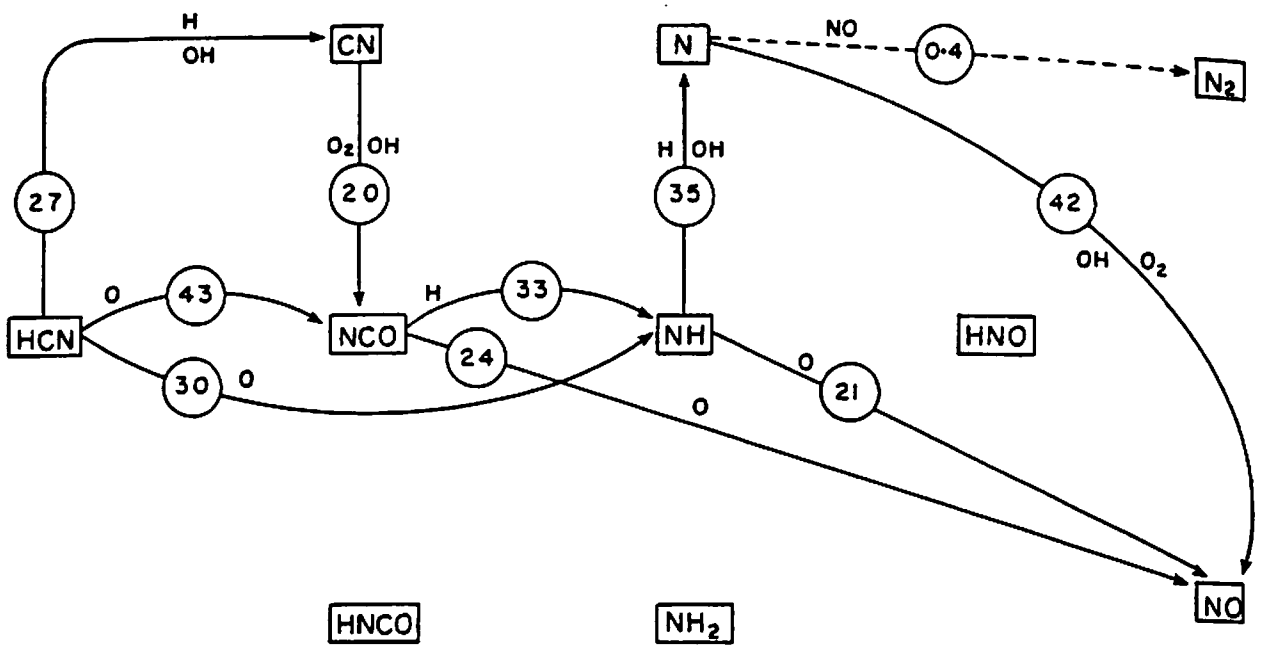

Fig. A8.8 Major reaction paths in the conversion of HCN to NO and N_2. The conditions are identical to Fig. A8.1, except ϕ=0.8.

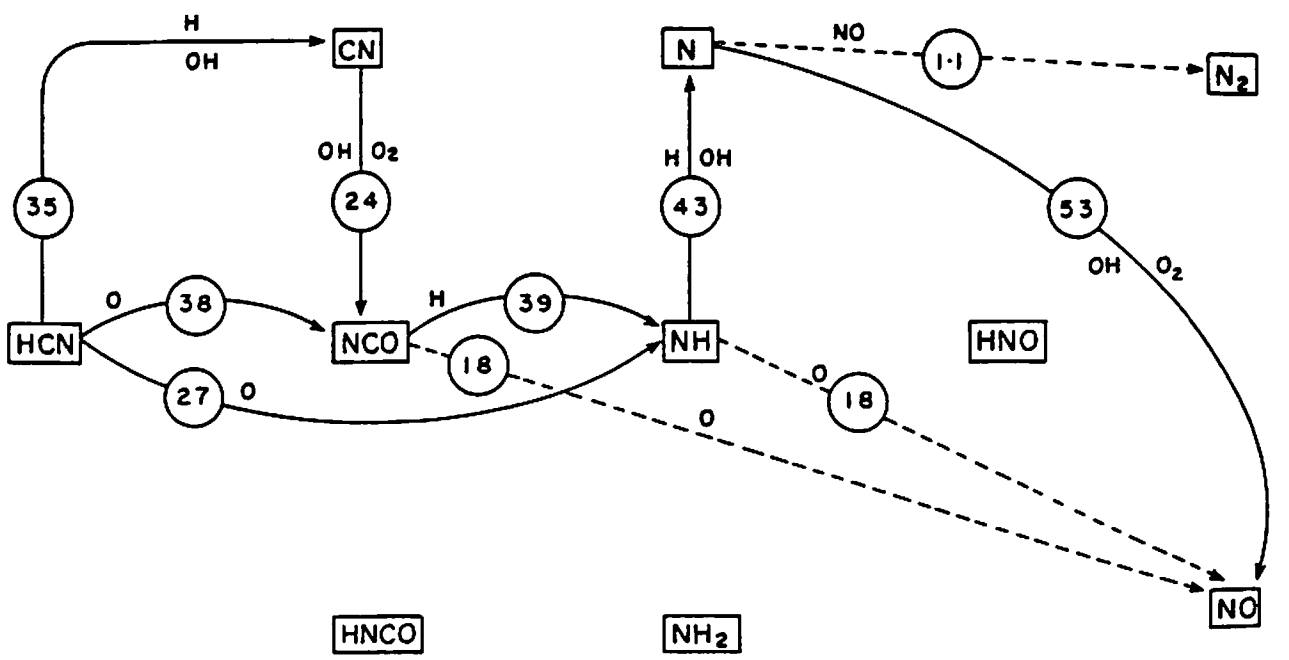

Fig. A8.9 Major reaction paths in the conversion of HCN to NO and N_2. The conditions are identical to Fig. A8.1, except ϕ=1.2.

A8.3 Discussion

The consistency of the model presented above can be checked against the experimental results of Miller, et al. for low-pressure H_2/O_2/argon/HCN flames (p=30 Torr) [6]. Miller observed substantial nitrogen yields at low pressures, with increasing stoichiometries leading to more N_2. Under similar conditions (T=1300°K, p=30 Torr and H_2:O_2:HCN:Ar=27:13:2:9958), the present model predicts χ_{N_2}=0.5% and χ_{NO}=0.8% at steady state, while Miller has observed χ_{N_2}=0.6% and χ_{NO}=0.7%. Thus, the model appears consistent with relevant experimental observations. A comparison of Miller's observed time-histories with model predictions has not been attempted, because the temperature profiles observed in the experiments are markedly different from the constant temperature assumed in the model.

By incorporating the fuel-nitrogen chemistry in the mechanism for post-flame combustion of H_2/CO mixtures, the present model predicts instantaneous and nearly quantitative conversion of HCN to nitric oxide. Unfortunately, such a fast NO yield is in contradiction with stable species profiles observed in hydrocarbon flames. De Soete conducted experiments in C_2H_2/O_2/argon atmospheric flames seeded with C_2N_2, NH_3 or N_2 [10]. Puechberty and Cottereau studied low-pressure CH_4/O_2 flames doped with NH_3. In both experiments, the HCN profiles exhibited a much slower decay in the post-flame gases than the present model would predict. This discrepancy in the time-histories of stable species can be attributed to various intrinsic differences between real hydrocarbon/air flames and the assumptions of the present model. As mentioned earlier, high radical concentrations characteristic of CO/H_2/O_2 combustion are expected to accelerate the kinetics of HCN disappearance in the model. On the other hand, strong diffusion fluxes of H, O and (to a lesser extent) OH are essential to explain the behavior of a premixed flame. These fluxes are driven by steep concentration gradients present in the reaction zone. Thus, the resulting proportions of H, O and OH entering the post-flame gases of a real flame should be different from the corresponding predictions of the present model. Nevertheless, it is reasonable to assume that approximate relative proportions of active species

such as O, H and OH are predicted by the model, and that Fig. A8.3 provides a rough estimate of the relative importance of the major reaction paths, despite the failure of the model to reproduce correct time-histories.

Current research on the detailed chemistry of hydrocarbon flames should result in better predictions of the absolute levels of active radicals, and a refined model of the fuel-nitrogen mechanism. However, potential discrepancies may still arise from the assumption of a fast and quantitative production of HCN from fuel-nitrogen, and the corresponding failure to include a mechanism of HCN formation in the reaction zone. In fact, a few experiments have shown that peak HCN concentrations can be noticeably smaller than initial fuel-nitrogen levels, and that HCN forms at a finite rate in the reaction zone. Such observations were made by De Soete in atmospheric C_2H_2/O_2/argon flames doped with C_2N_2 or NH_3 [10], and by Puechberty and Cottereau in low-pressure CH_4/O_2 flames seeded with NH_3 [4].

To explain this behavior, Puechberty and Cottereau proposed a mechanism for the conversion of NH_3 to HCN in the reaction zone [4],

$$\text{(fuel-nitrogen}=NH_3) \rightarrow NH_2 \rightarrow NH \rightarrow \left\{ \begin{array}{l} NO \rightarrow \left\{ \begin{array}{l} \xrightarrow{CH_3} HCN \\ \xrightarrow{NH,NH_2} N_2 \end{array} \right. \\ N \rightarrow \left\{ \begin{array}{l} NO \rightarrow HCN \\ \quad\;\; \rightarrow N_2 \end{array} \right. \end{array} \right. \qquad \text{(A8.7)}$$

Note that this mechanism includes reactions which bypass HCN to form molecular nitrogen directly. In addition, nitric oxide is a precursor of HCN by reactions with hydrocarbon radicals. The abundance of such radicals in the reaction zone can conceivably promote the conversion of NO to HCN rather than the reverse mechanism which we have studied. Thus, the rate of HCN formation in the reaction zone may be governed by two competing mechanisms, one which converts NO to HCN by reactions with hydrocarbon radicals, and the other that converts HCN to NCO, NH, N, and eventually NO. The maximum HCN concentration corresponds to a steady-

state level achieved between the two competing mechanisms, and can thus be smaller than the initial fuel-nitrogen content. After the reaction zone, a slower conversion of HCN to NO takes place in the post flame gases, where a depleted radical pool results in slower kinetics. The absence of hydrocarbon radicals prevents further reconversion of NO to HCN, except in very rich flames, where hydrocarbon breakthrough is possible. The mechanism of the HCN breakdown can be described using the simplified sequence (see Fig. 1.1),

$$\mathrm{HCN}\left\{\begin{array}{l} \xrightarrow[\mathrm{OH}]{\mathrm{H}} \mathrm{CN} \\ \xrightarrow[\mathrm{O}]{} \mathrm{NCO} \xrightarrow[\mathrm{H}]{} \mathrm{NH} \xrightarrow[\mathrm{OH}]{\mathrm{H}} \mathrm{N}\left\{\begin{array}{l} \xrightarrow{\mathrm{OH}} \mathrm{NO} \\ \xrightarrow[\mathrm{NO}]{} \mathrm{N_2} \end{array}\right. \end{array}\right. \qquad \text{(A8.8)}$$

Thus, the formation of HCN in the reaction zone may prove an essential feature of the mechanism; different sources of fuel-nitrogen may yield different amounts of HCN, and promote different rates of N_2 production in the reaction zone. For example, note that Crowhurst and Simmons [75] have observed lower conversion rates of ammonia to NO than the corresponding rates of pyridine to NO. More generally, the rate of HCN formation in the reaction zone may depend on the nature of the nitrogen bonding to the fuel-nitrogen compound. The subsequent conversion of HCN to NO in the post-flame gases could be affected by the efficiency of the initial HCN formation. Therefore, a complete study of the fuel-nitrogen mechanism should also focus on the formation of HCN in the reaction zone. Puechberty and Cottereau [4] have postulated that the formation of HCN from NH_3 results from the reactions of early nitric oxide with hydrocarbon radicals. This observation suggests that further experimental work should focus on the high temperature study of elementary reactions such as

$$\begin{aligned} \mathrm{NO} + \mathrm{CH_i} &\rightarrow \mathrm{HCN} + \mathrm{OH_{i-1}}, \\ \mathrm{N_2} + \mathrm{CH_i} &\rightarrow \mathrm{HCN} + \mathrm{NH_{i-1}} \quad (i=1,2,3). \end{aligned} \qquad \text{(A8.9)}$$

References

[1] K. Wark and C. F. Warner: Air Pollution: Its Origin and Control, 2nd ed., Harper and Row, NY (1981).

[2] Ya. B. Zeldovich: J. Acta Physicochim. URSS, 21, 577 (1946).

[3] C. Morley: Combustion and Flame, 27, 189 (1976).

[4] D. Puechberty and M. J. Cottereau: Combustion and Flame, 51, 299 (1983).

[5] B. S. Haynes: Prog. Astron., 62, 359 (1978).

[6] J. A. Miller, M. C. Branch, W. J. McLean, D. W. Chandler, M. D. Smooke, and R. J. Kee: Accepted for presentation at the 20th Symposium (International) on Combustion, University of Michigan, August 1984.

[7] A. N. Hayhurst and I. M. Vince: Prog. Energy Combust. Sci., 6, 35 (1980).

[8] C. P. Fenimore: 13th Symposium (International) on Combustion, The Combustion Institute, Pittsburgh, PA, p. 373 (1971).

[9] B. S. Haynes: Combustion and Flame, 28, 113 (1977).

[10] G. G. De Soete: 15th Symposium (International) on Combustion, The Combustion Institute, Pittsburgh, PA, p. 1093 (1975).

[11] W. M. Shaub: Ph. D. Thesis, Cornell University, Ithaca, NY (1976).

[12] J. N. Mulvihill and L. F. Phillips: 15th Symposium (International) on Combustion, The Combustion Institute, Pittsburgh, PA, p. 1113 (1975).

[13] D. L. Baulch, J. Duxbury, S. J. Grant, D. C. Montague: J. of Phys. and Chem. Ref. Data, 10, Suppl. 1, p. 1/576 (1981).

[14] P. Roth, R. Lohr, and H. D. Hermanns: Ber. Bunsenges. Phys. Chem., 84, 835 (1980).

[15] P. B. Davies and B. A. Thrush: Trans. Faraday Soc., 64, 1836 (1968).

[16] R. A. Perry and C. F. Melius: Accepted for presentation at the 20th Symposium (International) on Combustion, University of Michigan, August 1984.

[17] W. R. Anderson, J. A. Vanderhoff, A. J. Kotlar, M. A. Dewilde, and R. A. Beyer: J. Chem. Phys., 77, 1677 (1982).

[18] G. E. Bullock and R. Cooper: J. Chem. Soc. Faraday Trans., 68, 2175 (1972).

[19] C. T. Bowman and R. K. Hanson: J. Phys. Chem., 83, 757 (1979).

[20] H. Mirels: Phys. Fluids, 9, 1265 (1966).

[21] P. C. T. De Boer and J. A. Miller: Proceedings of the 10th International Shock Tube Symposium, G. Kamimoto, Ed., The Shock Tube Research Society, Japan, p.796 (1975).

[22] R. K. Hanson and S. Salimian: Chemistry of Combuston Reactions, Chapter 6, Survey of Rate Constants in the N/H/O System, W. Gardiner, Ed., Springer Verlag (1984).

[23] D. W. Setser and B. A. Thrush: Proc. Roy. Soc., A288, 256 (1965).

[24] M. B. Colket: J. Quant. Spectrosc. Radiat. Transfer, 31, 7 (1984).

[25] G. Herzberg: Molecular Spectra and Molecular Structure - I. Spectra of Diatomic Molecules, Van Nostrand Reinhold, NY (1950).

[26] I. Kovacs: Rotational Structure in the Spectra of Diatomic Molecules, Elsevier, NY (1969).

[27] R. J. Spindler: J. Quant. Spectrosc. Radiat. Transfer, 5, 165 (1965).

[28] R. G. Bennett and F. W. Dalby: J. Chem. Phys., 36, 399 (1962).

[29] R. K. Hanson, J. P. Monat, and C. H. Kruger: J. Quant. Spectrosc. Radiat. Transfer, 16, 705 (1976).

[30] T. R. Todd, C. M. Clayton, W. B. Telfair, T. K. McCubbin, Jr., and J. Pliva: J. Mol. Spectrosc., 62, 201 (1976).

[31] P. L. Varghese and R. K. Hanson: J. Quant. Spectrosc. Radiat. Transfer, 26, 339 (1981).

[32] R. K. Hanson: Proceedings of the 11th International Symposium on Shock Tubes and Waves, University of Washington Press, Seattle, Washington, p. 432 (1978).

[33] R. C. Millikan and D. R. White: J. Chem. Phys., 39, 3209 (1963).

[34] L. D. Gray Young: J. Quant. Spectrosc. Radiat. Transfer, 11, 1265 (1971).

[35] L. D. Gray Young: J. Quant. Spectrosc. Radiat. Transfer, 12, 307 (1972).

[36] J. Pliva: J. Mol. Spectrosc., 25, 62 (1968).

[37] J. Pliva: J. Mol. Spectrosc., 27, 461 (1968).

[38] P. L. Varghese: Ph.D. Thesis, Stanford University, Stanford, California (1983).

[39] L. J. Drummond: Comb. Sci. and Tech., 1, 415 (1970).

[40] D. A. Bittker and V. J. Scullin: General Chemical Kinetics Computer Program for Static and Flow Reactors, with Application to Combustion and Shock Tube Kinetics, NASA TN D-6586 (1972).

[41] K. J. Schmatjko and J. Wolfrum: 16th Symposium (International) on Combustion, The Combustion Institute, Pittsburgh, PA, p. 819 (1977).

[42] J. C. Boden and B. A. Thrush: Proc. Roy. Soc., A305, 107 (1968).

[43] N. Basco: Proc. Roy. Soc., A283, 302 (1965).

[44] A. Lifshitz and M. Frenklach: Int. J. Chem. Kinet., 12, 159 (1980).

[45] M. B. Colket: Int. J. Chem. Kinet., 16, 353 (1984).

[46] E. C. Rea and R. K. Hanson: Conference on Laser and Electro-Optics, paper # Thu 7-1, Baltimore, May 17-20 (1983).

[47] H. Reisler, M. Mangir, and C. Wittig: Chem. Phys., 47, 49 (1980).

[48] R. N. Dixon: Phil. Trans. Roy. Soc. London, A252, 165 (1960).

[49] J. T. Hougen: J. Chem. Phys., 36, 519 (1962).

[50] G. Herzberg: Ref. [25], p. 232.

[51] R. Mavrodineanu and H. Boiteaux: Flame Spectroscopy, Wiley, NY (1965).

[52] R. Renner: Z. Physik, 92, 172 (1934).

[53] J. A. Pople: Mol. Phys., 3, 16 (1960).

[54] D. E. Milligan and M. E. Jacox: J. Chem. Phys., 47, 5157 (1967).

[55] E. C. Rea, S. Salimian, and R. K. Hanson: Applied Optics, 23, 1691 (1984).

[56] T. R. Charlton, T. Okamura, and B. A. Thrush: Chem. Phys. Lett., 89, 98 (1982).

[57] W. L. Smith and P. A. Warsop: Trans. Faraday Soc., 64, 1165 (1968).

[58] T. E. Sharp and H. M. Rosenstock: J. Chem. Phys., 41, 3453 (1964).

[59] R. N. Dixon: Can. J. Phys., 38, 10 (1960).

[60] B. J. Sullivan, G. P. Smith, and D. R. Crosley: Chem. Phys. Lett., 96, 307 (1983).

[61] G. Herzberg: Ref. [25], p. 405.

[62] A. H. Bowker and G. J. Lieberman: Engineering Statistics, 2nd ed., Prentice Hall, Englewood Cliffs, New Jersey (1972).

[63] JANAF Thermochemical Tables, D. R. Stull and H. Prophet, Project Directors, Natl. Bur. Stand., Washington D.C., NBS 37, 2nd ed. (1971).

[64] W. G. Vincenti and C. H. Kruger: Introduction to Physical Gas Dynamics, R. E. Krieger Publishing Co., Huntington, NY, p. 223 (1977).

[65] C. F. Melius and J. S. Binkley: Fall 1983 Meeting of the Western States Section of the Combustion Institute, paper # WSS/CI 83-61.

[66] G. Herzberg: Molecular Spectra and Molecular Structure - II. Infrared and Raman Spectra of Polyatomic Molecules, Van Nostrand Reinhold, NY (1945).

[67] G. Herzberg: Molecular Spectra and Molecular Structure - III. Electronis Spectra and Electronic Structure of Polyatomic Molecules, Van Nostrand Reinhold, NY (1966).

[68] J. E. Dove and W. S. Nip: Can. J. Chem., 52, 1171 (1974).

[69] A. Szekely, R. K. Hanson, and C. T. Bowman: Int. J. Chem. Kinet., 15, 915 (1983).

[70] E. A. Albers, K. Hoyermann, H. Schacke, K. J. Schmatjko, H. Gg. Wagner, and J. Wolfrum: 15th Symposium (International) on Combustion, The Combustion Institute, Pittsburgh, PA, p. 765 (1975).

[71] A. Szekely, R. K. Hanson, and C. T. Bowman: Int. J. Chem. Kinet., 15, 1237 (1983).

[72] A. Szekely: Ph.D. Thesis, Stanford University, Stanford, California (1984).

[73] J. Duterque, R. Borghi, and H. Tichtinsky: Comb. Sci. and Tech., 26, 1 (1981).

[74] C. Morley: 18th Symposium (International) on Combustion, The Combustion Institute, Pittsburgh, PA, p. 23 (1981).

[75] D. Crowhurst and R. F. Simmons: Combustion and Flame, 51, 289 (1983).

[76] A. H. Shapiro: The Dynamics and Thermodynamics of Compressible Fluid Flow, Vol 1, Ronald, NY (1953).

[77] J. N. Bradley: Shock Waves in Chemistry and Physics, John Wiley and Sons, NY (1962).

[78] G. Herzberg: Ref. [25], p. 248.

[79] G. Herzberg: Ref. [25], p. 222.

[80] G. Herzberg: Ref. [25], p. 250.

[81] S. S. Penner: Quantitative Molecular Spectroscopy and Gas Emissivities, Addison-Wesley, Reading, Mass. (1959).

[82] T. Fueno, K. Tabayashi, and O. Kajimoto: J. Phys. Chem., 77, 575 (1973).

[83] J. L. Dunham: Phys. Rev., 41, 721 (1932).

[84] M. Abramovitz and I. A. Stegun: Handbook of Mathematical Functions, Dover Publications, NY (1970), pp. 298, 325.

[85] W. L. Flower: Ph.D. Thesis, Stanford University, Stanford, California (1976).

[86] W. C. Gardiner, Jr.: Rates and Mechanism of Chemical Reactions, Benjamin, Menlo Park, California (1969).

[87] Handbook of Chemistry and Physics, R. C. Weast, Ed., CRC Press, Cleveland, Ohio (1974), p. E-224.

[88] A. P. Thorne: Spectrophysics, Chapman and Hall Science Paperbacks, London (1974).

[89] J. I. Steinfeld: Molecules and Radiation: An Introduction to Modern Molecular Spectroscopy, The MIT Press, Cambridge, Mass. (1979).

[90] D. Miller and M. Frenklach: Int. J. Chem. Kinet., 15, 677 (1983).

[91] A. Szekely, R. K. Hanson, and C. T. Bowman: J. Phys. Chem., 88, 666 (1984).

[92] M. W. Slack: J. Chem. Phys., 64, 228 (1976).

[93] Unpublished estimates based on transition state theory and best fits of CN records in experiments at 1600°K, 1 atm with $N_2O:C_2N_2:Ar=25:4:971$.

[94] N. Cohen and K. R. Westberg: Chemical Kinetics Data Sheets for High Temperature Chemical Reactions, Aerospace Corporation, ATR-82 (7888)-3 (1982).

[95] G. Dixon-Lewis and D. J. Williams: Comprehensive Chemical Kinetics, 17, 1, C. H. Bamford and C. F. H. Tipper, Ed., Elsevier,

Amsterdam.

[96] L. F. Phillips: Combustion and Flame, 35, 233 (1979).

[97] R. C. Peterson: Ph.D. Thesis, Purdue University, West Lafayette, Ind. (1981).

[98] O. I. Smith, S. I. Tseregounis, and Z. Yijie: Spring 1983 Meeting of the Western States Section of the Combustion Institute.

[99] C. J. Jachimowski and W. M. Houghton: Combustion and Flame, 17, 25 (1971).

[100] D. L. Baulch and D. D. Drysdale: Combustion and Flame, 23, 215 (1974).

[101] G. Herzberg: Ref [25], p. 520.

[102] R. P. Lucht, R. C. Peterson, and N. M. Laurendeau: "Fundamentals of Absorption Spectroscopy for Selected Diatomic Flame Radicals", Report No. PURDU-CL-78-06, Purdue University, West Lafayette, Indiana (1978).

[103] S. W. Benson: Thermochemical Kinetics, 2nd ed., John Wiley, NY (1976).

[104] J. S. Binkley and M. J. Frisch: Int. J. Quantum Chem., in press (1983).

[105] J. O. Hirschfelder, C. F. Curtiss, and R. B. Bird: Molecular Theory of Gases and Liquids, Wiley, NY (1954).

[106] C. T. Bowman: "Proceedings of the Symposium on Emissions from Continuous Combustion Systems", General Motors Research Laboratories, Warren, MI, September 27-28, 1971, Plenum Press, NY (1972), p. 98.